MC 0241. Quarterly Report, NO. 59. MIT Research Laboratory of Electronics. 15 October 1960

BOX 7 FOLDER 24

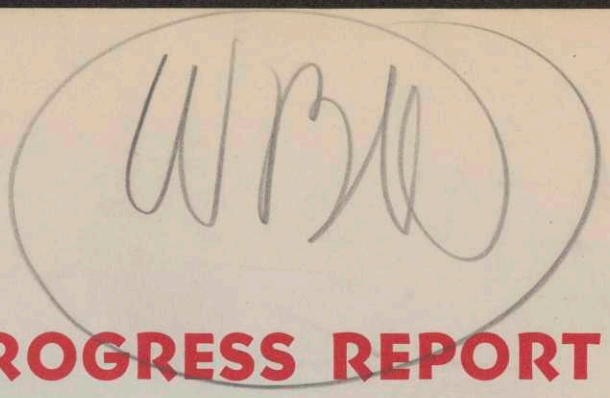

QUARTERLY PROGRESS REPORT

No. 59

OCTOBER 15, 1960

MASSACHUSETTS INSTITUTE OF TECHNOLOGY
RESEARCH LABORATORY OF ELECTRONICS
CAMBRIDGE, MASSACHUSETTS

The Research Laboratory of Electronics is an interdepartmental laboratory of the Department of Electrical Engineering and the Department of Physics.

The research reported in this document was made possible in part by support extended the Massachusetts Institute of Technology, Research Laboratory of Electronics, jointly by the U. S. Army (Signal Corps), the U. S. Navy (Office of Naval Research), and the U.S. Air Force (Office of Scientific Research, Air Research and Development Command), under Signal Corps Contract DA36-039-sc-78108, Department of the Army Task 3-99-20-001 and Project 3-99-00-000.

MASSACHUSETTS INSTITUTE OF TECHNOLOGY

RESEARCH LABORATORY OF ELECTRONICS

QUARTERLY PROGRESS REPORT No. 59

October 15, 1960

Submitted by: J. B. Wiesner
G. G. Harvey
H. J. Zimmermann

TABLE OF CONTENTS

CONTENTS

CONTENTS

CONTENTS

PERSONNEL

Administration

Professor J. B. Wiesner, Director
Professor G. G. Harvey, Associate Director
Professor H. J. Zimmermann, Associate Director
Mr. R. A. Sayers, Personnel and Business Manager
Mr. C. B. Leard, Purchasing Agent
Mr. J. H. Hewitt, Librarian

Advisory Committee

Professor G. S. Brown
Professor N. H. Frank
Professor G. G. Harvey
Professor A. G. Hill
Professor J. B. Wiesner
Professor H. J. Zimmermann

Faculty, Instructors, and Research Associates

Adler, R. B.
Algazi, V. R.
Allis, W. P.
Arden, D. N.
Arthurs, E.
Baghdady, E. J.
Barlow, J. S.
Barnett, M. P.
Bekefi, G.
Bers, A.
Billman, K. W.
Bitter, F.
Bose, A . G.
Bradley, L. C., III
Brandt, B.
Brazier, Mary A. B.
Brown, G. S.
Brown, S. C.
Caldwell, S. H.
Carabateas, E.
Chomsky, A. N.
Chu, L. J.
Clark, M., Jr.
Cochran, J. F.
Dallaire, R.
Davenport, W. B., Jr.
Dean, L. W., III
Dennis, J. B.
Dinneen, D. A.
East, D. A.
Eden, M.
Edgerton, H. E.
Elias, P.
Fano, R. M.
Fay, R. D.
Fletcher, E. W.
Frank, N. H.
Fraser, C.
Freeman, Margaret Z.
Garland, C. W.
Geisler, C. D.
Goldstein, M. H., Jr.
Graham, J. W.
Green, D. M.
Gruber, S.
Guillemin, E. A.
Gyftopoulos, E. P.
Halle, M.
Harvey, G. G.
Haus, H. A.
Hennie, F. C., III
Hill, A. G.
Hofstetter, E. M.
Howard, R. A.
Huffman, D. A.
Ingard, K. U.
Jackson, W. D.
Jacobs, I. M.
Jakobson, R.
Jelinek, F.
Kellner, W. G.
King, J. G.
Klima, E. S.
Kyhl, R. L.
Lee, Y. W.
Lettvin, J. Y.
Locke, W. N.
Loeb, A. L.
Mason, S. J.
Massa, R. J.
Mawardi, O. K.
Maxwell, E.
McCarthy, J.
Melzack, R.
Minsky, M. L.
More, T., Jr.
Nottingham, W. B.
Onesto, N. M.
Peake, W. T.
Penfield, P., Jr.
Radford, W. H.
Rafuse, R. P.
Rogers, H., Jr.
Rose, D. J.
Rosenblith, W. A.
Rosenfeld, J. L.
Schetzen, M.
Schreiber, W. F.
Schwab, W. C.
Searle, C. L.
Shannon, C. E.
Siebert, W. McC.
Smullin, L. D.
Stark, L.
Stevens, K. N.
Stockham, T. G., Jr.
Strandberg, M. W. P.
Sundström, T. I.
Swets, J. A.
Teager, H.
Thornton, R. D.
Tisza, L.
Wall, P. D.
Watanabe, T.
Waugh, J. S.
Whitehouse, D. R.
Whitney, W. M.
Wiesner, J. B.
Wolga, G. J.
Woodson, H. H.
Wozencraft, J. M.
Yngve, V. H.
Zacharias, J. R.
Zimmermann, H. J.

Staff Members and Visitors

Badessa, R. S.
Bates, V. J.
Bell, C. G.
Bennett, Marian C.
Berendsen, H. J. C.
Berger, Eda
Bosche, Carol M.
Brady, P. T.
Brown, R. M.

PERSONNEL

Staff Members and Visitors (continued)

Buhl, D.
Campbell, Elizabeth J.
Carter, E. J. D.
Cerrillo-Lichter, M.
Charney, Elinor K.
Clark, W. A., Jr.
Crist, A. H.
Dupree, T. H.
Farley, B. G.
Ferretti, E. F.
Fields, H.
Fowler, P.
Fujimura, O.
Gerstein, G. L.
Goffin, F. B.
Hall, R. B.
Hayward, G. G.
Head, Avis M.
Hennel, J.
Hewitt, J. H.
Hirsch, H. R.
Hirshfield, J. L.
Holst, P. A.
House, A. S.
Howland, B.
Ingersoll, J. G.
Ingraham, E. C.
Kalin, T. A.
Kannel, Muriel
Kent, R. L.
Keyes, R. V., Jr.
Kiang, N. Y-S.
Kikuchi, M.
Leard, C. B.
Lenneberg, E. H.
Levitan, Ilana
Lieberman, D.
Matthews, G. H.
McCarthy, J. J.
McCulloch, W. S.
McFarlane, R. A.
Nelson, A. H.
O'Brien, D. F.
O'Brien, F. J.
Ogawa, T.
Parikh, R. J.
Pennell, Martha M.
Percival, W. K.
Pitteway, M. L. V.
Pitts, W. H.
Puotinen, D.
Rosebury, F.
Russell, S. R.
Ryan, L. W.
Sandel, T. T.
Satterthwait, A. C.
Sayers, R. A.
Shiffman, C . A.
Smith, P. L.
Smythe, Miriam C.
Stroke, H. H.
Thomas, Helen L.
Verbeek, L. A. M.
Viertel, J. J.
Vineyard, G. C.
Weiss, N. O.
Whitney, R. E.

Research Assistants and Students

Abrahams, P. W.
Abrams, R. A.
Aldrich, J. A.
Allen, J.
Andre, Patricia A.
Andrews, J. M., Jr.
Angelbeck, A. W.
Arazi, E. R.
Arditti, F. D.
Arons, K.
Arunasalam, V.
Asano, S.
Babcock, J. H.
Baldwin, D. E.
Barrett, H. H.
Bellert, Irene
Bennett, J. L.
Blatt, H.
Bliss, J. C.
Bluestein, H. G.
Blum, M.
Blutt, J. R.
Bobrow, D. G.
Bowers, H. C.
Brassert, W. L.
Brayton, R. K.
Breslau, L. R.
Bronfin, B. R.
Brown, H. H., Jr.
Brown, J. E.
Buckley, D. J.
Cahlander, D. A.
Callahan, J. C.
Carr, P. H.
Chi, C. H.
Chiang, T.
Chorney, P.
Clapp, P. C.
Clauser, M. J.
Coccoli, J. D.
Conklin, J. B., Jr.
Cooper, L. Y.
Cooper, R. S.
Cowan, J. D.
Crawford, C. K.
Cunningham, J. E.
Davis, J. W.
DeLong, D. F., Jr.
Dennis, Jane H.
Diamond, B. L.
Dirkman, R. J.
Dix, D. M.
Donadieu, L. J.
Duncan, R. S.
Einarsson, G.
Ernst, H. A.
Feldman, W. C.
Ferrara, J. M.
Fessenden, T. J.
Fohl, T.
Fork, R. L.
Franciszek, K.
Frankel, N. E.
Frankenthal, S.
Freyheit, P. J.
Fujisaki, H.
Futrelle, R. P.
Gallager, R. G.
Gaven, J. V., Jr.
Gesteland, R. C.
Getty, W. D.
Ghais, A. F.
Gibbons, J. V.
Gill, S. P.

Research Assistants and Students (continued)

Glenn, W. H., Jr.
Goblick, T. J., Jr.
Golub, B. P.
Golub, R.
Grant, W. J. C.
Grayzel, A. I.
Greene, R. L.
Griffin, R. H.
Gronemann, U. F.
Hall, J. L., II
Harvey, P. C.
Hecker, M. H. L.
Heinz, J. M.
Heiser, W. H.
Helgesson, A. L.
Hemami, H.
Higier, T.
Hoag, E.
Hodes, L.
Hogan, D. L.
Homeyer, W. G.
Hsieh, H. Y.
Huang, T. S.
Hull, R. J.
Hutchinson, B. H., Jr.
Impink, A. J., Jr.
Ingraham, J. C.
Ivie, E. L.
Jeffers, W. A., Jr.
Johnson, C. S., Jr.
Jones, J. J.
Jones, W. L.
Kailath, T.
Kamen, E. L.
Kelley, P. L.
Ketterer, F. J.
Killias, H. R.
Kleinrock, L.
Kliman, G. B.
Klimowski, P.
Kniazzeh, A. G. F.
Knowlton, K. C.
Kocher, D. G.
Kornacker, K.
Krischer, C.
Larrabee, W., IV
Levine, S.
Levison, W. H.
Lewis, A. T.
Lidsky, L. M.
Liegeois, F. A.
Luce, D. A.
Luke, K. P.
Luckham, D. C.
Lyden, H. A.
Lyon, R. W.
Macurdy, W. B
Magid, L. M.
Maley, M. J.
Maling, G. C., Jr.
Maloney, R. E.
Manning, R. E.
Mannis, F.
Mark, R. G.
Martens, E. J.
Martins, R. B. C.
McWilliams, I. G.
Melcher, J. R.
Mennitt, P. G.
Metzadour, C.
Miller, S. R.
Molnar, C. E.
Monck, C.
Morey, C. F.
Morse, D. L.
Nelson, R. E.
Nolan, J. J., Jr.
Oder, R. R.
Oliver, D. W.
Onyshkevych, L. S.
Pan, J. W.
Park, D. J. M., Jr.
Park, K. C.
Parker, D.
Paul, A. P.
Penhune, J. P.
Peskoff, A.
Pfeiffer, R. R.
Piacsek, S. A.
Pierce, A. D.
Pierson, E. S.
Poduska, J. W.
Poeltinger, A.
Popper, L. A.
Price, G. H.
Radoski, H. R.
Reich, D. L.
Reiffen, B.
Rich, Myrna L.
Roberts, L. G.
Robertson, P. T.
Robinson, C. C.
Robinson, C. E.
Rogers, A. H., Jr.
Ron, A.
Rothleder, S. D.
Rummler, W. D.
Russell, S. B.
Saharian, A.
Sakrison, D. J.
Scarpato, R. R.
Schell, A. G.
Schlossberg, H.
Schneider, A. J.
Schuler, C. J., Jr.
Scott, A. C.
Serafim, P. E.
Shaffner, R. O.
Shane, J. R.
Sinclair, D. C.
Sklar, J. R.
Smallwood, R. D.
Smith, W. W.
Solomon, J.
Spinrad, R. J.
Steelman, J. E.
Stegen, G. R.
Stiglitz, I. G.
Sträussnigg, Rosemarie
Strong, W. J.
Sutherland, I. E.
Tank, Winifred F.
Taub, A.
Telfer, R. B.
Templeton, J. E.
Tepley, N.
Theodoridis, G.
Thornburg, C. O.
Tredwell, J.
Troxel, D. E.
Turnquist, D. V.
Van Trees, H. L., Jr.
Vanwormhoudt, M. C.
Voyenli, K-F.
Walter, W. T.
Weiner, D. D.
Weiner, M. A.
Weinreb, S.
Weiss, R.
Weiss, T. F.
Wemple, S. H.
Wernlein, C. E., Jr.
Wilensky, S.
Willke, H. L.
Wilson, G. L.
Wingerson, R. C.
Winograd, S.
Witzke, K. G.
Wolf, R. P.
Yoshikawa, S.
Zauderer, B.
Ziv, J.

PERSONNEL

Industrial Fellows	Sponsors
Buntschuh, C. D.	ITT Laboratories
Duda, R. O.	Hughes Aircraft Corporation
Hart, T.	ITT Laboratories
Lee, H. B.	Radio Corporation of America
Lipsett, M. S.	Radio Corporation of America
Pomorska, Krystyna	Research Laboratory of Electronics
Rosenshein, J. S.	ITT Laboratories
Rossoni, Paola M.	Research Laboratory of Electronics
Starr, A. W.	Radio Corporation of America

Drafting

Navedonsky, C. P., Foreman
Porter, Jean M.
Rollins, I. E.
Valja, Leida

Machine Shop

Keefe, J. B., Foreman
Barnet, F. J.
Bletzer, P. W.
Brennan, J.
Bunick, F. J.
Cabral, M., Jr.
Carter, C. E.
Coyle, J. E.
Gibbons, W. D.
Liljeholm, F. H.
Marshall, J. J.
McLean, J. J.
Mosby, W. J.
Reimann, W.
Sanromá, J. B.
Schmid, E.
Smart, D. A.

Secretaries

Bertozzi, Norma
Brown, Eileen A.
Burnham, Deborah D.
Clark, Carol
Crimmings, Anne F.
Daly, Marguerite A.
DeToma, Ida M.
Dordoni, Joan M.
Fuller, Margot A.
Galbraith, Joan B.
Gazan, Margaret M.
Geller, Elaine J.
Glode, Linda
Grande, Esther D.
Iorio, Patricia A.
Lesser, Sara L.
Loeb, Charlotte G.
Lund, Barbara J.
McEntee, Doris
Morneault, Beverly A.
Morneault, Diane M.
Nason, Judith T.
Nieroda, Victoria E.
Omansky, Betsey H.
Quiram, Inge
Rhodes, Helen E.
Ritchie, Gail N.
Sarkisian, Nancy
Scalleri, Mary B.
Scanlon, Dorothea C.
Smith, Barbara A.
Smith, Clare F.
Smitherman, Jean C.
Spark, Barbara J.
Staffiere, Rose Carol
Szochalewicz, Olga
Thompson, Willa
Toebes, Rita K.
Van Schaik, Jacoba
Vesey, Patricia Ann
Wilson, Marian

Stock Rooms

Bella, C. J., Foreman
Audette, A. G.
Brosnahan, J. P.
Cloran, H. J.
Doiron, E. J.
Gregor, C. A.
Haggerty, R. H.
Murphy, R. T.
Nolund, J. F.
Riley, J. F.
Sharib, G.
Sincuk, J.

PERSONNEL

Technicians and Assistants

Albert, Aurice V.
Alley, L. E., III
Arnold, Jane B.
Axelrod, F. S.
Bardho, E. L.
Barrett, J. W.
Barrows, F. W.
Bridges, C. A.
Catalan, H. R.
Connolly, J. T.
Cook, T., Jr.
Delmore, Carole A.
Diver, B. J.
Donahue, P. D.
Fitzgerald, E. W., Jr.
Flavin, Dymphna T.
Gay, H. D.
Greenwood, E. L.
Hahn, Ursula
Harris, J. M.
Hewson, Carole A.
Kaplan, R. E.
Karas, P.
Katz, R. F.
Kelly, M. A.
Kierstead, J. D.
Kittredge, W. R.
Konopacki, J. F.
Kulpa, S. M.
Leach, G. M., Jr.
Levine, S. L.
Lindsley, J. R.
McKenzie, J. A.
Morrison, D. G.
Mulligan, W. J.
Nardo, F. K.
Neal, R. W.
North, D. K.
Papa, D. C.
Perrone, T. J.
Plotkin, H. A.
Pratt, D. B.
Remington, L. E., Jr.
Rivard, Janet L.
Savage, R. L.
Schwabe, W. J.
Sears, A. R.
Seid, R. J.
Sewall, Susan T.
Smith, Carlotta S.
Spielman, S.
Sprague, L. E.
Stucki, M. J.
Surh, J-H.
Thompson, J. E.
Thompson, S. W.
Toebes, Lois A.
Tortolano, A. J.
Tracy, T. F., Jr.
Traub, A. C., Jr.
Wagner, R. A.
Whitman, E. C.
Yeager, S. K., Jr.
Yee, F. Q.

Technicians' Shop

Berg, A. E., Foreman
Calileo, D. W.
Fownes, Marilyn R.
Lander, H. J.
Lorden, G. J.

Tube Laboratory

Staff

Haus, H. A.
Smullin, L. D.
Rosebury, F.
Ryan, L. W.

Glass Blowers

DiGiacomo, R. M.
Doucette, W. F.

Technicians

Cox, Alice G.
Drucker, A.
MacDonald, A. A.

MEETING PAPERS PRESENTED

Foreign Service Institute, Department of State, Washington, D.C.
June 7, 1960

N. Chomsky, On generative grammar (invited)

Congrès International "Tubes Hyperfréquences," Munich, Germany
June 7-11, 1960

A. Bers, Space-charge theory of gap interaction with application to multicavity klystrons

ONR Symposium on Principles of Self-Organization, Allerton House, University of Illinois, Monticello, Illinois
June 8-9, 1960

M. Blum, The construction of infallible nets with unreliable neurons (invited)

J. D. Cowan, Many-valued logics and homeostatic mechanisms (invited)

W. S. McCulloch, What puzzles me most? (invited)

L. A. M. Verbeek, Analysis and synthesis of error-minimizing neuronal nets liable to deaths and fits (invited)

American Electroencephalographic Society Meeting, West Harwich, Massachusetts
June 8-11, 1960

J. S. Barlow, F. R. Ervin, G. A. Talland, and M. Victor, An analysis of the EEG in Korsakov's psychosis

Fifty-ninth Meeting, Acoustical Society of America, Brown University, Providence, Rhode Island
June 9-11, 1960

L. W. Dean III, Scattering of sound by sound

Symposium on Abnormal Nervous Function, Boston, Massachusetts
June 12-14, 1960

M. A. B. Brazier, Oscillatory phenomena in the normal and abnormal brain (invited)

Summer Program, "Computers, Science, and Engineering," University of Michigan, Ann Arbor, Michigan
June 13-24, 1960

B. G. Farley, Five lectures in the section on Programming Concepts, Automata, and Adaptive Systems (invited)

American Physical Society June Meeting, McGill University, Montreal, Canada
June 15-17, 1960

G. Bekefi, Microwave measurements of a plasma temperature

S. J. Buchsbaum, L. Mower, and S. C. Brown, Interaction of a bounded microwave field with a cold plasma in a magnetic field

S. Gruber, Receiving-antenna influence on cyclotron radiation measurements

J. L. Hirshfield, Line profiles of cyclotron radiation

D. J. Rose, Energy balance in a thermonuclear reactor

D. R. Whitehouse and G. Bekefi, Diffusion and heat conduction of a weakly ionized plasma

Fourth Berkeley Symposium on Mathematical Statistics, University of California, Berkeley, California
June 20-July 29, 1960

M. Eden, A two-dimensional growth process

Barth Foundation Symposium on Biosimulation, Locarno, Switzerland
June 29-July 5, 1960

W. S. McCulloch, Logisticon: A proper probabilistic multiple truth valued logic for theory of parallel computer composed of threshold devices (invited)

Scuola di perfezionamento in fisica teorica e nucleare, sezione di cibernetica, Naples, Italy
July 8, 1960

W. S. McCulloch, Logisticon (invited)

Mathematics Institute Colloquium on Information and Speech, Johannes Gutenberg University, Mainz, Germany
July 11, 1960

W. S. McCulloch, Logisticon: A proper probabilistic multiple truth valued logic for theory of parallel computer composed of threshold devices (invited)

Seminar of Professor F. Buchthal's Group, Institute of Neurology, University of Copenhagen, Denmark
July 13, 1960

W. S. McCulloch, A proper logic for neurology (invited)

International Conference on Medical Electronics, London
July 21-27, 1960

W. H. Levison and H. Sherman, The measurement of mitral regurgitation by indicator dilution techniques

Fifth International Congress of the International Union of Crystallography, Cambridge, England
Aug. 17-22, 1960

A. L. Loeb, A modular algebra for the description and classification of crystal structures

International Conference on Poetics, Warsaw, Poland
Aug. 18-28, 1960

R. H. Abernathy, Mathematical linguistics and poetics

Teaching Institute of the American Society for Pharmacology and Experimental Therapeutics, Seattle, Washington
Aug. 21-25, 1960

G. L. Gerstein and W. A. Rosenblith, The processing of neuroelectric data; average responses and firing patterns of single neurons (invited)

1960 Western Electronic Show and Convention, San Francisco, California
Aug. 23-26, 1960

E. J. Baghdady, A linear-cancellation technique for suppressing impulse noise

International Conference on Logic and Philosophy of Science, Stanford, California
Aug. 23-Sept. 2, 1960

N. Chomsky, Explanatory models in linguistics (invited)

Summer Institute in Biophysical Science, Cambridge, Massachusetts
Aug. 28-Sept. 9, 1960

G. L. Gerstein, The electrical activity of single units in the auditory cortex (invited)

W. T. Peake, Auditory nerve responses: An input to the central nervous system (invited)

W. A. Rosenblith, Quantitative assessment of the electrical activity of the nervous system (invited)

Fourth London Symposium on Information Theory, London
Aug. 29-Sept. 3, 1960

M. Eden and M. Halle, A characterization of cursive writing

B. G. Farley and W. A. Clark, Jr., Activity in networks of neuron-like elements

T. Kailath, Optimum receivers for randomly varying channels

J. A. Swets and D. M. Green, Sequential observations by human observers of signals in noise

J. M. Wozencraft and M. Horstein, Coding for two-way channels

MEETING PAPERS PRESENTED (continued)

International Conference on Nuclear Structure, Queens University, Kingston, Ontario, Canada
Aug. 29-Sept. 3, 1960

H. H. Stroke and R. J. Blin-Stoyle, Configuration mixing and the effects of distributed nuclear magnetization on hyperfine structure in odd A nuclei

Sixth International Conference on Low Temperature Physics, University of Toronto, Toronto, Canada
Aug. 29-Sept. 3, 1960

J. F. Cochran and Pieternella Cochran, The specific heat of super conductors near the critical temperature

Seminar, Stazione Zoologica, Naples, Italy
Aug. 30, 1960

M. H. Goldstein, Jr., A mathematical model for neuroelectric responses (invited)

JOURNAL ARTICLES ACCEPTED FOR PUBLICATION

(Reprints, if available, may be obtained from the Document Room, 26-327, Research Laboratory of Electronics, Massachusetts Institute of Technology, Cambridge 39, Massachusetts.)

G. Ascarelli and S. C. Brown, Recombination of electrons and donors in n-type germanium (Phys. Rev.)

S. J. Buchsbaum, L. Mower, and S. C. Brown, Interaction between cold plasmas and guided electromagnetic waves (Phys. Fluids)

W. A. Clark, M. H. Goldstein, Jr., R. M. Brown, D. F. O'Brien, and H. E. Zieman, The average response computer, a digital device for computing averages and amplitude and time histograms of electrophysiological resopnses (Trans. IRE, PGME)

G. L. Gerstein and N. Y-S. Kiang, An approach to the quantitative analysis of electrophysiological data from single neurons (Biophys. J.)

M. Harwit, Measurement of thermal fluctuations in radiation (Phys. Rev.)

N. Y-S. Kiang and T. T. Sandel, "Off"-responses from the auditory cortex of unanesthetized cats (Arch. Ital. Biol. (Pisa))

H. R. Maturana, J. Y. Lettvin, W. S. McCulloch, and W. H. Pitts, Anatomy and physiology of vision in the frog (Rana pipiens) (J. Gen. Physiol. Supplement)

T. T. Sandel and N. Y-S. Kiang, "Off"-responses from the auditory cortex of anesthetized cats: Effects of stimulus parameters (Arch. Ital. Biol. (Pisa))

J. A. Swets, Detection theory and psychophysics: a review (Psychometrika)

V. H. Yngve, A model and an hypothesis for language structure (Proc. Am. Phil. Soc.)

LETTERS TO THE EDITOR ACCEPTED FOR PUBLICATION

E. R. Pike and J. Ladell, The Lorentz factor in powder diffraction (Acta Cryst.)

TECHNICAL REPORTS PUBLISHED

(These and previously published technical reports, if available, may be obtained from the Document Room, 26-327, Research Laboratory of Electronics, Massachusetts Institute of Technology, Cambridge 39, Massachusetts.)

269 M. V. Cerrillo, On the Mode of Convergence and Its Correction by Methods of Linear Summability

361 R. J. McLaughlin, FM Weaker-Signal Suppression with Narrow-Band Limiters

363 M. W. P. Strandberg, Unidirectional Paramagnetic Amplifier Design

364 M. Harwit, Measurement of Fluctuations in Radiation from a Source in Thermal Equilibrium (also Technical Report 364, Naval Supersonic Laboratory)

373 W. B. Nottingham, The Thermionic Energy Converter

SPECIAL PUBLICATIONS

E. J. Baghdady, Signal-cancellation techniques for capturing the weaker of two cochannel FM signals (Electromagnetic Wave Propagation, Academic Press, New York, 1960)

J. S. Barlow, A small electronic averager and variance computer for evoked potentials of the brain (Medical Electronics, Iliffe and Sons, Ltd., London, 1960)

J. F. Campbell, Jr., The voltage-current characteristics of a surface-dominated junction (Report on Twentieth Annual Conference on Physical Electronics, Massachusetts Institute of Technology, Cambridge, Mass., March 24-26, 1960)

C. F. Ehret and J. S. Barlow, Toward a realistic model of a biological period-measuring mechanism (Cold Spring Harbor Symposia on Quantitative Biology XXV)

B. G. Farley and W. A. Clark, Jr., Activity in networks of neuron-like elements (Proc. Conference on Aeronautical and Navigational Electronics, May 24, 1960, Trans. IRE, PGANE)

W. B. Nottingham, A simplified method for the computation of the electrical properties of a close-spaced thermionic converter (Report on Twentieth Annual Conference on Physical Electronics, Massachusetts Institute of Technology, Cambridge, Mass., March 24-26, 1960)

W. A. Rosenblith, The electric activity of the nervous system (Quality and Quantity, edited by Daniel Lerner, Glencoe Free Press)

T. T. Sandel, Quantitative methods in the analysis of neuroelectric activity (Medical Electronics, Iliffe and Sons, Ltd., London, 1960)

V. H. Yngve, The depth hypothesis (Proc. Symposia in Applied Mathematics, Vol. XII)

Introduction

This report, the fifty-ninth in a series of quarterly progress reports issued by the Research Laboratory of Electronics, contains a review of the research activities of the Laboratory for the three-month period ending August 31, 1960. Since this is a preliminary report, no results should be considered final.

I. PHYSICAL ELECTRONICS

Prof. W. B. Nottingham
J. F. Campbell, Jr.
D. S. Dunavan
T. Fohl
L. E. Sprague

A. PHYSICAL ELECTRONICS IN THE SOLID STATE

1. THE VOLTAGE-CURRENT CHARACTERISTIC OF SURFACE-DOMINATED SILICON JUNCTIONS

The results of this research were presented by J. F. Campbell, Jr. to the Department of Physics, M. I. T., July 1960, in a thesis that was accepted in partial fulfillment of the requirements for the degree of Doctor of Philosophy.

W. B. Nottingham

2. THE TEMPERATURE DEPENDENCE OF VARIOUS CURRENT COMPONENTS IN GERMANIUM ESAKI DIODES

This study has been completed by D. S. Dunavan. A thesis is being prepared for submission to the Department of Physics, M. I. T., in partial fulfillment of the requirements for the degree of Master of Science.

W. B. Nottingham

II. PLASMA DYNAMICS

A. PLASMA PHYSICS*

Prof. S. C. Brown
Prof. W. P. Allis
Prof. D. J. Rose
Prof. D. R. Whitehouse
Dr. G. Bekefi
Dr. B. Brandt
Dr. S. Gruber
Dr. J. L. Hirshfield
C. D. Buntschuh
J. D. Coccoli
E. W. Fitzgerald
S. Frankenthal
P. J. Freyheit
R. B. Hall
W. R. Kittredge
J. J. McCarthy
W. J. Mulligan
J. J. Nolan, Jr.

1. RADIATION FROM PLASMAS WITH NON-MAXWELLIAN DISTRIBUTIONS

In the interpretation of measurements (1, 2, 3) of the incoherent microwave radiation from plasmas, it is generally assumed that the radiation temperature T_r equals the electron temperature T_e. Here, we investigate departures from this equality when the electrons do not have a Maxwellian velocity distribution.

Consider a plasma in a steady state, in which electrons of concentration n collide with ions or atoms of concentration N. When the steady state is established for both the radiation and the electron gas, the rate of emission of radiation in the frequency interval between ω and $(\omega+d\omega)$ balances the rate of absorption. Incoherent scattering of radiation is neglected here (4, 5).

Let $Q_r(w)$ be the cross section for spontaneous emission of radiation of energy $\hbar\omega$ (for one polarization of the wave) by an electron of velocity w. Let G(w) be the cross section per unit intensity of radiation for stimulated emission, and H(v) be the cross section per unit intensity for stimulated absorption of a photon $\hbar\omega$ by an electron of velocity v. Equating the rate of energy radiated in a given direction with the rate of energy absorbed in that direction, we obtain (for one polarization),

$$\int Nn\, w[Q_r(w)+G(w)B(\omega, T_r)]\, 4\pi\, f(w)\, w^2\, dw\hbar\omega$$

$$= \int Nn\, v\, H(v)\, B(\omega, T_r)\, 4\pi\, f(v)\, v^2\, dv\hbar\omega \qquad (1)$$

where f is the distribution of electron velocities normalized so that $\int_0^\infty f(v)\, 4\pi\, v^2\, dv = 1$, $B(\omega,T_r)$ is the steady-state intensity, and w and v are related by

$$(m/2)[w^2-v^2] = \hbar\omega$$

$$w\, dw = v\, dv \qquad (2)$$

---

*This work was supported in part by the Atomic Energy Commission under Contract AT(30-1)-1842; in part by the Air Force Cambridge Research Center under Contract AF-19(604)-5992; and in part by National Science Foundation under Grant G-9330.

(II. PLASMA DYNAMICS)

The cross sections are independent of the nature of the steady state that prevails in the radiating medium. Their interrelationship is obtained (6) by assuming f to be a Maxwellian distribution, with T_r equal to the electron temperature $T_e = 2\bar{u}/3k$ (where $\bar{u}$ is the mean electron energy), and with the intensity $B(\omega, T_e)$ per unit radian frequency interval equal to the Planck function, $(\hbar\omega^3/8\pi^3c^2)[\exp(\hbar\omega/kT_e)-1]^{-1}$. Then we have

$$Q_r(w)/H(v) = (\hbar\omega^3/8\pi^3c^2)(v/w)^2$$

and (3)

$$Q_r(w)/G(w) = (\hbar\omega^3/8\pi^3c^2)$$

Substituting Eqs. 2 and 3 in Eq. 1, we obtain

$$B(\omega, T_r) = \frac{\hbar\omega^3}{8\pi^3c^2} \int w^2 Q_r(w)\, f(w)\, v\, dv \Big/ \int w^2 Q_r(w)[f(v)-f(w)]\, v\, dv \qquad (4)$$

Equation 4 gives the black-body radiation intensity of a plasma with an arbitrary distribution of electron velocities f and an arbitrary radiation cross section Q_r. In using Eq. 4, we set $B(\omega, T_r)$ equal to $(\hbar\omega^3/8\pi^3c^2)[\exp(\hbar\omega/kT_r)-1]^{-1}$, and thus define the radiation temperature T_r:

$$[\exp(\hbar\omega/kT_r)-1]^{-1} = \int w^2 Q_r(w)\, f(w)\, v\, dv \Big/ \int w^2 Q_r(w)[f(v)-f(w)]\, v\, dv \qquad (5)$$

When $f(v) = \exp\left(-mv^2/2kT_e\right)$, it can be shown that $T_r = T_e$ for any dependence of Q_r on w. At low frequencies, $\hbar\omega/kT_r \ll 1$, $w \to v$, $f(v) \to f(w) - (\hbar\omega/mv)\, \partial f/\partial v$, and Eq. 5 reduces to

$$kT_r = -m \int_0^\infty Q_r(v)\, f(v)\, v^3\, dv \Big/ \int_0^\infty Q_r(v)\, \frac{\partial f(v)}{\partial v}\, v^2\, dv \qquad (6)$$

In applying Eq. 6 to specific cases it is helpful to replace the radiation cross section Q_r by an absorption cross section that can be more easily deduced from measured quantities. In obtaining this absorption cross section, we also indicate how Eq. 6 is derived from the rf conductivity of the plasma.

The intensity of spontaneous emission j_ω is

$$j_\omega = \int Nn\, v Q_r(v)\, 4\pi\, f(v)\, v^2\, dv\hbar\omega \qquad (7)$$

The absorption coefficient α_ω for a tenuous plasma of refractive index close to unity and of low absorptivity (assumptions that are implicit throughout these calculations) is related (1) to the real part of the rf conductivity σ_r by

$$a_\omega = \sigma_r/\epsilon_o c \tag{8}$$

where a_ω is the total absorption, that is, the stimulated absorption reduced by the stimulated emission. The conductivity of a low-temperature plasma (7) (with contributions from ion motion neglected) is given by

$$\sigma_r = -\int (4\pi\, Nn\, e^2/3m\omega^2)\, R(v)\, \frac{\partial f(v)}{\partial v}\, v^4\, dv \tag{9}$$

where e and m are the electron charge and mass, respectively, and R(v) is an absorption cross section whose exact form depends on frequency and on the presence or absence of external magnetic fields. We shall define R(v) when we treat particular cases. To relate $Q_r(v)$ to R(v), we use Kirchhoff's law, $j_\omega = a_\omega B(\omega, T_r)$, in conjunction with Eqs. 7, 8, and 9. We assume f(v) to be Maxwellian (with $T_r = T_e$), and obtain the relation between Q_r and R(v):

$$Q_r(v) = \left(e^2/24\pi^3 c^3 \epsilon_o\right) R(v)\, v^2\, d\omega/\hbar\omega \tag{10}$$

Substituting Eq. 10 for Q_r in Eq. 7, and setting the ratio j_ω/a_ω equal to $B(\omega, T_r)$, we find that

$$kT_r = -m \int_0^\infty R(v)\, f(v)\, v^5\, dv \Big/ \int_0^\infty R(v)\, \frac{\partial f(v)}{\partial v}\, v^4\, dv \tag{11}$$

which is identical with Eq. 6 with R replaced by Q_r.

a. Examples

In making computations from Eq. 11 we shall assume for simplicity, that the distribution function $f = \exp[-b(v/\bar{v})^\ell]$, where b and ℓ are positive constants, and $\bar{v}$ is the mean electron velocity.

(i) Bremsstrahlung

For bremsstrahlung, radiation originates from collisions of electrons with atoms or ions. In this case R(v) is given by

$$R(v) = \frac{\omega^2 Q_m(v)}{\omega^2 + [NvQ_m(v)]^2} \tag{12}$$

where $Q_m(v)$ is the collision cross section for momentum transfer (8). We note that at high frequencies (or at low values of N) R(v) varies proportionally as $Q_m(v)$, while at low frequencies (or at high values of N) R(v) varies as $v^{-2}Q_m^{-1}(v)$.

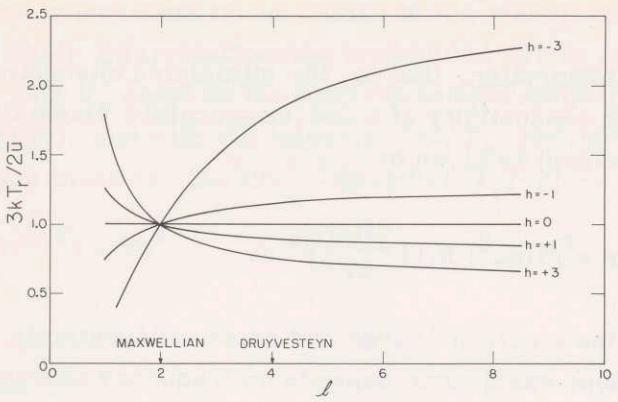

Fig. II-1. Radiation temperature for bremsstrahlung as a function of the distribution of electron velocities; $f(v) \propto \exp[-b(v/\bar{v})]$ and $Q_m(v) = a(v/\bar{v})^{h-1}$.

Figure II-1 shows how the ratio $(3kT_r/2\bar{u})$ varies with the distribution function for different cross sections, $Q_m(v)$. The computations were made in the limit of high frequencies and with the assumption that $Q_m(v) = a(v/\bar{v})^{h-1}$, where a and h are constants. We see that the ratio $(3kT_r/2\bar{u})$ is equal to unity in two cases: when f is Maxwellian, $\ell = 2$; and when $Q_m(v)$ varies inversely as the velocity, h = 0 — that is, when the collisions occur at a constant mean-free time. The departure from unity is greatest for large negative values of h (h = −3 is valid, approximately, in a fully ionized gas).

(ii) Radiation in the Presence of a Magnetic Field

Electrons also radiate as a result of their orbital motion in the magnetic field. The absorption of the wave α_ω depends on θ, the angle between the direction of observation of the radiation and the magnetic field. For purposes of calculation, we assume that only the elliptically polarized wave, whose electric vector rotates with the electrons, contributes significantly to α_ω. This limits the calculations to frequencies not far removed from the electron cyclotron frequency, ω_b. The absorption cross section R(v) then becomes (2)

$$R(v) = \frac{\omega^2 Q_m(v)[(1 + \cos^2\theta)/2]}{(\omega-\omega_b)^2 + (NvQ_m(v))^2} \qquad (13)$$

The frequency spectrum of R(v) given in Eq. 13 is characteristic of a pressure-broadened Lorentzian line. Equation 13 neglects Doppler shift of the radiation that results from the thermal motion of the electrons, and it also neglects the higher harmonics of the cyclotron radiation (9). Integrals that result from a substitution of Eq. 13 in Eq. 11 were evaluated with the aid of functions tabulated by Dingle, Arndt, and Roy (10).

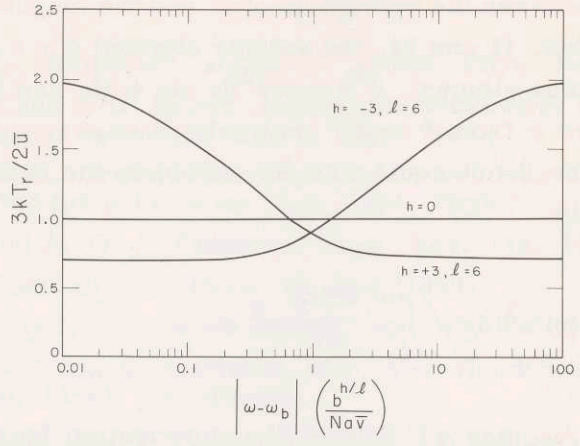

Fig. II-2. Radiation temperature for cyclotron radiation as a function of frequency (pressure broadening).

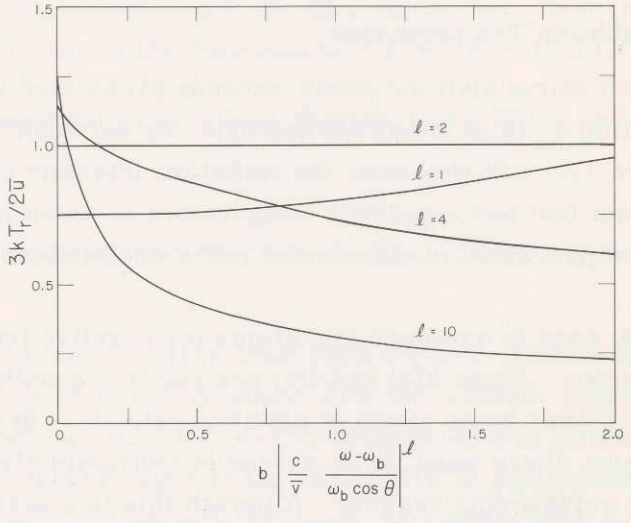

Fig. II-3. Radiation temperature as a function of frequency for cyclotron radiation (Doppler broadening).

Figure II-2 shows a plot of $(3kT_r/2u)$ as a function of frequency. As in Fig. II-1, large departures of the radiation temperature T_r from the electron temperature T_e occur for h = -3.

When thermal motion of the electrons becomes important (Doppler effect), Eq. 13 has the form

$$R(v) = \frac{\omega^2 Q_m(v)[(1 + \cos^2\theta)/2]}{[\omega - \omega_b(1 - (v/c)\cos\phi\cos\theta)]^2 + [NvQ_m(v)]^2} \qquad (14)$$

where ϕ is the angle between the directions of v and the magnetic field. In making calculations of T_r from Eqs. 11 and 14, the volume element $d^3v = 4\pi v^2 dv$ of Eq. 11 must be replaced by the volume element, $d^3v = 2\pi v^2 dv \sin\phi\, d\phi$, and the integrands of Eq. 11 must be integrated over ϕ from 0 to 2π. In the limit of zero collision frequency (i.e., $\langle NvQ_m(v) \rangle \to 0$), and for θ not equal to $\pi/2$, we obtain the radiation temperature for Doppler broadening only:

$$kT_r = -m \int_\Delta^\infty f(v)\, v^3\, dv \Big/ \int_\Delta^\infty \frac{\partial f(v)}{\partial v}\, v^2\, dv \tag{15}$$

where $\Delta = c|(\omega - \omega_b)|/\omega_b \cos\theta$. Use of the distribution functions of the form $f(v) = \exp[-b(v/v)^\ell]$ leads to solutions of Eq. 15 in terms of incomplete gamma functions (11).

Figure II-3 illustrates how T_r varies with frequency in the vicinity of $\omega = \omega_b$.

(iii) Negative Radiation Temperatures

A system in which stimulated emission exceeds stimulated absorption exhibits a negative total absorption α_ω (Eqs. 8 and 9), and thus, by Kirchhoff's law, has a negative radiation temperature (12). In this case the radiation intensity can greatly exceed the intensity from a system that has a positive temperature because in this instance, the electromagnetic waves generated at some point within the medium are amplified in traversing the medium.

Equation 11 can be used to establish conditions for negative temperatures in plasmas, at microwave frequencies. Since R(v) and f(v) are positive quantities, T_r can be negative only if $\partial f(v)/\partial v > 0$ over some range of electron velocity. In other words, in some region of velocity space, there must be an excess of energetic electrons, as compared with the population in neighboring regions. Although this is a necessary condition, the attainment of a negative temperature depends on the precise variation of R(v) with v. A second necessary condition is obtained by integrating by parts the denominator D of Eq. 11. Since $f(\infty) = 0$,

$$D = -f(0)[R(v)v^4]_{v=0} - \int_0^\infty f(v)\, \frac{\partial}{\partial v}\, [R(v)v^4]\, dv \tag{16}$$

from which it follows, that T_r can be negative only if $d[R(v)v^4]/dv < 0$, over some finite region of electron velocity.

Criteria similar to these were given by Twiss (5), who applied them to several specific radiation processes.

G. Bekefi, J. H. Hirshfield

References

1. G. Bekefi, J. L. Hirshfield, and S. C. Brown, Phys. Rev. 116, 1051 (1959).

2. J. L. Hirshfield and S. C. Brown, Incoherent microwave radiation from plasmas in magnetic fields (submitted for publication to Phys. Rev.).

3. G. Bekefi and S. C. Brown, Microwave measurements of the radiation temperature of plasmas (submitted for publication to J. Appl. Phys.).

4. A. V. Phelps and A. O. McCoubrey, Phys. Rev. 118, 1561 (1960).

5. R. Q. Twiss, Australian J. Phys. 11, 564 (1958).

6. G. Cillié, Monthly Notices Roy. Astron. Soc. 92, 820 (1932).

7. W. P. Allis, Motions of electrons and ions, Handbuch der Physik, Vol. 21 (Springer Verlag, Berlin, 1956), pp. 383-444.

8. S. C. Brown, Basic Data of Plasma Physics (Technology Press of Massachusetts Institute of Technology, Cambridge, Mass., and John Wiley and Sons, Inc., New York, 1959).

9. J. L. Hirshfield and S. C. Brown, Cyclotron radiation from a hot plasma (submitted for publication to Phys. Fluids).

10. R. B. Dingle, D. Arndt, and S. K. Roy, Appl. Sci. Research B6, 144-164 (1957).

11. K. Pearson, Tables of the Incomplete Gamma-Function (H. M. Stationery Office, London, 1922).

12. C. Kittel, Elementary Statistical Physics (John Wiley and Sons, Inc., New York, 1958).

2. CESIUM VAPOR TECHNIQUES IN THE PRODUCTION OF FULLY IONIZED PLASMAS

Because of the need for a fairly long fully-ionized plasma column with which to experiment and because of the difficulties with the cesium beam methods previously used (1), the use of cesium vapor for plasma production was attempted. This method is similar to the use of mercury vapor in the production of gas discharges; however, all ionization is done, as with the beam techniques, by contact with a hot tungsten surface. The tube constructed is shown schematically in Fig. II-4.

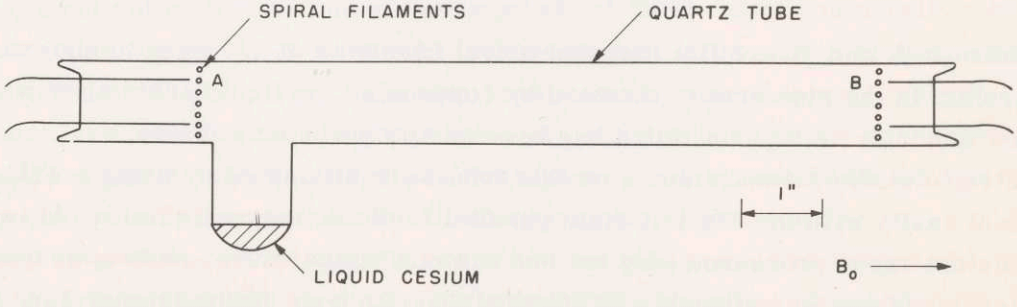

Fig. II-4. Cesium-vapor tube.

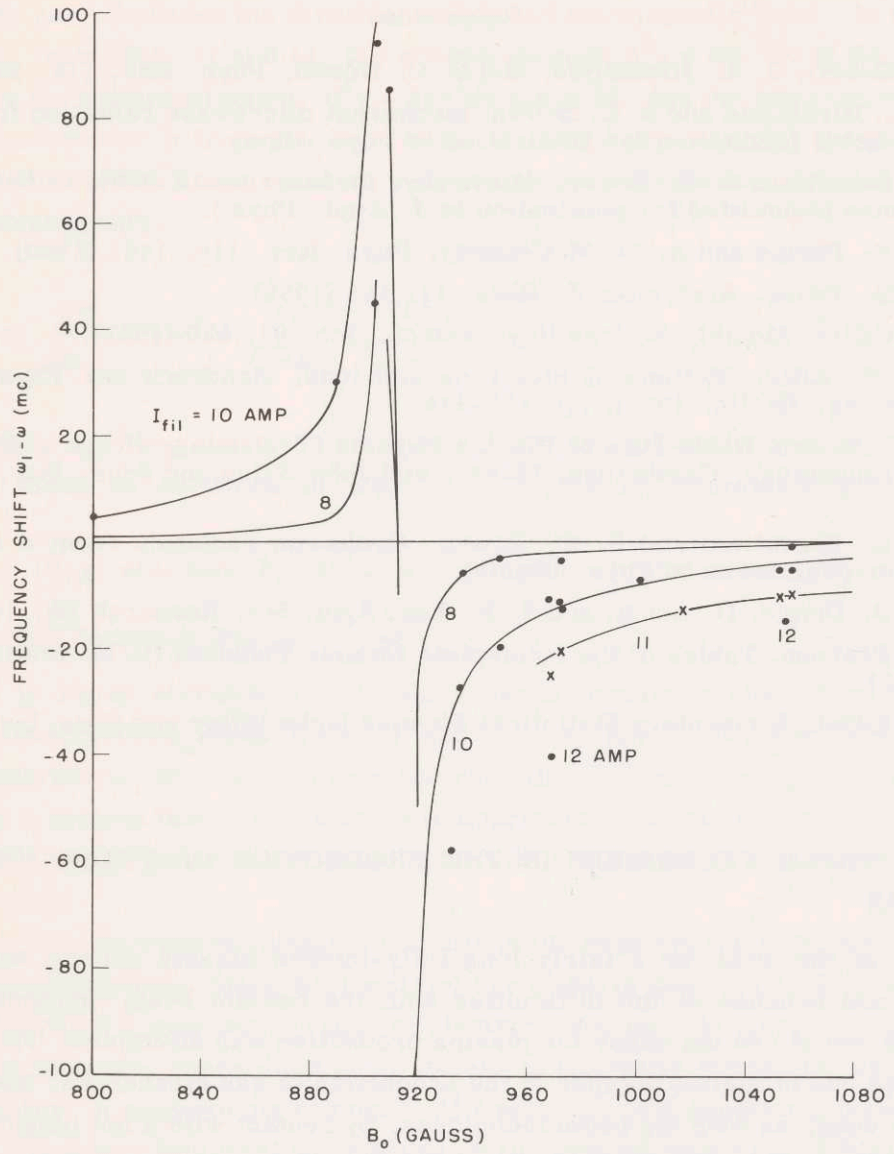

Fig. II-5. Frequency shift of room-temperature cesium plasma.

Filaments A and B are flat tungsten spiral filaments of 5/8 inch diameter. The liquid cesium in the side arm is obtained by condensing the liquid cesium from capsules contained in another side arm which has been sealed off under vacuum.

Electron-density measurements on this tube were attempted by using a TM_{020} mode cylindrical cavity with the electric field parallel to the dc magnetic field. At two different cesium vapor pressures (dry ice and acetone temperature, and room temperature) these measurements were found to be impossible. As soon as the temperature of the tungsten filaments was brought to a high value the cavity Q would steadily decrease until

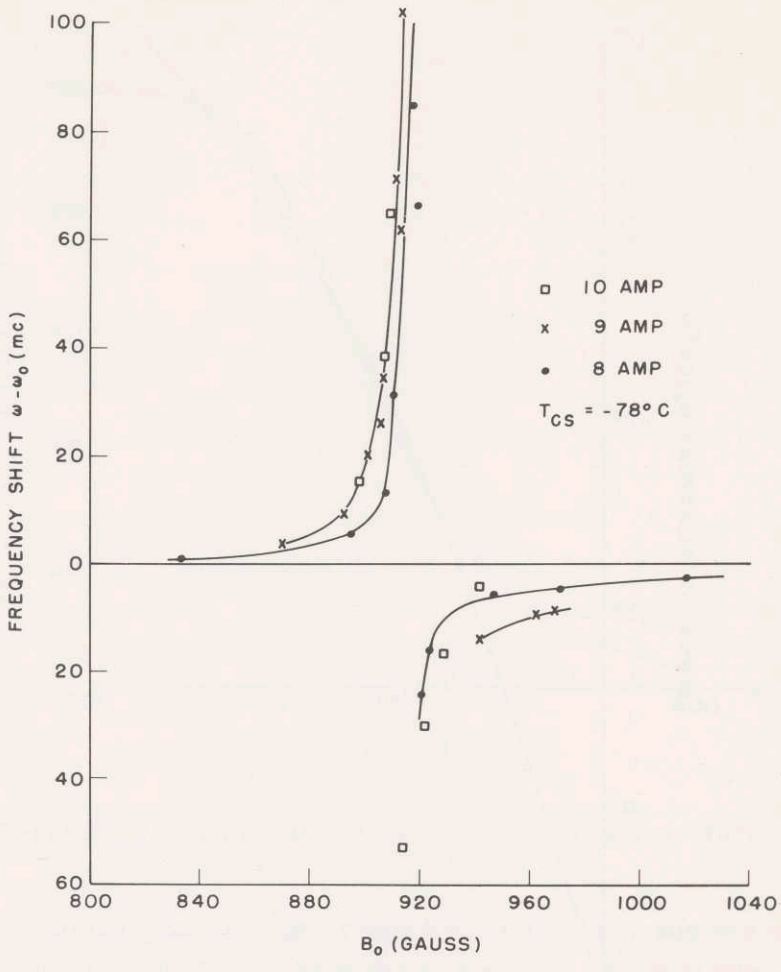

Fig. II-6. Frequency shift of -77°C cesium plasma versus magnetic field.

the absorption could not be found. As a result, no measurements were obtained with the use of this cavity.

In place of the TM_{020} cavity, a TM_{010} mode cavity with the electric field transverse to the dc magnetic field was used for measurement of the electron density. The second cavity did not suffer the malady of the longitudinal-field cavity and density measurements were obtained. Figure II-5 shows the frequency shift of the cavity plotted versus the dc magnetic field. These curves, at room-temperature cesium vapor pressure, indicate that there are insufficient electrons for every ion produced on the hot tungsten surface to produce complete space-charge neutralization. This is seen from the fact that the density continues to increase as the filament current is increased.

Frequency-shift curves with the cesium at -77°C were also obtained and are shown in Fig. II-6. In contrast to the room-temperature results, increasing the filament temperature does very little to increase the electron density because much fewer neutral

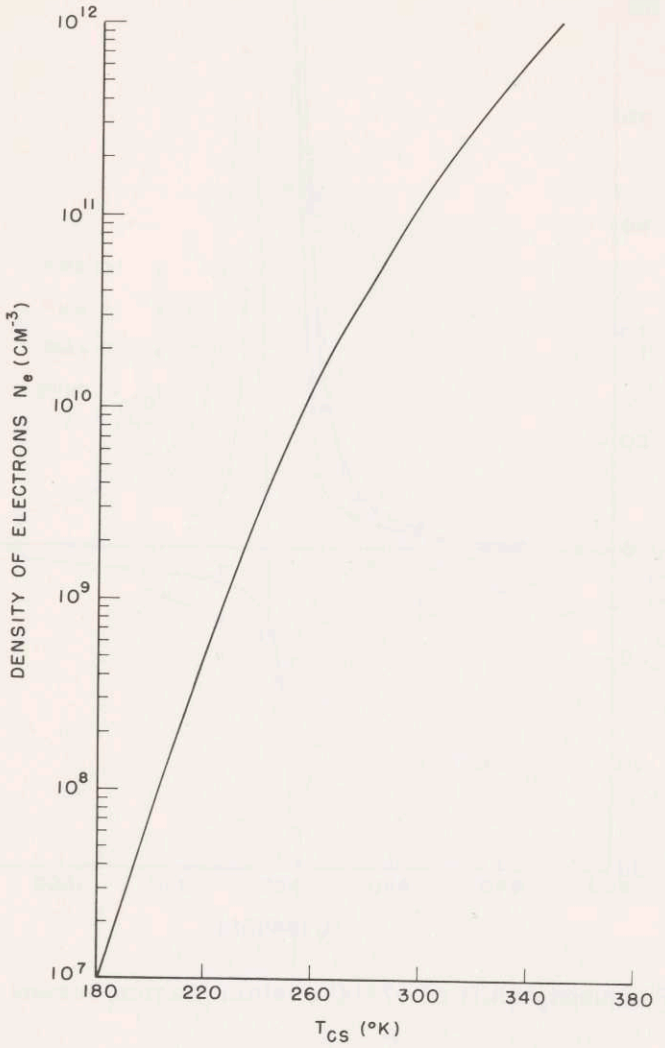

Fig. II-7. Recombination-limited electron density versus T_{Cs}. Plasma length, 13 inches; $\alpha = 3.4 \times 10^{-10}$ cm^3 T^{-1}.

cesium atoms are available for ionization on the hot tungsten surfaces.

Calculation of the electron density from the frequency shift and the known magnetic field yields an approximate density of

$$N_e = 8 \times 10^8 \text{ electrons/cc} \quad (1)$$

at $T_{Cs} = 293°K$ and I = 12 amp, and

$$N_e = 8 \times 10^7 \text{ electrons/cc} \quad (2)$$

at $T_{Cs} = 200°K$.

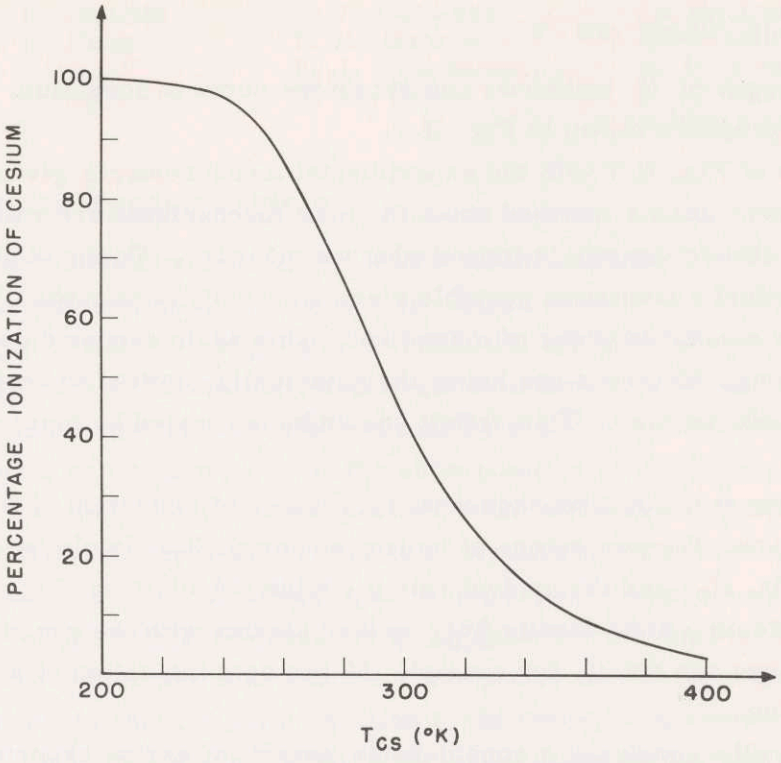

Fig. II-8. Percentage of ionization of cesium versus temperature of cesium.

The electron densities given in Eqs. 1 and 2 are quite low, and one wonders what the fundamental limitations on achieving high densities are. Presumably, there can be no diffusion caused by ion-atom collisions, since the mean-free path (2) at a temperature of 300°K is of the order of magnitude of 10 meters. Another loss mechanism that can be examined is that caused by electron-ion radiative recombination. Thus, in order to find the electron-density limitations, the total loss is assumed to be due only to recombination, and the production rate is assumed to be limited only by the arrival rate of neutral cesium on the hot tungsten filaments. The total loss of ions per second is, then,

$$\frac{dN_i}{dt} = \alpha N_i^2 V \tag{3}$$

where α is the recombination coefficient, and V is the total volume of plasma. Equation 3 is set equal to the arrival rate u_a of neutral cesium atoms (2) which is dependent on the temperature of cesium, T_{Cs}. We then obtain

$$\alpha N_i^2 L = u_a \tag{4}$$

where L is the plasma column length. Using the recombination coefficient (3),

$$\alpha = 3.4 \times 10^{-10} (\text{cm}^3\ \text{sec}^{-1}) \tag{5}$$

and the tube length of 13 inches we can obtain the curve of maximum electron density versus cesium pressure shown in Fig. II-7.

Comparison of Fig. II-7 with the experimental measurements given by Eqs. 1 and 2 shows that the conclusions reached about the loss mechanisms are valid. At 200°K the recombination limited density is indeed what we measure. On the other hand, at room temperature we find a maximum possible electron density nearly two orders of magnitude greater than the measured order of magnitude. This again supports our general conclusion that not enough electrons are being thermionically emitted to neutralize the space charge of all produced ions. This deficit should be corrected by increasing the filament current.

We have, thus far, not discussed what percentage of ionization is obtainable with the cesium-vapor tube. The percentage of ionization versus T_{Cs} is plotted in Fig. II-8; here we have used Fig. II-7 and the arrival rate u_a in the calculation. It can be observed that one can never obtain a high-density fully ionized plasma with the use of a cesium-vapor tube; however, one can obtain, for example, 50 per cent ionization at a density of nearly 10^{11} electrons/cc.

Since, generally speaking, a considerable amount of useful experimentation on the properties of fully ionized plasmas can be obtained with even 50 per cent ionization, the further usefulness of the cesium-vapor tube seems to be evident, and, because of its relative simplicity, it should provide a convenient source with which to work.

R. B. Hall, B. Brandt

References

1. R. B. Hall and G. Bekefi, Cesium plasma, Quarterly Progress Report No. 55, Research Laboratory of Electronics, M.I.T., Oct. 15, 1959, p. 16; No. 56, Jan. 15, 1960, p. 20.

2. W. B. Nottingham, Cesium plasma diode as heat to electrical power transducer, Internal Memorandum, Research Laboratory of Electronics, M.I.T., 1959.

3. S. C. Brown, Basic Data of Plasma Physics (Technology Press of Massachusetts Institute of Technology, Cambridge, Mass., and John Wiley and Sons, Inc., New York, 1959), p. 195.

II-B. PLASMA ELECTRONICS*

Prof. L. D. Smullin
Prof. H. A. Haus
Prof. A. Bers
Prof. D. J. Rose
P. Chorney
L. J. Donadieu
T. H. Dupree
T. J. Fessenden
W. D. Getty
L. M. Lidsky
A. Peskoff
S. D. Rothleder
R. C. Wingerson
S. Yoshikawa

1. THERMAL NOISE FROM PLASMAS

Thermal noise radiated by a plasma at a uniform temperature can be evaluated if the absorption characteristics of the plasma are known (1, 2). This method fails when the plasma is not at a uniform temperature. When the deviation of the distribution functions of the charge carriers from the equilibrium distribution is small, and this includes all cases for which a temperature can be reasonably defined, we would expect that the radiated noise power can be computed as the superposition of the noise powers radiated from the various volume elements of the plasma, each element at a particular temperature radiating the noise power it would radiate at equilibrium if kept at the same temperature. Such an analysis calls for an approach to the fluctuation problem that considers each differential volume element separately as an absorber and emitter of noise power. It calls for the introduction into Maxwell's equations of a source term that is analogous to the source terms in the Langevin equation in the theory of Brownian motion (3). The main problem is, then, the determination of the time- and space-correlation functions of the source term. Aside from their use in problems involving radiation from plasmas, the correlation functions can give helpful insight into the fluctuation processes.

As a first step toward the solution of the complete problem, the correlation functions of the source term have been determined for a uniform plasma, with the use of thermodynamic considerations. The method is applicable to any uniform linear medium for which the relation between the electric field and driven-current density $\bar{J}_d$ can be written in the form

$$\bar{J}_d = \bar{\bar{D}} \cdot \bar{E} \tag{1}$$

where $\bar{\bar{D}}$ is a linear tensor operator in the time and space variables. Maxwell's equations can be written in the form

$$\nabla \times \bar{E} = -\mu_o \frac{\partial \bar{H}}{\partial t} \tag{2}$$

$$\nabla \times \bar{H} = \epsilon_o \frac{\partial \bar{E}}{\partial t} + \bar{\bar{D}} \cdot \bar{E} + \bar{K} \tag{3}$$

where $\bar{K}$ is the source current density. We introduce Fourier transforms in time

*This work was supported in part by National Science Foundation under Grant G-9330.

through the use of periodic substitute functions defined by, for example,

$$\bar{K}(t, \bar{r}, T) = \bar{K}(t, \bar{r}) \qquad -(T/2) < t < (T/2)$$
$$\bar{K}(t+nT, \bar{r}, T) = \bar{K}(t, \bar{r}, T) \tag{4}$$

The Fourier transform of $\bar{K}(t, \bar{r}, T)$ is $\bar{K}(\omega, \bar{r}, T)$.

It is convenient to imagine the uniform medium enclosed in a very large cubic cavity. The field quantities could be expanded in terms of the normal (solenoidal and divergence) modes of the cavity in the usual way. Here, we use modes satisfying periodic boundary conditions (traveling waves). Furthermore, we do not separate the modes into solenoidal and divergence modes but use modes that have both a divergence and a curl. We comprise in one "mode," characterized by a propagation vector $\bar{k}$, the three vector functions

$$\bar{i}_x e^{-j\bar{k}\cdot\bar{r}}, \quad \bar{i}_y e^{-j\bar{k}\cdot\bar{r}}, \quad \bar{i}_z e^{-j\bar{k}\cdot\bar{r}}$$

The propagation vector $\bar{k}$ assumes the values

$$\bar{k} = \frac{2\pi m}{L}\bar{i}_x + \frac{2\pi n}{L}\bar{i}_y + \frac{2\pi p}{L}\bar{i}_z \tag{5}$$

where m, n, and p are integers, and L is the linear dimension of the cube. In the limit $L \to \infty$ the propagation constant may assume a continuous range of values.

Now let us consider any field quantity, say $\bar{K}(\omega, \bar{r}, T)$. When expanded in terms of the normal modes it becomes

$$\bar{K}(\omega, \bar{r}, T) = \sum_{\bar{k}} \bar{K}(\omega, \bar{k}, T, L)\, e^{-j\bar{k}\cdot\bar{r}} \tag{6}$$

where

$$\bar{K}(\omega, \bar{k}, T, L) = \frac{1}{L^3} \int \bar{K}(\omega, \bar{r}, T)\, e^{j\bar{k}\cdot\bar{r}}\, d\bar{r}$$

Introducing these expansions into Maxwell's equations, and omitting the reference to the variables $(\omega, \bar{k}, T, L)$, we obtain

$$-j\bar{k} \times \bar{E} = -j\omega\mu_o \bar{H} \tag{7}$$

$$-j\bar{k} \times \bar{H} = j\omega\epsilon_o \bar{E} + \bar{\bar{D}} \cdot \bar{E} + \bar{K} \tag{8}$$

where $\bar{\bar{D}}$ is now a tensor with components that are algebraic functions of ω and $\bar{k}$.

Equations 7 and 8 may be written in a form that leads directly to an equivalent circuit for the amplitude of each mode. We set $\frac{j\omega\epsilon_o}{|\bar{k}|} \to j\omega C$. We replace the two following square tensors by matrices of third order:

$$\frac{1}{|\bar{k}|}\,\bar{\bar{D}}(\omega, \bar{k}) \rightarrow Y_{ij}$$

$$\frac{1}{j\omega\mu_o|\bar{k}|}\left[\bar{k}^2\,\bar{\bar{I}} - \bar{k}\bar{k}\right] \rightarrow Z_{ij}^{-1}$$

with i, j = x, y, z. We replace the vectors by column matrices of third order:

$$L^{3/2}\frac{1}{\sqrt{|\bar{k}|}}\,\bar{K}(\omega, \bar{k}, T, L) \rightarrow I_{(s)i}$$

$$L^{3/2}\sqrt{|\bar{k}|}\;\bar{E}(\omega, \bar{k}, T, L) \rightarrow V_i \tag{9}$$

$$-jL^{3/2}\frac{\bar{k}\times\bar{H}(\omega, \bar{k}, T, L)}{\sqrt{k}} \rightarrow I_i$$

with i = x, y, z. Using this notation, for each "mode," $\bar{k}$, we may write two matrix equations that follow directly from Eqs. 7 and 8:

$$V_i = -Z_{ij}I_j \tag{10}$$

$$I_i = j\omega CV_i + Y_{ij}V_j + I_{(s)i} \tag{11}$$

The "voltages" and "currents" incorporating the three spatial components of the electric and magnetic fields have been normalized so that, for example,

$$\frac{1}{2}C\overline{|V_x|^2} = \frac{1}{2}\epsilon_o\overline{E_x(\omega, \bar{k}, T, L)\;E_x^*(\omega, \bar{k}, T, L)}\;L^3 \tag{12}$$

gives the energy storage of the x-component of the electric field of the mode $\bar{k}$ at the frequency ω and within the frequency interval $\Delta\omega$. A corresponding relation exists for all other energy storages. Similarly, for $\bar{K} = I_{si} = 0$,

$$\frac{1}{2}\overline{\left(V_iI_i^* + I_iV_i^*\right)} = \frac{1}{2}\overline{V_i\left(Y_{ij} + Y_{ji}^*\right)V_j^*} = \left(\bar{E}^*\cdot\bar{\bar{D}}\cdot\bar{E} + \bar{E}\cdot\bar{\bar{D}}^*\cdot\bar{E}^*\right)L^3 \tag{13}$$

is the power dissipated in the mode $\bar{k}$. Equation 13 shows that for a dissipative medium the tensor

$$\bar{\bar{D}} + \bar{\bar{D}}^\dagger$$

is positive definite or semidefinite for all real values of ω and $\bar{k}$.

We may now use the equivalent circuit (Eqs. 10, 11) to obtain the statistical

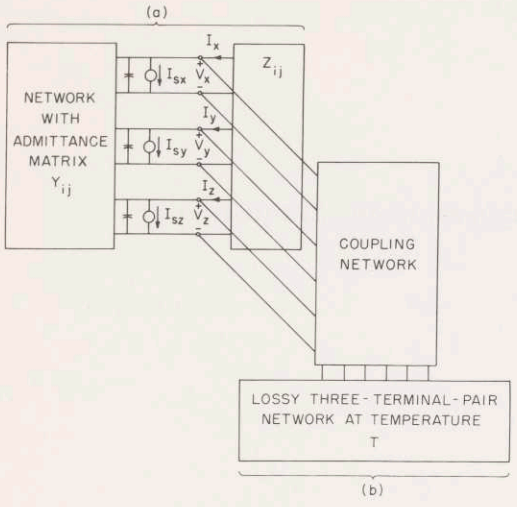

Fig. II-9. Coupling of cavity to electromagnetic system.

properties of $\overline{\overline{K}}(\omega, \bar{k}, T, L)$.

If the cavity is at temperature T and coupled to another electromagnetic system at the same temperature, the power received by the cavity must equal the power emitted by it. In principle, any particular mode of the cavity could be coupled in a lossless manner with some other three terminal-pair network with the aid of an appropriately phased distribution of pickup antennas. Using the equivalent circuit for the excitation of the mode, we can represent the coupling scheme as shown in Fig. II-9. We can now borrow the results derived for linear circuits with thermal noise (2). The condition that there be no net power flow between the two three terminal-pair networks (a) and (b), of which network (b) has internal noise sources corresponding to a uniform temperature T of the network, will be met if, and only if, the noise current generators of network (a) satisfy the requirement (2)

$$\overline{I_{si} I_{sj}^*} = \kappa T \Delta f \left(Y_{ij} + Y_{ji}^* \right) \tag{14}$$

where κ is Boltzmann's constant. We use the letter T for temperature and for the period of the substitute process. Since the temperature always appears in conjunction with κ, no confusion should arise. (The impedance matrix Z_{ij} does not enter into expression 14 because of its lossless, anti-Hermitian character, $Z_{ij} = -Z_{ji}^*$.) Introducing the explicit expressions for I_{si} and Y_{ij} from the equivalent circuit for the cavity mode, we obtain

$$L^3 \overline{\overline{K}(\omega, \bar{k}, T, L)\, \overline{\overline{K}}^*(\omega, \bar{k}, T, L)} = \left[\overline{\overline{D}}(\omega, \bar{k}) + \overline{\overline{D}}^{\dagger}(\omega, \bar{k}) \right] \kappa T \Delta f \tag{15}$$

where the dagger indicates the complex conjugate transpose of the tensor $\overline{\overline{D}}$.

Next, consider two different modes characterized by the propagation constants $\bar{k}$ and $\bar{k}'$. For each of these modes an equation of the form of Eq. 15 holds as a consequence of the network theoretical law (Eq. 14). A lossless coupling between these two modes results in the equivalent circuit of Fig. II-9. The net power transfer between the two networks will equal zero if and only if the noise sources of networks (a) and (b) are uncorrelated

$$L^3 \overline{K(\omega, \bar{k}, T, L)\, K^*(\omega, \bar{k}', T, L)} = 0 \qquad \bar{k} \neq \bar{k}' \tag{16}$$

Equations 15 and 16 yield, in the limit $T \to \infty$, $L \to \infty$, for the Fourier transform of the correlation function

$$\bar{\bar{S}}_K(\omega, \bar{k}) = \frac{\kappa T}{(2\pi)^4} \left[\bar{\bar{D}}(\omega, \bar{k}) + \bar{\bar{D}}^\dagger(\omega, \bar{k})\right] \tag{17}$$

(See ref. 4.) This law is a generalization of the Nyquist formula to distributed media.

The space-time correlation function is found from the inverse Fourier transform

$$\bar{\bar{R}}_K(\tau, \rho) = \frac{\kappa T}{(2\pi)^4} \int_{\bar{k}} \int_{\omega} \left[\bar{\bar{D}}(\omega, \bar{k}) + \bar{\bar{D}}^\dagger(\omega, \bar{k})\right] e^{j\omega\tau - j\bar{k}\rho}\, d\bar{k}d\omega \tag{18}$$

a. Application to an Electron Plasma

In a plasma in the absence of an applied dc magnetic field the field and driven-current density of the longitudinal plasma waves are related by the following relationship:

$$J_{dx}(\omega, \bar{k}) = DE_x = \left(j \frac{e}{m} \int \frac{u(\partial f_o/\partial u)}{(\omega - uk)}\, du\right) E_x \tag{19}$$

Since only the real part of D enters into the computation of the correlation function, we are interested only in Re(D) for real ω and k. Using the proper path and integration in the u-plane (5), as shown in Fig. II-10, we find that the only contribution to Re(D) comes from the integration around the semicircle:

$$\mathrm{Re}(D) = \frac{e}{mk} \pi u \left.\frac{\partial f_o}{\partial u}\right|_{u=\omega/k}$$

$$= \omega_p \epsilon_o \left(\frac{\pi}{2}\right)^{1/2} \frac{\omega^2}{\omega_p^2} \frac{1}{(ka)^3} \exp\left[-\frac{\omega^2}{2\omega_p^2 (ka)^2}\right] \qquad k > 0 \tag{20}$$

with

$$\omega_p^2 = \frac{e^2}{m} \frac{n_o}{\epsilon_o}$$

and

$$a^2 = \frac{\kappa T}{m\omega p^2}$$

where a is the Debye radius.

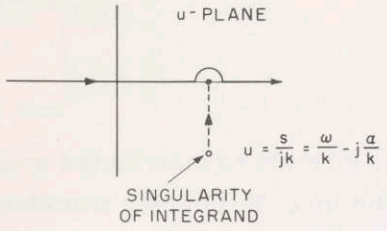

Fig. II-10. Integration path in u-plane for Eq. 4.

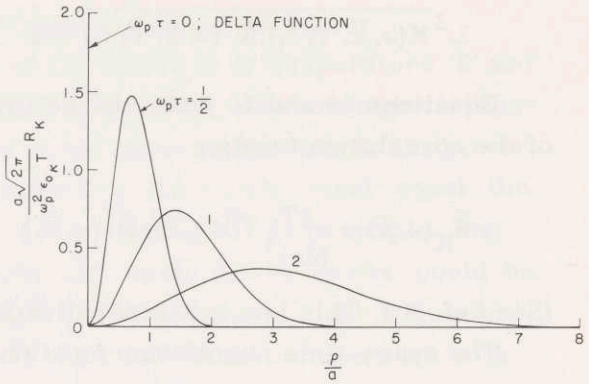

Fig. II-11. Plot of R_K versus ρ/a with $\omega_p\tau$ as parameters.

When $k < 0$, the path of integration in the u-plane has to be indented downward. We find that Re(D) is symmetric in k. Using Eq. 18 in one-dimension, we find

$$R_K(\tau, \rho) = \frac{e^2}{(2\pi)^{1/2}} \left(\frac{\kappa T}{m}\right)^{1/2} n_o \frac{m\rho^2}{\kappa T|\tau|^3} \exp\left(-\frac{1}{2}\frac{m\rho^2}{\kappa T \tau^2}\right) \tag{21a}$$

$$R_K(\tau, 0) = 2e^2 \left(\frac{\kappa T}{m}\right)^{1/2} n_o \delta(\tau) \tag{21b}$$

and

$$R_K(0, \rho) = \frac{e^2}{m} \kappa T n_o \delta(\rho) \tag{21c}$$

Figure II-11 shows cuts through $R_K(\tau, \rho)$ at various values of $\omega_p\tau$ as a function of ρ/a. The maxima of the graphs in Fig. II-11 lie at $\rho_m = (2\kappa T/m)^{1/2} \tau$ and decrease inversely with τ. (Compare Eq. 21a.) The maxima of the crosscorrelation "move out at a speed" corresponding in order of magnitude to the thermal velocity of the electrons.

The self-correlation of $\overline{K}(t, \bar{r})$ is a delta function indicating a random excitation with very (ideally, infinitely) short relaxation time. Similarly, the crosscorrelation of $\overline{K}(t+\tau, \bar{r})$ and $K(t, \bar{r}')$ is zero for all values of $\bar{r} \neq \bar{r}'$ and $\tau = 0$. This means that the noise excitations at different points in the plasma are mutually correlated only after the time necessary for thermal electrons at $\bar{r}$ to have moved to $\bar{r}'$, and vice versa. The function $R_K(\tau, \rho)$ is proportional to the particle density n_o, and does not depend in any other way upon n_o. Since R_K can be ascribed to the random fluctuations of the particle density, its proportionality to n_o is a simple consequence of the Gaussian law of the mean-square deviation of a random number. Equation 21a does not change character with the density of the plasma and shows, therefore, that the same fluctuation laws that produce the

source current are applicable to dense, as well as to rarefied, plasmas. For the latter, however, it is not difficult to derive R_K from physical reasoning. It can be shown that the following form for the ensemble average of the density function perturbation f_1 is valid for a thin plasma:

$$\overline{uvf_1(t, x, u)\, f_1(t+\tau, x', v)}\, dudv = uf_o(u)\, \delta\left(\tau - \frac{x'-x}{u}\right) \delta(u-v)\, dudv \qquad (22)$$

with $\rho = x' - x$; and δ, the Dirac delta function.

Using Eq. 22 and noting that the source-current density K is given by $K = e \int uf_1(t, x, u)\, du$, we have for the correlation function, $\overline{K(t+\tau, x)\, K(t, x)}$, the result of Eqs. 21.

Thus the flucutation formulas (Eqs. 21) for a thin plasma can be derived from physical reasoning alone. It is the merit of the general relation (Eq. 18) that it yields a result that is correct for dense, as well as thin, plasmas.

H. A. Haus

References

1. S. M. Rytov, Theory of Electrical Fluctuations and Thermal Radiation (Izd-vo Akademiia Nauk S. S. S. R., Moscow, 1953).

2. H. A. Haus and R. B. Adler, Circuit Theory of Linear Noisy Networks (Technology Press of Massachusetts Institute of Technology, Cambridge, Mass., and John Wiley and Sons, Inc., New York, 1959).

3. N. Wax, Selected Papers on Noise and Stochastic Processes (Dover Publications, Inc., New York, 1954).

4. Compare the laws used here with their one-dimensional counterparts in W. B. Davenport and W. L. Root, An Introduction to the Theory of Random Signals and Noise (McGraw-Hill Publishing Company, New York, 1958).

5. L. Landau, Electron oscillations treated by the Laplace transform method, J. Phys. (U. S. S. R.) 10, 25 (1946).

2. HOLLOW-CATHODE DISCHARGE

The experimental study of the hollow-cathode discharge and its interaction with an injected electron beam continues. New equipment required for the continuation of experiments described in Quarterly Progress Report No. 58 (pages 35-41) is being designed and fabricated.

The interaction of the discharge and a pulsed electron beam injected along the discharge axis was observed over a wide range of discharge operating conditions. The method used for injection of the electron beam was previously described (1). Observations were made of the current pulse produced by beam electrons collected by the hollow

cathode. We observed that the magnitude of the current pulse is a function of the discharge parameters. The peak-to-peak magnitude was greatest when the discharge current and pressure were relatively low, and the magnitude decreased continually with increasing current or pressure until the pulse was no longer visible in the noise. We also observed the collected current pulse when no discharge was running, but the gas flow through the hollow cathode and the potential of the hollow cathode were the same as those that exist under discharge operating conditions. Some of the prominent characteristics of the current pulse wave shape under these conditions were also present in the current pulse observed when the discharge was running. In particular, the pulses have a negative peak, caused by charge flow that is opposite to the flow of the collected electrons, which takes several microseconds to decay. From this observation we concluded that the response to the injected electron beam is closely related to the dynamics of the hollow cathode itself, as well as to the dynamics of the electron-beam interaction with the discharge.

The effect of the discharge column on the reflection of microwave energy from the end of an open waveguide was studied with the use of the method previously described (1). The frequency range covered was 12.4-18 kmc. The discharge column passes approximately 1 cm from the open end of a rectangular waveguide. An electronically swept backward-wave oscillator was used as a signal source. Recordings were made, with and without the discharge running, of the output of a crystal detector mounted on an H-plane Tee. Comparisons made of the two recordings, which were obtained for a wide variety of discharge operating conditions, indicate that the oscillator frequency was always less than the plasma resonant frequency. Further experiments at higher frequencies, which will include measurement of transmission as well as reflection, are being planned.

A new vacuum chamber for the hollow-cathode discharge is under construction. A fivefold increase in pumping speed is expected because of rearrangement of the vacuum pump system. If operation of the discharge at lower pressures is possible, it is hoped that troublesome discharges occurring in the electron gun will be eliminated.

W. D. Getty, L. D. Smullin

References

1. W. D. Getty and L. D. Smullin, Experimental results of the study of the hollow-cathode discharge, Quarterly Progress Report No. 58, Research Laboratory of Electronics, M.I.T., July 15, 1960, pp. 35-41.

3. STUDIES OF THE HOLLOW-CATHODE DISCHARGE PLASMA

The hollow-cathode discharge plasma facility now in use is basically similar to that described in previous reports (1, 2). The experiments carried out during the last

quarterly period were mainly of an exploratory nature, and serve primarily to indicate promising avenues of research. However, enough detailed work has been carried out to enable us to describe and explain, in some detail, the properties of the external plasma column. The operational mechanism of the cathode itself remains in doubt, although several experiments have been devised and will soon be performed, which we hope will clarify this point. Our discussion is divided arbitrarily into several sections.

a. Cathode Variations

(i) High-current cathodes. The addition of tantalum radiating fins to a cathode tube with slightly thicker walls, for reduction of resistive heating, results in a significant increase in arc current capacity. One cathode configuration has been operated for short periods at 240 amp (>3000 amp/cm^2 at the orifice) with no sign of impending failure. Further trials will be performed when an adequate power supply becomes available. With an improved design of the radiating fins, a similar cathode was operated over the range 3-200 amp.

(ii) Large-diameter cathodes. Several sizes of tantalum tubing have been employed. The largest, thus far, is of 0.5-inch I.D. tubing. Operation was stable with a 0.5-inch diameter external plasma, 6 inches in length, for arc currents in excess of 90 amp. The external pressure at this current was approximately 2×10^{-3} mm. The instability at lower currents appears to be caused by conductive heat transfer to the cathode mounting. The operating temperature appears to be extraordinarily low, and further investigation of this point is planned.

(iii) Cathode material. Because tantalum undergoes a destructive reaction in a hydrogen atmosphere, several tungsten cathodes were constructed and used for the generation of a hydrogen-arc plasma. The region of stable operation of the hydrogen arc is smaller than the stable region for the other gases used and, for this reason, the bulk of the work discussed in this report refers to an argon-arc plasma.

b. Configuration Variations

(i) Gas flow and pressure. A study was made of the variation of electrical parameters with both gas flow and ambient pressure as independent variables. The pressure was varied from 10^{-4} to 5×10^{-3} mm Hg and flow from 0.1 to 3.0 cc-atm/sec. The results show a strong dependence of electrical properties of the arc upon ambient pressure, which has not yet been adequately explained.

(ii) Baffled reflex arc. A series of experiments was performed in which both the cathode and an annular anode were located at the same end of the magnetic-field region (see Fig. II-12). By control of the apertures of the three diffusion pumps, it is possible to control the relative pressures in the right-hand and left-hand regions. In particular, we found that the background pressure in the arc region may be reduced by at least a

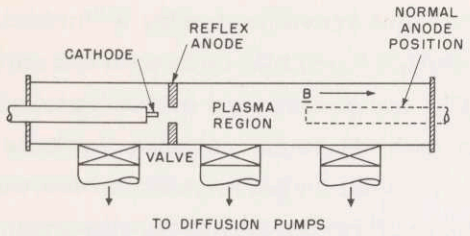

Fig. II-12. Experimental arrangement for reflex arc operation.

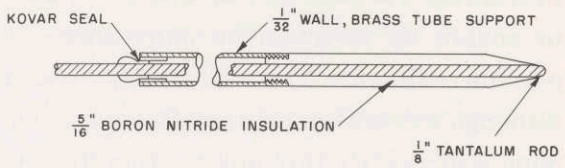

Fig. II-13. Probe detail.

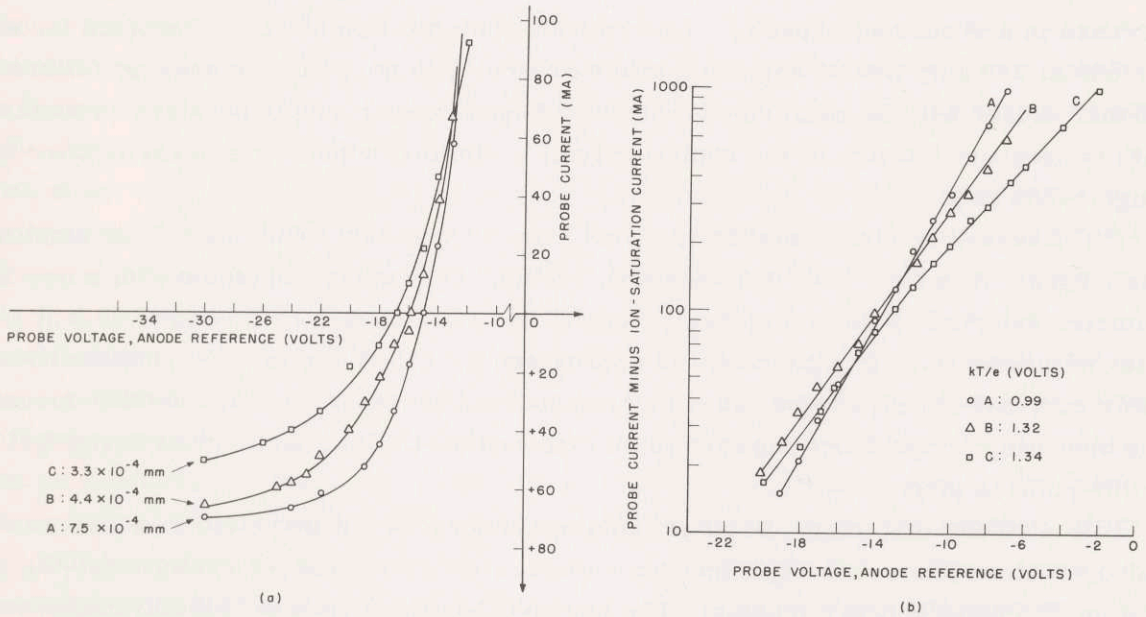

Fig. II-14. (a) Probe characteristics for several neutral argon gas pressures for reflex arc arrangement: arc current, approximately 20 amp; axial magnetic field, approximately 400 gauss; background argon pressure for each measurement is indicated on curves. (b) Semilogarithmic plot of data presented in (a). Temperatures for each case were determined from simple probe theory.

factor of 3 by throttling the left-hand pump (Fig. II-12) while reducing the gas flow rate.

c. Preliminary Diagnostics

(i) Probes. The plasma energy and density attained in the operation of the hollow-cathode discharge plasma are such that application of the standard "nonperturbing" analytic techniques is rendered quite difficult. Because of this, recourse was had to the use of ordinary Langmuir probes (see Fig. II-13). The comparatively large size is used for several reasons: (a) The probe is large compared with the electron Larmor radius

and small compared with that of the ions. This leads to some simplification of interpretation. (b) A large heat capacity and conductivity are necessary because of the high plasma density. (c) The edge effect is rendered reasonably small.

Pulsed techniques were ruled out, at least for the present, because of the very high noise level at several kilocycles.

A set of probe curves for slightly differing ambient pressures is presented in Fig. II-14a and -14b. A plasma temperature of approximately 1 volt and density of approximately 5×10^{12}, as shown in the curves, is quite representative of the normal operating range.

The shape of the probe curve is strongly dependent upon the orientation of the probe face with respect to the magnetic-field lines. For a probe perpendicular to the main B_z field, it is found that the ratio of electron-to-ion saturation currents is in the range 10-100, whereas classical probe theory predicts a value of at least $(m_i/m_e)^{1/2} \approx 280$ for argon. This is accounted for by the fact that electrons are hindered in their motion across field lines, and only those in the flux tube intersecting the probe face are drawn by the probe. This tube is quickly drained, and the electron current drawn is then more accurately a measure of diffusion into the flux tube than it is of local electron density. The ion saturation current, because of its small magnitude and because the ions may, to first order, be considered unaffected by the fields used, is indicative of the local density. This affords a convenient measure of plasma density variation within the apparatus and may, with the assumption of equal ion and electron temperature, be converted to absolute density. This is a conservative assumption in the density because it is extremely unlikely that the ion temperature exceeds that of the electrons.

Several other points are apparent from inspection of the curves. The electron current curve is quite accurately logarithmic. Comparison of charge density to the neutral density, as shown by the background pressure, indicates fractional ionization greater than 25 per cent at 20 amp.

(ii) Noise measurements. The noise signals imposed on both biased and floating probes were investigated for the frequency range from dc to approximately 1 mc. Although results, thus far, are inconclusive and somewhat nonreproducible, it appears that a strong signal with a frequency of 500 cps-10 kc is usually present. It is believed that this is caused by $\vec{E} \times \vec{B}$ rotation about the axis of the discharge, an effect similar to that observed by Nedeigh (3).

The discharge appears, under some conditions, to have two stable modes of operation, as indicated by sharp (approximately 50 per cent) changes in probe saturation current and noise level. This is similar to the observations of Lehnart (4), although in one case the change is discontinuous.

A probe situated at one side of the arc will show a dip (approximately 10 per cent) in ion saturation current if a probe placed diametrically opposite is driven at

approximately 900 cps. This may be ascribed to a sound wave in the sense of Alfvèn (5).

d. Other Observations

(i) Pulsed arc experiments. Pulsing of the arc current to significantly higher values than normal by discharge of a capacitor bank through the operating arc appears to be a very useful technique and several trials of this technique have been performed. It is interesting to note that the decay of the capacitive charge is given quite accurately by using the value of plasma resistance as given by Spitzer (6) and taking T = 10, 000°K. This is obviously fortuitous because the presence of sheaths and primary (high-energy) electrons obviates the applicability of simple theory.

(ii) "Short-circuited" field lines. Generally, field lines intersect the glass tube and therefore are not short-circuited in the sense of Simon (6). For this case, the ion saturation current at the walls is approximately 5 ma for the nominal probe size. If a grounded metal shorting plate is used, the ion saturation current drops to 0. 3 ma at the same position. The variation of transverse diffusion with differing return current paths is seen to be a quite pronounced effect.

e. Discussion

The values of plasma energy and density as measured by probes (1 ev, 5×10^{12} cm^{-3}) are corroborated by several other measurements: microwave measurements by Getty (7) that show the plasma to be opaque up to 17 kmc; estimates based on current density in the visible beam; spectrographic studies (2); and the observation that the floating potential is most negative at the center of the beam, and increases monotonically toward the walls (8). Comparison of these figures with the neutral-particle density at the operating pressures directly indicates that the fractional ionization is at least 25 per cent for arc current of 20 amp. At 1 ev the coulomb cross section (approximately 6×10^{4} $angstrom^{2}$) so greatly exceeds the neutral scattering cross section (<10 $angstrom^{2}$) that there can be no doubt that the plasma behavior is determined by electrostatic interactions; that is, we have a "highly ionized plasma."

Calculation of the Larmor radii of the confined particles indicates that the plasma generated is subject to hybrid confinement with magnetic confinement of the electrons and electrostatic confinement of the ions. This is further borne out by the observation of floating-potential variation.

f. Work in Progress

Several types of more sophisticated probe techniques (multipole, magnetic, and capacitive) are either planned or in use. Arc pulsing techniques are being refined and

give promise of achieving virtually 100 per cent ionization. The geometry of the system is particularly amenable to analysis and an intensive study of diffusion and resistivity in a transverse magnetic field will be carried out.

L. M. Lidsky, S. D. Rothleder, S. Yoshikawa

References

1. W. D. Getty, A low-pressure gas-arc device, Quarterly Progress Report No. 57, Research Laboratory of Electronics, M.I.T., April 15, 1960, pp. 27-29.

2. D. J. Rose, L. M. Lidsky, S. D. Rothleder, and S. Yoshikawa, Experimental results on the hollow-cathode discharge, Quarterly Progress Report No. 58, Research Laboratory of Electronics, M.I.T., July 15, 1960, pp. 41-44.

3. R. V. Nedeigh, Effect of pressure gradient on a magnetically columnated arc, Proc. Second International Conference on the Peaceful Uses of Atomic Energy, Geneva, September 1958, Vol. 31, p. 315.

4. B. Lehnart, Positive column in a longitudinal magnetic field, Proc. Second International Conference on the Peaceful Uses of Atomic Energy, Geneva, September 1958, Vol. 32, p. 349; F. C. Hoh and B. Lehnart, Phys. Fluids 3, 600 (1960).

5. H. Alfvèn, Phys. Fluids 3, 606 (1960).

6. A. Simon, Diffusion of arc plasma across a magnetic field, Proc. Second International Conference on the Peaceful Uses of Atomic Energy, Geneva, September 1958, Vol. 32, p. 343.

7. W. D. Getty, Research Laboratory of Electronics, M.I.T. (personal communication, May 1960).

8. Oak Ridge National Laboratory Semiannual Report, Oak Ridge, Tennessee, June 1960.

4. SUPERCONDUCTING SOLENOIDS – EFFECTS OF MAGNETIC FIELDS AND CURRENTS ON THE SUPERCONDUCTING TRANSITION

Small superconducting solenoids made of niobium (columbium) wire have been reported to generate magnetic fields up to 8 kilogauss (1, 2). The development of a large-volume solenoid for use in plasma research (3, 4) is the main objective of this work. The usefulness of such a solenoid would be greatly increased if it is capable of generating stronger magnetic fields. Therefore an investigation of the dependence of the superconducting-to-normal transition in niobium upon magnetic field, current temperature, treatment of the material, and other factors was started.

The first studies were made on niobium wire. Some of the wire was annealed by the manufacturer after the final drawing; in other samples this final anneal was omitted. It is apparent from published reports that the critical field of niobium varies greatly (values up to 12 kilogauss at 1.5°K have been reported (5)) and depends upon the heat treatment of the material and other factors (1, 5, 6).

The arrangement of the experiment is shown in Fig. II-15. The sample wire,

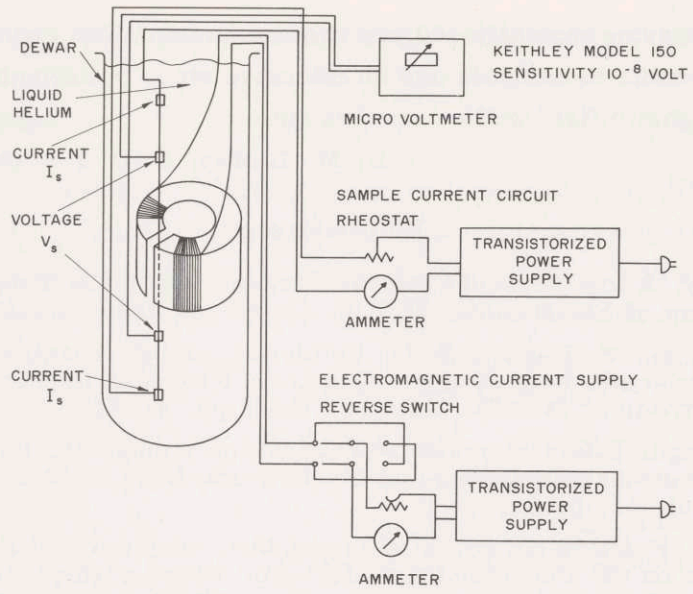

Fig. II-15. Schematic view of the experimental arrangement for the study of magnetic field-current relationship.

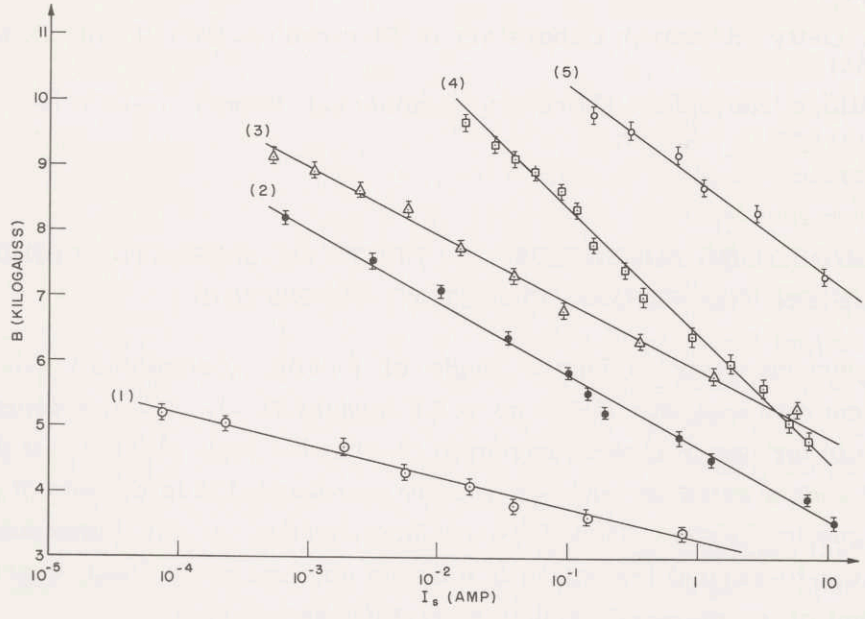

Fig. II-16. Magnetic field versus current for constant V_s (10^{-8} volt).

(1) Annealed wire (5AS-1), 0.005 inch, 4.2°K.
(2) Unannealed wire (7US-1), 0.007 inch, 4.2°K.
(3) Unannealed wire (4UN-1), 0.004 inch, 4.2°K.
(4) Unannealed wire (4US-2), 0.004 inch, 1.67°K.
(5) Unannealed wire (4UN-1), 0.004 inch, 1.56°K.

provided with current and voltage leads, is inserted into the gap of a small iron-core superconducting electromagnet (1) where it is exposed to a transverse magnetic field. The entire device is immersed in liquid helium either at atmospheric pressure (4.2°K) or at a reduced pressure as low as 4 mm (1.6°K).

The procedure adopted was to set the magnetic field, and then increase the sample current, I_s, until a voltage, V_s, can just be observed across the voltage leads. The current is increased again, and V_s versus I_s is measured. The procedure is repeated at different magnetic fields, B.

Figure II-16 shows the B versus log I_s plot for the minimum detectable V_s (10^{-8} volt) for a number of samples. The B versus log I data are well approximated by straight lines in all cases; this fact indicates a relation of the form

$$I = I_o e^{-KB} \tag{1}$$

The values of I_o and K for our experiments are given in Table II-1 for two temperatures.

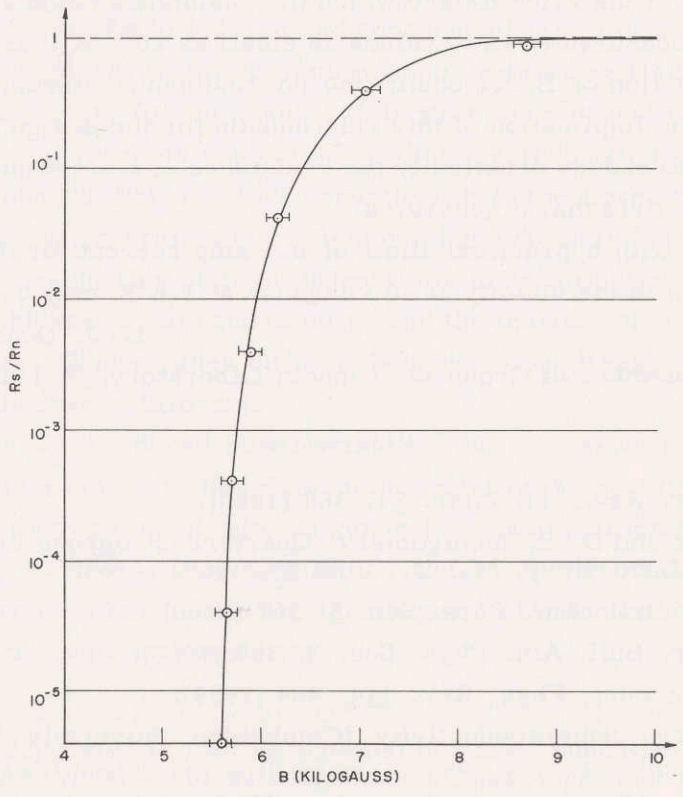

Fig. II-17. Relative resistance versus magnetic field at constant sample current. (I_s = 50 ma; sample 4US-7.)

Table II-1.

	4.2°K		1.6°K	
	I_o (amp)	K $(\text{kilogauss})^{-1}$	I_o (amp)	K $(\text{kilogauss})^{-1}$
Annealed wire	2.1×10^7	4.84		
Unannealed wire (7US-1, 4US-2)	1.49×10^4	2.04	1.2×10^3	1.11
Unannealed wire (4UN-1)	5.2×10^5	2.23	1.04×10^6	1.58

It is clear that the transition occurs at higher magnetic fields when the wire is unannealed, the temperature reduced, and the current reduced. Samples 7US-1 and 4UN-1 were made from different lots of unannealed wire from the same manufacturer. The reasons for the differences in their properties are not yet understood.

Figure II-17 shows a log R_s/R_n versus B plot at constant I_s, for a particular sample; $R_s = V_s/I_s$; and R_n is the value toward which the resistance tends as B becomes large. The value R_s was measured down to values as small as 10^{-5} R_n, and although it is a rapidly varying function of B, we could find no resistance discontinuity in any of the samples tested. The implication of this relationship for the design of magnets is that one should be able to reduce drastically the resistance of a solenoid by a slight reduction in the magnetic field that it generates.

It appears that with a practical limit of 0.1 amp current for 0.004-inch diameter niobium wire, fields in the vicinity of 10 kilogauss at 1.6°K may be feasible.

L. J. Donadieu, S. H. Autler

(S. H. Autler is a member of Group 82, Lincoln Laboratory, M.I.T.)

References

1. S. H. Autler, Rev. Sci. Instr. 31, 369 (1960).

2. S. H. Autler and D. B. Montgomery, Quarterly Progress Report on Solid State Research, Lincoln Laboratory, M.I.T., July 15, 1960, p. 63.

3. D. J. Rose, Bull. Am. Phys. Soc. 5, 367 (1960).

4. S. H. Autler, Bull. Am. Phys. Soc. 5, 367 (1960).

5. T. G. Berlincourt, Phys. Rev. 114, 969 (1959).

6. D. Shoenberg, Superconductivity (Cambridge University Press, London, 1960), p. 224.

II-C. PLASMA MAGNETOHYDRODYNAMICS AND ENERGY CONVERSION*

Prof. O. K. Mawardi
Prof. H. H. Woodson
Prof. J. A. Fay
Prof. W. D. Jackson
Prof. D. C. Pridmore-Brown
Prof. A. H. Shapiro
Dr. R. Gajewski†
T. I. Sundström
G. W. Bukow
L. Y. Cooper
R. S. Cooper
D. M. Dix
D. A. East
W. H. Heiser
G. B. Kliman
A. T. Lewis
J. K. Oddson
J. P. Penhune
E. S. Pierson
J. W. Poduska
K-F. Voyenli
B. Zauderer

1. THE MAGNETOHYDRODYNAMIC RAYLEIGH PROBLEM FOR THE NONCONDUCTING PLATE

a. Introduction

The classical Rayleigh problem can be extended to magnetohydrodynamics by considering the motion caused by the impulsive start, in a direction parallel to itself (the x-axis), of an infinite flat plate (the $y = 0$ plane) immersed in an infinite extent of an incompressible, viscous, electrically-conducting fluid initially at rest, with a magnetic field applied over space.

It is obvious that for the applied field parallel to the plate no electromagnetic effects are present, since no current is induced and consequently the Lorentz body force vanishes and hence no forces act on the fluid other than those expressed in the usual Navier-Stokes equations. However, for the applied field with a component perpendicular to the plate, there are induced currents and corresponding electromagnetic body forces. The problem is governed by the Navier-Stokes equations with the Lorentz force included, and Maxwell's equations. In general, the problem can be treated as four cases: the first two, for an infinitely conducting plate of either finite or infinitesimal thickness; the third, for a plate of finite thickness and conductivity; and the fourth, for a nonconducting plate of arbitrary thickness. These cases differ in boundary conditions, and the solutions for each are therefore decidedly different.

The basic problem considered here is that of the nonconducting plate with an applied field that is transverse to the plate and parallel to the +y axis. The problem is of interest because it gives insight into the general character of the flow to be expected in many practical applications, such as flow about obstacles and flow at nonconducting boundaries. This problem has been solved inadequately by Rossow (1, 2) and discussed inaccurately by Carrier and Greenspan (3).

---

*This work was supported in part by National Science Foundation under Grant G-9330; in part by Contract AF19(604)-4551 with Air Force Cambridge Research Center; and in part by WADD Contract AF33(616)-3984.

†Sloan Foreign Postdoctoral Fellow, from the Institute for Nuclear Research, Warsaw, Poland.

In Rossow's first solution, the assumption was made that the induced magnetic field is negligible. This assumption restricts the solution to the regime $\epsilon \equiv \sigma\mu\nu \ll 1$, and, although the numerical results are reliable in this regime, the solution completely suppresses the Alfvèn wave mechanism, and therefore does not provide a valid representation of the character of the flow. Rossow (2), in his second solution, lifts the restriction $\epsilon \ll 1$ and attempts to obtain the solution with two different sets of boundary conditions. However, neither set is compatible with a physically realizable situation, and the solution to his second case is incorrect. As we shall see, the primary difficulty is attributable to application of unrealistic boundary conditions.

Carrier and Greenspan began a treatment of the problem, but failed to carry it through because of a paradox observed in the general solution of the velocity profile in the limit as $t \to \infty$. They found that the velocity distribution in this limit is of the form $u = A + C \exp[-b(y)]$. Since they imply that this is a steady-state solution, they conclude that $\underline{E}$ must be nonzero because $\underline{J} = \sigma(\underline{E}+\underline{v}\times\underline{B})$ must certainly be zero as $y \to \infty$ in order for the induced field, that is, $\int_0^\infty J dy$, to be finite, and hence at $y \to \infty$, $\underline{E} = -\underline{v} \times \underline{B} = AB_{applied}$. They now observe that a finite $\underline{E}$ in steady state can only be due to a charge accumulation, and it is agreed that such an accumulation is quite artificial. This argument will be found invalid upon closer inspection of the meaning of the "steady-state" velocity distribution. Such a solution proposed by Carrier and Greenspan is valid as $t \to \infty$ only for $y \ll at$, where a is the Alfvèn velocity. It will be shown that an Alfvèn wave leaves the plate initially, and the implications of such a wave in an infinite space must produce a solution which, in fact, is never a steady-state solution. The general solution proposed by Carrier and Greenspan will be seen to be quite valid at $t \to \infty$, but only far behind the Alfvèn wave. With an understanding of the unsteadiness caused by the Alfvèn wave propagation the artificial charge accumulation is indeed seen to be nonexistent.

The solution for the problem of the infinitely conducting plate was obtained by Chang and Yen (4). They obtained exact solutions for a fluid with $\epsilon = 1$, and approximate solutions for other values of ϵ in which simplification of the equations could be made so that closed-form solutions might be extracted.

In view of these remarks, the purpose of this report is first, to obtain the solution to our nonconducting-plate problem, and second, to clear up some misconceptions that have been raised by other authors. Particular emphasis will be placed on the nature and number of boundary conditions to be employed.

b. Formulation of the Problem

Before proceeding to the formulation of the problem, it will be beneficial to give a qualitative physical picture. Initially, after the plate is set in motion, the motion of the

fluid induces a current in the positive z-direction. The Lorentz force is then acting to retard the fluid. However, the current tends to produce a longitudinal component of the magnetic field, which, in turn, produces an electric field that opposes the initial current. This induction is then responsible for the Alfvèn wave, which propagates and diffuses from the plate.

In the following analysis, fluid properties are considered constant and isotropic. The plate velocity is assumed to be much less than that of the speed of light, and the usual magnetohydrodynamic assumptions of neglecting the Maxwellian displacement currents and charge accumulation are made. The governing equations may be simplified by noting that since the plate is infinite in extent, no variable depends on either x or z. Then, from the continuity equation, $v^* = 0$, where the asterisk denotes a dimensionless variable. From the divergenceless properties of $\underline{B}^*$ and $\underline{E}^*$, we obtain $E_y^* = 0$, $B_y^* = B_o$, where B_o is the applied magnetic field. From $\nabla \cdot J = 0$, we have $J_y = 0$. The values of E_x^*, w^*, J_x^*, and B_z^* can be determined by investigating the initiating mechanism of the problem. As the plate is moved, a current J_z^* is induced. This current results in an induced B_x^* and consequently in the induced E_z^*. Since no further coupling of the equations exists, it is evident that the values of E_x^*, w^*, J_x^*, and B_z^* are no different from their initial values of zero. The variables in the problem are therefore reduced to u^*, B_x^*, J_z^*, and E_z^*, which are governed by the following equations:

$$\frac{\partial E_z^*}{\partial y^*} = -\frac{\partial B_x^*}{\partial t^*} \tag{1}$$

$$\mu J_z^* = -\frac{\partial B_x^*}{\partial y^*} \tag{2}$$

$$J_z^* = \sigma\left(E_z^* + u^* B_o^*\right) \tag{3}$$

$$\frac{\partial u^*}{\partial t^*} = \nu \frac{\partial^2 u^*}{\partial y^{*2}} - J_z^* \frac{B_o^*}{\rho} \tag{4}$$

(To be precise, the pressure is a fifth variable. However, it is given by the uncoupled equation $\partial p^*/\partial y^* = J_z^* B_x^*$ and will not be considered here.)

It is essential to examine Eqs. 1-4 at this stage, before any further reduction, to determine the number and nature of the boundary conditions. It is seen that one boundary condition is required on E_z^*, one boundary and one initial condition on B_x^*, and one initial and two boundary conditions on u^*. It is also permissible to substitute a boundary condition on J_z^* in place of the boundary condition on either (but not both) E_z^* or B_x^*. The boundary conditions for the present problem are

$$\left.\begin{aligned} E_z^* &= 0 && \text{as } y^* \to \infty,\ t^* \geq 0 \\ B_x^* &= 0 && \text{at } y^* > 0,\ t^* = 0 \\ B_x^* &= 0 && \text{at } y^* = 0,\ t^* \geq 0 \\ u^* &= 0 && \text{at } y^* > 0,\ t^* = 0 \\ u^* &= U_o^* && \text{at } y^* = 0,\ t > 0 \\ u^* &= 0 && \text{as } y^* \to \infty,\ t \geq 0 \end{aligned}\right\} \tag{5}$$

The first and last of these conditions arise from the fact that the motion of the plate is the initiating mechanism, and hence at distances far from the plate disturbances should diminish. The third condition arises from the symmetry of the problem and the fact that B_x^* must be continuous across the plate. That is, the lines of force must be symmetrical about the plate; furthermore, since B_x^* is continuous across the plate, the slope of the lines of force is also continuous; hence the lines of force are perpendicular to the plate at the plate and B_x^* equals zero.

The problem may now be formulated in more convenient terms by first introducing the following dimensionless variables: $B = B_x^*/B_o^*$, $u = u^*/a$, $y = y^* a/\nu$, $t = a^2 t^*/\nu$, $\epsilon = \sigma\mu\nu$, $U_o = U_o^*/a$, $J = J_z^* \nu\mu/B_o^* a$, $E - E_z^*/aB_o^*$. Eliminating J and E from Eqs. 1-4 yields

$$\left(\frac{\partial}{\partial t} - \frac{\partial^2}{\partial y^2}\right) u = \frac{\partial B}{\partial y} \tag{6}$$

$$\left(\frac{\partial}{\partial t} - \frac{1}{\epsilon}\frac{\partial^2}{\partial y^2}\right) B = \frac{\partial u}{\partial y} \tag{7}$$

Since this elimination involved differentiation of Eq. 3, the additional requirement that Eq. 3 must be satisfied at some boundary is necessary. If we select $y \to \infty$ as the appropriate boundary, the first of conditions 5 combined with Eq. 3 leads to the condition $\partial B/\partial y = 0$ as $y \to \infty$. This last condition and the last five conditions of Eqs. 5 are the appropriate boundary conditions for Eqs. 6 and 7. Finally, Eqs. 6 and 7 can be combined to yield:

$$\left\{\frac{\partial^4}{\partial y^4} - (1+\epsilon)\frac{\partial^3}{\partial y^2 \partial t} - \epsilon\frac{\partial^2}{\partial y^2} + \epsilon\frac{\partial^2}{\partial t^2}\right\}\begin{Bmatrix} u \\ B_x \end{Bmatrix} = 0 \tag{8}$$

This equation, with the boundary conditions on B and u previously formulated, and the requirement that Eqs. 6 and 7 be satisfied, is the complete mathematical formulation of the problem.

c. Solutions and Discussion

(i) Solutions in Transformed Space

The problem is solved by using the method of Laplace transformation. The transforms of u and B are represented by $\bar{u}$ and $\bar{B}$, respectively. The solutions for $\bar{u}$ and $\bar{B}$ that satisfy the given boundary and initial conditions are

$$\bar{u} = \frac{\left(p-D_2^2\right) D_1}{\left(p-D_2^2\right) D_1 - \left(p-D_1^2\right) D_2} \frac{U}{p} \exp(D_1 y) + \frac{\left(p-D_1^2\right) D_2}{\left(p-D_1^2\right) D_2 - \left(p-D_2^2\right) D_1} \frac{U}{p} \exp(D_2 y) \tag{9}$$

$$\bar{B} = \frac{\left(p-D_2^2\right)\left(p-D_1^2\right)}{\left(p-D_2^2\right) D_1 - \left(p-D_1^2\right) D_2} \frac{U}{p} \exp(D_1 y) - \exp(D_2 y) \tag{10}$$

where D_1 and D_2 are given by

$$D_{1,2} = -\frac{1}{2}\{[\epsilon+(1+\epsilon+2\epsilon^{1/2})p]^{1/2} \pm [\epsilon+(1+\epsilon-2\epsilon^{1/2})p]^{1/2}\}$$

The general inversion of these equations for an exact solution involves an extremely large amount of manipulation; such solutions will not be dealt with here as they are not readily interpretable.

(ii) Exact Solution for $\epsilon = 1$

For this special case, the exact solution can be obtained with the aid of an inversion table (5). The solutions for u, B, and J are given by

$$\frac{u}{U_o} = \frac{1}{4}[1+\exp(y)]\,\operatorname{erfc}\left(\frac{y}{2t^{1/2}} + \frac{t^{1/2}}{2}\right) + \frac{1}{4}[1+\exp(-y)]\,\operatorname{erfc}\left(\frac{y}{2t^{1/2}} - \frac{t^{1/2}}{2}\right) \tag{11}$$

$$\frac{B}{U_o} = \frac{1}{4}[1-\exp(y)]\,\operatorname{erfc}\left(\frac{y}{2t^{1/2}} + \frac{t^{1/2}}{2}\right) - \frac{1}{4}[1-\exp(-y)]\,\operatorname{erfc}\left(\frac{y}{2t^{1/2}} - \frac{t^{1/2}}{2}\right) \tag{12}$$

$$\begin{aligned}\frac{J}{U_o} = {} & \frac{1}{4(\pi t)^{1/2}} \exp\left\{-\left(\frac{y}{2t^{1/2}} - \frac{t^{1/2}}{2}\right)^2\right\}[\exp(-y)-1] \\ & - \frac{1}{4(\pi t)^{1/2}} \exp\left\{-\left(\frac{y}{2t^{1/2}} - \frac{t^{1/2}}{2}\right)^2\right\}[\exp(-y)-1] \\ & + \frac{1}{4}\exp(y)\,\operatorname{erfc}\left(\frac{y}{2t^{1/2}} + \frac{t^{1/2}}{2}\right) + \frac{1}{4}\exp(-y)\,\operatorname{erfc}\left(\frac{y}{2t^{1/2}} - \frac{t^{1/2}}{2}\right)\end{aligned} \tag{13}$$

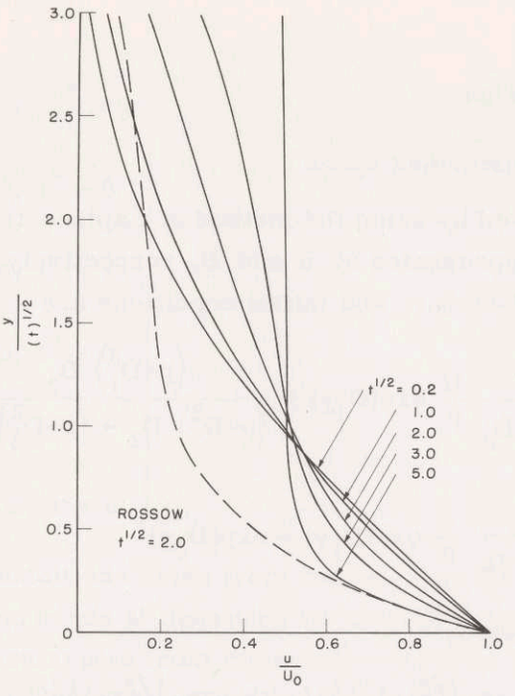

Fig. II-18. Velocity profiles for $\epsilon = 1$.

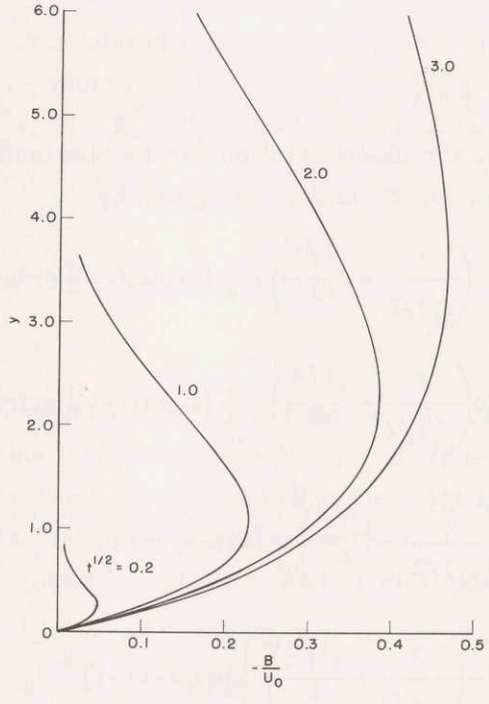

Fig. II-19. Magnetic field profiles for $\epsilon = 1$.

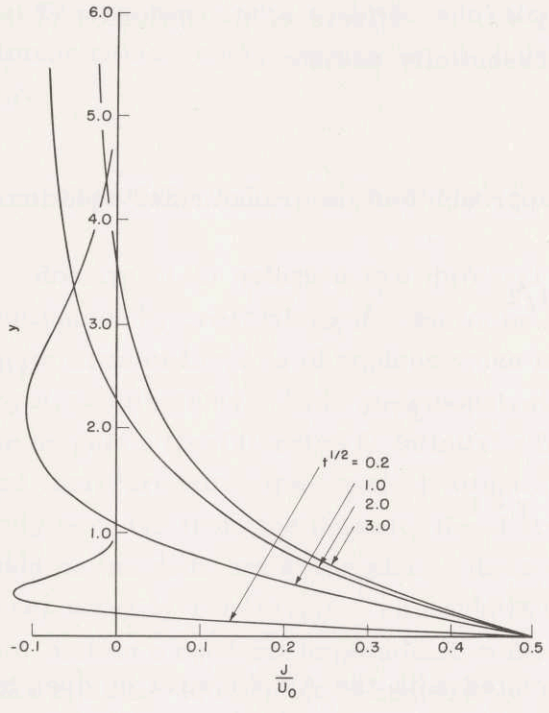

Fig. II-20. Current-density distribution for $\epsilon = 1$.

The solution for E can be obtained from Eq. 3, if desired.

These solutions for u, B, and J are plotted in Figs. II-18, II-19, and II-20. The physical phenomena portrayed by these solutions is described as follows. At t = 0, a viscous shear wave is generated by the motion of the plate. This shear wave, in turn, produces an Alfvèn wave (actually, a continuous succession of Alfvèn waves) and by this action is itself diminished. The eventual magnitudes of the two waves are dependent upon the ratio of the magnetic to viscous forces (ϵ) and are equal in this special case. The Alfvèn wave propagates at a velocity u = 1 and diffuses, while the viscous wave remains stationary and undergoes a finite diffusion that is limited by the electromagnetic forces that are not associated with the Alfvèn wave. Thus, at $t \gg 1$, when the Alfvèn wave is far from the plate, the velocity profile in the viscous layer next to the plate is time-independent (the thickness of the layer remains constant). These phenomena can be detected by observing the form of the solutions at various times. At $t \ll 1$ ($t^{1/2} = 0.2$, for example), the Alfvèn wave has not been fully generated, viscous forces predominate, and the solution differs but little from the classical Rayleigh solution. For $t \gg 1$, three regimes of flow are observed. For $y < t^{1/2}$, the viscous wave dominates, and has essentially reached its maximum amount of dispersion; the forces of inertia are zero. For $t^{1/2} < y \ll t$, the effect of diffusion of both waves is negligible, the region is current-free, and the resulting velocity is governed by the magnitude of the Alfvèn wave. In this special case, since the waves are of equal strength, the velocity is $U_o/2$. The adjacent region,

$y \approx t$, is dominated by the Alfvèn wave. For $y \gg t$, the effects of the diffusion of the Alfvèn wave are negligible, and the fluid is essentially undisturbed.

(iii) Solution as $t \to \infty$

This solution is obtained by allowing p to approach 0 in the transformed equations. The solutions for u and B are given by

$$\frac{u}{U_o} = (1+\epsilon^{1/2})^{-1} \exp(-\epsilon^{1/2}y) + \epsilon^{1/2}/1 + \epsilon^{1/2} \qquad y < t$$

$$\frac{u}{U_o} = (1+\epsilon^{1/2})^{-1} \exp(-\epsilon^{1/2}y) \qquad y > t \tag{14}$$

$$\frac{B}{U_o} = -\epsilon^{1/2}(1+\epsilon^{1/2})^{-1}[1-\exp(-\epsilon^{1/2}y)] \qquad y < t$$

$$\frac{B}{U_o} = \epsilon^{1/2}(1+\epsilon^{1/2})^{-1} \exp(-\epsilon^{1/2}y) \qquad y > t \tag{15}$$

It is observed that the change in velocity associated with the Alfvèn wave is given by $\epsilon^{1/2}/(1+\epsilon^{1/2})$. Unfortunately, the mathematical formalism involved completely suppresses the diffusion of the Alfvèn wave, and hence the solutions for $y > t$ are those to be attributed only to dispersion of the viscous wave.

(iv) Solution for $\epsilon \ll 1 (\sigma \to 0)$

This solution is for the case most often encountered in practice. By performing the appropriate limiting process, the solutions for u and B are found to be

$$\frac{u}{U_o} = \frac{1}{2} \exp(\epsilon^{1/2}y) \operatorname{erfc}\left[\frac{y}{2t^{1/2}} + (\epsilon t)^{1/2}\right] + \frac{1}{2} \exp(-\epsilon^{1/2}y) \operatorname{erfc}\left[\frac{y}{2t^{1/2}} - (\epsilon t)^{1/2}\right] \tag{16}$$

$$\frac{B}{U_o} = -\frac{\epsilon^{1/2}}{2}\left\{\exp(\epsilon^{1/2}y) \operatorname{erfc}\left[\frac{y}{2t^{1/2}} - (\epsilon t)^{1/2}\right]\right.$$

$$\left. - \exp(-\epsilon^{1/2}y) \operatorname{erfc}\left[\frac{y}{2t^{1/2}} + (\epsilon t)^{1/2}\right] - 2\operatorname{erf}(\epsilon t)^{1/2}\right\} \tag{17}$$

The solution for u is identical with that obtained by Rossow (1). It completely suppresses the Alfvèn wave, and hence the solutions will be accurate relatively close to the plate, but will not be accurate far from the plate, where the Alfvèn mechanism is dominant (however small) in any case.

The solution for $\epsilon \ll 1 (\nu \to 0)$ can also be obtained, but it necessitates a change in dimensionless variables and is of little practical interest; therefore it is omitted here.

d. Comparison of Our Solutions with Previous Work

Rossow (1, 2) selected two different sets of boundary conditions which he chose to distinguish by prescribing motion to the lines of force. The concept of prescribing motion to the lines of force is of dubious value in this problem and must be carefully applied to physical situations. This is demonstrated by his implication that moving the source of the magnetic field (located at infinity) will impart a uniform motion to the magnetic field and therefore alter the physical situation appreciably. It is obvious that if the plate is truly very far from the magnet, the disturbances caused by any motion of the magnet must be insignificant at the plate. Rossow's first case (the so-called field fixed-to-plate case) actually represents a situation in which at the same instant when the plate is set into motion a nonzero longitudinal component of the magnetic field is also prescribed. This situation is difficult to conceive on a physical basis and corresponds neither to the problem considered in this paper nor to the problem to which Rossow presumably addressed himself.

In reference to the boundary conditions employed by Rossow (6), it is evident that the initial conditions on $\partial u/\partial t$, J_z, and E_z are superfluous, while a necessary boundary condition on u has been omitted.

Rossow (2) implies that his second case is identical with the problem considered here. A representative solution for the $\epsilon = 1$ case is shown in Fig. II-18 for the purpose of comparison. The disagreement is severe and can be traced to the boundary condition on E. Rossow used the condition $E = 0$ at the plate, thereby implying that as $y \to \infty$, E is not zero. This contradicts the physical situation. Also, it is verified by direct substitution that the solutions for B and u proposed by Rossow do not satisfy the equation of motion (4).

D. M. Dix, L. Y. Cooper

References

1. V. J. Rossow, NACA Report 1358, 1958.

2. V. J. Rossow, Phys. Fluids 3, 395 (1960).

3. G. F. Carrier and H. Greenspan, J. Fluid Mech. 7, 22 (1960).

4. C. C. Chang and J. T. Yen, Phys. Fluids 2, 303 (1959).

5. G. A. Campbell and R. M. Foster, Fourier Integrals (D. Van Nostrand Company, Inc., New York, 1948).

6. V. J. Rossow, Phys. Fluids, op. cit.; see Table 1.

2. PLASMA MAGNETOHYDRODYNAMIC EXPERIMENTS

The objective of the present work on the magnetically driven shock tube is to study the phenomena that result from strong interaction between the plasma behind a shock front and a magnetic field. Strong interaction means that the gas flow strongly affects the magnetic field, which requires a high magnetic Reynolds number, and the magnetic field strongly affects the gas flow, which requires a high magnetic pressure.

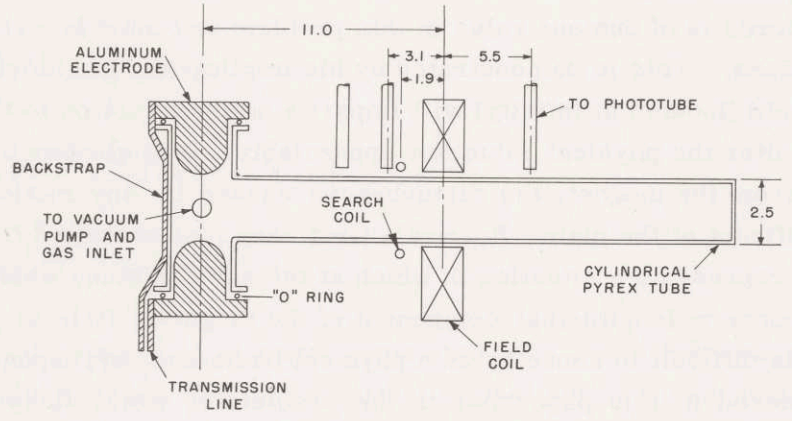

Fig. II-21. Sketch of shock tube showing details of construction and placement of field and search coils for experiment. (Dimensions in cm.)

After some minor modifications to the shock-tube equipment described in Quarterly Progress Report No. 51 (pages 28-30), attempts were made to obtain strong interactions. With the experimental arrangement of shock tube, field coil, search coil, and phototubes shown in Fig. II-21, measurements were first made at low magnetic-field strengths to determine the effect of the gas flow on the magnetic field. The results are shown graphically in Fig. II-22, in which the fractional flux change in the search coil is plotted as a function of the magnetic Reynolds number. The magnetic Reynolds number was calculated by using the conventional approach for calculating conductivity in a shock tube and with the tube radius used as a characteristic length. It is evident from Fig. II-22 that although a rather large magnetic Reynolds number is reached, the gas flow only moderately affects the magnetic field, changing it approximately 18 per cent for the best conditions achievable with the equipment. The curve of Fig. II-22 was taken with a maximum magnetic field of 1000 gauss. These results are similar to those obtained by Turner and Eastmond (1).

The conditions at the highest magnetic Reynolds number obtained, as shown in Fig. II-22, were chosen to try to change the gas flow by applying a magnetic field. The field coil was pulsed by a relay system from a 220-volt dc line to obtain fields as high as

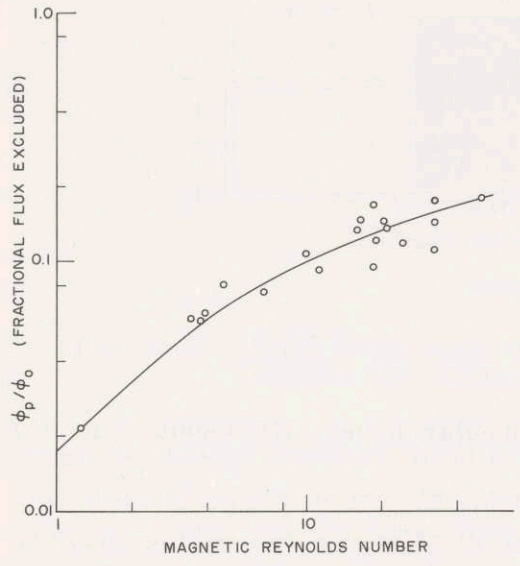

Fig. II-22. Fraction of flux excluded by a shock as a function of magnetic Reynolds number.

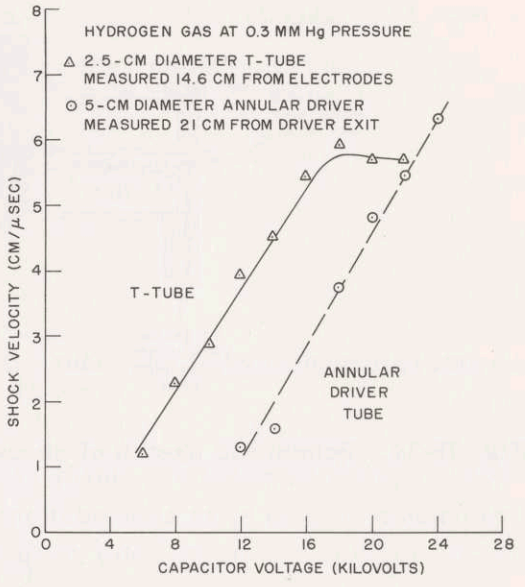

Fig. II-23. Shock velocity versus voltage for two types of shock tube.

6000 gauss. There were no measurable effects on the gas flow as indicated by the fractional flux change in the search coil, light output from the phototubes, or time of traversal of the gas through the field region. Order-of-magnitude calculations indicated that there should have been a measurable interaction.

The fact that there was no change in gas flow caused by the presence of the strong magnetic field may be the result of two effects. The magnetic Reynolds number may not be high enough to yield an appreciable field-free plasma for magnetic pressure to act on; or the magnetic pressure may not be high enough. Order-of-magnitude calculations indicate that either effect is equally likely, and so we decided to construct a shock tube to yield a higher magnetic Reynolds number.

In order to increase the magnetic Reynolds number, the velocity, characteristic length or conductivity (which depends strongly on velocity) must be increased. The plot of shock velocity versus voltage at constant pressure for the T-tube shown in Fig. II-23 shows that the obtainable velocity is definitely limited. This limitation appears to result from the decrease in driving effectiveness because the harder the tube is driven, the faster the initial shock leaves the discharge region. The T-tube is a very inefficient driver; less than 1 per cent of the energy stored in the capacitor bank is transferred to the gas behind the initial shock front. To improve the driving efficiency we decided to use an annular driver like Patrick's (2). With the expected increase in driving efficiency the shock-tube diameter was doubled. A drawing of the new shock tube with annular driver is shown schematically in Fig. II-24, and a plot of shock velocity versus

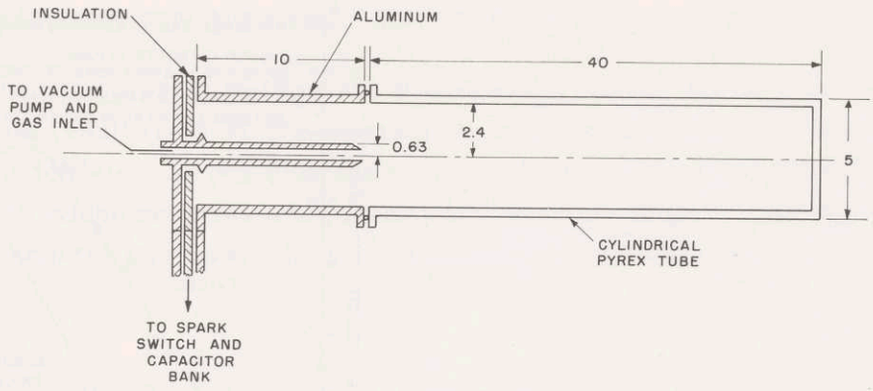

Fig. II-24. Schematic sketch of shock tube with annular driver. (Dimensions in cm.)

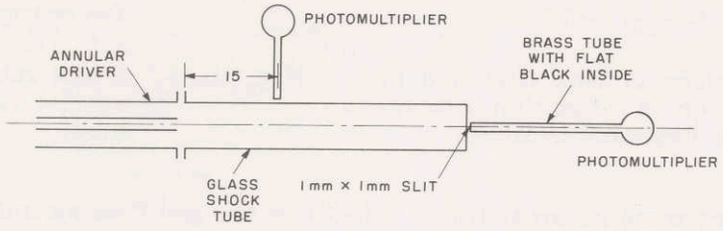

Fig. II-25. Experimental arrangement for viewing light output along the axis of shock tube.

voltage for a pressure of 0.3 mm Hg of hydrogen is shown in Fig. II-23. Comparison of the two curves in Fig. II-23 shows that, at least within the range of voltages used, the annular driver is much more effective than the T type of driver. Because the diameter of the new tube is doubled, at a given velocity the gas behind the shock front has more than four times as much energy as in the T-tube.

To properly perform the interaction experiments, a plane shock in the cylindrical tube is needed. The annular driver produces a toroidal-shaped shock wave that must form into a plane shock before experiments can be performed. Approximate theory indicates that after the shock wave has traveled a distance of approximately 3 tube diameters from the driver it should be plane. To verify this approximately the experiment shown schematically in Fig. II-25 was performed. The photomultiplier aimed along the axis of the shock tube was arranged to view a small cone no larger than the inner conductor of the annular driver. The photomultiplier placed 15 cm from the driver senses light across the shock-tube diameter. When a shock was produced with a capacitor voltage of 20 kv in hydrogen at 0.3 mm Hg pressure, the oscilloscope traces of Fig. II-26 were recorded. It is evident that light is present along the tube axis after the shock has traveled down the tube a distance of approximately 3 tube diameters. Thus, at distances greater that 15 cm

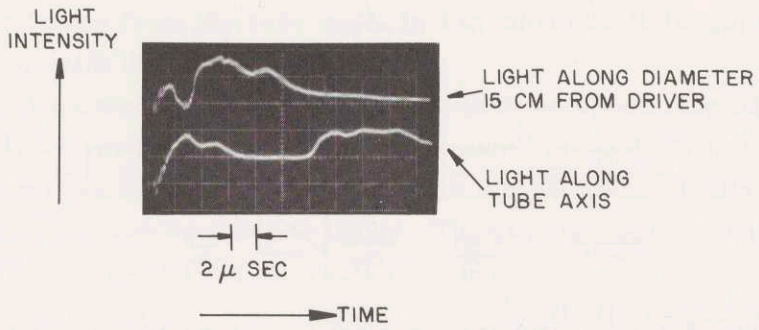

Fig. II-26. Light 15 cm from driver along the tube axis in hydrogen: pressure, 0.3 mm Hg; capacitor voltage, 20 kv.

from the driver, the shock front is approximately plane. In the oscilloscope trace of Fig. II-25 the increase in light intensity along the tube axis at 14 μsec is caused by the reflection of the shock wave from the end of the shock tube. Similar records of the photo-tube outputs at pressures higher than 0.3 mm Hg showed that the light reaches the tube axis in approximately the same time interval regardless of pressure, which indicates that for higher pressures the shock becomes plane in less distance than 3 tube diameters.

To obtain a measure of the improvement in magnetic Reynolds number and in the effect of the gas on the magnetic field with the new shock tube, the experimental arrangement of Fig. II-27 was used to obtain the data points shown in Fig. II-28 of fractional flux change in the search coil versus magnetic Reynolds number. The dashed curve in Fig. II-28 is taken from Fig. II-22 for comparison. It is evident that the plasma in the new shock tube affects the magnetic field more strongly than it did in the T-tube by a factor of approximately 40 per cent.

The data points in Fig. II-28 show that for high magnetic Reynolds numbers the fractional flux change decreases with increasing field and therefore the field appears to affect the gas flow. Probably this occurs because the ionized gas has not reached the center of the tube by the time the field region is reached. Figure II-26 shows that for a magnetic Reynolds number around 20 the ionized gas has certainly reached the center of the tube by the time the shock front reaches the magnetic field region; consequently, this point was chosen to make a measurement of fractional flux change as a function of magnetic flux density. The experimental arrangement of Fig. II-27 was used with a relay pulsing system for the field coil to obtain the data plotted in Fig. II-29. It is evident that the gas flow is affected by the magnetic field. At low field strengths the fractional flux change is independent of magnetic field strength, as it should be if the gas flow is unaffected. As the field strength is increased, the fractional flux change decreases, which indicates that the gas flow is probably being channeled by the magnetic field. Further evidence of channeling is the fact that at higher field strengths the traversal time of the shock front through the field region is decreased, and thus it appears that

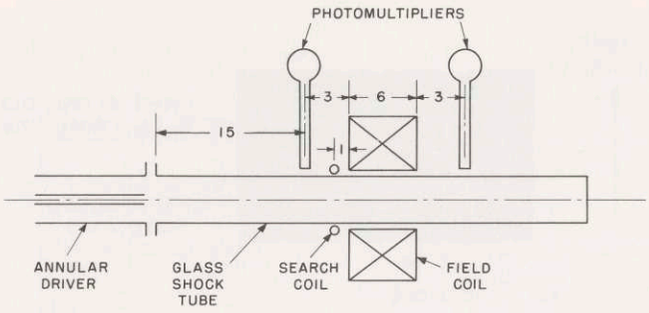

Fig. II-27. Experimental arrangement for interaction experiments with a 5-cm diameter shock tube having annular driver.

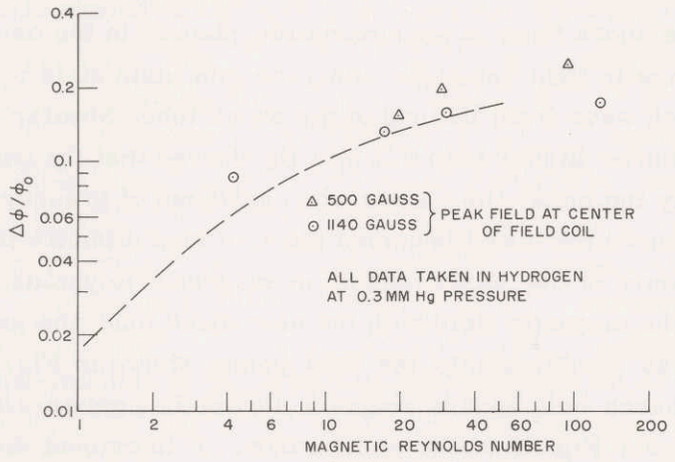

Fig. II-28. Fractional flux excluded in 5-cm diameter shock tube.

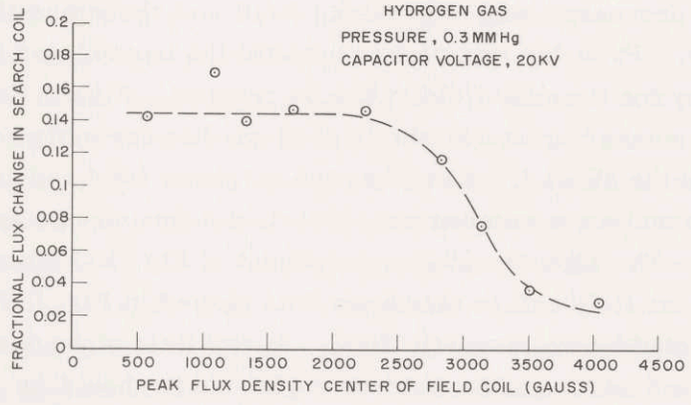

Fig. II-29. Fractional flux change in search coil as a function of flux density in 5-cm diameter shock tube.

the plasma is pushed away from the tube walls by the magnetic field and the drag on the gas caused by contact with the walls is reduced.

The experimental evidence presented indicates that the shock tube illustrated schematically in Fig. II-24, with its associated equipment, is an instrument in which the strong interaction between the ionized gas behind an almost adiabatically expanding shock front and a magnetic field can be made to occur. Thus the equipment can be used to study the detailed properties of the strong interaction.

H. H. Woodson, A. T. Lewis

References

1. E. B. Turner and E. J. Eastmond, Conductivity measurements of deuterium plasmas at magnetic Reynolds numbers greater than unity, Report GM-TR-0165-00514, Space Technology Laboratory, Los Angeles, California, December 1958.

2. R. M. Patrick, A description of a propulsion device which employs a magnetic field as the driving force, Report No. 28, AVCO Research Laboratory, Wilmington, Massachusetts, May 1958.

III. SOLID STATE PHYSICS

Prof. W. P. Allis	Prof. G. G. Harvey	L. L. Isaacs
Prof. S. C. Brown	Dr. K. W. Billman	J. Silverman
Prof. C. W. Garland	Dr. E. R. Pike	R. Weber
	T. Higier	

A. RESEARCH COMPLETED

1. THE ELASTIC CONSTANTS OF CADMIUM FROM 4.2°K TO 300°K

A thesis with this title was presented by J. Silverman to the Department of Chemistry, M. I. T., May 17, 1960, and was accepted in partial fulfillment of the requirements for the degree of Doctor of Philosophy.

C. W. Garland

2. THE LOW-TEMPERATURE SPECIFIC HEAT OF A LINEAR POLYMER

Under this title, L. L. Isaacs submitted to the Department of Chemistry, M. I. T., a thesis that was accepted in partial fulfillment of the requirements for the degree of Doctor of Philosophy (August 19, 1960).

C. W. Garland

IV. MICROWAVE SPECTROSCOPY*

Prof. M. W. P. Strandberg
Prof. R. L. Kyhl
Dr. R. A. McFarlane
Dr. G. J. Wolga
J. M. Andrews, Jr.
P. H. Carr
P. C. Clapp
W. J. C. Grant
R. H. Griffin
J. G. Ingersoll
E. C. Ingraham
S. Ingvesson
J. D. Kierstead
M. S. Lipsett
D. W. Oliver
W. J. Schwabe
J. D. Stettler
A. H. Thiele
M. T. Uy
S. H. Wemple
R. M-C. Wu

A. ATOMIC RECOMBINATIONS

The side-arm method for observing chemical recombinations described in the Quarterly Progress Report of April 15, 1958, page 24, is being used to study oxygen-atom recombination within the gas volume and on surfaces. Two modes of volume recombination have been considered:

(a) $O + O_2 + O_2 \rightleftharpoons O_3 + O_2$

$O_3 + O \rightleftharpoons O_2 + O_2$

(b) $O + O + O_2 \rightleftharpoons O_2 + O_2$

Reaction (a), involving ozone as an intermediate, proceeds at a rate that is proportional to the atomic oxygen concentration; reaction (b), the direct process, proceeds with a rate constant that varies quadratically with the atomic oxygen concentration.

For reaction (a) and surface recombination, a steady-state solution of the diffusion equation in a cylindrical geometry was obtained. Green's function for this problem was used to generate a perturbation solution that includes the direct volume recombination reaction (b).

Analysis of data taken, thus far, indicates a surface recombination efficiency of 1.3×10^{-5} and a rate constant for reaction (a) of 1.7×10^{14} cm^6 mole^{-2} sec^{-1}. Our data show that only reaction (a) contributes appreciably to volume recombination at room temperature.

D. W. Oliver

B. THE GENERATION OF MICROWAVE PHONONS

A readily available source of coherent, monochromatic phonons offers a very powerful tool for the study of the vibrations of a periodic lattice and the interaction of these vibrations with paramagnetic impurity atoms. This interaction is responsible for spin-lattice relaxation. A conventional quartz transducer can serve as a source at a frequency of 10 mc (1). In general, interaction cross sections are too small to be observed at this frequency (2), and because the interaction increases with frequency, the construction of a microwave phonon generator is desirable. We have constructed such a phonon generator at X-band and phonons have been observed at temperatures from 1.5°K to 2°K.

*This work was supported in part by Signal Corps Contract DA36-039-sc-74895.

(IV. MICROWAVE SPECTROSCOPY)

Phonon packets are generated by means of the piezoelectric effect at the end surface of a quartz rod inserted into the high electric-field region of a re-entrant cavity that is driven by a pulsed microwave source (3). These packets travel down the rod, are reflected from the other end, and return to the generating surface where a small fraction of the acoustic energy is converted into microwave energy. This energy is detected by means of a superheterodyne receiver. As many as eight acoustic echoes have been observed (Fig. IV-1). The number is critically dependent upon the tolerances to which the quartz rod is cut.

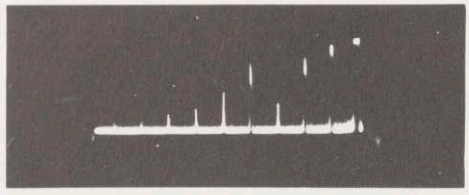

Fig. IV-1. Oscilloscope trace of phonon packets as a function of time. (Separation between pulses, 10 μsec; time increases toward the left.)

After observing the acoustic echoes, we irradiated the quartz rod with gamma rays from a Co^{60} source in order to produce paramagnetic F-centers. No decrease in the number of echoes was observed after irradiation. The end of the rod opposite the phonon-generating surface was inserted into a rectangular cavity in which the electron paramagnetic resonance was observed, but no saturation effects from a phonon-spin interaction were observed. Since present detection sensitivity is already high, our efforts will be directed toward increasing the absorbed energy by increasing the acoustic power level.

P. H. Carr

References

1. R. D. Mattuck, Phonon-spin absorption cross sections in paramagnetic crystals, Quarterly Progress Report, Research Laboratory of Electronics, M.I.T., July 15, 1958, pp. 26-27.

2. R. D. Mattuck, Phonon-Spin Absorption in Paramagnetic Crystals, Ph.D. Thesis, Department of Physics, M.I.T., May 1959.

3. Conversations and correspondence with E. H. Jacobsen of General Electric Research Laboratories, Schenectady, N.Y., have been of great use to us in designing this generator.

V. NUCLEAR MAGNETIC RESONANCE AND HYPERFINE STRUCTURE

Prof. F. Bitter
Prof. J. S. Waugh
Dr. L. C. Bradley III
Dr. P. C. Brot
Dr. H. H. Stroke
Dr. J. F. Waymouth
R. L. Fork
J. V. Gaven, Jr.
H. R. Hirsch
R. J. Hull
C. S. Johnson, Jr.
Ilana Levitan
J. H. Loehlin
F. Mannis
I. G. McWilliams
P. G. Mennitt
S. R. Miller
C. J. Schuler, Jr.
W. W. Smith
C. V. Stager
W. T. Walter

A. THE HYPERFINE STRUCTURE OF RADIO-THALLIUM 199 AND 200

The hyperfine structure and isotope shift of Tl^{200} and Tl^{199} have been measured spectroscopically. The procedure described in Quarterly Progress Report No. 51 (pages 51-52) and Quarterly Progress Report No. 52 (page 32) has been followed except for changes that will be discussed here.

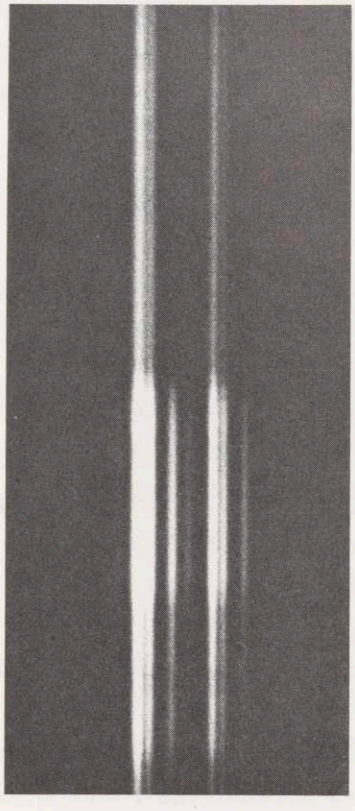

Fig. V-1. The 5350 A line of thallium. The components from left to right belong to isotopes 205, 203, 199, 200, 205, 203, and 199, respectively. The upper part of the picture is the Tl^{203} and Tl^{205} calibration spectrum.

An extra mirror (1) was used in the 40-ft monochromator of the Spectroscopy Laboratory, M. I. T., to allow the simultaneous recording of the two resonance lines of thallium at 3776 A and 5350 A. Two improvements were made in the preparation of the light source. First, more atoms were produced for the source by going to the internal beam of the cyclotron. This procedure increased the number of atoms in the lamp by a

factor of nearly 5. Second, approximately 1 μgm of indium in the form of indium chloride was placed in the lamp. It had been found experimentally that a small amount of such impurity in the lamp increased the useful life of the lamp appreciably. The calibration of the plates was improved by using an Osram thallium lamp. The spectrum emitted by this lamp is extremely stable and reliable for photographic work. Finally, to prevent overexposure of the radio-thallium spectrum, a rotating step sector was placed before the slit of the spectrograph.

The measurements previously made on Tl^{199} have been confirmed within an accuracy of approximately 2 per cent. New data were obtained from a spectrogram of both isotopes in the green line (see Fig. V-1). This plate, just as the plate of the ultraviolet line, showed a single line for Tl^{200}; thus it is confirmed that its hyperfine structure is indeed less than the observed linewidth (~40 mk). This is consistent with the extremely small hfs separations that have been observed by means of atomic-beam magnetic-resonance techniques in other odd-odd isotopes of thallium. The measured isotope shifts between Tl^{199} and Tl^{205} are 164 mk and 177 mk for the ultraviolet and green lines, respectively. The corresponding values for Tl^{200}-Tl^{205} are 148 mk and 169 mk. The accuracy of these results is approximately ±5 mk.

R. J. Hull, H. H. Stroke

References

1. K. K. Y. Li and H. H. Stroke, Quarterly Progress Report No. 55, Research Laboratory of Electronics, M. I. T., Oct. 15, 1959, p. 60.

B. HYPERFINE STRUCTURE IN THE $^3P_1$ LEVEL OF Hg^{197*}

The hyperfine structure of Hg^{197*} has been measured in the $^3P_1$ level with greater accuracy than that obtained in previous spectroscopic work (1). The level-crossing and double-resonance experiments were used to obtain the hfs separations, and the isotope shift was determined by a magnetic-scanning experiment.

The level crossing described in Quarterly Progress Report No. 58 (page 101) has been identified as the intersection between the F = 15/2, m = 15/2 and F = 13/2, m = 11/2 levels. This crossing occurs at a field whose proton-resonance frequency is 33,364.2 ± 8.0 kc. A double resonance has been observed between the F = 15/2, m = 15/2 and F = 15/2, m = 13/2 levels with a radio frequency of 3053.91 ± .02 mc and a magnetic field proton-resonance frequency of 24,268.4 ± 4.8 kc. With the use of magnetic scanning, the separation between the Hg^{197*}, F = 11/2 and Hg^{198} levels at zero field has been measured as 19,360 ± 130 mc.

In order to use these data for the calculation of the Hg^{197*} hyperfine structure, it is necessary to know the electronic g value of the $^3P_1$ level. Level-crossing experiments

Table V-1. Hyperfine structure in the $^3P_1$ level of Hg^{197*}

Quantity	Value (mc)
W_L	18246 ± 14
W_H	14236 ± 20
W_I	2240 ± 130
A	-2328.8 ± 1.7
B	-901 ± 13

Explanation of Symbols

W_L: The separation between the F = 15/2 and F = 13/2 levels at zero field.
W_H: The separation between the F = 13/2 and F = 11/2 levels at zero field.
W_I: The isotope shift of Hg^{197*} relative to Hg^{198}.
A: The magnetic dipole interaction constant.
B: The electric quadrupole interaction constant.

in Hg^{199} and Hg^{197} and a double-resonance experiment in Hg^{198} lead to the value, 1.4861 ± .00036.

Table V-1 gives the numerical results pertinent to the hyperfine structure of Hg^{197*}. The limits of error are three times the standard deviation of the individual measurements from the mean of the quantity. A much more detailed report of this work, together with an interpretation of the data in terms of nuclear moments, is contained in a thesis (2) that has been submitted to the Department of Physics and in a paper, based on the thesis, which will be submitted for publication to the Journal of the Optical Society of America.

H. R. Hirsch

References

1. A. C. Melissinos and S. P. Davis, Dipole and quadrupole moments of the isomeric Hg^{197*} nucleus; Isomeric isotope shift, Phys. Rev. 115, 130 (1959).

2. H. R. Hirsch, Hyperfine Structure in the $^3P_1$ Level of the Twenty-Four Hour Isomer of Mercury 197, Ph. D. Thesis, Department of Physics, M. I. T., 1960.

C. HYPERFINE STRUCTURE IN THE $^3P_1$ STATE OF Hg^{197}

The previously described experiment (1) on the hyperfine structure of Hg^{199} has been extended to the 65-hr half-life isotope Hg^{197}. The value of the zero-field hfs splitting is 23,086.37 ± 0.02 mc. The error is the probable error obtained from a

least-square fit of the data. Systematic errors have been estimated and are believed to be smaller than the probable error quoted here.

C. V. Stager

References

1. C. V. Stager, Hyperfine structure of the $^3P_1$ state of Hg^{199}, Quarterly Progress Report No. 57, Research Laboratory of Electronics, M. I. T., April 15, 1960, p. 63.

D. DIRECT MEASUREMENT OF THE HYPERFINE SPLITTING OF THE $^3P_1$ LEVEL OF Hg^{197*}

The hyperfine interval F = 13/2→F = 11/2 of the $^3P_1$ level of Hg^{197*} (nuclear isomer; half-life, 23 hours, nuclear spin I = 13/2) was measured by the direct double-resonance method developed by Kohler (1, 2, 3). The sample of Hg^{197*} was prepared by bombardment of gold with deuterons and extracted by following the technique of Bitter et al. (4).

The double-resonance experiment was made possible by the fortuitous coincidence of the $^3P_1$ level of Hg^{196} with the $^3P_1$ F = 13/2 level of Hg^{197*}. We therefore used a lamp and an absorption filter cell, both of which contained Hg^{196} enriched to a value of 8.5 per cent.

The data obtained both at zero field and with weak magnetic-field sweep indicate that (a) the interval F = 13/2→F = 11/2 is 14,234.86 ± 0.09 mc; (b) the value I = 13/2 of the nuclear spin is confirmed.

P. C. Brot

References

1. R. H. Kohler, Hyperfine structure of the $^3P_1$ state of mercury by double-resonance methods, Quarterly Progress Report, Research Laboratory of Electronics, M. I. T., July 15, 1956, pp. 20-21.

2. R. H. Kohler, Heavy absorption of a spectral line, Quarterly Progress Report No. 52, Research Laboratory of Electronics, M. I. T., Jan. 15, 1959, pp. 32-37.

3. R. H. Kohler, Detection of double resonance by frequency change: Application to Hg^{201} (submitted for publication to Phys. Rev.).

4. F. Bitter, S. P. Davis, B. Richter, and J. E. R. Young, Optical studies of radioactive mercury, Phys. Rev. 96, 1531 (1954).

VI. MICROWAVE ELECTRONICS*

Prof. L. D. Smullin
Prof. H. A. Haus
Prof. A. Bers
C. G. Alexander
K. Arons
J. Hennel
R. B. McCullough
D. L. Morse
W. D. Rummler
W. K. Rushforth

A. THE X-LINE SLOW-WAVE STRUCTURE

In Quarterly Progress Report No. 56 (pages 104-107) some preliminary measurements performed on an elementary X-line were presented. Detailed measurements have been made on several variations of this structure to ascertain the factors that determine the edges of the lowest passband.

The X-lines that were tested were made from obstacles like that shown in Fig. VI-1, separated by hollow cylindrical spacers. Figure VI-2 is a schematic drawing of an X-line showing the geometric parameters of the structure. The angle a denotes the angular displacement of even-numbered bars with respect to odd-numbered bars.

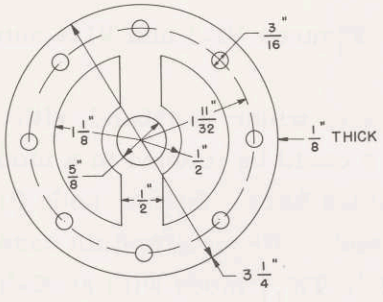

Fig. VI-1. X-line obstacle.

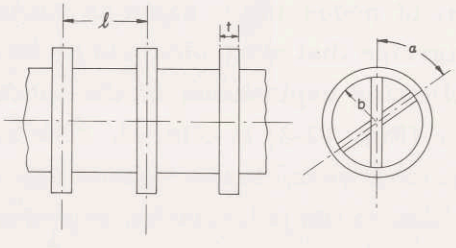

Fig. VI-2. Schematic drawing of the X-line showing geometric parameters.

The ω-β diagrams of several X-lines that were tested were obtained by short-circuiting a section of the periodic structure having a length $N\ell$. For each passband of the structure, this short-circuited line has N + 1 resonant frequencies. The line is resonant when the phase shift per period is

$$\beta_o = \frac{p\pi}{N\ell} \qquad p = 0, 1, 2, \ldots, N \tag{1}$$

The resonances are identified by moving a metallic needle along the axis of the structure (this perturbs only the E_z-field) and counting the number of nodes in the field pattern.

*This work was supported in part by Purchase Order DDL B-00306 with Lincoln Laboratory, a center for research operated by Massachusetts Institute of Technology with the joint support of the U.S. Army, Navy, and Air Force under Air Force Contract AF19(604)-5200.

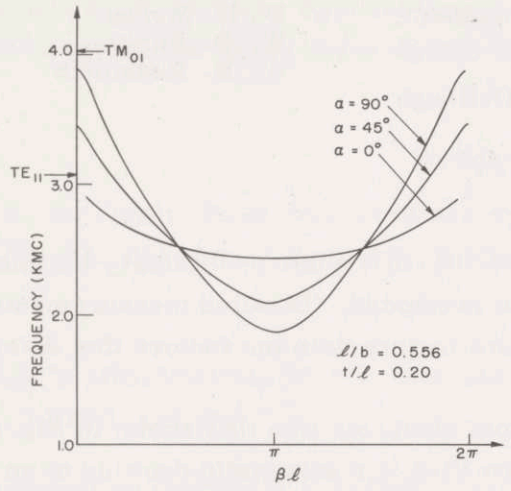

Fig. VI-3. ω-β diagrams for three values of α.

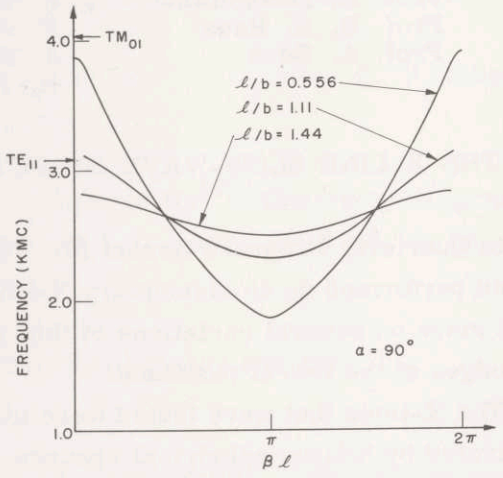

Fig. VI-4. ω-β diagrams for three values of ℓ/b.

The number of nodes is the same as the index p in Eq. 1. Figures VI-3 and VI-4 show the ω-β diagrams that were obtained by this method.

The following explanation of the increased dispersion and wider passband with increased α (Fig. VI-3) is offered. The structure with $\alpha = 0$ could be likened to a mode filter if the bars were closely spaced thin wires instead of thick bars. Such a mode filter would remove the polarization degeneracy of the TE_{11} mode. Hence, for this case, the mode of propagation may be viewed as a slightly perturbed TE_{11} mode with an E-field polarization normal to the bars. A possible justification for this line of reasoning is that the zeroth mode of the resonator does not exist (there is no TE_{110} mode in a circular cylindrical cavity), but the dispersion curve approaches the TE_{11} cutoff as $\beta\ell$ approaches zero.

For the other extreme (α=90°) shown in Fig. VI-3 we may apply a similar line of reasoning. Since adjacent bars are at right angles, and the spacing between the bars is small, no mode resembling a TE_{11} mode is likely to propagate. The upper cutoff frequency in this case is near the TM_{01} cutoff frequency. As the angle α is increased from zero to 90°, the upper band edge moves from near the TE_{11} cutoff to the TM_{01} cutoff.

This same line of reasoning can be used to explain the effect of varying ℓ/b on the upper cutoff frequency (Fig. VI-4). For large ℓ/b we might expect a wave similar to a TE_{11} wave to propagate. As ℓ/b is decreased, the upper cutoff frequency increases and approaches the TM_{01} cutoff, as before.

Another pronounced effect of increasing α is the depression of the lower cutoff frequency. This can best be explained by considering the π resonance, the frequency of which corresponds to the lower cutoff frequency, as a resonance between adjacent wires.

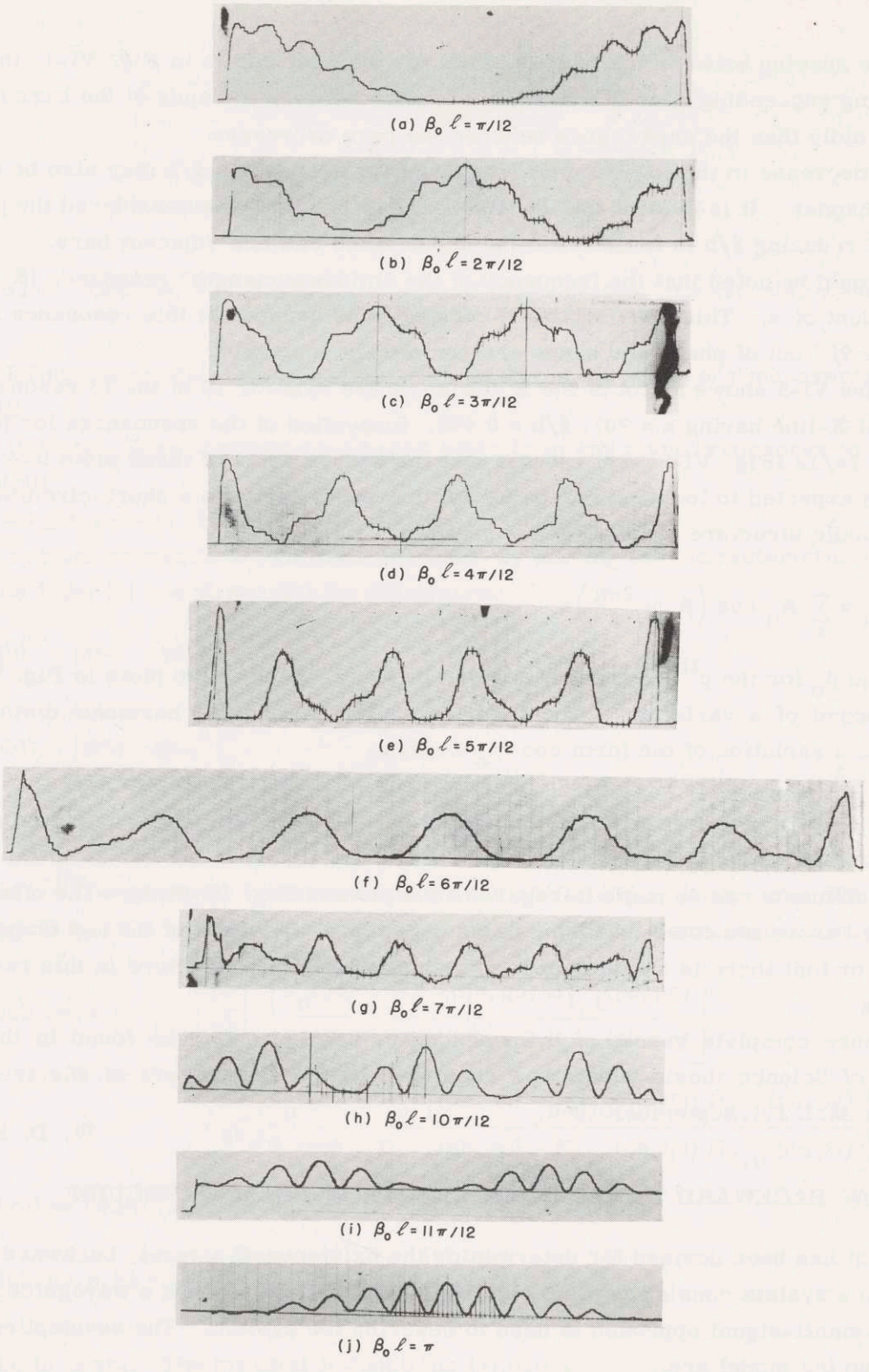

Fig. VI-5. Plots of E_z^2 for a resonated X-line of 12 sections: $\ell/b = 0.556$; $t/\ell = 0.20$; $a = 90°$.

Since the spacing between the bars is small for the case shown in Fig. VI-3, the effect of rotating succeeding bars is that the inductance between the ends of the bars increases more rapidly than the capacitance between the bars decreases.

The decrease in the lower cutoff frequency for decreasing ℓ/b may also be explained in this manner. It is evident that for the range of ℓ/b that was considered the principal effect of reducing ℓ/b is to increase the capacitance between adjacent bars.

It should be noted that the frequency of the "mid-wavelength" resonance ($\beta_o \ell = \pi/2$) is independent of α. This does not seem unreasonable because at this resonance adjacent bars are 90° out of phase and hence are completely uncoupled.

Figure VI-5 shows a plot of the E_z^2 fields on the axis for 10 of the 13 resonances of a 12-cell X-line having $\alpha = 90°$, $\ell/b = 0.556$. Inspection of the resonances for $\beta_o \ell = \pi/12$ to $\beta_o \ell = 7\pi/12$ (Fig. VI-5a-5g) reveals that the square roots of these plots look as they might be expected to look. It can be shown that the E_z-field in a short-circuited section of a periodic structure of length $N\ell$ is given by

$$E_z = \sum_n A_n \cos \left(\beta_o - \frac{2\pi n}{\ell} \right) z \qquad (2)$$

where the β_o for the p^{th} resonance is given by Eq. 1. Each of the plots in Fig. VI-5a-5g is composed of a variation of the form $\cos \beta_o z$ plus a visible harmonic distortion that indicates a variation of the form $\cos (\beta_o - 2\pi/\ell)\, z$.

The E_z^2 field plot in Fig. VI-5h breaks into 3 sections. This plot was assigned a value of β_o in accordance with the number of nodes in the field pattern, but no way has been found to synthesize such a field plot from the terms of the series in Eq. 2. The same statements can be made in regard to the plots of Fig. VI-5i, 5j. The effect that is described above indicates that there is an anomaly in the shape of the ω-β diagram in this region, or that there is another mode of propagation in the structure in this range of frequencies.

A more complete report of the work described here may be found in the author's Master of Science thesis which was submitted to the Department of Electrical Engineering, M. I. T., September 1960.

W. D. Rummler

B. SLOW BACKWARD WAVES IN AN ELECTRON-BEAM WAVEGUIDE

A test has been devised for determining the existence of natural, backward, slow waves in a system consisting of an electron beam drifting through a waveguide. The linearized small-signal approach is used to describe the system. The assumptions used in setting up the model are:

(a) Neutralized electron beam drifting in a waveguide, free of static electric fields, having perfectly conducting walls.

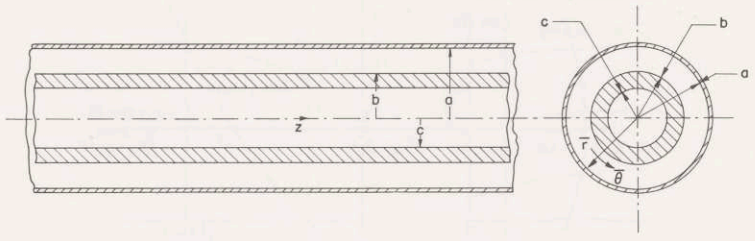

Fig. VI-6. Geometry of the hollow electron-beam system in a circular waveguide.

(b) Infinite magnetic-focusing field oriented in the direction of time-average electron drift.

(c) Uniform, time-average charge and velocity in any plane transverse to the direction of drift.

(d) Single-valued, time-average velocity and density.

The system propagation constants are found by solving the characteristic set of equations (see Hahn (1) and Ramo (2)) for the system:

$$(qb)^2 = (kb)^2 - (\beta b)^2 \tag{1}$$

$$(pb)^2 = \left[(kb)^2 - (\beta b)^2\right]\left[1 - \frac{(\beta_p b)^2}{(\beta_e - \beta)^2 b^2}\right] \tag{2}$$

$$D(pb, qb, a, b, c) = 0 \tag{3}$$

where an $e^{-j\beta z}$ dependence has been assumed for all field quantities. For TM waves in a cylindrical system in which the electron beam and drift tube are concentric, we have

$$D(pb, qb, a, b, c) = \left[\frac{pb}{qb}\right]^2 \left[\frac{J_o(qc)}{J_1(qc)} \cdot \frac{H_{0,0}(qb, qa)\, H_{1,1}(pb, pc)}{H_{1,0}(qb, qa)\, H_{0,0}(pb, pc)}\right]$$

$$- \frac{pb}{qb}\left[\frac{J_o(qc)}{J_1(qc)} \cdot \frac{H_{0,1}(pb, pc)}{H_{0,0}(pb, pc)} + \frac{H_{0,0}(qb, qa)\, H_{1,0}(pb, pc)}{H_{1,0}(qb, qa)\, H_{0,0}(pb, pc)}\right] + 1 \tag{4}$$

for the hollow beam (Fig. VI-6); and

$$D(pb, qb, a, b) = pb\, \frac{J_1(pb)}{J_o(pb)} - qb\, \frac{H_{1,0}(qb, qa)}{H_{0,0}(qb, qa)} \tag{5}$$

for the solid beam. The biradial H-functions (3) are

$$H_{m,n}(x, y) = \frac{\pi}{2}\left[J_m(x) N_n(y) - N_m(x) J_n(y)\right] \tag{6}$$

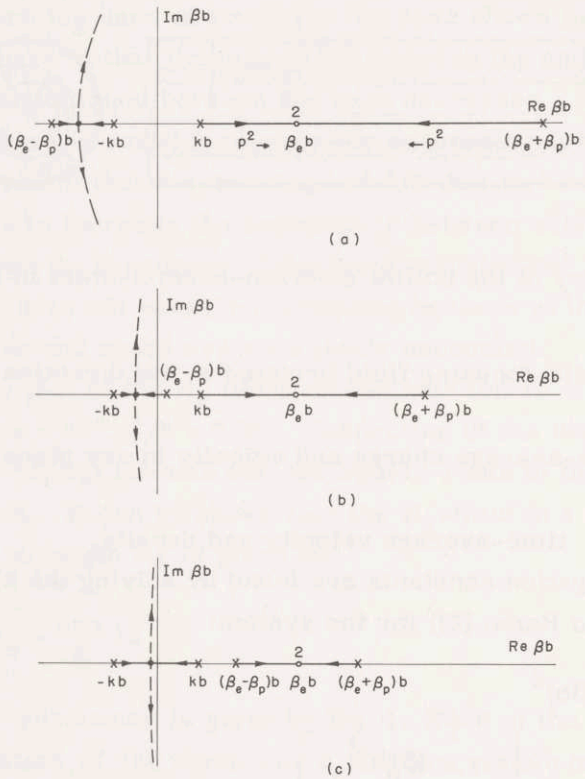

Fig. VI-7. Root locus plots for Eq. 2 with $(pb)^2$ real and positive: (a) $\omega_p/\omega > \left(1 + \frac{v_o}{c}\right)$; (b) $\left(1 - \frac{v_o}{c}\right) < \omega_p/\omega < \left(1 + \frac{v_o}{c}\right)$; (c) $\omega_p/\omega < \left(1 + \frac{v_o}{c}\right)$.

For purely propagating slow waves, $(qb)^2$ must be negative and real. The boundary conditions do not allow $(pb)^2$ to be negative and real when $(qb)^2$ is negative and real, nor can $(pb)^2$ be complex under these conditions. Hence, $(pb)^2$ must be positive and real.

The possible values of βb that satisfy Eq. 2 can be represented graphically with the aid of a root locus diagram. Figure VI-7 shows root locus diagrams for $(pb)^2$ positive and real and with fixed values of $\beta_e b$ and kb, for three different values of $\beta_p b$. The arrows on the loci of Fig. VI-7 show the direction of displacement of the values of βb that satisfy Eq. 2 as $(pb)^2$ is increased. The loci of Fig. VI-7 for complex βb are dotted because the complex βb will not satisfy Eq. 3 when $(pb)^2$ is positive and real. Figure VI-7a shows the condition for which βb is negative, real, and larger than kb. The diagram shows that for backward slow waves to exist $(\beta_e - \beta_p)$ b must be less than -kb (that is, $\omega_p/\omega > 1 + v_o/c$). With this condition satisfied, backward slow waves will exist if the boundary condition equation, Eq. 3, is satisfied simultaneously.

The solution of Eq. 3, for $(pb)^2$ real and positive with $(qb)^2$ real and negative for either the hollow or solid beam, can be presented in the form shown in Fig. VI-8b.

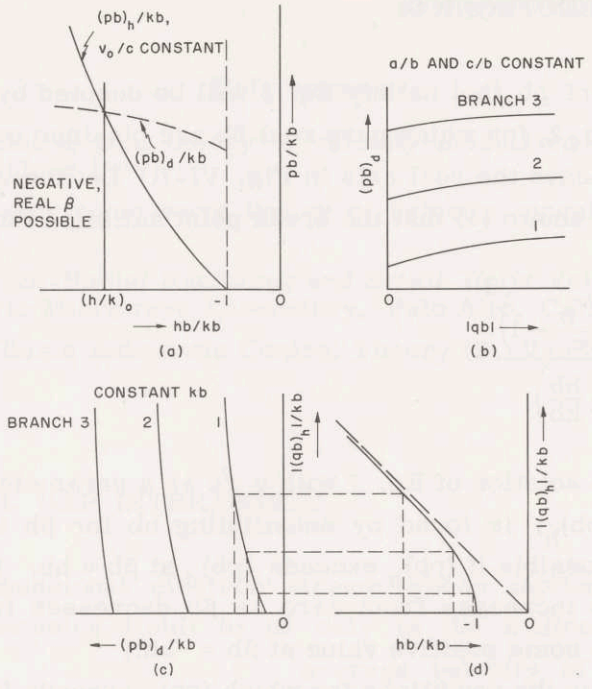

Fig. VI-8. Demonstration of the solution for negative real β when $\omega_p/\omega > \left(1 + \frac{v_o}{c}\right)$.

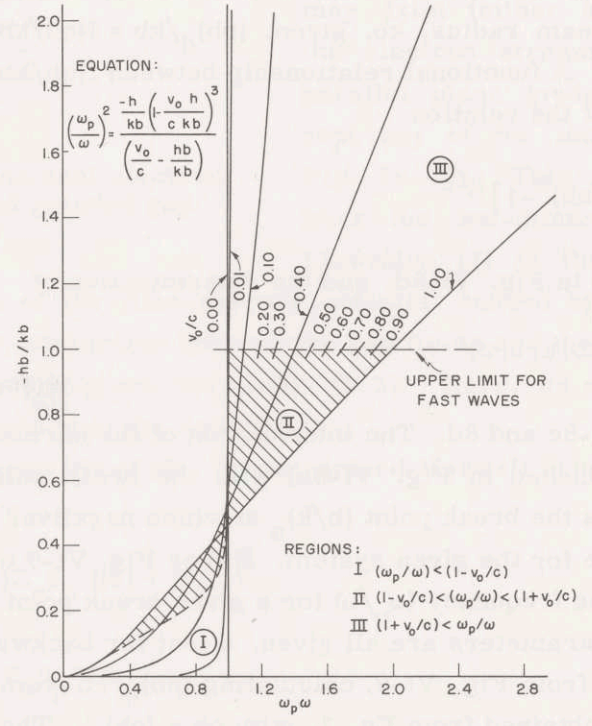

Fig. VI-9. Variation of break point with ω_p/ω and v_o/c for $(pb)^2$ positive and real.

Hereafter, the values of pb that satisfy Eq. 3 will be denoted by $(pb)_d$. The maximum value of $(pb)^2$, from Eq. 2, for which pure real βb are obtained occurs at the break point, where the dotted loci leave the real axis in Fig. VI-7. Let the value of βb at the break point be hb. It can be shown (4) that the break point satisfies the expression

$$\left(\frac{\omega_p}{\omega}\right)^2 = \frac{\frac{hb}{kb}\left(\frac{hb}{kb}\cdot\frac{v_o}{c}-1\right)^3}{\left(\frac{v_o}{c}-\frac{hb}{kb}\right)} \tag{7}$$

Figure VI-9 shows the solution of Eq. 7 with v_o/c as a parameter. The value of $(pb)^2$ at the break point, $(pb)_h$, is found by substituting hb for βb in Eq. 2. Backward slow waves will be possible if $(pb)_h$ exceeds $(pb)_d$ at βb = hb. (Note that the value of pb = f(βb, kb, β_pb, β_eb) increases from zero as βb decreases from -kb, while $(pb)_d$ increases slowly from some positive value at βb = -kb.)

A method for finding the conditions for which $(pb)_h$ exceeds $(pb)_d$ is demonstrated in Fig. VI-8. Specification of the average drift velocity, v_o/c, gives a particular solution of $(pb)_h = f(hb/kb, v_o/c)$, as indicated by the solid curve of Fig. VI-8a (note that the break point variable is on the abscissa). Specification of beam and drift-tube radii determines $(pb)_d = f(qb, a, b, c)$ from the boundary condition determinantal equations (Fig. VI-8b). With the normalized beam radius, kb, given, $(pb)_d/kb = f(qb/kb, a, b, c)$ and hb/kb may be found (Fig. VI-8c). A functional relationship between f(qb/kb, a, b, c) and hb/kb may be found with the aid of the relation

$$|qb|_h/kb = [(hb/kb)^2-1]^{1/2} \tag{8}$$

Equation 8 is sketched in Fig. VI-8d; and the determination of

$$(pb)_d/kb = f(hb/kb, a, b, c) \tag{9}$$

is indicated in Fig. VI-8c and 8d. The intersection of the normalized boundary condition curve (Eq. 9 shown dashed in Fig. VI-8a) with the break point curve, as shown in Fig. VI-8a, determines the break point $(h/k)_o$ at which negative, real, propagation constants become possible for the given system. Either Fig. VI-9 or Eq. 7 may be used to find the relative plasma frequency (ω_p/ω) for a given break point hb/kb.

When the system parameters are all given, a test for backward slow waves may be made by finding hb/kb from Fig. VI-9, calculating $(pb)_h/kb$ from Eq. 2, and comparing the result with $(pb)_d$, obtained from Eq. 3, with $qh = (qb)_h$. The variation of the break point as a function of v_o/c can be found, once $(pb)_d/kb$ is known.

C. G. Alexander, A. Bers

References

1. W. C. Hahn, Small-signal theory of velocity-modulated electron beams, Gen. Elec. Rev. 42, 258-70 (June 1939).

2. S. Ramo, The electronic-wave theory of velocity-modulation tubes, Proc. IRE 27, 757-763 (1939).

3. C. K. Birdsall, Bi-Radial Functions and Sheath Helix Velocity Curves, Informal Report, General Electric Microwave Laboratory, Palo Alto, California, 1953.

4. G. J. Murphy, Basic Automatic Control Theory (D. Van Nostrand Company, Inc., New York, 1957).

C. ONE-DIMENSIONAL GAP INTERACTION

Consider a one-dimensional electron stream whose motion is constrained (by an infinite magnetic-focusing field) to be only in the z-direction. Let the time-average velocity of the stream be v_o and the time-average charge density be ρ_o. The time-average electron density is neutralized by a stationary ion background. Fields external to this system may exist (either applied or induced by the electron stream) between two infinite parallel plane grids that do not intercept any of the moving charges (see Fig. IV-10). This system is different from the one-dimensional gap system of Llewellyn (1) in that between the planes there is no depression of the time-average potential caused by space charge.

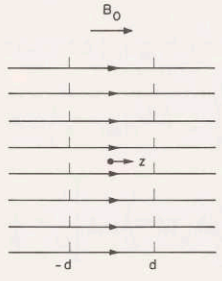

Fig. VI-10. One-dimensional electron stream and gridded gap.

The solution for the interaction between the gap fields and the space-charge fields is a special case of the theory given previously (2, 3). Here, we shall give a numerical evaluation of the parameters in the solution.

For the region between the grids, the linearized Maxwell equation, and the force and continuity equations give

$$\left(j\beta_e + \frac{\partial}{\partial z}\right) V(z) = jZ_o\beta_p I(z) + E_z^c(z) \tag{1}$$

$$\left(j\beta_e + \frac{\partial}{\partial z}\right) I(z) = jY_o\beta_p V(z) \tag{2}$$

where $\beta_e = \omega/v_o$ is the electron phase constant, $\beta_p = \omega_p/v_o$ is the plasma phase constant, $V(z) = mv_o v(z)/e$ is the kinetic voltage, $E_z^c(z)$ is the electric field resulting from charges

on the grids, $I(z) = \sigma J(z)$ is the beam-current modulation (σ is a particular cross-section area transverse to z) and

$$Y_o = \frac{1}{Z_o} = \omega \epsilon_o \sigma \beta_p = \frac{I_o}{R(R+1)\, V_o} \frac{\omega}{\omega_p} \tag{3}$$

with $R = \left(1+v_o^2/c^2\right)^{-1/2}$; I_o, the time-average beam current; and V_o, the time-average beam voltage. Equations 1, 2, and 3 apply to an electron stream with relativistic time-average velocities. The electron mass m in the definitions of kinetic voltage and of the plasma frequency $\left(\omega_p^2 = m\rho_o/e\epsilon_o\right)$ is the longitudinal mass, $m = m_o R^3$.

The interaction can be conveniently described by the following linear representation

$$\begin{bmatrix} V(z) \\ I(z) \\ \hline I_g \end{bmatrix} = \left[\begin{array}{cc|c} A & B & a \\ C & D & b \\ \hline c & c & Y_{e\ell} \end{array}\right] \begin{bmatrix} V(-d) \\ I(-d) \\ \hline V_g \end{bmatrix} \tag{4}$$

or in matrix form with the partitioning as shown in Eq. 4:

$$\begin{bmatrix} \underline{\underline{B}}_2 \\ \hline I_g \end{bmatrix} = \left[\begin{array}{c|c} \underline{\underline{D}} & \underline{\underline{K}} \\ \hline \underline{\underline{\Gamma}} & Y_{e\ell} \end{array}\right] \begin{bmatrix} \underline{\underline{B}}_1 \\ \hline V_g \end{bmatrix}$$

$$= \left[\begin{array}{c|c} \underline{\underline{D}}_{g2} & \underline{\underline{0}} \\ \hline \underline{\underline{0}} & 1 \end{array}\right] \left[\begin{array}{c|c} \underline{\underline{I}} & \underline{\underline{K}}_g \\ \hline \underline{\underline{\Gamma}}_g & Y_{e\ell} \end{array}\right] \left[\begin{array}{c|c} \underline{\underline{D}}_{1g} & \underline{\underline{0}} \\ \hline \underline{\underline{0}} & 1 \end{array}\right] \begin{bmatrix} \underline{\underline{B}}_1 \\ \hline V_g \end{bmatrix} \tag{5}$$

The drift matrix $D = D_{g2}D_{1g}$ describes the drifting transformation of the modulations on the beam in the absence of circuit fields between the grids

$$A = D = \frac{1}{2}\left\{\exp[-j\beta_+(d+z)]+\exp[-j\beta_-(d+z)]\right\} = \cos\beta_p(d+z)\exp[-j\beta_e(d+z)] \tag{6}$$

$$B = \frac{1}{2} Z_o\left\{\exp[-j\beta_+(d+z)]-\exp[-j\beta_-(d+z)]\right\} = jZ_o \sin\beta_p(d+z)\exp[-j\beta_e(d+z)] \tag{7}$$

$$C = \frac{1}{2} Y_o\left\{\exp[-j\beta_+(d+z)]-\exp[-j\beta_-(d+z)]\right\} = jY_o \sin\beta_p(d+z)\exp[-j\beta_e(d+z)] \tag{8}$$

where

$$\beta_+ = \beta_e - \beta_p \tag{9}$$

and

$$\beta_- = \beta_e + \beta_p \tag{10}$$

are, respectively, the fast and slow space-charge wave propagation constants of the

natural system of a freely drifting electron stream. The coupling matrices $\underline{\underline{K}}_g$ and $\underline{\underline{\Gamma}}_g$ are given by

$$\underline{\underline{K}}_g = \begin{bmatrix} M \\ Y_o N \end{bmatrix} \tag{11}$$

$$\underline{\underline{\Gamma}}_g = \begin{bmatrix} Y_o N^* & M^* \end{bmatrix} \tag{12}$$

where

$$M = \frac{1}{2}(M_+ + M_-) \tag{13}$$

$$N = \frac{1}{2}(M_+ - M_-) \tag{14}$$

and

$$M_\pm = \int_{-d}^{d} E_z^c(z)\, e^{j\beta_\pm z}\, dz \tag{15}$$

The electronic-loading admittance $Y_{e\ell} = G_{e\ell} + jB_{e\ell}$ is found to be

$$G_{e\ell} = \mathrm{Re}\left(Y_o M N^*\right) = \frac{1}{4} Y_o \left[|M_+|^2 - |M_-|^2 \right] \tag{16}$$

$$B_{e\ell} = \frac{1}{4} Y_o \left[\mathrm{Im}\left(2M_+ M_-^*\, e^{jz\beta_p d}\right) - \mathrm{Re} \int_{-d}^{d} 4M_+(z)\, M_-(z)\, e^{jz\beta_p z}\, dz \right] \tag{17}$$

Equations 11-17 are for an arbitrary variation of the electric field $E_z^c(z)$ between the grids. For a uniform circuit field

$$\begin{aligned} E_z^c(z) &= \frac{1}{2d} \qquad |z| \leq d \\ &= 0 \qquad |z| \geq d \end{aligned} \tag{18}$$

we have

$$M_\pm = \frac{\sin \beta_\pm d}{\beta_\pm d} \tag{19}$$

from which M and N follow readily. The electronic-loading admittance is found to be

$$G_{e\ell} = \frac{1}{4} Y_o \left[\left(\frac{\sin \beta_+ d}{\beta_+ d} \right)^2 - \left(\frac{\sin \beta_- d}{\beta_- d} \right)^2 \right] \tag{20}$$

$$B_{e\ell} = \frac{1}{4} Y_o \left[\frac{\sin \beta_+ d \cos \beta_+ d - \beta_+ d}{(\beta_+ d)^2} - \frac{\sin \beta_- d \cos \beta_- d - \beta_- d}{(\beta_- d)^2} \right] \tag{21}$$

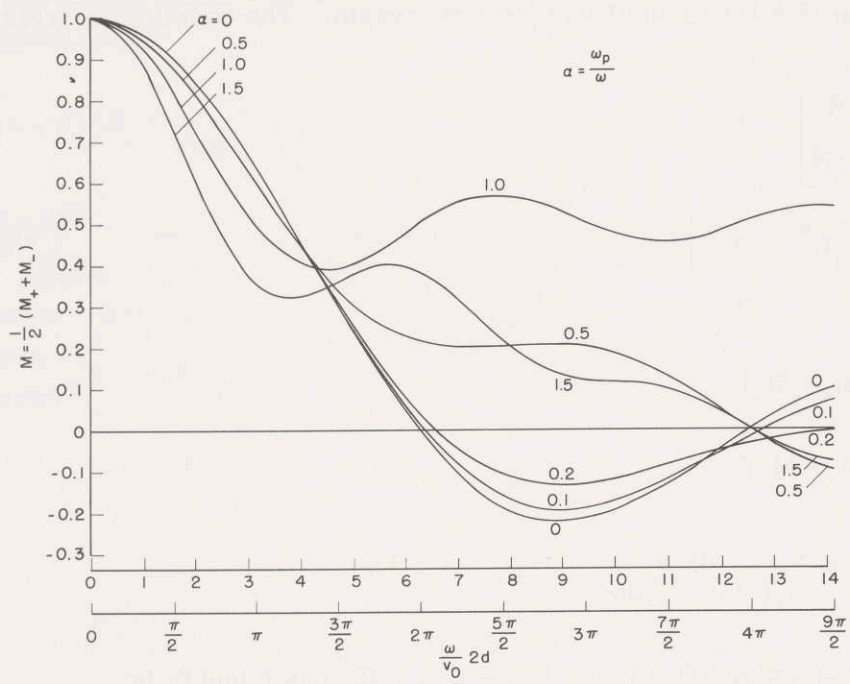

Fig. VI-11. Voltage-gap coupling coefficient.

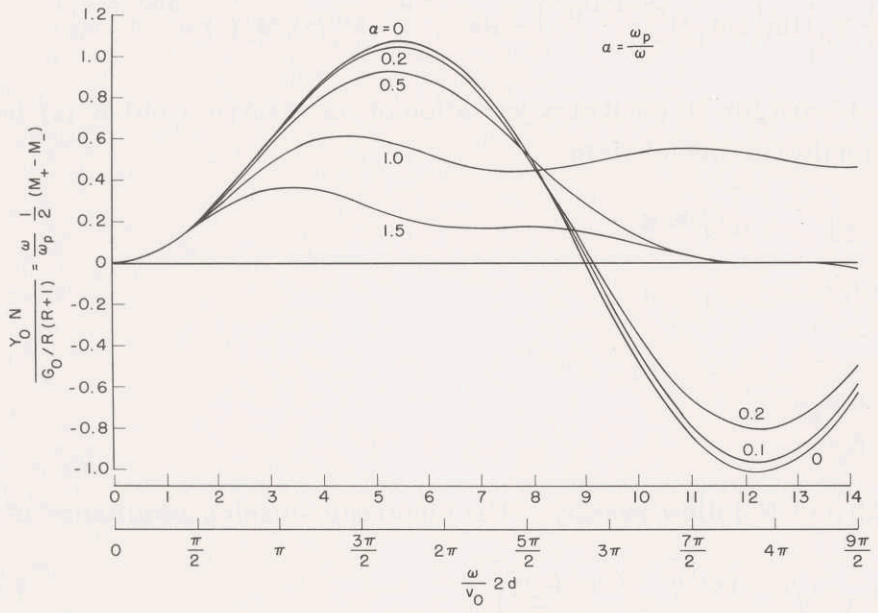

Fig. VI-12. Current-gap coupling coefficient.

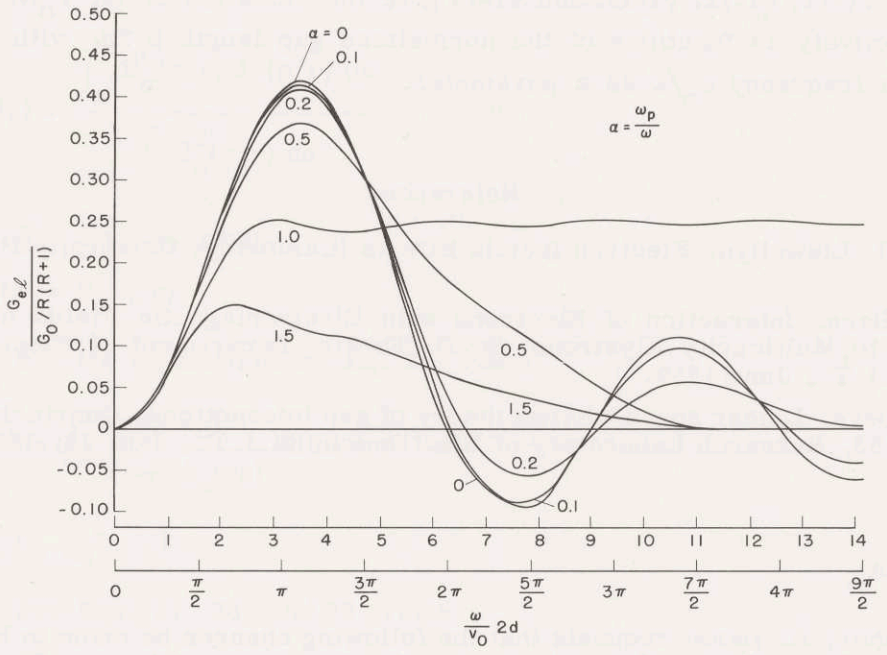

Fig. VI-13. Electronic-loading conductance.

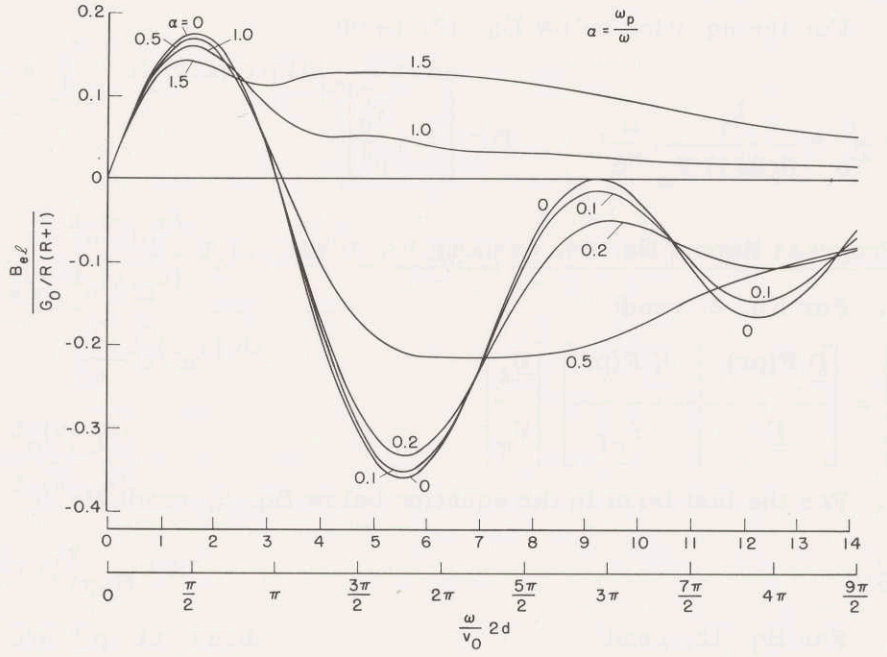

Fig. VI-14. Electronic-loading susceptance.

Figures VI-11, VI-12, VI-13, and VI-14 give the variation of M, $Y_o N$, $G_{e\ell}$, and $B_{e\ell}$, respectively as functions of the normalized gap length $\beta_e 2d$, with the normalized plasma frequency ω_p/ω as a parameter.

A. Bers

References

1. F. B. Llewellyn, Electron Inertia Effects (Cambridge University Press, London, 1941).

2. A. Bers, Interaction of Electrons with Electromagnetic Fields of Gaps with Application to Multicavity Klystrons, Sc. D. Thesis, Department of Electrical Engineering, M. I. T., June 1959.

3. A. Bers, Linear space-charge theory of gap interactions, Quarterly Progress Report No. 52, Research Laboratory of Electronics, M. I. T., Jan. 15, 1959, pp. 39-43.

D. ERRATA

[The author, A. Bers, requests that the following changes be made in his discussions of the space-charge theory of gap interaction that have appeared in our Quarterly Progress Reports. Ed.]

Quarterly Progress Report No. 52, January 15, 1959

Page 41. For the equation below Eq. 12, read:

$$Y_o = \frac{1}{Z_o} = \frac{I_o}{R(R+1)\, V_o} \frac{\omega}{\omega_q}; \qquad R = \left[1 - \frac{v_o^2}{c^2}\right]^{-1/2}$$

Quarterly Progress Report No. 55, October 15, 1959

Page 66. For Eq. 2, read:

$$\begin{bmatrix} \underline{\underline{B}}_2 \\ \hline I_g \end{bmatrix} = \left[\begin{array}{c|c} \underline{\underline{D}}\, F(pr) & \underline{\underline{K}}\, F(pr) \\ \hline \underline{\underline{\Gamma}} & Y_{e\ell} \end{array}\right] \begin{bmatrix} \underline{\underline{B}}_1 \\ \hline V_g \end{bmatrix}$$

Page 66. For the last term in the equation below Eq. 5, read:

$$\left(k = \frac{\omega}{c}\right)$$

Page 67. For Eq. 12, read:

$$Y_{on} = \frac{I_o}{R(R+1)\, V_o} \frac{\omega}{\omega_{qn}}; \qquad R = \left[1 - \frac{v_o^2}{c^2}\right]^{-1/2}$$

Page 68. For Eq. 24, read:

$$C_n E_c(z) = \frac{\int_\sigma E_c(z, r)\, J_o(p_n r)\, da}{\int_\sigma J_o^2(p_n r)\, da}$$

Page 68. For Eq. 25, read:

$$C_B E_c(z) = E_c(z, b)$$

Page 68. For the equation below Eq. 25, read:

$$E_c(z, r) = \frac{1}{2\pi} \int_{-\infty}^{\infty} \frac{J_o(vr)}{J_o(va)}\, M(u)\, e^{-juz}\, du$$

$$v^2 = -u^2 + k^2$$

Page 68. For Eqs. 27, 28, and 29, read:

$$a_{n,B} = \frac{1}{2}\left[M_{+n,B} C_{+n,B} \exp(-j\beta_{+n,B}) + M_{-n,B} C_{-n,B} \exp(-j\beta_{-n,B} z)\right]$$

$$b_{n,B} = \frac{1}{2} Y_{on,B}\left[M_{+n,B} C_{+n,B} \exp(-j\beta_{+n,B} z) - M_{-n,B} C_{-n,B} \exp(-j\beta_{-n,B} z)\right]$$

$$M_{\pm n,B} = \int_{-\infty}^{\infty} E_c(z, a) \exp(j\beta_{\pm n,B} z)\, dz$$

with

$$C_{\pm n} = \frac{\int_\sigma \frac{J_o(v_{\pm n} r)}{J_o(v_{\pm n} a)}\, J_o(p_n r)\, da}{\int_\sigma J_o^2(p_n r)\, da}$$

$$C_{\pm B} = \frac{J_o(v_{\pm B} b)}{J_o(v_{\pm B} a)}$$

$$v_{\pm n,B}^2 = -\beta_{\pm n,B}^2 + k^2$$

Page 69. For Eq. 32, read:

$$c_{n,B} = \frac{1}{2} Y_{on,B}\left[M_{+n,B}^* K_{+n,B} \exp(-j\beta_{+n,B} \ell) - M_{-n,B}^* K_{-n,B} \exp(-j\beta_{-n,B} \ell)\right]$$

Page 69. For Eq. 33, read:

$$d_{n,B} = \frac{1}{2}\left[M^{*}_{+n,B} K_{+n,B} \exp(-j\beta_{+n,B}\ell) + M^{*}_{-n,B} K_{-n,B} \exp(-j\beta_{-n,B}\ell)\right]$$

Page 69. For Eq. 34, read:

$$K_{\pm n} = C_{\pm n} \frac{1}{\sigma} \int_{\sigma} J_o^2(p_n r)\, da$$

Page 69. For Eq. 35, read:

$$K_{\pm B} = C_{\pm B}$$

Page 69. For Eq. 36, read:

$$G_{e\ell n,B} = \frac{1}{4} Y_{on,B}\left[|M_{+n,B}|^2 C_{+n,B} K_{+n,B} - |M_{-n,B}|^2 C_{-n,B} K_{-n,B}\right]$$

Page 69. For Eq. 38, read:

$$B_{e\ell n,B} = \frac{1}{4} Y_{on,B}\, \mathrm{Im}\left[2M_{+} K_{+} M^{*}_{-} K_{-} \exp(j2\beta_{qn,B}\ell)\right] - 4\omega\left(W_k - W_e^p\right)_{V_g=1}$$

where

$$W_k = \frac{1}{4}\epsilon_o \int_{\sigma} da \int dz\, |\beta_p a(z)|^2 J_o^2(pr)$$

and

$$W_e^p = \frac{1}{4}\epsilon_o \int_{\sigma} da \int dz \left|\frac{D}{Dz}\, a(z) J_o(pr) - E_z^c(z, r)\right|^2$$

Quarterly Progress Report No. 56, January 15, 1960

Page 98. For Eq. 1, read:

$$\begin{bmatrix} \underline{\underline{B}}_{II} \\ I_g \end{bmatrix} = \left[\begin{array}{c|c} \underline{\underline{D}}_{I,II} F(r) & D_{gII}\, \underline{\underline{K}}_g F(r) \\ \hline \underline{\underline{\Gamma}}_g\, \underline{\underline{D}}_{Ig} & Y_{e\ell} \end{array}\right] \begin{bmatrix} \underline{\underline{B}}_{I} \\ V_g \end{bmatrix}$$

Page 98. For Eq. 5, read:

$$M_k = \frac{1}{2}\left[M_{+k} C_{+k} + M_{-k} C_{-k}\right]$$

Page 100. For Eq. 6, read:

$$N_k = \frac{1}{2}\left[M_{+k} C_{+k} - M_{-k} C_{-k}\right]$$

Page 100. For Eq. 8, read:

$$M'_k = \frac{1}{2}\left[M^{*}_{+k} K_{+k} + M^{*}_{-k} K_{-k}\right]$$

Page 100. For Eq. 9, read:

$$N'_k = \frac{1}{2}\left[M^*_{+k}K_{+k} - M^*_{-k}K_{-k}\right]$$

Page 100. For Eq. 10, read:

$$\begin{bmatrix} \underline{\underline{B}}_I \\ I_g \end{bmatrix} = \left[\begin{array}{c|c} \underline{\underline{D}}_{gII}F(r) & \underline{\underline{0}} \\ \hline \underline{\underline{0}} & 1 \end{array}\right]\left[\begin{array}{c|c} \underline{\underline{I}} & \underline{\underline{K}}_g \\ \hline \underline{\underline{\Gamma}}_g & Y_{e\ell} \end{array}\right]\left[\begin{array}{c|c} \underline{\underline{D}}_{Ig} & \underline{\underline{0}} \\ \hline \underline{\underline{0}} & 1 \end{array}\right]$$

Page 100. For Eq. 12, read:

$$G_{e\ell} = \frac{1}{4}\sum_k Y_{ok}\left[|M_{+k}|^2 C_{+k}K_{+k} - |M_{-k}|^2 C_{-k}K_{-k}\right]$$

E. TRANSMISSION ZEROS OF THE FOUR-CAVITY KLYSTRON

The transfer impedance (defined here as the ratio of the output gap voltage to the input gap source current) of the four-cavity klystron (1) can be expressed as

$$\frac{V_{g4}}{I_{s1}} = y_{41}Z_4Z_1T_4 \tag{1}$$

$$T_4 = 1 + \frac{y_{42}y_{21}}{y_{41}}Z_2 + \frac{y_{43}y_{31}}{y_{41}}Z_3 + \frac{y_{43}y_{32}y_{21}}{y_{41}}Z_2Z_3 \tag{2}$$

where Z_k is the impedance of the k^{th} cavity and y_{kj} is the klystron transconductance between identical gaps j and k.

$$y_{kj} = 2G_{e\ell}\left[\cos\theta_{kj} + j\frac{M^2Y_o}{2G_{e\ell}}\sin\theta_{kj}\right]\exp(-j\theta_e)_{kj} \tag{3}$$

If we use the narrow-band approximation for the cavity impedance, the transmission function of Eq. 2 becomes the ratio of two second-degree polynomials. In the examples given below, a shift of origin and a normalization have been introduced; the (R/Q) ratios and the real part of the poles, α, of the second and third cavities are assumed to be equal. Thus the poles of the transmission function are located at $-\alpha \pm j1$. The position of the zeros is then determined by the values of the gap factor $a = Y_oM^2/2G_{e\ell}$, the center-gap to center-gap drift lengths, $\theta_{kj} = (2\pi\ell/\lambda_q)$, the external loading factor $b = G_{e\ell}/(G_c+G_{e\ell})$, gain per stage $g = 2ab$, and the position of the poles (2).

EXAMPLE 1: Figures VI-15 and VI-16 show the loci of the transmission zeros for an equal drift length klystron with a two-pole Butterworth distribution (α=1). Klystron A

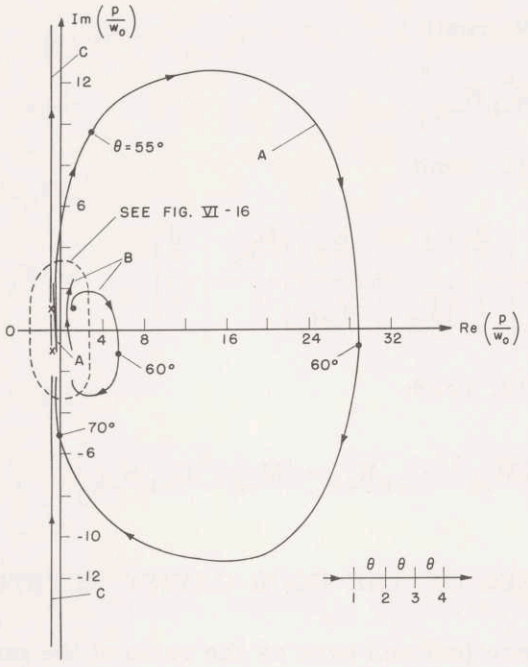

Fig. VI-15. Equal drift length loci (Example 1).

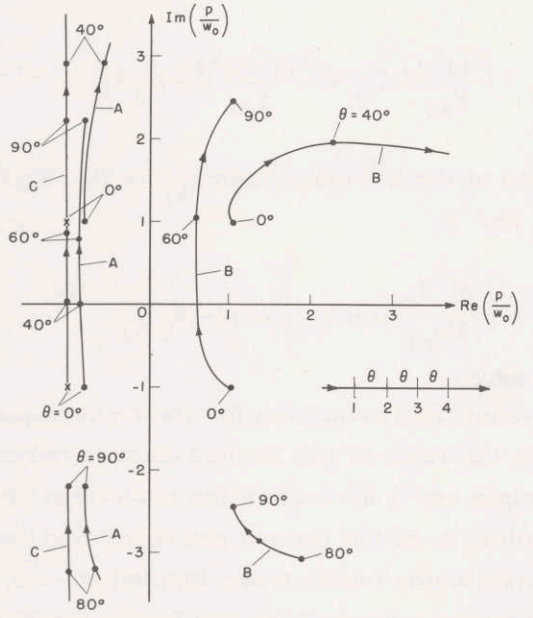

Fig. VI-16. Enlargement of loci near the origin (Example 1).

(a=10, b=0.1, g=2) is a short-gap klystron with low electronic loading. Klystron B (a=1.5, b=1, g=3) is a long-gap klystron with large electronic loading. Klystron C (a=∞, b=0, g=2) is the limiting case of a klystron having gaps of zero length and zero electronic loading. The loci of klystron C are based on the commonly used approximate description of gap interaction (3). These loci are to be compared with those of klystrons A and B, which are based on a complete description of gap interaction that properly accounts for electronic loading and remodulations of both kinetic voltage and beam current.

Examination of Figs. IV-15 and IV-16 reveals the following trends: (a) The area of the loci increases as the gap factor a is increased. (b) The value of the external-loading factor b largely determines whether or not the loci will enter the left half-plane. For large values (near unity) of b, the loci lie entirely in the right half-plane. (c) The zero loci of klystron A follow the loci of klystron C fairly closely, except when θ_{41} approaches 180°. At this point, one zero of klystron C goes to infinity, while the zero of klystron A moves far out of the passband into the right half-plane, but remains at a finite distance from the passband. Note that a zero far out in the right half-plane represents a large, nearly constant multiplier of the power-gain function throughout the passband. (d) Each zero may be associated with a particular pole — that pole which is directly opposite the zero at θ = 0°. The zero associated with the low-frequency pole moves upward out of the passband as θ increases. Its real part decreases slightly and then increases to its original value. The zero associated with the high-frequency pole moves in a large clockwise quasi circle.

EXAMPLE 2: For this example we have again assumed equal drift lengths, and a

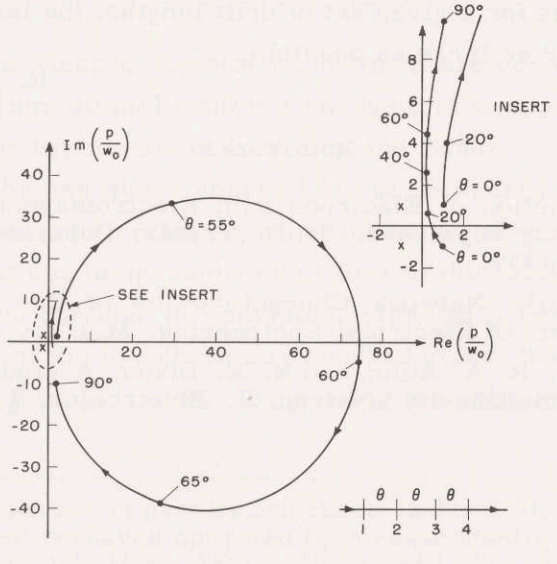

Fig. VI-17. Equal drift length loci (Example 2).

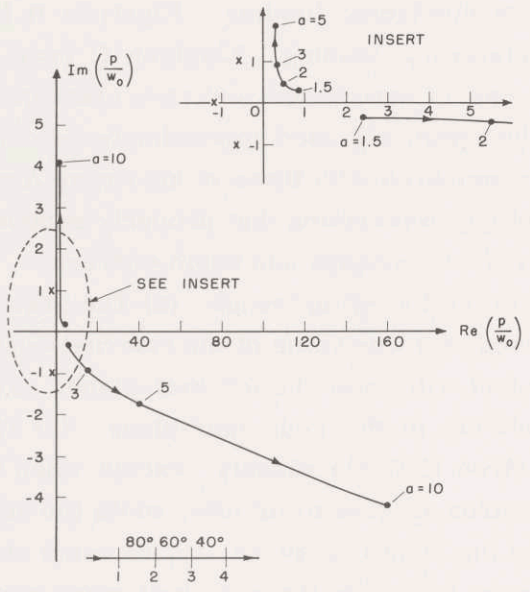

Fig. IV-18. Locus for 80°-60°-40° klystron with variable gap factor, a (Example 3).

Butterworth pole distribution for the second and third cavities. The gap factor is 5; the electronic loading is large, b = 1; the gain per stage is 10. Figure IV-17 shows that the loci are quite similar to those of Example 1. However, the zeros have moved farther out of the passband at $\theta = 90°$. This difference may be attributed to the fact that the gain per stage is much higher.

EXAMPLE 3: The pole positions have been chosen so as to produce a maximally flat response (in the absence of zeros) with the first three cavities, $a = 1/\sqrt{3}$. The electronic loading is large, b = 1, and the output cavity is assumed to have a bandwidth equal to or larger than the over-all tube bandwidth. This requirement on the output cavity is common in high-power klystrons for achieving efficient power transfer to the load over the passband. The drift lengths decrease in the direction of motion of the electron beam: $\theta_{12} = 80°$, $\theta_{23} = 60°$, $\theta_{34} = 40°$. Thus the klystron of this example should be a good approximation to a high-power klystron. Figure VI-18 gives the zero loci as a function of the gap factor. We can see that increasing the gap factor shifts the zeros farther away from the passband. Thus for a given set of drift lengths, the largest gain will be obtained by making the gap factor as large as possible.

R. H. McCullough, A. Bers

References

1. A. Bers, Interaction of Electrons with Electromagnetic Fields of Gaps with Application to Multicavity Klystrons, Sc. D. Thesis, Department of Electrical Engineering, M. I. T., June 1959.

2. R. H. McCullough, Network Characteristics of the Multicavity Klystron, S. M. Thesis, Department of Electrical Engineering, M. I. T., September 1960.

3. K. H. Kreuchen, B. A. Auld, and N. E. Dixon, A study of the broadband frequency response of the multicavity klystron, J. Electronics, 2, 529 (1957).

VII. MOLECULAR BEAMS*

Prof. J. R. Zacharias
Prof. J. G. King
Prof. C. L. Searle
Dr. R. F. C. Vessot
H. H. Brown, Jr.
R. Golub
E. L. Kamen
F. J. O'Brien
R. Weiss

A. SEARCH FOR A SMALL CHARGE CARRIED BY MOLECULES

The suggestion by Lyttleton and Bondi (1) that hydrogen atoms might carry a charge of approximately 2×10^{-18} of an elementary charge has stimulated a number of investigators to undertake experiments designed to measure this charge. At least two methods have been used; atomic beam deflection experiments (2, 3), and the method of Piccard and Kessler (4). The results published thus far are listed in Table VII-1. In this paper

Table VII-1. Upper limit on the charge carried by various molecules.

Molecule	Charge (elementary charge/molecule)	Experimental Method
CO_2	$\leq 2 \times 10^{-19}$	Piccard-Kessler (ref. 4)
CsI	$\leq 4 \times 10^{-13}$	Molecular beam (ref. 2)
A	$< 8 \times 10^{-20}$	Piccard-Kessler (ref. 5)
N_2	$< 12 \times 10^{-20}$	Piccard-Kessler (ref. 5)
CsF	$\leq 2 \times 10^{-14}$	Molecular beam (ref. 3)
KF	$\leq 1 \times 10^{-13}$	Molecular beam (ref. 3)
n	$< 6 \times 10^{-12}$	Molecular beam (ref. 6)

preliminary results of a Piccard-Kessler experiment are reported in which hydrogen molecules (and also helium atoms) exhibit a charge that is approximately 40 times less than that required by the hypothesis of Lyttleton and Bondi.

In our experiment the gas whose charge is to be measured is allowed to escape from an electrically insulated metal container connected to an electrometer. While the gas is escaping, a current that can be measured will flow to the container if the gas is charged. The charge on each atom can then be computed, although it is essential to distinguish charge carried by each of the hypothetically charged atoms from charge carried by ions, electrons, and charged dust particles. By passing the escaping gas through a de-ionizer

*This work was supported in part by Purchase Order DDL B-00306 with Lincoln Laboratory, a center for research operated by Massachusetts Institute of Technology with the joint support of the U. S. Army, Navy, and Air Force under Air Force Contract AF 19(604)-5200.

consisting of a coaxial capacitor charged by a battery within the container, ions and electrons, because of their relatively high mobilities, can be swept from the gas stream, while atoms carrying the hypothetical charge of 10^{-18} of an electron charge will be unaffected. Dust particles, which range in size from molecules to visible grains, may be sufficiently massive to pass through the de-ionizer, but their effect is likely to be both erratic and cumulative.

By recording the pressure and the output of the electrometer, both as a function of time, on a two-channel recorder, it is not only possible to measure the total charge carried by the gas, but also to see that the potential-versus-time curve has the expected shape for the flow of a uniformly charged gas. The course to be followed by the experimenter is plain. If the atoms seem to be charged, the computed charge per atom must be independent of all parameters, such as de-ionizer potential and polarity, rate of gas efflux, pressure, bias potential of the container with respect to ground, and, of course, details of apparatus construction and gas handling. It is to be expected that the charge per atom will be different for different gases. On the other hand, if the atoms appear uncharged, it is important to make certain that the electrometer is sensitive during the gas efflux and that mechanisms that might cancel a genuine effect are eliminated. Such cancellation is most likely to occur at the end of the outlet pipe from the container.

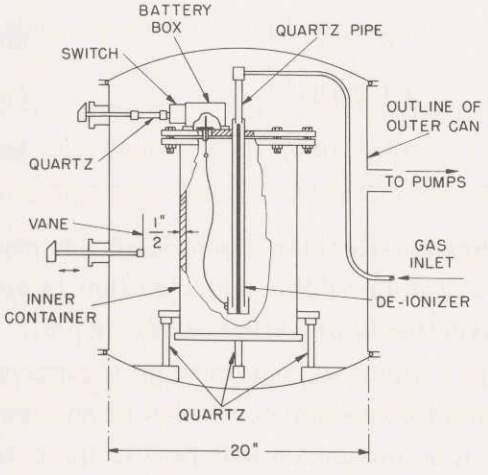

Fig. VII-1. Scale drawing of the apparatus.

Figure VII-1 is a scale drawing of the apparatus. The outer can serves both as a vacuum envelope and as an electrical shield for the container (11.2 liters) which stands on three quartz supports and is filled with gas through a quartz pipe. This quartz pipe is metalized at its ends so that it can be soft-soldered into place. Although it was designed to stand a pressure of 1000 psi, the container was usually operated at a pressure

of 265 psi. The outer can was pumped to 10^{-6} mm Hg to prevent electrical leakage and to reduce undesirable thermal effects. The central electrode of the de-ionizer is insulated by Teflon spacers and maintained at ±90 volts, or zero volt with respect to ground, as determined by the setting of a switch in the battery box that is visible on top of the container. The switch can be controlled from outside by the insulated shaft. The approximate contact potential to ground of the container can be determined by a movable vane. The gas that is to be investigated is admitted to the container through a porous bronze filter with 5-μ pores, an electrostatic precipitator, and needle valves for controlling the flow. A pressure transducer generates a signal proportional to the pressure in the container which can be recorded on one channel of a two-channel Sanborn recorder. Filling the container rapidly resulted invariably in the appearance of erratic voltages when the gas was allowed to escape. This is believed to be due to the stirring up of a cloud of dust within the container because pumping it down and then filling it slowly always restored normal performance. All of the runs reported here were made with filling times of one-half hour, or more, which appeared to give reproducible results.

The gas escapes from the container through an external regulator that maintains constant pressure on a needle valve adjusted to give the desired rate of flow. It was thus possible to obtain a nearly linear drop in pressure in the container with respect to time. It was found that the pressure-versus-time curve departed from linearity because of temperature changes within the needle valve during the flow of gas. The pressure transducer was calibrated, and the behavior of the pressure-versus-time recording when the gas flow was suddenly stopped was examined closely. It was concluded that the pressure recordings are accurate and can be used as reliable indicators of the amount of gas in the container.

Potential changes of the container with respect to the outer can are measured with a GL5674 electrometer whose output is amplified by a chopper amplifier and recorded on the other channel of the Sanborn recorder. Potential differences of 10^{-4} volt, or currents of approximately 10^{3} electrons per second, can be detected. The time constant is 60 ± 5 sec which agrees with the time constant predicted from independent measurements of the electrometer grid resistance and capacitance, 10^{12} ohms and 60 μμf, respectively. The ground return of the electrometer is connected through a low-impedance voltage supply that makes it possible to place the container at different potentials with respect to the outer can. When the potential of the container was +0.01 volt, moving the vane was found to have negligible effect. Calibrating signals may be introduced at the ground end of the electrometer grid resistor. Since the time constant of the electrometer was determined by the input circuit, the rms noise voltage should be $(kT/C)^{1/2}$, which is approximately 10 μv, so that the electrometer performance is within a factor of 10 of that which might ultimately be obtained. Frequent calibrations of the electrometer were made with signals close to the minimum detectable signal

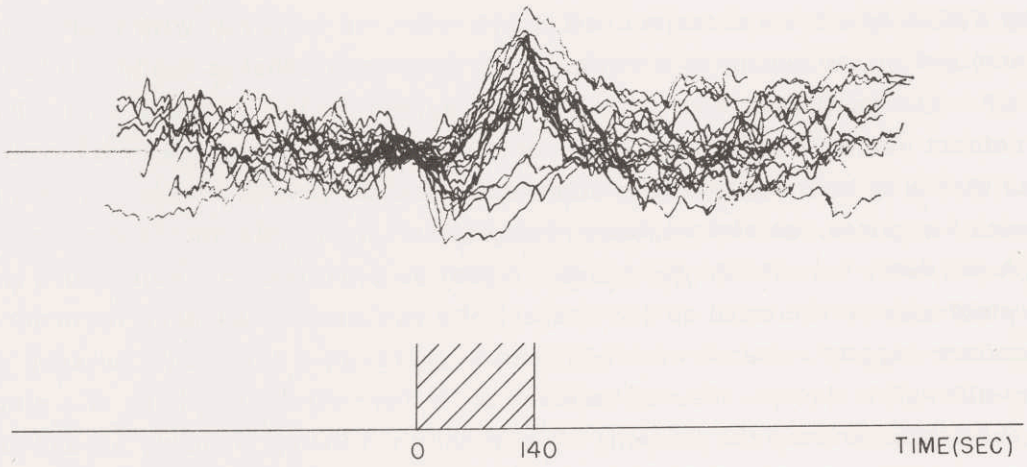

Fig. VII-2. Superimposed electrometer recordings of 21 hydrogen runs.

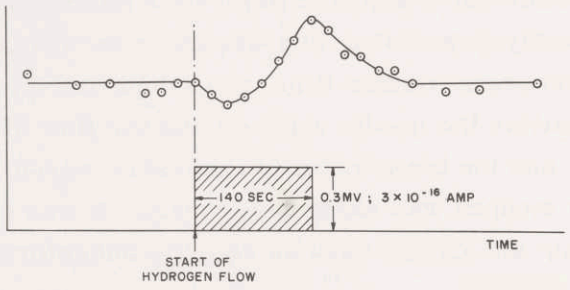

Fig. VII-3. Average curve constructed from the data of Fig. VII-2.

introduced at the ground end of the electrometer grid resistor. No consistent dependence of the electrometer sensitivity on the polarity of the calibrated signal, the amount of gas in the container, the polarity of the de-ionizer or any other parameter was found. Calibrations were also made while the gas was flowing from the container, and the sensitivity was found to be normal.

A charged gas leaving the container would induce charges on its inner wall and thus cause a current to flow in the electrometer grid resistor. To make certain that the electrometer was sensitive to the flow of such charges, a small probe was put in the container and connected by a shielded lead to a voltage source that was made to vary linearly with time; from the estimated capacitance between the probe and the container, the rate of voltage rise, and the size of the electrometer response, the value of the electrometer sensitivity could be determined and it was found to agree well with the value obtained by direct calibration.

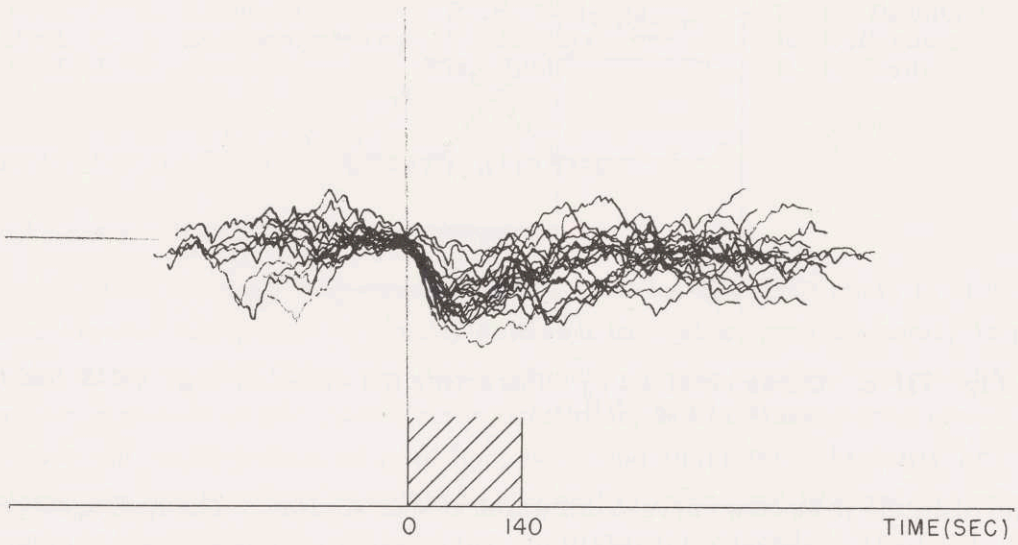

Fig. VII-4. Superimposed electrometer recordings of 19 helium runs.

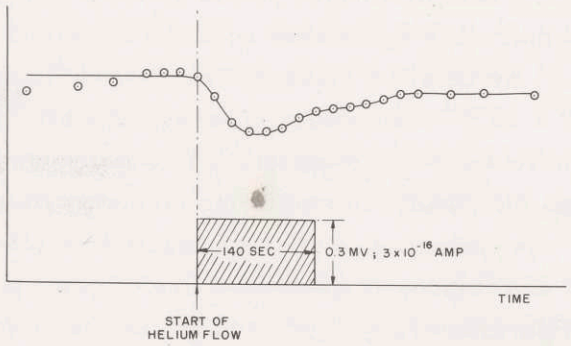

Fig. VII-5. Average curve constructed from the data of Fig. VII-4.

The 21 hydrogen and 19 helium runs at 265 psi and 140-sec efflux time (selected only because these parameters were the same) yielded electrometer recordings that are superimposed in Figs. VII-2 and VII-4, normalized at the start of flow. Average curves that were constructed for hydrogen and helium are plotted in Figs. VII-3 and VII-5. The shaded rectangle, 0.3 mv high and 140 sec long, represents 2.7×10^5 elementary charges, which is the amount of charge that would be observed if each of the 5.4×10^{20} molecules carried 5×10^{24} of an elementary charge. The apparent charge per molecule, determined from the average curves, is $2.5 \pm 1.5 \times 10^{-20}$ elementary charge/molecule for hydrogen, and $-4 \pm 2 \times 10^{-20}$ elementary charge/molecule for helium. The charge on hydrogen appears to be negative; the charge on helium, to be positive.

None of the recordings looks like the computed curve, which is plotted in Fig. VII-6,

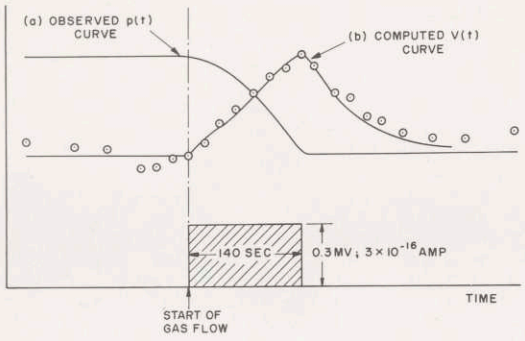

Fig. VII-6. Curve obtained by subtracting the curve of Fig. VII-5 from the curve of Fig. VII-3.

together with the pressure curve from which it was derived. The hydrogen curve goes negative and then positive, and the helium curve has a negative maximum that is too early by 30 sec. If it is assumed that the helium effect is spurious and that whatever produces it is likewise present in the hydrogen runs, the helium curve may be subtracted from the hydrogen curve. This procedure yields a curve (represented by circles in Fig. VII-6) that is in remarkable agreement with the computed curve. If this agreement is taken to be significant, we obtain a value of $7 \pm 2.5 \times 10^{-20}$ elementary charge/molecule for hydrogen, and $0 \pm 2 \times 10^{-20}$ elementary charge/molecule for helium.

The electrometer deflections recorded are still not understood; but the nature of these results, as well as the results of numerous side experiments, eliminates a few of the possible causes for the deflection, such as capacitative effects, piezoelectricity, and thermoelectricity. New and improved apparatus, use of other gases, including deuterium, and wider variations of parameters will provide the answer. In any case, the charge that we found for the hydrogen molecule, by interpreting our experiment in the obvious way, is far less than that required for the hydrogen atom by the hypothesis of Lyttleton and Bondi. A molecular-beam experiment is under way with cesium, but the difficulties of achieving sufficient sensitivity with hydrogen (and later atomic hydrogen) are considerable.

J. G. King

References

1. R. A. Lyttleton and H. Bondi, Proc. Roy. Soc. (London) A252, 313 (1959).
2. V. W. Hughes, Phys. Rev. 105, 170 (1957).
3. J. C. Zorn, G. E. Chamberlain, and V. W. Hughes, Bull. Am. Phys. Soc. Ser. II 5, 36 (1960).
4. A. Piccard and E. Kessler, Arch. Sci. Phys. et Nat. 7, 340 (1925).
5. A. M. Hillas and T. E. Cranshaw, Nature 184, 892 (1959).
6. I. Shapiro and V. Estulin, Soviet Phys. – JETP 3, 626 (1957).

VIII. SATELLITE TIME-DILATION MEASUREMENT*

Prof. J. R. Zacharias
Prof. C. L. Searle
Prof. J. W. Graham
R. S. Badessa
V. J. Bates
D. Buhl
B. L. Diamond
R. Huibonhoa
R. L. Kent

A. CRYSTAL OSCILLATOR STABILITY STUDIES

1. Crystal Locked-Oscillator Development

For applications in which long-term stability (that is, low drift rate) is of primary importance, crystal dissipation is usually held to a low value, approximately 10 microwatts. This tends to slow down the aging process in the crystal, but results in a relatively low signal-to-noise ratio for the oscillator, with accompanying phase fluctuations. Hence the requirements of good long-term and short-term stability are somewhat incompatible. In an effort to obtain high stability over time intervals ranging from a few seconds to several hours, we used two oscillators in cascade. The first, a Hycon Model 101C Ultra Stable Oscillator, employs low-level drive on the crystal to obtain long-term stability. The second crystal oscillator circuit is similar except that the crystal dissipation is greatly increased to provide a high signal-to-noise ratio at the expense of reduced long-term stability. A small signal is injected from the Hycon oscillator into the resonant circuit of the second oscillator to produce a phase lock. The locking bandwidth is kept small (approximately ±5 cps at 5 mc) so that only the slow variations of the injection frequency will be followed by the locked oscillator. The output is a signal whose short-term stability is self-determined and whose long-term drift is controlled by the injection signal.

In order for the locked oscillator to maintain the long-term stability of the injection signal, the locking phase must remain constant over the interval that is of interest. For example, a 1°/min rate-of-change of locking phase is equivalent to a frequency error at 5 mc of 1×10^{-11}. To prevent the error from exceeding 1×10^{-12}, for a locking range of ±5 cps, the permissible drift rate of the second oscillator is

$$\dot{\Delta f} \approx \Delta f_{max} \quad \dot{\phi} \approx 2.5 \times 10^{-5} \text{ cps/sec at 5 mc}$$

or

$$\frac{\dot{\Delta f}}{f} \approx 3 \times 10^{-10}/\text{min}$$

where Δf_{max} is the locking half-bandwidth, and $\dot{\phi}$ is the rate-of-change of locking phase.

*This work was supported in part by National Aeronautics and Space Administration under Contract NASw-143; and in part by Purchase Order DDL B-00306 with Lincoln Laboratory, a center for research operated by Massachusetts Institute of Technology under the joint support of the U.S. Army, Navy, and Air Force under Air Force Contract AF19(604)-5200.

(VIII. SATELLITE TIME-DILATION MEASUREMENT)

Rather than employing oven-temperature control on the locked oscillator crystal, the thermal time constant was increased by embedding the crystal in a large block of glass-wool insulating material. Typical locking phase drift rates that have been achieved fall in the range 0.05°/min to 0.1°/min.

2. Short-Term Stability and Spectrum Measurements

Using the system described in Quarterly Progress Report No. 58 (pages 127-130) with the oscillators described above, we performed short-term comparison measurements of two similar crystal oscillators. These measurements indicate that instabilities of 1×10^{-10}, averaged over a 2-minute interval, are common, with occasional drifts of $2\text{-}3 \times 10^{-10}$ occurring during the same interval.

Power spectrum measurements were also conducted with the use of a modified General Radio 738 A Wave Analyzer. In these experiments, a 10-sec interval of the 1-kc beat from the oscillator stability-measurement system is recorded on tape at 15 in./sec and played back as an endless loop at 60 in./sec. Since the wave-analyzer bandwidth is approximately 4 cps and the net multiplication is now increased by a factor of 4 to 40,000, the fractional resolution bandwidth referred to the original oscillators is 4 cps/40,000 × 1 mc or 1×10^{-10}. The power spectra obtained have essentially the same shape that they would have if a clean audio signal had been fed directly to the analyzer. This shows that there are no instabilities greater than 1×10^{-10} occurring at rates faster than 0.4 cps, this rate being determined by the length of tape data used.

C. L. Searle, R. S. Badessa, V. J. Bates, D. Buhl, R. L. Kent

IX. STROBOSCOPIC RESEARCH

Prof. H. E. Edgerton
L. R. Breslau

A. PRESSURE-TESTING FACILITY FOR OCEANOGRAPHIC EQUIPMENT

Because equipment that is used in oceanography is subjected to such high pressures, the strength of the casings for the underwater devices should be tested. Recently, we built a test facility that is based on the one devised and used by the Woods Hole Oceanographic Institution for several years. L. Hoadley of W. H. O. I. gave us assistance in our design problems, and the Research Committee of the National Geographic Society provided the funds.

A 16-inch Naval Ordnance shell of a type that is no longer of military importance (HC projectile Mark 13, Mode 1) was obtained from the U. S. Navy. This shell, which weighs 1900 lb, provides a volume that is 9.7 inches in diameter and 36 inches long. The chamber is filled with water and pumped up to the desired pressure.

After several unsuccessful attempts were made to weld a pressure-resisting plug into the regular nose cone of the shell, a nose plug was made with 6-inch diameter shaft material. It was then found that expansion of the shell caused the nose plug to open sufficiently to blow out the 1/8-inch O-ring. This problem was solved by chilling the nose cone in liquid air before screwing it in place as tightly as possible with a 4-foot pipe wrench with a 3-foot pipe extension on the handle.

A brass retainer ring was installed at the breech end of the shell, as shown in

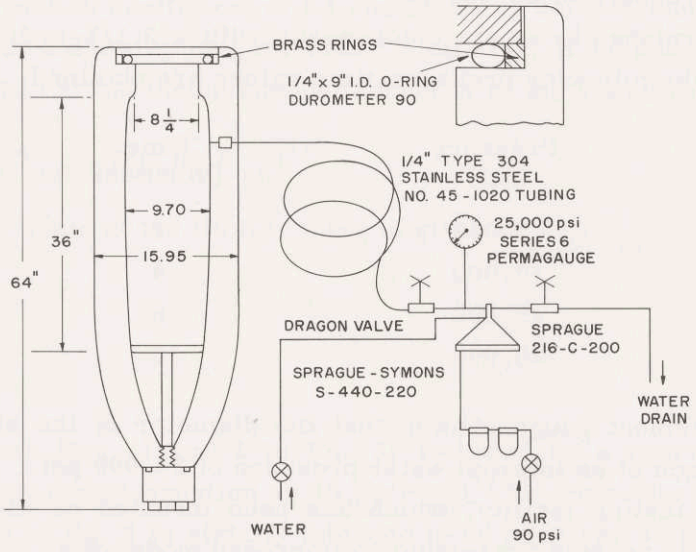

Fig. IX-1. Hydraulic and air systems for pump used with pressure-testing facility.

Fig. IX-2. Mobile mount for pressure-testing facility; pressure cylinder is shown suspended from crane.

Fig. IX-1. This ring is in contact with a flat area on the breech plug at the end of the travel. The ring is 0.25 inch thick so as to match the seating of a hard rubber O-ring (durometer 90) that has an inner diameter of 9 inches.

During several tests of the nose plug, an O-ring of durometer 70 was used at the breech. This ring became wedged into the crack between the brass ring and the breech plug. Removal was extremely difficult. Heat was applied to the shell with a torch, then a crane was used to put 3000 ft-lb of torque on the breech plug.

It was found that there were some slight defects on the surface of the breech plug which resulted in a crack where the O-ring extruded. The brass ring was made level with grinding compound, and a hone was used on the breech-plug surface. Even after grinding, a 70-durometer O-ring at an internal pressure of 10,000 psi became slightly extruded. Durometer-90 O-rings of the same size are now used with success, although slight extrusion occurs at a pressure of 20,000 psi.

When air is furnished by an air compressor with a 3 1/2-inch stroke and a 3-inch diameter piston, the following pressure-time values are obtained:

Pressure (psi)	Time (minutes)
5,000	1
10,000	4
15,000	6
20,000	15

A dial displacement gauge showed that the diameter of the shell expanded approximately 16/1000 inch at an internal water pressure of 20,000 psi.

The pressure testing facility, which has been mounted on wheels for mobility (Fig. IX-2), is being readied for testing an improved model of an underwater camera and several cameras for bathyscaph use.

H. E. Edgerton

X. MODULATION THEORY AND SYSTEMS

Prof. E. J. Baghdady
Prof. J. B. Wiesner
J. T. Boatwright, Jr.
A. L. Helgesson
B. H. Hutchinson, Jr.
R. B. C. Martins
C. Metzadour
D. D. Weiner

A. SIGNAL-TO-NOISE RATIOS IN LIMITERS WITH REGENERATIVE FEEDBACK

Consider the block diagram of Fig. X-1 in which the S and N symbols represent the mean-square values of signal and noise at the principal points, when a sinusoid of constant amplitude E_s and instantaneous frequency ω_i plus an independent random-fluctuation

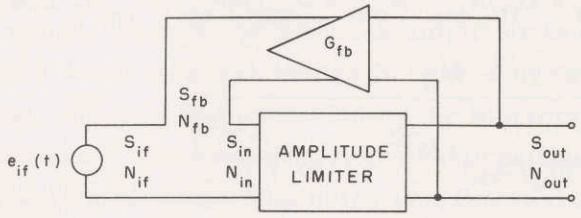

Fig. X-1. Limiter with regenerative feedback.

noise of total mean-square value N_{if} is applied across the i-f terminals. To start with, if $n_{if}(t)$ denotes the i-f sample noise time function and $n_{fb}(t)$ the noise fed back, then we have

$$N_{in} = \overline{[n_{if}(t)+n_{fb}(t)]^2} = N_{if} + N_{fb} + 2\rho(N_{if}N_{fb})^{1/2} \tag{1}$$

where ρ is the correlation coefficient of i-f and feedback noises, and the bar denotes the time average over a suitably long interval. Similarly, if we assume that the feedback phase shift $\phi_{fb}(\omega_i)$ at the instantaneous frequency of the signal is negligible, we have

$$S_{in} = S_{if} + G_{fb}^2 S_{out} + 2G_{fb}(S_{if}S_{out})^{1/2} \tag{2}$$

The S/N mean power ratio at the limiter input is given by S_{in}/N_{in}.

If we now write

$$\frac{S_{out}}{N_{out}} = \gamma \frac{S_{in}}{N_{in}} \tag{3}$$

then substitution from Eqs. 1 and 2 in Eq. 3, followed by a rearrangement of the terms, leads to a quadratic equation in $(S_{out}/N_{out})^{1/2}$. Since the square-root quantity in the third term of Eq. 2 is strictly intended to be positive, so is $(S_{out}/N_{out})^{1/2}$, and of the two roots of the quadratic equation only the positive one is acceptable. This argument leads to

$$\left(\frac{S_{out}}{N_{out}}\right)^{1/2} \Big/ \left(\frac{S_{if}}{N_{if}}\right)^{1/2} = -\rho(S_{fb}/S_{if})^{1/2} + \left[\gamma\left\{1+(S_{fb}/S_{if})^{1/2}\right\}^2 - (1-\rho^2)(S_{fb}/S_{if})\right]^{1/2} \tag{4}$$

The right-hand side of Eq. 4 gives the factor by which the ratio of rms signal to rms noise has been altered in going from the input to the output of the limiter with regenerative feedback under the assumption (to be examined later) that a feedback quasi-stationary state exists in which signal and noise have the mean-square values that appear at the output in Fig. X-1. In discussing the significance of this result, it is helpful to have an expression for the mean-square value of the noise fed back. Such an expression follows from the relations $N_{fb} = G_{fb}^2 N_{out}$, $N_{out} = S_{out}/(S_{out}/N_{out})$, and Eq. 4. The result is

$$N_{fb} = \frac{N_{if}}{\left[-\rho+\left\{\gamma\left[1+(S_{if}/S_{fb})^{1/2}\right]^2 - (1-\rho^2)\right\}^{1/2}\right]^2} \tag{5}$$

$$= \frac{N_{if}}{\left[-\rho+\left\{\gamma+(\rho^2-1)\right\}^{1/2}\right]^2} \qquad \text{for large values of } (S_{fb}/S_{if})^{1/2} \tag{6}$$

$$= (S_{fb}/\gamma S_{if})\, N_{if} \qquad \text{for small values of } (S_{fb}/S_{if})^{1/2} \tag{7}$$

The expression on the right in Eq. 4 involves three quantities that we must examine closely. First, there is the quantity γ that relates the signal-to-noise mean power ratios at the input and output of the limiter in accordance with Eq. 3. This quantity, γ, is a complicated function of S_{in}/N_{in}. For the case of gaussian noise at the input of the limiter, γ was computed by Davenport (1). But, in the present problem, the limiter action alters the statistics of the noise so that it is no longer gaussian. Consequently, the noise at the input of the limiter is the sum of gaussian noise from the i-f amplifier and non-gaussian noise from the feedback terminals, and the two add up to non-gaussian noise. Therefore γ for the limiter in the feedback steady state cannot be expected to be exactly the same as the function computed by Davenport. But it can be expected to behave in a similar manner as a function of $(S/N)_{in}$; in particular, it exceeds unity for the larger values of $(S/N)_{in}$ and becomes less than unity for very low $(S/N)_{in}$. Note from Eq. 7 that when the signal component fed back is weak relative to the signal coming from the i-f amplifier, the noise fed back is small compared with the i-f noise from the i-f terminals. Under this condition the resultant noise at the limiter input is largely made up of the i-f noise, and its statistics are therefore approximately gaussian if the i-f noise is gaussian. Consequently, under conditions of strong input signal relative to the amount of feedback present, γ is given very closely by Davenport's curve. The problem of determining γ analytically in the feedback steady state when S_{fb} is not small compared

with S_{if} is formidable and it remains unsolved.

It is important to observe that the right-hand side of Eq. 4 will exceed unity, provided that

$$\gamma > \frac{1 + 2\rho(S_{fb}/S_{if})^{1/2} + \frac{S_{fb}}{S_{if}}}{\left[1+(S_{fb}/S_{if})^{1/2}\right]^2} \tag{8}$$

Fortunately, the right-hand member of this inequality is ≤ 1 for all $\rho \leq 1$.

Second, there is the correlation coefficient, ρ, of the noise coming from the i-f amplifier and the noise coming through the feedback amplifier to the input of the limiter. Decorrelation between the i-f and feedback noises is caused by two mechanisms that are present in the loop. First, there is decorrelation by the memoryless amplitude limiting of the sum of signal plus noise. The amount of noise decorrelation that results from memoryless amplitude limiting of signal plus noise is a function of the S/N ratio at the limiter input. For gaussian noise at the limiter input, the correlation coefficient of input and output noise can be computed directly from expressions derived by Davenport (1). The results show that the correlation coefficient is slightly below 0.95 for $(S/N)_{in} < 1/10$ and approximately 0.71 for $(S/N)_{in} > 10$, with a smooth transition in between. Second, there is decorrelation as a result of delay in transmission around the loop. The autocorrelation function of filtered fluctuation noise falls off at a rate that depends upon the noise bandwidth, the exact shape of the curve being a function of the shape of the noise-power spectral density at the filter output. The mathematical reason for this lies, of course, in the fact that the autocorrelation function of the noise is the inverse Fourier transform of its power spectral density. But the physical reason can perhaps be seen by tracing the noise back to its source, where it is generated as a random superposition of short pulses, with a resultant power spectral density that is essentially uniform over the passband of the intervening concatenation of filters that precede the point of observation. At the point of observation, the noise is therefore a superposition of the impulse responses of the over-all filter to the noise "impulses" from the source. The ability to extrapolate the noise waveform into the future is therefore essentially lost if the "future" comes one or more overall-filter time constants later.

Now, the resultant noise at the limiter input is the sum of the i-f noise and the noise fed back. Since the correlation coefficient of the i-f noise and the limiter input noise is given by

$$\rho_{if,\,in} = (N_{if}/N_{in})^{1/2} + \rho(N_{fb}/N_{in})^{1/2}$$

decorrelation by the limiter and by the delay in transmission around the loop ensures that

the limiter input noise starts the cycle around the loop with only a partial correlation with the i-f noise. When the level of the voltage fed back is large in comparison with the level at the i-f terminals, approximation 6 shows that the resultant noise at the limiter input is, to a large extent, made up of the noise fed back. Therefore in the feedback steady state, the instantaneous behavior of the noise present across the feedback terminals tends to be little influenced by the instantaneous behavior of the i-f noise over a past that may stretch over intervals that are in excess of the decorrelation time of the i-f noise.

Thus, even though no analytical solution now exists for the exact behavior of the correlation coefficient (ρ in Eq. 4) of the i-f and feedback noises in the feedback steady state as a function of the relative i-f signal and noise conditions, ρ^2 can certainly be expected to be negligible as compared with unity and can be dropped in the second term in Eq. 4. It may even be assumed to be so low as not to materially influence the result in Eq. 4, even though it multiplies a quantity for which large values are desirable (as we shall indicate presently). It is interesting to observe that negative values of ρ (which are not unlikely) are advantageous because the first term in Eq. 4 is thereby transformed into an asset. Note that nonzero ρ of either sign is an asset in the second term in Eq. 4.

Finally, there is the quantity S_{fb}/S_{if} on the right-hand side of Eq. 4. This quantity represents the ratio of mean-square values of the signal component fed back and the signal component introduced at the i-f terminals. The larger this ratio is, the greater the improvement in S/N ratio indicated in Eq. 4. Large values of this ratio also ensure smaller values of ρ, and should increase the value of γ. But there are bounds (imposed by the feedback phase shift at the instantaneous frequency of the signal) on how large we can allow S_{fb}/S_{if} to be before we begin to violate the assumption of feedback quasi-stationary state which underlies the validity of the argument leading to Eq. 4.

When the S/N mean power ratio at the input of the limiter is large, the mean-square value, S_{out}, of the signal component can be expected to be essentially $k^2/2$, where k is the amplitude that the signal component at the limiter output would have in the absence of the noise. Using Eq. 3, we can then write

$$N_{out} = (k^2/2\gamma)/(S_{in}/N_{in}) \tag{9}$$

Under these conditions the limiter operates on the sum of signal plus noise present at its input in a manner that improves the signal relative to the noise by keeping the amplitude of the signal component substantially constant and depressing the relative mean-square value of the noise. The condition that leads to this (with $\rho = 0$, for simplicity) can be expressed in the form

$$\frac{S_{in}}{N_{if}} > b + \frac{S_{fb}}{\gamma N_{if}} \tag{10}$$

where b is a threshold value that can be determined from the curve that describes S_{out} as a function of $(S/N)_{in}$ by seeking the smallest value of $(S/N)_{in}$ for which $S_{out} \approx k^2/2$. For gaussian noise (plus a sinusoid) at the input of the limiter, the value of b is around 3. If we set $S_{out} = k^2/2$ in expression 10 and write $E_{fb} = kG_{fb}$, we have

$$\frac{(E_s+E_{fb})^2/2}{N_{if}} > b + \frac{E_{fb}^2/2}{\gamma N_{if}} \tag{11}$$

By straightforward manipulations, inequality 11 can be reduced to

$$\left(\frac{E_s^2/2}{N_{if}}\right)^{1/2} > \left(b + \frac{E_{fb}^2/2}{\gamma N_{if}}\right)^{1/2} - \left(\frac{E_{fb}^2/2}{N_{if}}\right)^{1/2} \tag{12}$$

Inequality 12 defines the threshold that must be exceeded by the ratio of rms signal and rms noise at the i-f terminals shown in Fig. X-1 in order that $(S/N)_{in} > b$, which, in turn, ensures that $S_{out} \approx k^2/2$. In deriving this condition, we have assumed that a feedback quasi-stationary state exists, and that $\rho = 0$.

It is clear from the preceding discussion that substantial signal improvement in the presence of relatively strong random noise (and full limiter saturation) can be guaranteed only by choosing E_{fb} to be large compared with E_s (and greater than the threshold of limiter saturation). The regenerative signal-booster arrangement of Fig. X-1 should therefore oscillate (2) in the absence of a signal, and the oscillation should be sufficiently strong relative to the input noise to bring about an acceptable degree of FM noise quieting. By "FM noise quieting" we mean a compression of the instantaneous-frequency excursions of the output from the scheme in the manner experienced when a sinusoid of adequate strength is added to the noise — which amounts to a narrowing of the probability density function of the instantaneous frequency of the output in the absence of an input signal. If, in the absence of signal, the amplitude of the oscillation is reduced below the adequate-quieting level relative to the total applied noise, the level of the noise disturbance on the oscillation frequency will rise. The output from the oscillator eventually loses all semblance of coherence when the noise takes effective control.

The improvement in S/N ratio that results from the regenerative feedback may or may not be sufficient to raise the signal from below to above a preassigned threshold of acceptable reception, subject to the value of $(S_{fb}/S_{if})^{1/2}$. The theoretical upper limit on the permissible value of $(S_{fb}/S_{if})^{1/2}$ in a given circuit is set by the maximum value of feedback phase shift encountered by the signal around the loop. This limitation is imposed by the fact that — oscillation or no oscillation — a feedback quasi-stationary state must first be established around the loop. For example, suppose that the oscillation amplitude (as seen at the feedback terminals) must exceed a value $E_{osc,th}$ in order that

the output S/N ratio in Eq. 4 exceed the threshold of acceptable noise performance of the FM demodulator used after the oscillating limiter. An input sinusoidal carrier whose frequency coincides with the frequency of in-phase feedback is indistinguishable from the oscillation at the output of the limiter. Therefore, the threshold that the input amplitude E_s of this sinusoid must exceed is zero if $E_{osc} > E_{osc,th}$. However, if the frequency of the applied sinusoid is changed to a value ω_i at which a phase-shift deviation $\phi_{fb}(\omega_i)$ from in-phase feedback is experienced, then as long as

$$(E_{osc}/E_s) \sin |\phi_{fb}(\omega_i)| < 1 \tag{13}$$

the signal should override the noise in the output when $E_{osc} > E_{osc,th}$. Satisfaction of this condition by the input sinusoid enables this sinusoid to shift the mean frequency about which the compressed fluctuations in the instantaneous frequency of the output occur to the desired value, ω_i. The regenerative action boosts the signal amplitude at the limiter input to a value that fluctuates with time in synchronism with a slow modulation in $\omega_i(t)$, but this magnitude will, at worst, very nearly equal E_{osc} at instants of time when $\phi_{fb}(\omega_i)$ attains its maximum permissible value. Therefore, the relatively weak signal, which (by itself) would have been suppressed by the total noise, when applied to a conventional FM demodulator, is boosted by the regenerative action of the "locked" oscillating limiter to the higher level that it must have in order to override the noise. If E_{osc} is adjusted so that it equals the threshold value $E_{osc,th}$, then E_s must satisfy the condition

$$E_s > E_{osc,th} \sin |\phi_{fb}(\omega_i)|_{max} \tag{14}$$

In order to determine the amount of reduction in the threshold of satisfactory reception indicated by condition 14, we must first relate $E_{osc,th}$ to the noise threshold, $E_{n,th}$, of the FM demodulator. This can be done with the aid of Eq. 4. Thus, in terms of $E_{n,th}$, condition 14 can be written as

$$E_s > \left\{ \frac{\rho + \left(\rho^2 + \gamma\left(1 + \sin |\phi_{fb}(\omega_i)|_{max}\right)^2 - 1\right)^{1/2}}{\gamma\left(1 + \sin |\phi_{fb}(\omega_i)|_{max}\right)^2 - 1} \sin |\phi_{fb}(\omega_i)|_{max} \right\} E_{n,th} \tag{15}$$

If we assume that $\rho = 0$, and design the feedback loop so that $|\phi_{fb}(\omega_i)|_{max} \ll 1$, condition 15 can be simplified in the form

$$E_s > \left\{ \frac{\sin |\phi_{fb}(\omega_i)|_{max}}{(\gamma-1)^{1/2}} \right\} E_{n,th} \tag{16}$$

The noise threshold that E_s must exceed is thus reduced by the factor in braces in conditions 15 and 16. If $|\phi_{fb}(\omega_i)|_{max} = 5°$ (or 0.087 rad), E_s can be nearly -20 db below $E_{n,th}$.

From the definition of $E_{osc,th}$, it is clear that the signal need only override the noise components that fall in the immediate neighborhood of its instantaneous frequency in order to satisfy the "locking" condition. In a sense, this indicates that in the oscillating limiter the signal, in effect, combats noise density rather than total noise.

E. J. Baghdady

References

1. W. B. Davenport, Jr., Signal-to-noise ratios in bandpass limiters, J. Appl. Phys. 24, 720-727 (1953); see especially Fig. 5.

2. E. J. Baghdady, FM interference and noise suppression properties of the oscillating limiter, IRE National Convention Record, Part 8, 1959, pp. 13-39; Trans. IRE, PGVC-13, pp. 37-63 (1959).

XI. STATISTICAL COMMUNICATION THEORY

Prof. Y. W. Lee
Prof. A. G. Bose
Prof. I. M. Jacobs
Prof. J. B. Wiesner
A. D. Hause
H. Hemami
J. D. Holmes
K. L. Jordan, Jr.
D. J. Sakrison
M. Schetzen
H. L. Van Trees, Jr.
S. Weinreb
C. E. Wernlein, Jr.
G. D. Zames

A. WORK COMPLETED

1. NONLINEAR LEAST-SQUARE FILTERING AND FREQUENCY MODULATION

The present study has been completed by A. D. Hause. In September 1960, he submitted the results to the Department of Electrical Engineering, M.I.T., as a thesis in partial fulfillment of the requirements for the degree of Doctor of Science. The study will also be published as Technical Report 371.

Y. W. Lee

2. DISCRETE REPRESENTATION OF RANDOM SIGNALS

This study was completed and presented by K. L. Jordan, Jr. as a thesis in partial fulfillment of the requirements for the degree of Doctor of Science, Department of Electrical Engineering, M.I.T., September 1960. The study will also be published as Technical Report 378.

Y. W. Lee

3. NONLINEAR OPERATORS FOR SYSTEM ANALYSIS

This study has been completed by G. D. Zames. It was submitted as a thesis in partial fulfillment of the requirements for the degree of Doctor of Science, Department of Electrical Engineering, M.I.T., September 1960, and will also be published as Technical Report 370.

Y. W. Lee

B. A COMPARISON OF THE LAGUERRE SET WITH AN OPTIMUM SET FOR THE EXPANSION OF THE PAST OF A CERTAIN RANDOM PROCESS

As has been stated previously (1, 2), the optimum expansion of the past of a random process x(t) with respect to a weighted mean-square error involves the solution of the integral equation

$$\int_{-\infty}^{0} G(s)\, R(s,t)\, G(t)\, \phi_n(t)\, dt = \lambda_n \phi_n(s) \qquad -\infty < s \leq 0 \tag{1}$$

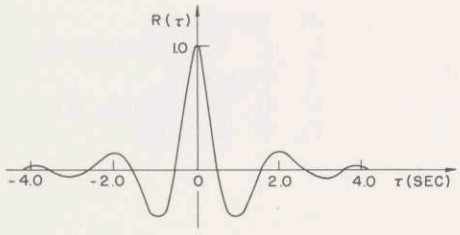

Fig. XI-1. Autocorrelation function of the process to be expanded.

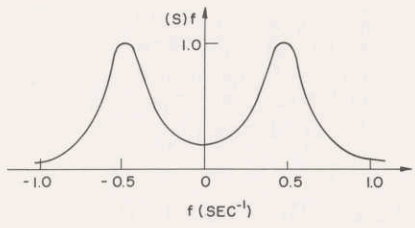

Fig. XI-2. Power density spectrum of the process to be expanded.

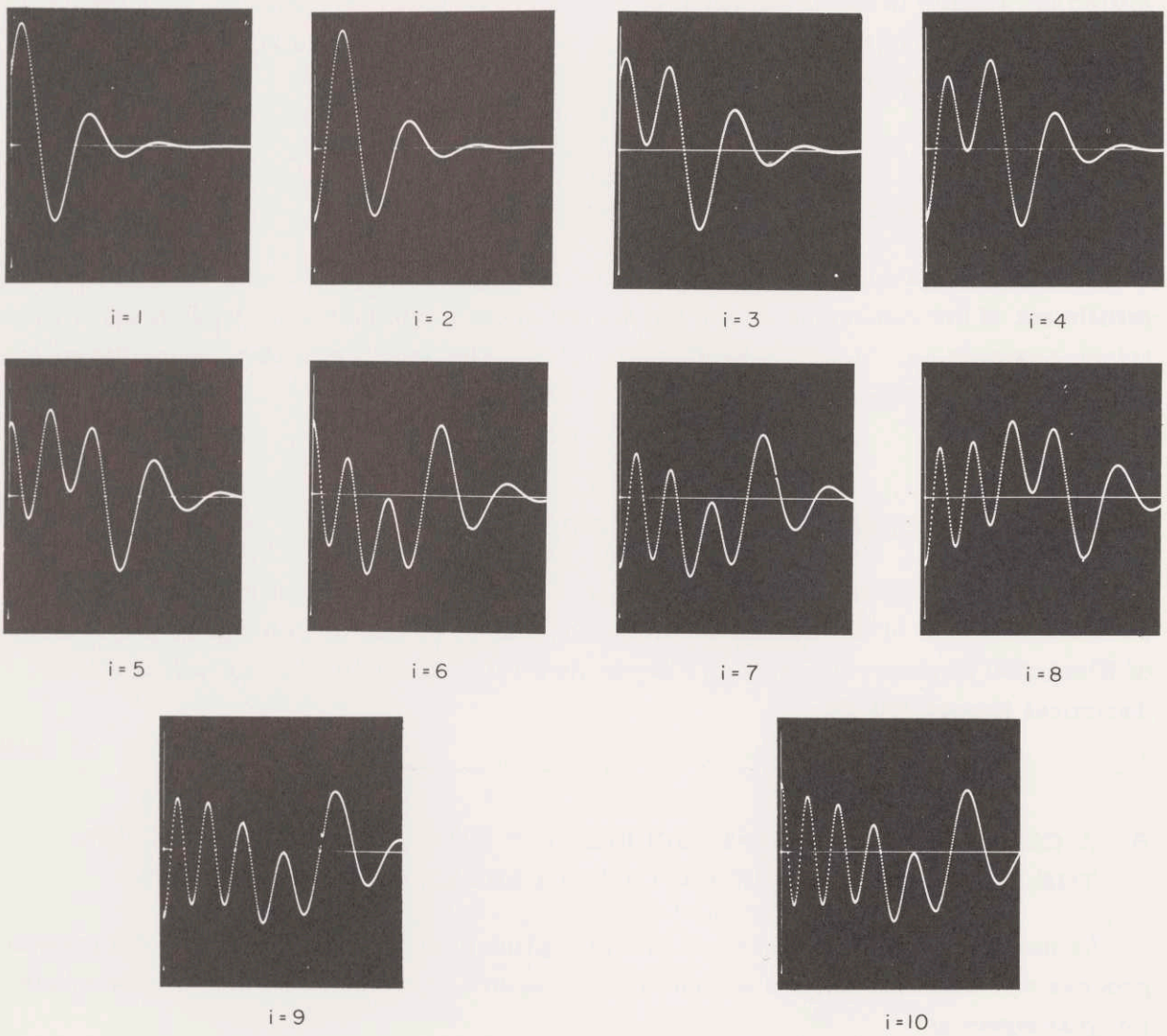

Fig. XI-3. Orthonormal set of solutions of Eq. 2.

where G(t) is the weighting function over the past of the random process x(t), and R(s, t) is the correlation function. We also note that the set $\{\phi_n(t)\}$ is the set that minimizes the mean square error of a finite-term expansion of the process

$$G(t)\, x(t) \qquad t \leq 0$$

We have developed a computer program for the solution of equations of the form of Eq. 1 on the IBM 704 computer at the Computation Center, M. I. T. This program was used on a particular example, and the resulting set of functions was used to make finite-term expansions of a sample function of the process obtained in the laboratory.

For our example we chose a stationary process with the correlation function

$$R(\tau) = \exp[-|\tau|] \cos 3\tau$$

and a weighting function $G(t) = \exp[t/4]$. The correlation function and power density spectrum of the process are shown in Figs. XI-1 and XI-2. The process was obtained in the laboratory by passing white noise through a linear filter with the proper transfer function.

The integral equation

$$\int_0^\infty \exp\left[-\frac{s}{4}-\frac{t}{4}-|s-t|\right] \cos 3(s-t)\, \phi_n(t)\, dt = \lambda_n \phi_n(s) \qquad 0 \leq s < \infty \tag{2}$$

in which we have reversed the sign of the argument for convenience, was solved by means of the program. The first 10 solutions are shown in Fig. XI-3.

The approximations of a sample function of the process over a period of time of 7.5 sec, made with the use of the solutions or eigenfunctions of the integral equation and Laguerre functions for n = 1, . . . , 10, 15, and 20 terms, are shown in Fig. XI-4. It is seen that the eigenfunctions do much better, especially in approximating the higher frequency portions, than the Laguerre functions. This is because the Laguerre functions have Fourier transforms of the form

$$\frac{1}{n!} \frac{\left(j2\pi f-\frac{1}{2}\right)^n}{\left(j2\pi f+\frac{1}{2}\right)^{n+1}} \qquad n = 0, 1, 2, \ldots$$

so that most of their energy is near the origin. It is seen from Fig. XI-2,

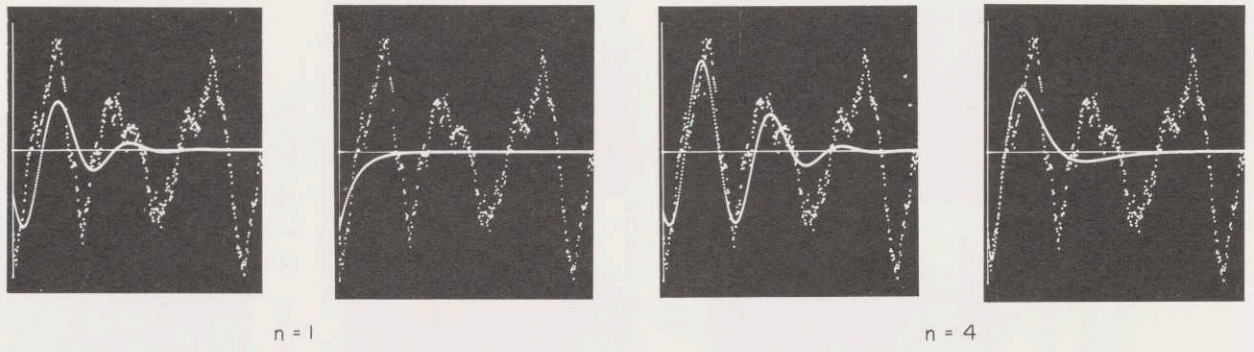

n = 1

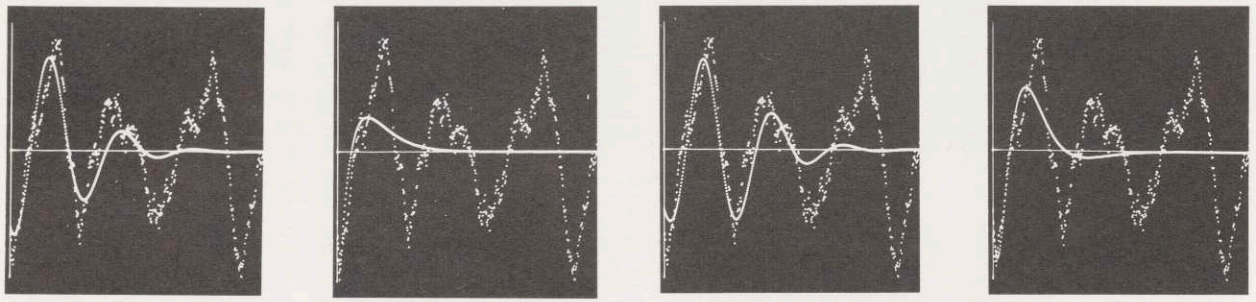

n = 2

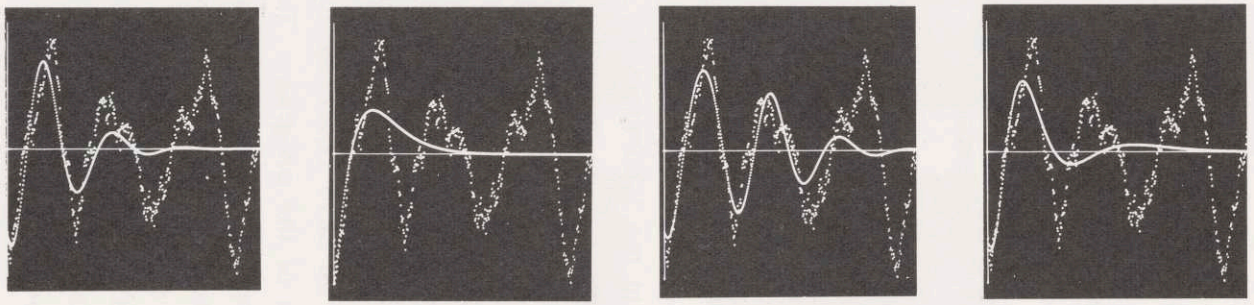

n = 3

EIGENFUNCTION LAGUERRE

n = 4

n = 5

n = 6

EIGENFUNCTION LAGUERRE

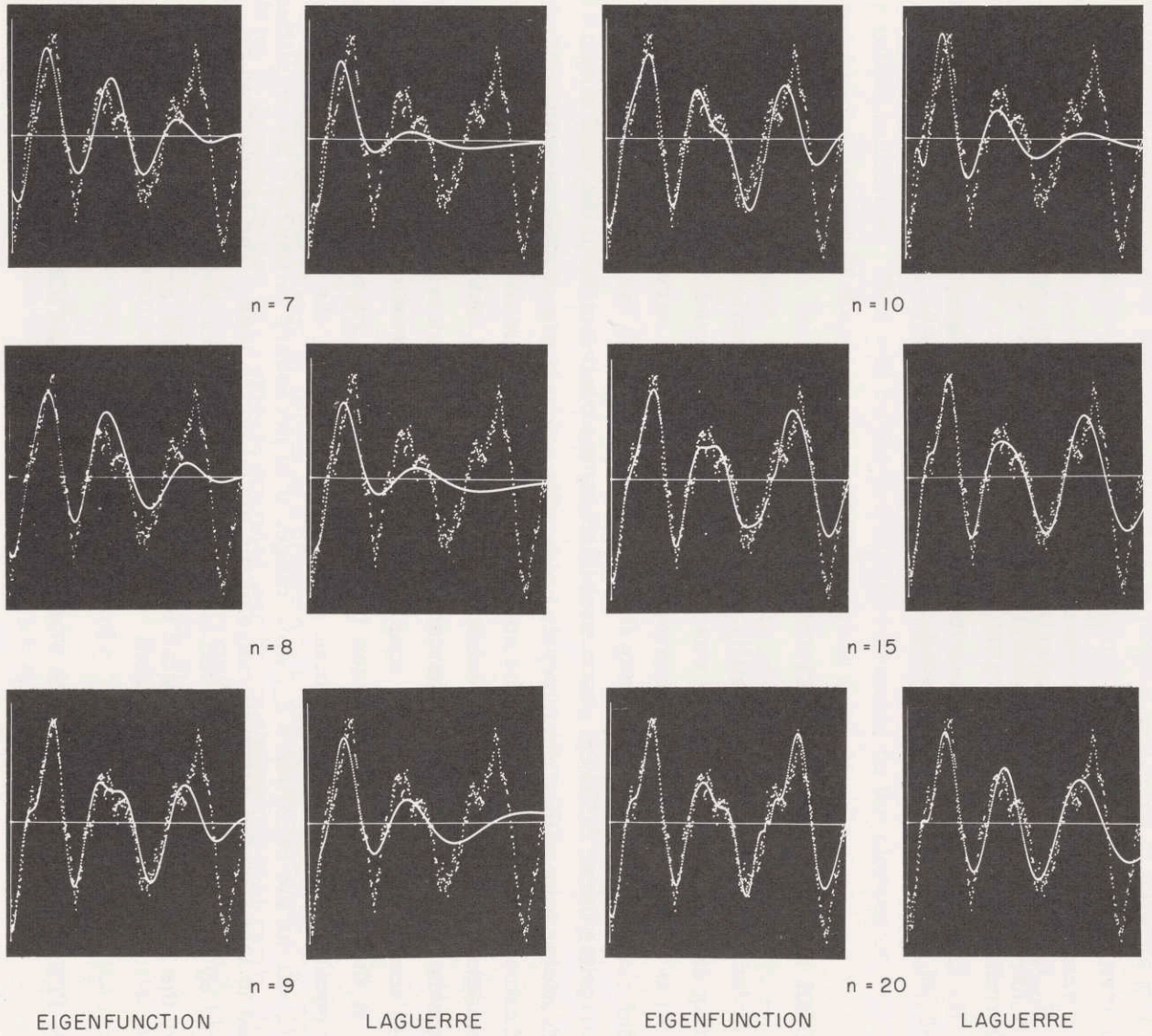

Fig. XI-4. Comparison of the expansion of a sample of the process with the use of the eigenfunctions of Eq. 2 and Laguerre functions.

however, that most of the energy in the random process is not near the origin so that the performance of the Laguerre functions is not expected to be near optimum.

K. L. Jordan, Jr.

References

1. K. L. Jordan, Jr., Characterization of random signals with an application to nonstationary linear systems, Quarterly Progress Report No. 56, Research Laboratory of Electronics, M.I.T., Jan. 15, 1960, pp. 117-125.

2. K. L. Jordan, Jr., Discrete Representations of Random Signals, Sc.D. Thesis, Department of Electrical Engineering, M.I.T., Aug. 22, 1960.

C. NOISE ANALYSIS IN MAGNETIC TAPE RECORDING

In order to examine the possibility of increasing the dynamic range in magnetic tape recording an analysis of the noise was made on an Ampex Model 351 recorder. Autocorrelation analysis was used to conveniently distinguish the various components of the recorder output noise. By analyzing the recorder output with the tape not running and with it running under different erasure conditions, the contribution to the total output noise from the tape noise, the 60-cycle noise, the remnant signal after erasure by bulk and machine-head methods, and the noise in the electronic amplifiers was determined. The results of this analysis can be found in the writer's S.M. thesis, "Noise Analysis in Magnetic Tape Recording," Department of Electrical Engineering, M.I.T., June 1960.

This analysis has shown that, consistent with good engineering design, the noise power at the machine output caused by the recording and reproducing amplifiers is nearly equal (within 2 db) to the noise power resulting from the tape itself. Thus, in order to extend the recorder's dynamic range, it is necessary to improve the amplifiers and also to increase the dynamic range of the signal on the tape. The former can be achieved by better circuit design and construction. Use of nonlinear pre-emphasis to achieve the latter will be investigated by other members of the group.

P. Piqué

D. AN ITERATIVE PROCEDURE FOR SYSTEM OPTIMIZATION

1. Introduction

We are interested in the following general problem. We are given a system, with k variable parameters $x_1, x_2, \ldots x_k$, which operates on an input v(t) and produces an output q(t). Corresponding to the input there is a desired output d(t), and we wish to minimize the performance criterion

$$M(\underline{x}) = E\{W[d(t)-q(t)]\,|\,\underline{x}\}$$

where W(e) is some non-negative function of the error, d - q.

One approach to the problem would be to use an iterative method; that is, we start with an initial parameter setting and attempt to make a sequence of adjustments which ultimately results in the optimum parameter setting. Such a procedure is useless, however, unless it can be shown that the iterative method used converges in some meaningful sense. Here stochastic approximation methods are used to show convergence. These methods are essentially gradient methods; that is, at each step we attempt to measure the direction in which $M(\underline{x})$ decreases fastest and then change the parameter setting some amount a_n in that direction. Such methods are useful only in situations in which $M(\underline{x})$ has a unique minimum. This will be the principal restriction on the classes of systems and weighting functions of the error to which the method is applicable.

Here we consider, in particular, the design of nonlinear (or linear) filters and predictors. Throughout we denote the k-tuple of parameters $x_1, x_2, \ldots x_k$ by a k-dimensional vector $\underline{x}$. The usual inner product,

$$\sum_{i=1}^{k} x_i y_i$$

is denoted $[\underline{x}, \underline{y}]$, and the k-dimensional Euclidean norm, $\|\underline{x}\|$. A unit setting of the parameter x_i and zero setting of the other k - 1 parameters will be represented by the unit vector $\underline{e}_i$, i = 1, 2, ... k.

The discussion will be carried out in terms of sampled or discrete time parameter signals and systems. A remark at the end of this report will indicate the extension of the analysis to the continuous case.

2. Physical Design Procedure

We consider the design of filters and predictors of the form shown in Fig. XI-5. The form is general in that any compact operator can be approximated arbitrarily closely by the given form if a sufficiently large number of terms is used (1, 2). It is assumed that v(m) and d(m) are the outputs of stationary ergodic sources.

The iterative adjustment is made as follows: Suppose we are at the n^{th} iteration and the parameters are at the setting $\underline{x}_n$. Let $Y_n(m) = W[d_n(m)-q_n(m)]$. We then make the 2k measurements, $Y_n^1, Y_n^2, \ldots Y_n^{2k}$, where

Y_n^1 is an observation with parameter setting $\underline{x} = \underline{x}_n + c_n\underline{e}_1$

Y_n^2 is an observation with parameter setting $\underline{x} = \underline{x}_n - c_n\underline{e}_1$

$\vdots$

Y_n^{2k-1} is an observation with parameter setting $\underline{x} = \underline{x}_n + c_n\underline{e}_k$

Y_n^{2k} is an observation with parameter setting $\underline{x} = \underline{x}_n - c_n\underline{e}_k$

We then form the vector

$$\underline{Y}_n = \left[\left(Y_n^1 - Y_n^2\right), \ldots, \left(Y_n^{2k-1} - Y_n^{2k}\right)\right] \tag{1}$$

and determine the next parameter setting in the iterative procedure by

$$\underline{x}_{n+1} = \underline{x}_n - \frac{a_n}{c_n} \underline{Y}_n \tag{2}$$

where $\{a_n\}$ and $\{c_n\}$ are sequences of positive numbers whose properties will be described later. This completes the n^{th} iteration of the procedure.

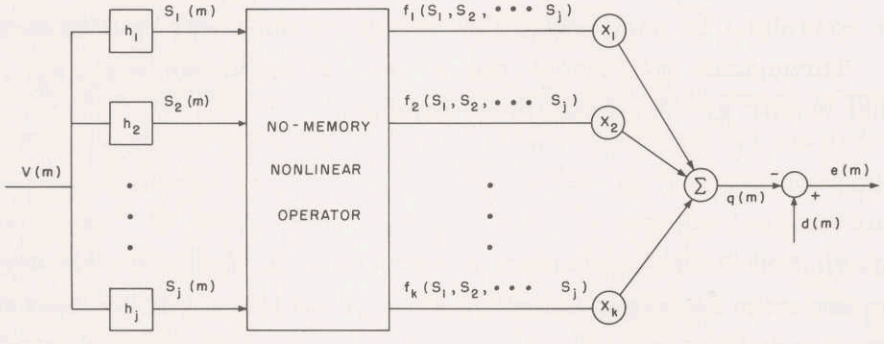

Fig. XI-5. Form of filter to be designed.

If the design is being carried out on a computer, each of the 2k measurements for the n^{th} iteration may be carried out by using the data v(m), v(m−1) . . . , where m is the time at which the n^{th} iteration is initiated. If the design is being carried out on an operational system or analog thereof, the measurements must then be made by using v(m), v(m−1), . . . for Y_n^1, . . . , and v(m+2k), v(m+2k−1), . . . for Y_n^{2k}. The observation Y_n^i need not be made with just one sample of the output data but can be taken with the parameters fixed over several samples, and the average used for Y_n^i (i=1, 2, . . . 2k). Our theory will include all such variations.

We must place a restriction on the time interval between successive iterations, however. Thus, if for the n^{th} iteration the data v(m), v(m−1), . . . are used and the data v(m+s), v(m+s−1), . . . are used for the $n + 1^{th}$ iteration, convergence of the iterative procedure is guaranteed only for s sufficiently large. We also assume that at the start of the iterative procedure the linear memory units $h_1, h_2, \ldots h_j$ have been operating on the data long enough to come to equilibrium.

We shall now state some useful mathematical results and then show for what restrictions on the physical situation the mathematical results are applicable.

3. A Stochastic Approximation Theorem

We now state extensions of the work of Dupač (3) to the multidimensional case in which independence between samples is no longer assumed. At the outset, the proofs follow the lines of Dupač's proofs and, after a point, follow Dupač's almost exactly.

Consider the multidimensional regression function

$$M(\underline{x}) = \int Y \, dH(Y|\underline{x})$$

We assume that $M(\underline{x})$ has a unique minimum at $\underline{x} = \underline{\theta}$. Let $Y_{\underline{x}_n + c_n \underline{e}_i}$ denote an observation of Y with $\underline{x} = \underline{x}_n + c_n \underline{e}_i$ and let

$$\underline{Y}_n = \left[\ldots, Y_{\underline{x}_n + c_n \underline{e}_i} - Y_{\underline{x}_n - c_n \underline{e}_i}, \ldots \right]$$

$$\underline{M}_{c_n}(\underline{x}_n) = \frac{1}{c_n} \left[\ldots, M(\underline{x}_n + c_n \underline{e}_i) - M(\underline{x}_n - c_n \underline{e}_i), \ldots \right]$$

We now define our iterative procedure by the following recursion relation:

$$\underline{x}_{n+1} = \underline{x}_n + \frac{a_n}{c_n} \underline{Y}_n$$

In order to make some statements concerning the sequence $\{\underline{x}_n\}$ thus generated, we make the following assumptions:

(i) $E\left\{ \| \underline{Y}_n \|^2 | \underline{x}_n, \underline{x}_1 \right\} \leq \| E\{\underline{Y}_n | \underline{x}_n, \underline{x}_1\} \|^2 + S \qquad S < \infty$

(ii) (a) $K_o \| \underline{x} - \underline{\theta} \|^2 \leq [(\text{grad } M)(\underline{x}), -(\underline{x} - \underline{\theta})]$

(b) $\| (\text{grad } M)(\underline{x}) \| \leq K_1 \| \underline{x} - \underline{\theta} \| \qquad K_1 > K_o > 0$

(iii) (a) $E\{ \| E\{\underline{Y}_n | \underline{x}_n, \underline{x}_1\} - c_n \underline{M}_{c_n}(\underline{x}_n) \| \, | \underline{x}_1 \} = E\{ \| E\{\underline{Y}_n | \underline{x}_n, \underline{x}_n - \underline{x}_1\}$

$$- c_n \underline{M}_{c_n}(\underline{x}_n) \| \, | \underline{x}_1 \} \leq S_1 \frac{a_n}{c_n}$$

where $S_1 < \infty$, and $\underline{x}_n - \underline{x}_1 = \sum_{j=1}^{n-1} \frac{a_j}{c_j} \underline{Y}_j$.

(b) $\left| E\left\{ \| E\{\underline{Y}_n | \underline{x}_1, \underline{x}_n\} \|^2 - c_n^2 \| \underline{M}_{c_n}(\underline{x}_n) \|^2 | \underline{x}_1 \right\} \right| < S_2, \quad S_2 < \infty$

(iv) $\{a_n\}$ and $\{c_n\}$ are sequences of positive numbers satisfying

$$\sum_{n=1}^{\infty} a_n = \infty, \quad \sum_{n=1}^{\infty} a_n^2 < \infty, \quad \sum_{n=1}^{\infty} a_n c_n < \infty, \text{ and } \sum_{n=1}^{\infty} \frac{a_n^2}{c_n^2} < \infty$$

(v) $\underline{x}$ is constrained to a bounded, closed, convex set X, but is free to be varied inside X. (A set X is convex if $\underline{x}_1 \in X$, $\underline{x}_2 \in X$ implies $\alpha\underline{x}_1 + (1-\alpha)\underline{x}_2 \in X$ for $0 \leq \alpha \leq 1$.) Assumptions (i), (ii), and (iii) need hold only for $\underline{x} \in X$. It is assumed that X is chosen sufficiently large that $\underline{\theta} \in X$.

We now make the following statements:

STATEMENT 1: Assumptions (i)-(v) imply the convergence of $\|\underline{x}_n - \underline{\theta}\|$ to zero in the mean-square sense. That is,

$$\lim_{n\to\infty} E\left\{\|\underline{x}_n - \underline{\theta}\|^2 \,|\, \underline{x}_1\right\} = 0$$

We now set $a_n = a/n^{\alpha}$, $c_n = c/n^{\gamma}$, and in order to satisfy assumption (iv) we require $3/4 < \alpha \leq 1$, $1 - \alpha < \gamma < \alpha - 1/2$. We also require $a > 1/k_o$ if $\alpha = 1$.

STATEMENT 2: Assumptions (i)-(v) and the choice $\alpha = 1$, $\gamma = 1/4$ imply

$$E\left\{\|\underline{x}_n - \underline{\theta}\|^2 \,|\, \underline{x}_1\right\} = 0(1/n^{1/2})$$

The sequence $f(n) = 0(g(n))$ implies that

$$\overline{\lim_{n\to\infty}} \left(|f(n)|/|g(n)|\right) < +\infty$$

Furthermore, this choice is optimum in the sense that no other choice guarantees faster convergence for all $Y(\underline{x})$ that satisfy assumptions (i)-(v); that is, for $\alpha \neq 1$, $\gamma \neq 1/4$, there exists a $Y(\underline{x})$ that satisfies assumptions (i)-(v) for which

$$E\left\{\|\underline{x}_n - \underline{\theta}\|^2 \,|\, \underline{x}_1\right\} = 0\left(\frac{1}{n^{1/2}} - \epsilon\right) \text{ for some } \epsilon > 0$$

STATEMENT 3: With the additional assumption,

$$\left|\frac{\partial^3 M(\underline{x})}{\partial x_i^3}\right| \leq Q < \infty \qquad i = 1, 2, \ldots, k \text{ and } \underline{x} \in X$$

the choice $\alpha = 1$, $\gamma = 1/6$ implies

$$E\left\{\|\underline{x}_n - \underline{\theta}\|^2 \underline{x}_1\right\} = 0\left(\frac{1}{n^{2/3}}\right)$$

and this choice is, again, optimum in the sense of statement 2.

4. Convergence of the Design Procedure

We now turn to the physical design situation that was described in section 2 and proceed to show sufficient conditions for

$$Y = W[d(m)-q_{\underline{x}}(m)]$$

to satisfy the assumptions of section 3. If this is done, then the implications of the statements of section 3 to our design procedure are obvious.

First, we consider conditions that will insure the satisfaction of assumptions (i) and (ii); then, we consider assumption (iii). To guarantee that assumptions (i) and (ii) are satisfied, we make the following restrictions on the physical situation:

(a) v(m) and d(m) are the outputs of stationary ergodic sources and are uniformly bounded in absolute magnitude for all m with probability one.

(b) $\sum_{m=0}^{\infty} |h_i(m)| < \infty$; i = 1, 2, ... k. The $f_i(m) = f_i[S_1(m), S_2(m), \ldots S_j(m)]$ are continuous in $S_1, S_2, \ldots, S_j$ for i = 1, 2, ... k.

(c) $P\left\{\left|\sum_{i=1}^{k} (x_i-\theta_i)\, f_i(m)\right| \geq D\|\underline{x}-\underline{\theta}\|\right\} \geq \epsilon$ for $\underline{x} \in X$ and D, $\epsilon > 0$. Or, in terms of one sample function, there exists an N_o with the property that for $N > N_o$, $\frac{n}{2N+1} \geq \epsilon > 0$, where n is the number of occurrences, $-N \leq m \leq N$, of

$$\left|\sum_{i=1}^{k} (x_i-\theta_i)\, f_i(m)\right| \geq D\|\underline{x}-\underline{\theta}\| \quad \underline{x} \in X$$

(d) W(e) has continuous first and second derivatives.

(e) W(e) is strictly convex; that is, there exists an E > 0 with the property that

$$W[\alpha a+(1-\alpha)b] \leq \alpha W(a) + (1-\alpha)\, W(b) - E\alpha|a-b| \quad \text{for } 0 \leq \alpha \leq 1/2$$

Restrictions (a)-(c) provide no serious limitation on our physical situation. Restriction (a) will surely be satisfied, since the output of any physical source is always uniformly bounded. Restriction (b) requires only that the memory elements $h_1, h_2, \ldots h_j$ be stable and that the f_i be continuous, as all physical transducers are. Restriction (c) only requires that all the h and all the f differ from one another in the prescribed sense. Restriction (c) is satisfied, for instance, if the probability of the sequence of k plus and minus signs $S_{gn}(f_i(m))$, $S_{gn}(f_2(m))$, ..., $S_{gn}(f_k(m))$ taking on a certain sequence of k plus and minus signs is nonzero for each of the 2^k possible outcomes. (This is a sufficient, but by no means necessary, condition for restriction (c) to be satisfied.) Restriction (d) is no practical limitation; restriction (e) is the only serious limitation on our method.

To show that assumptions (i) and (ii) follow from restrictions (a)-(e), we use the ergodicity of the sources to write

$$M(\underline{x}) = E\{W[d(m)-q(m)]|\underline{x}\}$$

$$= \lim_{N\to\infty} \frac{1}{2N+1} \sum_{m=-N}^{N} W\left[d(m) - \sum_{i=1}^{k} x_i f_i(m)\right] \tag{3}$$

Assumption (i) now follows immediately from restriction (a) on the uniform boundedness of the sources and restriction (b) on the form of the filter.

To show that the upper inequality in assumption (ii) is satisfied, we use a Taylor's expansion about $\underline{x} = \underline{\theta}$ to write

$$\frac{\partial M(\underline{x})}{\partial x_j} = 0 + \sum_{i=1}^{k} (x_i - \theta_i) \left. \frac{\partial^2 M(\underline{x})}{\partial x_i \partial x_j} \right|_{\underline{x} = \underline{\theta} + x_i \tau_i \underline{e}_i} \tag{4}$$

where $0 < \tau_i < 1$ for an arbitrary j, with $j = 1, 2, \ldots k$. Thus, the upper inequality in assumption (ii) follows with

$$k_1 = k \cdot \sup_{\substack{i,j=1,2,\ldots k \\ \underline{x} \in X}} \left| \frac{\partial^2 M(\underline{x})}{\partial x_i \partial x_j} \right|$$

if all the $\frac{\partial^2 M(\underline{x})}{\partial x_i \partial x_j}$ $i, j = 1, 2, \ldots k$ are bounded for all $\underline{x} \in X$. To show this, we consider

$$S_N(\underline{x}) = \frac{1}{2N+1} \sum_{m=-N}^{N} W\left[d(m) - \sum_{i=1}^{k} x_i f_i(m) \right]$$

and

$$S_N^{ij}(\underline{x}) = \frac{1}{2N+1} \sum_{m=-N}^{N} W''\left[d(m) - \sum_{i=1}^{k} x_i f_i(m) \right] f_i(m)\, f_j(m)$$

The continuity of W" and the uniform boundedness of the $f_i(m)$, $i = 1, 2, \ldots k$, and d(m) imply the equicontinuity of $S_N^{ij}(\underline{x})$ for $\underline{x} \in X$. The Arzela-Ascoli theorem then guarantees the existence of a uniformly convergent subsequence N_t, and for this subsequence

$$\frac{\partial^2}{\partial x_i \partial x_j} \lim_{t \to \infty} S_{N_t}(\underline{x}) = \lim_{t \to \infty} \frac{\partial^2}{\partial x_i \partial x_j} S_{N_t}(\underline{x})$$

$$= \lim_{t \to \infty} S_{N_t}^{ij}(\underline{x}) \tag{5}$$

for all $\underline{x} \in X$. However, by our assumption of ergodic sources, $\lim_{N \to \infty} S_N^{ij}(\underline{x})$ is unique with probability one, and hence

$$\frac{\partial^2}{\partial x_i \partial x_j} M(\underline{x}) = \lim_{N \to \infty} \frac{1}{2N+1} \sum_{m=-N}^{N} W''\left[d(m) - \sum_{i=1}^{k} x_i f_i(m) \right] f_i(m)\, f_j(m) \tag{6}$$

with probability one for all $\underline{x} \in X$. But the right-hand side of Eq. 6 is bounded by restrictions (a) and (d), and we have established the upper inequality in assumption (ii).

We now turn to the lower inequality in assumption (ii). Using Eq. 3, restrictions (c), (e), and the convexity of X, we have

$$M[(1-\alpha)\underline{x}+\alpha\underline{\theta}] \leq (1-\alpha)\, M(\underline{x}) + \alpha M(\underline{\theta}) - \epsilon DE\alpha \left\| \underline{x}-\underline{\theta} \right\| \quad \text{for } 0 \leq \alpha \leq 1/2 \tag{7}$$

or

$$-\frac{M[\underline{x}+\alpha(\underline{\theta}-\underline{x})] - M(\underline{x})}{\alpha} \geq M(\underline{x}) - M(\underline{\theta}) + \epsilon DE \left\| \underline{x}-\underline{\theta} \right\|$$

$$\geq \epsilon DE \left\| \underline{x}-\underline{\theta} \right\| \quad \text{for } 0 \leq \alpha \leq 1/2 \tag{8}$$

The right-hand side of Eq. 8 is independent of α; hence, taking the limit of the left-hand side as α approaches zero, we have

$$\left[(\text{grad } M)(\underline{x}), \frac{-(\underline{x}-\underline{\theta})}{\left\| \underline{x}-\underline{\theta} \right\|} \right] \geq \epsilon DE \left\| \underline{x}-\underline{\theta} \right\| \tag{9}$$

as desired.

If we desire to use the results of statement 3, we need only require in addition that $W'''(e)$ be continuous for all values of the argument which occur under restrictions (a) and (b) and the assumption that $\underline{x} \in X$. The boundedness of

$$\left| \frac{\partial^3 M(\underline{x})}{\partial x_i^3} \right| \qquad i = 1, 2, \ldots k$$

under this added restriction is shown in the same manner as was the boundedness of

$$\left| \frac{\partial^2 M(\underline{x})}{\partial x_i \partial x_j} \right|$$

Assumption (iii) is a restriction that the process Y_n depends only remotely on the distant past and is not in itself unreasonable. It is this assumption that requires that some time interval S be left between iterations. In a future report sufficient conditions on the process v(t), d(t) which guarantee the satisfaction of assumption (iii) will be developed, and a comment will be added to extend the analysis to the continuous time parameter case.

Grateful acknowledgment is made for many helpful discussions with Dr. A. V. Balakrishnan and for the helpful cooperation of Space Technology Laboratories, Inc., Los Angeles, California.

D. J. Sakrison

(References on following page)

References

1. N. Wiener, Nonlinear Problems in Random Theory (Technology Press of Massachusetts Institute of Technology, Cambridge, Mass., and John Wiley and Sons, Inc., New York, 1958).

2. M. Brilliant, Theory of the Analysis of Nonlinear Systems, Technical Report 345, Research Laboratory of Electronics, M.I.T., March 3, 1958.

3. V. Dupač, On the Kiefer-Wolfowitz Approximation Method, Report 22G-008, Lincoln Laboratory, M.I.T., 24 Feb. 1960. (Translation of a paper in the Czech mathematical journal Casopis pro Pestovani Matematiky, Vol. 82, pp. 47-75, 1957.)

E. OPTIMUM SYNTHESIS OF A GAUSSIAN PROCESS FROM A NON-GAUSSIAN PROCESS

The transformation of non-Gaussian random processes into Gaussian processes was discussed in Quarterly Progress Report No. 58 (pages 165-170). In that report the question arose as to the extent of the class of random processes that could be so transformed with zero error. In this report we shall show that a sufficient condition for a random process to be a member of this class is that it be a stationary ergodic process and that it have a finite mean-square value, and that samples taken τ seconds apart become statistically independent as the separation, τ, becomes infinite. We shall refer to this class of functions as class G.

Wiener has shown (1) that any function, F, of our class G can be expanded uniquely in terms of his fundamental orthogonal functionals as

$$F(a) = \underset{N\to\infty}{\text{l.i.m.}} \sum_{\nu=0}^{N} A_\nu G_\nu[K_\nu, a] \tag{1}$$

in which a distinguishes one member of the Gaussian ergodic ensemble from another. In terms of Wiener's nonlinear network (2), which is schematically represented in Fig. XI-6, we can write Eq. 1 as

$$F(a) = \underset{N\to\infty}{\text{l.i.m.}} \sum_{\nu=0}^{N} A_\nu y_\nu(a) \tag{2}$$

in which $y_\nu(a)$ is the output of the nonlinear network represented by $G_\nu[K_\nu]$ as a result of the input $g(a)$ which is the a^{th} member of the Gaussian ensemble.

We shall first show that if $F(a)$ is only a single term of Eq. 1,

$$F(a) = y_m(a) \tag{3}$$

then there is a nonlinear network N, of the type described by Wiener (2), whose output is Gaussian when the input is F. To show this, we first note that Eq. 3 represents a

many-to-one mapping because many members of the α ensemble will produce the same output. Thus an inverse mapping from the F ensemble back to the whole α ensemble does not exist. However, we shall show that a mapping to a Gaussian ensemble which is a subset of the α ensemble does exist. To do this, denote the various outputs by F_β. Then we may order the α ensemble in a set of subsets such that the S_β subset of α is

$$S_\beta = \{\alpha: G_n[K_n, \alpha] = y_n(\alpha) \text{ for } n \neq m,\ G_m[K_m, \alpha] = F_\beta\} \tag{4}$$

That is, we gather together all of the members of the α ensemble that produce the same output F_β and call it the set S_β. We now form a new set, T_γ, by picking for each value of β, one member from S_β. This can be done in many ways. Thus, to each value of γ there corresponds a set, T_γ, each of whose members results in a different output, F_β. Also, different values of γ correspond to sets that differ from each other in at least one member. Now, each output, F_β, occurs with probability zero. Thus each set, S_β, has a measure zero relative to α; thus we can show that for each $\epsilon > 0$, there is an ordering

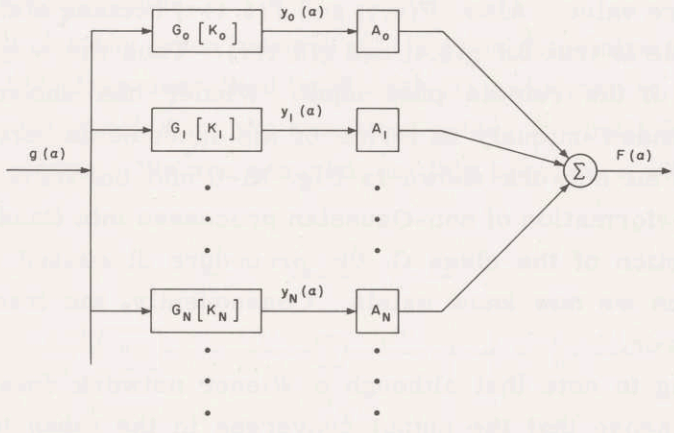

Fig. XI-6. Nonlinear network.

of the α ensemble so that for any set, T_γ, at least one member of the set is contained in every ϵ-neighborhood of the ordered set of α's. This effectively means that each set T_γ is dense in α. Now, since the α ensemble is ergodic, almost all dense subsets of α are also Gaussian ergodic ensembles. Thus, at least one set for some value of γ is a Gaussian ergodic ensemble. Denote each member of this ensemble δ. Then, from Eq. 3, we have

$$F(\delta) = y_m(\delta) \tag{5}$$

This equation now represents a one-to-one mapping and thus a right inverse exists. That is, there exists a network N for which

$$N[F(\delta)] = g(\delta) \tag{6}$$

To prove our statement for the general case, in which

$$F(\alpha) = \sum_{i=1}^{N} A_{m_i} y_{m_i}(\alpha) \tag{7}$$

we choose the set S_β to be

$$S_\beta = \left\{ \alpha : G_n[K_n, \alpha] = y_n(\alpha) \text{ for } n \neq m_i, \quad \sum_{i=1}^{N} A_{m_i} G_{m_i}\left[K_{m_i}, \alpha\right] = F_\beta \right\} \tag{8}$$

The proof is the same as before.

We have thus shown that any function of our class G may be transformed into a Gaussian process with zero error. We now note that the required network, N, is stable because its output has a finite mean-square value for an input that also has a finite mean-square value. Also, $F(\delta, t)$ and $F(\delta, t+\tau)$ become statistically independent as $\tau \to \infty$. The same is true for $g(\delta, t)$ and $g(\delta, t+\tau)$. Thus the output of N is asymptotically independent of the remote past input. Wiener has shown that all such networks can be expanded uniquely in terms of his fundamental orthogonal functionals. This is the form of the network shown in Fig. XI-6 and the form of the network that we used in the transformation of non-Gaussian processes into Gaussian processes (3). Thus, for any function of the class G, the procedure discussed previously searches out a set, δ, which we now know exists. Consequently, the transformation can be done with zero error.

It is interesting to note that although a Wiener network does not always possess an inverse in the sense that the output converges in the mean to a desired output, it always possesses an inverse in the sense that the output converges in probability to a desired output.

M. Schetzen

References

1. N. Wiener, Nonlinear Problems in Random Theory (Technology Press of Massachusetts Institute of Technology, Cambridge, Mass., and John Wiley and Sons, Inc., New York, 1958), p. 41.

2. Ibid., Lectures 10 and 11.

3. M. Schetzen, Optimum synthesis of a Gaussian process from a non-Gaussian process, Quarterly Progress Report No. 58, Research Laboratory of Electronics, M.I.T., July 15, 1960, pp. 165-170.

F. AN OPTIMUM METHOD FOR SIGNAL TRANSMISSION

1. Transmission with Irreducible Minimum Mean-Square Error

A problem in the statistical theory of communication is the design of optimum systems for the transmission and reception of messages through noisy channels. In this report, we shall describe a design of optimum systems for a class of messages for which the mean-square error is an irreducible minimum when the noise in the channel is Gaussian. The class of messages, which was discussed in Section XI-E, is the class that can be transformed into Gaussian random waves. We shall refer to this class as class G.

The general problem may be described by means of Fig. XI-7. The message, $f_m(t)$, is to be transmitted through a channel in which noise, $f_n(t)$, is added. The network N_2 is the optimum filter for the received signal $f_r(t)$, so that the output $f_o(t)$ approximates the message with minimum mean-square error, $\overline{e^2(t)} = \overline{[f_o(t)-f_m(t)]^2}$. In order that this error be an irreducible minimum, the message is optimally distorted by network N_1 to yield the signal, $f_s(t)$, for transmission through the channel. The problem is to determine the optimum combination of networks N_1 and N_2 for which the mean-square error, $\overline{e^2(t)}$, is an irreducible minimum.

We first note that, for any given network N_1, we can determine the optimum nonlinear filter, N_2, of the class described by Wiener (1) and shown in Fig. XI-8. It is determined by sequentially adjusting the amplifier gains, A_i, until the measured mean-square error is a minimum. We are assured that this procedure will always converge

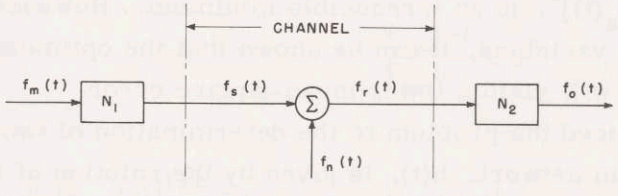

Fig. XI-7. An optimum transmitting-receiving system.

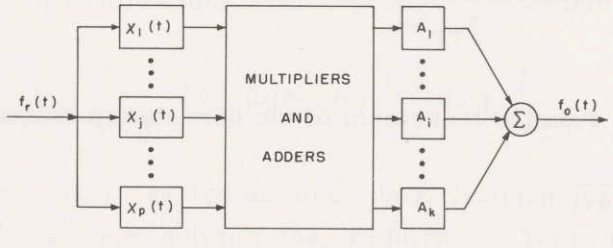

Fig. XI-8. Nonlinear network.

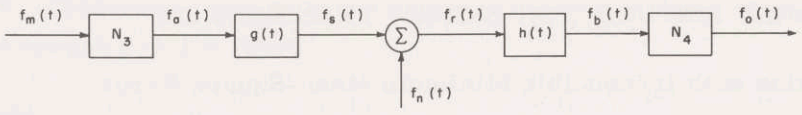

Fig. XI-9. Pertaining to the determination of the optimum system of Fig. XI-7.

since it has been shown that, for each order of nonlinearity, the set of possible outputs for various amplifier gains is a convex set (2). Thus the mean-square error is a minimum for a unique setting of the amplifier gains. However, in order to obtain the irreducible minimum mean-square error, the optimum distortion network, N_1, must also be determined. We shall now describe a procedure for determining the optimum network, N_1, if the noise in the channel is a Gaussian random variable and the message is a member of class G.

Consider the system depicted in Fig. XI-9. If the input, $f_m(t)$, is a member of class G, we can determine a nonlinear network, N_3, of the form depicted in Fig. XI-8, whose output, $f_a(t)$, is a Gaussian random variable (2). Furthermore, a right inverse exists. Thus, except for a possible delay, there exists a network N_4, also of the form depicted in Fig. XI-8, with the property that the network N_3 followed by N_4 is equivalent to a direct connection. We shall find that we do not need to determine the network N_4. We merely need to be assured of its existence to guarantee that our procedure is optimum. Let us assume for the moment that networks N_3 and N_4 have been determined and are placed as shown in Fig. XI-9. The problem is then to determine the optimum distorting network for $f_a(t)$ and receiving network for $f_b(t)$ for which the mean-square error, $\overline{e_1^2(t)} = \overline{[f_b(t)-f_a(t)]^2}$, is an irreducible minimum. However, since $f_a(t)$ and $f_b(t)$ are Gaussian random variables, it can be shown that the optimum system is linear and no nonlinear network will yield a lower mean-square error.

We thus have reduced the problem to the determination of two linear networks, h(t) and g(t). The optimum network, h(t), is given by the solution of the Wiener-Hopf equation. For such a network, the irremovable error (3) is given by

$$\overline{e_{irr}^2(t)} = \int_{-\infty}^{\infty} \frac{\Phi_{rr}(\omega)\,\Phi_{aa}(\omega) - |\Phi_{ra}(\omega)|^2}{\Phi_{rr}(\omega)}\,d\omega \tag{1}$$

in which $\Phi_{ij}(\omega)$ is the Fourier transform of the correlation function, $\phi_{ij}(\tau)$.

$$\phi_{ij}(\tau) = \overline{f_i(t)\,f_j(t+\tau)} \tag{2}$$

However, for our system,

$$f_r(t) = f_n(t) + \int_0^\infty g(x)\, f_a(t-x)\, dx \tag{3}$$

For simplicity, we shall assume $f_a(t)$ and $f_n(t)$ to be uncorrelated. Then

$$\begin{aligned} \Phi_{rr}(\omega) &= \Phi_{nn}(\omega) + |G(\omega)|^2\, \Phi_{aa}(\omega) \\ |\Phi_{ra}(\omega)|^2 &= |G(\omega)|^2\, \Phi_{aa}(\omega) \end{aligned} \tag{4}$$

and Eq. 1 becomes

$$\overline{e_{irr}^2(t)} = \int_{-\infty}^\infty \frac{\Phi_{nn}(\omega)\, \Phi_{aa}(\omega)}{\Phi_{nn}(\omega) + |G(\omega)|^2\, \Phi_{aa}(\omega)}\, d\omega \tag{5}$$

We now impose the constraint that the mean-square value of the transmitted wave, $f_s(t)$, be P. Then

$$\int_{-\infty}^\infty |G(\omega)|^2\, \Phi_{aa}(\omega)\, d\omega = P \tag{6}$$

The transfer function $G(\omega)$ that minimizes Eq. 5, subject to this constraint, is

$$|G_{opt}(\omega)|^2 = \begin{cases} \frac{1}{\beta}\left[\frac{\Phi_{nn}(\omega)}{\Phi_{aa}(\omega)}\right]^{1/2} - \frac{\Phi_{nn}(\omega)}{\Phi_{aa}(\omega)} & \frac{\Phi_{aa}(\omega)}{\Phi_{nn}(\omega)} \geqslant \beta^2 \\ 0 & \frac{\Phi_{aa}(\omega)}{\Phi_{nn}(\omega)} < \beta^2 \end{cases} \tag{7}$$

and

$$P = \frac{1}{\beta} \int_{\omega \in W} [\Phi_{nn}(\omega)\Phi_{aa}(\omega)]^{1/2}\, d\omega - \int_{\omega \in W} \Phi_{nn}(\omega)\, d\omega \tag{8}$$

in which the integration is carried out over the set W which is the set of frequencies for which $\frac{\Phi_{aa}(\omega)}{\Phi_{nn}(\omega)} \geqslant \beta^2$. The minimum irremovable error is then

$$E^2 = \min\left\{\overline{e_{irr}^2(t)}\right\} = \beta \int_{\omega \in W} [\Phi_{nn}(\omega)\Phi_{aa}(\omega)]^{1/2}\, d\omega + \int_{\omega \notin W} \Phi_{aa}(\omega)\, d\omega \tag{9}$$

in which the second integral is carried out over those frequencies that are not members of W. We note that the optimum solution may require $G_{opt}(\omega)$ to be zero over a range of frequencies. This is not physically realizable. For such cases, the optimum transfer

function is that which is equal to $|G_{opt}(\omega)|$ at those frequencies for which $|G_{opt}(\omega)| \neq 0$ and is as small as possible at those frequencies for which $|G_{opt}(\omega)| = 0$.

For example, let $\Phi_{aa}(\omega) = 1/(1+\omega^2)$, $\Phi_{nn}(\omega) = 1$ and choose $\beta = 10^{-3}$. Then the set of frequencies transmitted, W, is the set for which

$$\beta^2 = 10^{-6} \leq \frac{\Phi_{aa}(\omega)}{\Phi_{nn}(\omega)} = \frac{1}{1+\omega^2}$$

or

$$\omega < 10^3 \tag{10}$$

Then, from Eq. 8, the mean-square value of the transmitted wave is

$$P = 10^3 \int_{-10^3}^{10^3} \frac{1}{(1+\omega^2)^{1/2}}\, d\omega - \int_{-10^3}^{10^3} d\omega$$

$$= 2 \times 10^3 [\sinh^{-1} 10^3 - 1]$$

$$= 13.2 \times 10^3 \tag{11}$$

From Eq. 7, $|G_{opt}(\omega)|^2$ is given by

$$|G_{opt}(\omega)|^2 = \begin{cases} 10^3[1+\omega^2]^{1/2} - [1+\omega^2] & \omega < 10^3 \\ 0 & \omega \geq 10^3 \end{cases} \tag{12}$$

Figure XI-10 is a graph of $|G_{opt}(\omega)|$. The minimum irremovable error, E^2, is obtained from Eq. 9:

$$E^2 = 2 \times 10^{-3} \int_0^{10^3} \frac{1}{(1+\omega^2)^{1/2}}\, d\omega + 2 \int_{10^3}^{\infty} \frac{1}{1+\omega^2}\, d\omega$$

$$= 2 \times 10^{-3} [1 + \sinh^{-1} 10^3]$$

$$= 17.2 \times 10^{-3} \tag{13}$$

If we had used an amplifier of gain, $|G(\omega)| = A$, then for the same mean-square value of the transmitted wave, we would make $A^2 = \frac{P}{\pi}$. From Eq. 5, the irremovable error, $\overline{e_{irr}^2(t)}$, for this case is

$$\overline{e_{irr}^2(t)} = \int_{-\infty}^{\infty} \frac{\frac{1}{1+\omega^2}}{1+\frac{P}{\pi}\frac{1}{1+\omega^2}}\, d\omega$$

$$= \frac{\pi}{\left(1+\frac{P}{\pi}\right)^{1/2}}$$

$$= 48.4 \times 10^{-3} \qquad (14)$$

if we use the value of P from Eq. 11. Thus, we have reduced the irremovable mean-square error by a factor of 2.71 by the use of $|G_{opt}(\omega)|$ instead of an amplifier with constant gain. It should be noted that, for our solution, the phase of $G_{opt}(\omega)$ is arbitrary. Even so, in practice, $G_{opt}(\omega)$ should be chosen as a minimum-phase network in order to reduce the time delay in filtering the received signal, $f_r(t)$.

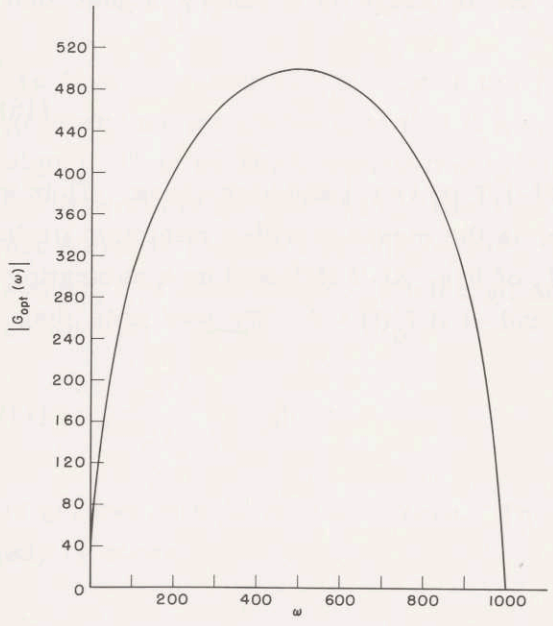

Fig. XI-10. Graph of $|G_{opt}(\omega)|$ versus ω for the example given.

The optimum transmitting-receiving system is thus designed by first determining network N_3 by the method previously described (2); $|G_{opt}(\omega)|$ is given by Eq. 7. The tandem connection of N_3 and g(t) is then the optimum distorting network, N_1, of Fig. XI-7. We now observe that it is not necessary to determine h(t) and N_4 in order to obtain the optimum receiving system. Rather, we may determine the optimum network, N_2, of Fig. XI-7 directly by the method discussed in this report. However, since $f_r(t)$ is a

Gaussian random variable, the amplifier gains A_i will not interact and only one adjustment of each amplifier gain will be necessary.

2. Transmission with Irreducible Minimum Probability of Error

We now shall show that by slightly modifying the optimum system described in section 1, we can transmit signals through Gaussian channels with an irreducible minimum probability of error. We shall limit our discussion to binary signals.

The method is based upon the fact that the output of a filter, which is within the minimum mean-square error of some desired output, is the conditional mean. Thus, from Fig. XI-7, if we let x be the amplitude of the message, then the output of the optimum filter, N_2, at time t_1 is

$$f_o(t_1) = \int_{-\infty}^{\infty} xP[x/f_r(t);t\leq t_1]\,dx \tag{15}$$

in which $P[x/f_r(t);t\leq t_1]$ is the probability that the message's amplitude was x, given the complete past of the received signal, $f_r(t)$. If the message is a binary signal that assumes the values +1 and −1, then

$$f_o(t_1) = P[1/f_r(t);t\leq t_1] - P[-1/f_r(t);t\leq t_1] \tag{16}$$

We note that $f_o(t_1) > 0$ only if $P[1/f_r(t);t\leq t_1] > P[-1/f_r(t);t\leq t_1]$ and vice versa. Thus we can form a signal which, at each instant of time, is the message with a minimum probability of error by having the optimum network N_2 of Fig. XI-7 followed by a saturating amplifier whose output, $f_c(t)$, is +1 if $f_o(t) > 0$, and −1 if $f_o(t) < 0$. We now note that since

$$1 = P[1/f_r(t);t\leq t_1] + P[-1/f_r(t);t\leq t_1] \tag{17}$$

we may write Eq. 16 as

$$f_o(t_1) = 2P[1/f_r(t);t\leq t_1] - 1 \tag{18}$$

Now, the mean-square error has been made an irreducible minimum by optimally distorting the message with network N_1. In terms of Eq. 18, this means that if the amplitude of the message is +1, then $P[1/f_r(t);t\leq t_1]$ is as close to +1 as is theoretically possible. Also, if the amplitude of the message is −1, then $P[1/f_r(t);t\leq t_1]$ is as close to zero as is theoretically possible. This implies that, at each instant of time, $f_c(t)$ is the message with an irreducible minimum probability of error. An example of a message for which this type of transmission would be desirable is infinitely clipped speech. If, however, the message is a sequence of binary digits that are positive or negative

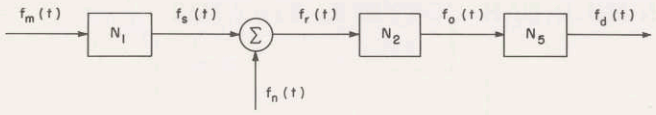

Fig. XI-11. An optimum system for binary digits.

pulses of duration T, the system that we have just described would not be the desired optimum. For such a signal, we desire the output also to be pulses of duration T that are +1 or -1 with an irreducible minimum probability of error. To accomplish this, we note that

$$\int_{t_1-T}^{t_1} P[x/f_r(t);t\leq t_1]\, dt_1$$

is the probability that the message pulse, which is known to exist in the interval (t_1-T, t_1), had the amplitude x, given the complete past of the received signal. From Eq. 16, we have

$$I_1 = \int_{t_1-T}^{t_1} f_o(t_1)\, dt_1 = \int_{t_1-T}^{t_1} P[1/f_r(t);t\leq t_1]\, dt_1 - \int_{t_1-T}^{t_1} P[-1/f_r(t);t\leq t_1]\, dt_1 \qquad (19)$$

We thus note that $I_1 > 0$ only if the probability that the binary digit was positive is greater than the probability that it was negative, given the complete past of the received signal. Thus we can transmit binary digits with an irreducible minimum probability of error with the system of Fig. XI-11. The networks N_1 and N_2 are the optimum networks described in section 1 of this report. The network N_5 has an output, $f_d(t)$, which is a sequence of binary digits. Each digit has an amplitude that is +1 or -1; the sign depends on whether

$$I_n = \int_{t_n-T}^{t_n} f_o(t)\, dt$$

is greater than or less than zero. The times $[t_n-T]$ are the known starting times of the binary digits.

M. Schetzen

References

1. N. Wiener, Nonlinear Problems in Random Theory (Technology Press of Massachusetts Institute of Technology, Cambridge, Mass., and John Wiley and Sons, Inc., New York, 1958).

2. M. Schetzen, Optimum synthesis of a Gaussian process from a non-Gaussian process, Quarterly Progress Report No. 58, Research Laboratory of Electronics, M.I.T., July 15, 1960, pp. 165-170.

3. Y. W. Lee, The Statistical Theory of Communication (John Wiley and Sons, Inc., New York, 1960).

G. OPTIMUM COMPENSATION FOR NONLINEAR CONTROL SYSTEMS

1. Nonlinear Compensation Problem

In feedback control systems the output is provided by a physical device capable of meeting the power requirements of the control system. To optimize the performance of the system, the input to these fixed elements must be altered in some manner. The presence of these fixed elements in the system provides the fundamental distinction between compensation problems and filter problems. For linear systems with random inputs, the relation between the two problems is well known.

For nonlinear systems, the relation between the two problems is still not clear. Physical systems are most easily described by differential equations. Classical nonlinear theory has been essentially a study of the solutions and properties of nonlinear differential equations. However, a general statistical optimization technique that makes use only of differential equations appears difficult to develop. The modern functional expansion techniques for treating statistical problems outlined by Wiener (1) provide a basis for solving the nonlinear optimization problem.

In this report a method of solving the nonlinear compensation problem by effectively combining the use of nonlinear differential equations and functional expansion techniques is outlined.

The general configuration of a feedback control system is shown in Fig. XI-12. Here, r(t) is a sample function from a stationary random process. The desired output of the over-all system is a function $y_d(t)$ which is related to either r(t) or the signal part of r(t) in some known manner. If there were no fixed elements, we would have the nonlinear filter problem illustrated in Fig. XI-13.

One method of solving this filter problem would be to specify the input-output relation of the filter to be of the form

$$y_b(t) = \int_0^t K_1(t-\tau_1)\, r(\tau_1)\, d\tau_1 + \int_0^t \int_0^t K_2(t-\tau_1, t-\tau_2)\, r(\tau_1)\, r(\tau_2)\, d\tau_1 d\tau_2 + \dots \qquad (1)$$

and then find a series of kernels $K_1, K_2, K_3, \dots$ so that the expected value of $[y(t)-y_b(t)]^2$ is minimized.

Now, if we could find a realizable system C_a or C_b with the property that $y_a(t) = y_b(t)$, then the original compensation problem would be solved.

The class of compensation problems to be considered may now be more clearly defined. It is assumed that the fixed elements may be described by a nonlinear differential equation of the form

$$P_1(x, x', x'', \dots x^{(r)}) = P_2(y, y', y'', \dots y^{(s)}) \qquad (2)$$

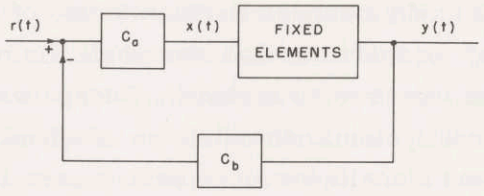

Fig. XI-12. General control system configuration.

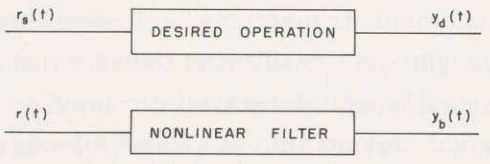

Fig. XI-13. Optimum filter.

where x is the input to the fixed elements, y is the output of the fixed elements, and P represents a function which is a polynomial. Typical examples of the occurrence of equations of this type are

$$ay'' + by' + cy + dy^3 = x \tag{3}$$

which represents motion with nonlinear restoring force;

$$ay'' + b(y')^2 + cy = x \tag{4}$$

which represents motion with nonlinear damping; and

$$ay'' + by' + cy = P(x) \tag{5}$$

which represents the general category of systems that are a cascade of a nonlinear no-memory polynomial device and a linear memory device.

More general polynomials such as

$$ay''y + b(y')^3 + cy^2 = dx + ex''x' + fx^3 \tag{6}$$

are included in this category.

Before outlining the method of solution of the stated compensation problem, related work should be reviewed. Recent work in the theory of optimum nonlinear systems uses the functional power-series representation conceived by Wiener (1). This is a generalization of the convolution integral. In this method, the output y is expressed as:

$$y(t) = \int_{-\infty}^{\infty} K_1(t-\tau)\, x(\tau)\, d\tau + \int_{-\infty}^{\infty}\int_{-\infty}^{\infty} K_2(t-\tau_1, t-\tau_2)\, x(\tau_1)\, x(\tau_2)\, d\tau_1 d\tau_2$$

$$+ \int_{-\infty}^{\infty}\int_{-\infty}^{\infty}\int_{-\infty}^{\infty} K_3(t-\tau_1, t-\tau_2, t-\tau_3)\, x(\tau_1)\, x(\tau_2)\, x(\tau_3)\, d\tau_1 d\tau_2 d\tau_3 + \ldots \tag{7}$$

Brilliant (2) developed a theory of analysis for nonlinear systems of this form. He developed methods for cascading, adding, and multiplying systems of this type. George (3) also used the functional representation. Working primarily with nonlinear systems that are composed of nonlinear no-memory devices and linear memory devices,

he developed an algebra for combining systems. He extended Brilliant's use of multidimensional transforms and developed many properties that we shall find useful. Although some results on Gaussian white-noise inputs were included, George worked principally with deterministic inputs. In control systems, the division of a nonlinear physical device into a linear memory part and a nonlinear no-memory part is often unwieldy and almost always artificial. By working directly with the differential equation of the physical system, there is a greater possibility of attaching the correct physical significance to one's final answer. Zames (4, 5) has dealt with the problem of inversion of functionals and feedback around functionals. He has developed an algorithm for determining the resultant kernels. The part of his work pertaining to control systems was deterministic.

As in linear systems, it seems that application of Wiener's concepts to filter problems has proceeded more rapidly than the application to control system problems. By combining the advantages of two different analytical techniques, it is hoped that a reasonably practical, general method of solution to a large class of nonlinear control problems may be found.

2. Method of Approach and Preliminary Results

The general configuration of a feedback control system is shown in Fig. XI-12. Let us consider two important special cases of this general configuration. For $C_b = 1$, we have the "series" compensation problem (Fig. XI-14a). For $C_a = 1$, we have the

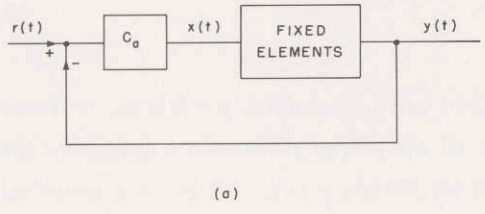

(a)

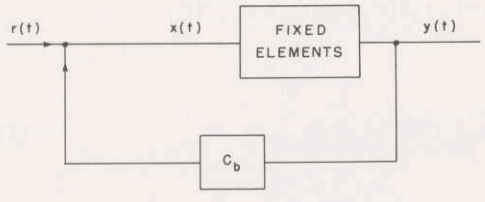

(b)

Fig. XI-14. (a) Series compensation. (b) Feedback compensation.

"feedback" compensation problem (Fig. XI-14b). In many cases the proper choice of configuration will be obvious. Presumably, there are cases in which a convergent

solution could be obtained by using both C_a and C_b when neither one alone would be satisfactory. These problems are subjects for future research.

Recall that the basic problem was, first, to find a set of kernels $K_1, K_2, K_3, \ldots K_n$ that specify the optimum nonlinear filter. For nonlinear operations on Gaussian inputs, an analytic solution for these kernels may be obtained by using Chesler's (6) techniques. For an arbitrary input, it appears that numerical methods will be required.

The basic equations describing the system in Fig. XI-14 are:

$$P_1(x, x', x'', \ldots x^{(r)}) = P_2(y, y', y'', \ldots y^{(s)}) \tag{8}$$

$$x(t) = \int_0^t C_1(t-\tau)\, e(\tau)\, d\tau + \int_0^t \int_0^t C_2(t-\tau_1, t-\tau_2)\, e(\tau_1)\, e(\tau_2)\, d\tau_1 d\tau_2 + \ldots \tag{9}$$

$$e(t) = r(t) - y(t) \tag{10}$$

$$y(t) = \int_0^t K_1(t-\tau)\, r(\tau)\, d\tau + \int_0^t \int_0^t K_2(t-\tau_1, t-\tau_2)\, r(\tau_1)\, r(\tau_2)\, d\tau_1 d\tau_2 + \ldots \tag{11}$$

For definiteness, consider fixed elements described by

$$y'' + ay' + by = x + dx^3 \tag{12}$$

or

$$L[y] = x + dx^3 \tag{13}$$

A straightforward approach would be to substitute Eqs. 9, 10, and 11 in Eq. 8. This gives an equation of the form

$$\begin{aligned}
&L\left[\int_0^t K_1(t-\tau)\, r(\tau)\, d\tau + \int_0^t \int_0^t K_2(t-\tau_1, t-\tau_2)\, r(\tau_1)\, r(\tau_2)\, d\tau_1 d\tau_2 + \ldots\right] \\
&= \left\{\int_0^t C_1(t-\tau)\left[r(\tau) - \int_0^\tau K_1(\tau-\epsilon)\, r(\epsilon)\, d\epsilon - \int_0^\tau \int_0^\tau K_2(\tau-\epsilon_1, \tau-\epsilon_2)\, r(\epsilon_1)\, r(\epsilon_2)\, d\epsilon_1 d\epsilon_2 + \ldots\right]\right. \\
&\quad + \int_0^t \int_0^t d\tau_1 d\tau_2 C_2(t-\tau_1, t-\tau_2)\left[r(\tau_1) - \int_0^{\tau_1} K_1(\tau_1-\epsilon)\, r(\epsilon)\, d\epsilon - \ldots\right]\left[r(\tau_2) - \int_0^{\tau_2} K_1(\tau_2-\epsilon)\, r(\epsilon)\, d\epsilon + \ldots\right] \\
&\quad + \iiint_0^t d\tau_1 d\tau_2 d\tau_3 C_3(t-\tau_1, t-\tau_2, t-\tau_3)\left[r(\tau_1) - \int_0^{\tau_1} K_1(\tau_1-\epsilon)\, r(\epsilon)\, d\epsilon + \ldots\right] \\
&\quad \times \left.\left[r(\tau_2) - \int_0^{\tau_2} K_1(\tau_2-\epsilon)\, r(\epsilon)\, d\epsilon + \ldots\right]\left[r(\tau_3) - \int_0^{\tau_3} K_1(\tau_3-\epsilon)\, r(\epsilon)\, d\epsilon + \ldots\right] + \ldots\right\} \\
&\quad + d\left\{\left[\int_0^t C_1(t-\tau)\left[r(\tau) - \int_0^\tau K_1(\tau-\epsilon)\, d\epsilon + \ldots\right] d\tau\right]^3 + 3\left[\int_0^t d\tau C_1(t-\tau)\left[r(\tau) - \int_0^\tau K_1(\tau-\epsilon)\, r(\epsilon)\, d\epsilon + \ldots\right]\right]^2\right. \\
&\quad \times \left[\int_0^t d\tau_1 d\tau_2 C_2(t-\tau_1, t-\tau_2)\left[r(\tau_1) - \int_0^{\tau_1} K_1(\tau_1-\epsilon)\, r(\epsilon)\, d\epsilon - \ldots\right]\right. \\
&\quad \times \left.\left.\left[r(\tau_2) - \int_0^{\tau_2} K_1(\tau_2-\epsilon)\, r(\epsilon)\, d\epsilon + \ldots\right]\right] + \ldots\right\}
\end{aligned} \tag{14}$$

By equating terms of the same order in r(t), a set of equations can be obtained that could be solved successively, not simultaneously, for the various C_m. The easiest approach to solving these equations is through multidimensional transform theory (3). Even with the use of transforms, a straightforward approach turns out to be too tedious to be valuable as a general method. An algorithm has been developed that gives the desired result in a much simpler fashion.

(a) Algorithm for Determining Series Compensator Kernels

The input-output relation of the fixed elements is described by a nonlinear differential equation. First, the terms are classified according to the order of their nonlinearity. Thus x^3, $x'(x'')^2$, $xx'x''$ are all third-order input terms. There is a basic expansion for all n^{th}-order terms. The algorithm developed enables us to write an equation for C_m in the transform domain by considering the expansion of the n^{th}-order terms directly. Consider the equation

$$ay^2y' + by^3 + cy^2 + d(y')^2 + L(y) = L(x) + ex^3 + fx'(x'')^2 + g\,xx'x'' \tag{15}$$

In order to solve for the m^{th}-order compensator kernel C_m, we can write an equation of the form

$$Q_m^3 + Q_m^2 + Q_m^1 = P_m^1 + P_m^3 \tag{16}$$

where Q_m^3 represents the contribution of all third-order output terms, P_m^1 represents the contribution of all linear input terms, and the other terms have similar definitions. The transform of the unknown kernel appears in P_m^1. All other quantities are known, so that the explicit answer follows immediately.

We shall see that the basic expansion for all n^{th}-order terms is a combination of different partitions. The difference between terms within a given order is taken into account by use of a characteristic coefficient that modifies the basic expansion.

Thus the problem is to find an efficient method for constructing the terms, P_m^n and Q_m^n.

(i) Construction of P_m^n; Contribution of an n^{th}-order nonlinearity of the input to an m^{th}-order series compensator kernel

P_m^n consists of a sum of m-n+1 terms. Thus, we may write

$$P_m^n = \sum_{i=n}^{m} P_m^n(i) \tag{17}$$

and determine each $P_m^n(i)$. $P_m^n(i)$ is constructed in three steps. First, form all partitions of m objects into n cells. For example, the partitions for m = 7 and n = 3 are:

(I) 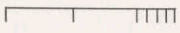

p_{115}

(II) 

p_{124}

(III) 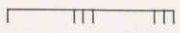

p_{133}

(IV) 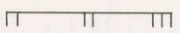

p_{223}

These are the basic or major partitions. Physically, each object represents a different frequency-domain variable. Second, consider all combinations of n compensator kernels C_j, where $\Sigma j = i$. For i = 5 and n = 3, the possible combinations are C_1, C_2, C_2 and C_1, C_1, C_3. Compare each set of kernels with each major partition in turn. Looking at p_{115} and C_1, C_2, C_2 first, we see that they could not occur together. C_2 represents a kernel that is a function of at least two variables, $C_2(S_1, S_2)$. But two of the partitions in p_{115} have only one variable in them. Thus, we cannot associate C_1, C_2, C_2 and p_{115}. Examples of correct associations are:

(Ia)

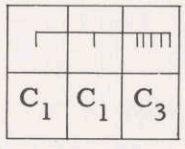

(IIa)

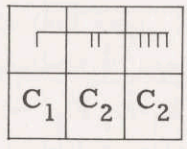

Third, look at the ways in which the optimum filter kernels K_β can combine with the compensator kernels C_j. Here, the necessary restriction is that $\Sigma \beta = m$ and that the total number of kernels $K_\beta = i$. For partition Ia, we see that suitable combinations are:

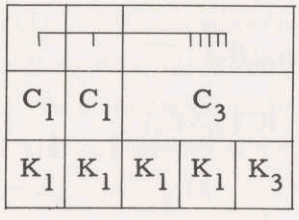

or

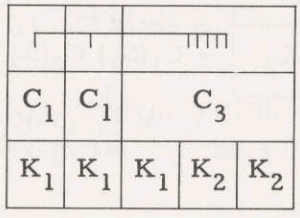

These represent the transformed terms:

$$[C_1(S_1)(1-K_1(S_1))][C_1(S_2)(1-K_1(S_2))][C_3(S_3,S_4,S_5+S_6+S_7)(1-K_1(S_3))(1-K_1(S_4))K_3(S_5,S_6,S_7)]$$

and

$$[C_1(S_1)(1-K_1(S_1))][C_1(S_2)(1-K_1(S_2))][C_3(S_3, S_4+S_5, S_6+S_7)(1-K_1(S_3))K_2(S_4, S_5)K_2(S_6, S_7)]$$

To complete $P_7^3(5)$, consider the remaining partitions and the kernels associated with them. In tabular form, the complete process and results are:

$P_7^3(5)$:

$p_{115} \rightarrow$

C_1	C_1	C_3		
K_1	K_1	K_1	K_1	K_3
C_1	C_1	C_3		
K_1	K_1	K_1	K_2	K_2

$\rightarrow C_1(S_1)\, C_1(S_2)\, C_3(S_3, S_4, S_5+S_6+S_7)$
$\times \prod_{i=1}^{4} [1-K_1(S_i)]\, K_3(S_5, S_6, S_7)$

$\rightarrow C_1(S_1)\, C_1(S_2)\, C_3(S_3, S_4+S_5, S_6+S_7)$
$\times \prod_{i=1}^{3} [1-K_1(S_i)]\, K_2(S_4, S_5)\, K_2(S_6, S_7)$

$p_{124} \rightarrow$

C_1	C_1	C_3
K_1	K_2	$K_1\, K_1\, K_2$
C_1	C_2	C_2
K_1	$K_1\, K_1$	$K_1\, K_3$
C_1	C_2	C_2
K_1	$K_1\, K_1$	$K_2\, K_2$

$\rightarrow C_1(S_1)\, C_1(S_2+S_3)\, C_3(S_4, S_5, S_6+S_7)$
$\times [1-K_1(S_1)]\, K_2(S_2, S_3)\, [1-K_1(S_4)]\, [1-K_1(S_5)]\, K_2(S_6, S_7)$

$\rightarrow C_1(S_1)\, C_2(S_2, S_3)\, C_2(S_4, S_5+S_6+S_7)$
$\times \prod_{i=1}^{4} [1-K_1(S_i)]\, K_3(S_5, S_6, S_7)$

$\rightarrow C_1(S_1)\, C_2(S_2, S_3)\, C_2(S_4+S_5, S_6+S_7)$
$\times \prod_{i=1}^{3} [1-K_1(S_i)]\, K_2(S_4, S_5)\, K_2(S_6, S_7)$

$p_{133} \rightarrow$

C_1	C_1	C_3
K_1	K_3	$K_1\, K_1\, K_1$
C_1	C_2	C_2
K_1	$K_1\, K_2$	$K_1\, K_2$

$\rightarrow C_1(S_1)\, C_1(S_2+S_3+S_4)\, C_3(S_5, S_6, S_7)$
$\times [1-K_1(S_1)]\, K_3(S_2, S_3, S_4) \prod_{i=5}^{7} [1-K_1(S_i)]$

$\rightarrow C_1(S_1)\, C_2(S_2, S_3+S_4)\, C_2(S_5, S_6+S_7)$
$\times \prod_{i=1, 2, 5} [1-K_1(S_i)]\, K_2(S_3, S_4)\, K_2(S_6, S_7)$

$p_{223} \rightarrow$

Π	Π	Π	
C_1	C_2	C_2	
K_2	$K_1\,K_1$	$K_1\,K_2$	$\rightarrow C_1(S_1+S_2)\,C_2(S_3,S_4)\,C_2(S_5,S_6+S_7)$
C_2	C_2	C_1	$\times K_2(S_1,S_2) \prod_{i=3,4,5} [1-K_1(S_i)]\,K_2(S_6,S_7)$
$K_1\,K_1$	$K_1\,K_1$	K_3	$\rightarrow C_2(S_1,S_2)\,C_2(S_3,S_4)\,C_1(S_5+S_6+S_7)$
C_1	C_1	C_3	$\times \prod_{i=1}^{4} \lvert 1-K_1(S_i)\rvert\,K_3(S_5,S_6,S_7)$
K_2	K_2	$K_1\,K_1\,K_1$	$\rightarrow C_1(S_1+S_2)\,C_1(S_3+S_4)\,C_3(S_5,S_6,S_7)$
			$\times K_2(S_1,S_2)\,K_2(S_3,S_4) \prod_{i=5}^{7} \lvert 1-K_1(S_i)\rvert$

There are three quantities that remain to be specified: the sign of each p, the numerical coefficient of each p, and the characteristic coefficient associated with each p.

(a) The sign of each p equals $(-1)^r$, where r is defined as the number of kernels K_β with a subscript β other than one.

(b) The numerical coefficient is determined by two multiplicative factors. The first factor is equal to the number of distinct arrangements that are possible by changing the ordering within the various subpartitions. (A subpartition is the partition within a specific kernel.) The second factor comes from the rearrangement of the various kernels in all possible distinct ways. This factor is simply equal to the number of permutations of n objects. Kernels with the same subscript and same number of variables are considered identical in this permutation.

(c) The characteristic coefficient is a function only of the argument of p and not of the particular kernel it represents. For example, the characteristic coefficient of x" x' x pertaining to p_{115} is

$$\frac{1}{3}\left[S_1^2S_2^1 \cdot \left(\sum_{i=3}^{7} S_i\right)^0 + S_2^2 \cdot \left(\sum_{i=3}^{7} S_i\right)^1 \cdot S_1^0 + \left(\sum_{i=3}^{7} S_1\right)^2 S_1^1S_2^0\right]$$

which reduces to

$$S_1^2S_2 + S_2^2\left(\sum_{i=3}^{7} S_i\right) + \left(\sum_{i=3}^{7} S_i\right)^2 S_1$$

This comes from the general rule of writing the variables as a product of a summation of S's. The number of S's in each sum is equal to the argument of the p function. The exponent to which each sum is raised is equal to the order of the respective derivative. The terms are then permuted. For a term containing no

derivatives, the characteristic coefficient is simply 1.

As an example, consider a typical term of $P_7^3(5)$.

$$p''_{124} = \begin{array}{|c|c|c|} \hline & | & || \\ \hline C_1 & C_2 & C_2 \\ \hline K_1 & K_1\,K_1 & K_1\,K_3 \\ \hline \end{array} \quad C_1(S_1)\, C_2(S_2, S_3)\, C_2(S_4, S_5+S_6+S_7) \times \prod_{i=1}^{4} [1-K_1(S_i)]\, K_3(S_5, S_6, S_7)$$

(a) r = 1, so the sign is $(-1)^1 = -1$.

(b) The first factor of the numerical coefficient is 2. This comes from rearranging the subpartition corresponding to $C_2(S_4, S_5+S_6+S_7)$. The second factor is 3.

(c) The characteristic coefficient is 1 because there are no derivatives. The complete term is

$$-6\; C_1(S_1)\; C_2(S_2, S_3)\; C_2(S_4, S_5+S_6+S_7) \prod_{i=1}^{4} [1-K_1(S_i)]\, K_3(S_5, S_6, S_7)$$

As one would expect, the compensator term is rather complicated. However, when we look at the examples and means of synthesis, we shall see that the kernels are built up by combinations of smaller, less formidable systems.

(ii) Construction of Q_m^n; Contribution of an n^{th}-order nonlinearity of the output to an m^{th}-order series compensator kernel

Nonlinear output terms are subject to similar, although simpler, expansion rules. By looking at the original equations, we see that

$$y(t)^n = \left\{ \int_0^t K_1(t-\tau)\, r(\tau)\, d\tau + \int_0^t \int_0^t K_2(t-\tau_1, t-\tau_2)\, r(\tau_1)\, r(\tau_2)\, d\tau_1 d\tau_2 + \ldots \right\}^n$$

Therefore, to find Q_m^n, we construct all possible partitions of m objects into n cells. For example, let n = 3 and m = 5. Possible partitions are:

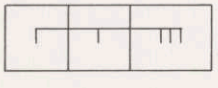

q_{113}

q_{122}

which represent $K_1(S_1)\, K_1(S_2)\, K_3(S_3, S_4, S_5)$ and $K_1(S_1)\, K_2(S_2, S_3)\, K_2(S_4, S_5)$, respectively.

The sign of each term is positive. The numerical coefficient is equal to the number of different ways in which the partition can be ordered. The characteristic coefficient

is determined in exactly the same manner as it was for an input term.

Note that in order to find the functional series representation of any device when the input-output relation is a differential equation, we apply the Q_m^n algorithm and get the answer directly.

We now have all of the parts of the algorithm that are necessary for writing equations for the series compensator kernels by inspection. In the concluding part of this report (to be published in Quarterly Progress Report No. 60, January 15, 1961) examples demonstrating this procedure and a similar procedure for feedback compensator kernels will be given.

H. L. Van Trees, Jr.

References

1. N. Wiener, Nonlinear Problems in Random Theory (Technology Press of Massachusetts Institute of Technology, Cambridge, Mass., and John Wiley and Sons, Inc., New York, 1958).

2. M. B. Brilliant, Theory of the Analysis of Nonlinear Systems, Technical Report 345, Research Laboratory of Electronics, M.I.T., March 3, 1958.

3. D. A. George, Continuous Nonlinear Systems, Technical Report 355, Research Laboratory of Electronics, M.I.T., July 22, 1959.

4. G. D. Zames, Nonlinear operators – cascading, inversion, and feedback, Quarterly Progress Report No. 53, Research Laboratory of Electronics, M.I.T., April 15, 1959, pp. 93-108.

5. G. D. Zames, Realizability of nonlinear filters and feedback systems, Quarterly Progress Report No. 56, Research Laboratory of Electronics, M.I.T., Jan. 15, 1960, pp. 137-143.

6. D. A. Chesler, Nonlinear Systems with Gaussian Inputs, Sc.D. Thesis, Department of Electrical Engineering, M.I.T., Jan. 11, 1960.

H. A PROBLEM IN RADIO ASTRONOMY*

A project has been initiated which will have as its goal the measurement of the galactic deuterium to hydrogen abundance ratio. This figure is of importance to the astrophysicist in the study of element synthesis in the universe. This measurement will be based upon comparison of the intensity of the 21-cm spectral line of atomic hydrogen with a similar line of atomic deuterium at 91.6 cm. The hydrogen line has been the subject of intensive observation since its detection, in 1951, by Ewen and Purcell. However, the deuterium line will be approximately a thousand times weaker and its presence has eluded four attempts at detection (1, 2, 3, 4). The conclusion drawn from these investigations is that the galactic deuterium to hydrogen abundance ratio is less than 1/4000,

*This research was supported in part by National Science Foundation under Grant G-13904.

which is just short of the probable terrestrial value of 1/6600. A further discussion of the radio astronomical aspects of the problem is given in a paper by the present writer (5).

The problem is essentially that of detecting a 0.025 per cent, 3-kc wide, dip in the noise power spectrum received by the antenna. An averaging time of approximately 4 weeks is needed to reduce statistical fluctuations to a sufficiently small value. Conventional analog radiometers are limited by lack of stability over the long period of time required for the measurement.

Our approach to this problem will be to use real-time digital autocorrelation of the incoming signal and then computer Fourier transformation to obtain the spectral density. The advantage of this method lies in the high degree of accuracy that can be obtained. The radiometer and correlator are now undergoing development.

The digital correlator is unique in that only one-bit samples of the incoming time function are used. That is, each sample is coded into a "1" if the polarity of the time function is greater than zero, or into a "0" if it is less than zero. For Gaussian time functions, the normalized one-bit autocorrelation function, $\rho_y(\tau)$, can be corrected to give the normalized true autocorrelation function, $\rho_x(\tau)$, by a simple relation derived by Van Vleck (6),

$$\rho_x(\tau) = \sin\left[\frac{\pi}{2}\rho_y(\tau)\right]$$

Our work (7) indicates that the rms fluctuation of the measured one-bit autocorrelation function is approximately $\pi/2$ times the rms fluctuation of an autocorrelation function derived from many-bit samples. This loss in rms fluctuation is far outweighed by the accuracy and speed with which the autocorrelation can be carried out. The one-bit correlator that is under construction will be capable of correlating a required 4 weeks of 30-kc information at 3-kc resolution in real time. The same operation with 36-bit words on the IBM 704 computer would require 16 years of computer time.

S. Weinreb

References

1. G. G. Getmanzev, K. S. Stankevitch, and V. S. Troitsky, Detection of monochromatic radio emission of deuterium from the center of the galaxy on a wavelength of 91.6 cm., Doklady Akad. Nauk S. S. S. R. 103, 783-786 (1955).

2. G. J. Stanley and R. Price, An investigation of monochromatic radio emission of deuterium from the galaxy, Nature 177, 1221-1222 (1956).

3. R. L. Adgie and J. S. Hey, Intensity of the radio line of galactic deuterium, Nature 179, 370 (1957).

(References continued on following page)

4. R. L. Adgie, An attempt to detect the 327 Mc. line of galactic deuterium, Paris Symposium on Radio Astronomy (Stanford University Press, Stanford University, Calif., 1958), pp. 352-354.

5. S. Weinreb, The Detection of UHF Radiation from Deuterium in Interstellar Space, S.B. Thesis, Department of Electrical Engineering, M.I.T., June 1958.

6. J. H. Van Vleck, The Spectrum of Clipped Noise, Report No. 51, Radio Research Laboratory, Harvard University, July 1943.

7. S. Weinreb, Autocorrelation Functions of Clipped Gaussian Processes, Internal Memorandum, Research Laboratory of Electronics, M.I.T., July 29, 1960.

XII. PROCESSING AND TRANSMISSION OF INFORMATION*

Prof. E. Arthurs
Prof. M. Eden
Prof. P. Elias
Prof. J. B. Dennis
Prof. R. M. Fano
Prof. E. M. Hofstetter
Prof. D. A. Huffman
Prof. W. F. Schreiber
Prof. C. E. Shannon
Prof. W. M. Siebert
Prof. J. M. Wozencraft

S. Asano
D. G. Detert
H. S. Ekre
H. A. Ernst
R. F. Ferretti
R. G. Gallager
T. J. Goblick, Jr.
U. F. Gronemann
F. C. Hennie III
M. Horstein
T. S. Huang
F. Jelinek

T. Kailath
A. Paul
J. C. Pennypacker
D. H. Pratt
D. L. Reich
B. Reiffen
L. G. Roberts
J. L. Rosenfeld
I. G. Stiglitz
N. K. H. Tam
H. P. Zeiger

A. WORK COMPLETED

1. LOW-DENSITY PARITY-CHECK CODES

This study was completed by R. G. Gallager and was accepted by the Department of Electrical Engineering, M.I.T., August 1960, as a thesis in partial fulfillment of the requirements for the degree of Doctor of Science.

P. Elias

2. SEQUENTIAL TRANSMISSION OF DIGITAL INFORMATION WITH FEEDBACK

This study was completed by M. Horstein and was accepted by the Department of Electrical Engineering, M.I.T., as a thesis in partial fulfillment of the requirements for the degree of Doctor of Science, August 1960. This research study will also be published as Technical Report 375.

P. Elias

3. SEQUENTIAL ENCODING AND DECODING FOR THE DISCRETE MEMORYLESS CHANNEL

This research was completed by B. Reiffen. The results were accepted as a thesis in partial fulfillment of the requirements for the degree of Doctor of Science, Department of Electrical Engineering, M.I.T., August 1960. This study will be published as a joint technical report with Lincoln Laboratory, M.I.T. (Research Laboratory of Electronics Technical Report 374, Lincoln Laboratory Technical Report 231).

P. Elias

*This work was supported in part by Purchase Order DDL B-00306 with Lincoln Laboratory, a center for research operated by Massachusetts Institute of Technology with the joint support of the U.S. Army, Navy, and Air Force under Air Force Contract AF19(604)-5200.

XIII. PHYSICAL ACOUSTICS*

Prof. U. Ingard
Prof. R. D. Fay
L. W. Dean III
G. C. Maling, Jr.
H. L. Willke, Jr.

A. DISTORTION OF LARGE-AMPLITUDE SOUND WAVES IN LIQUID HELIUM

Recent measurements indicate that nonlinear mixing effects become significant in the normal reflection of large-amplitude acoustic wave trains in liquid helium at an acoustic level that is approximately 10 times higher than that previously suspected.

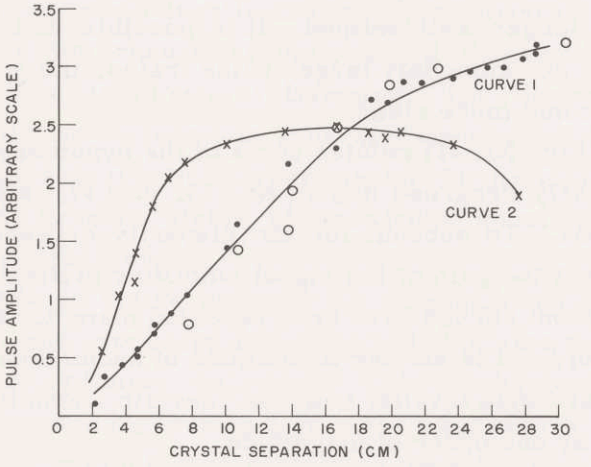

Fig. XIII-1. Amplitude of second harmonic in wave train plotted against separation distance between source and pickup transducers. T = 1.9°K; voltage on source transducer, 8 volts rms.

Curve 1 of Fig. XIII-1 shows the amplitude of the second harmonic in a wave train as a function of distance of travel from the source transducer; at the transducer, the wave is constrained to be sinusoidal. The source is driven with an 8-volt rms signal, at 1 mc/sec.

After being reflected from the pickup crystal, and again from the source, the wave train arrives a second time at the pickup crystal. The amplitude of the wave at its second reflection is shown by curve 2 of Fig. XIII-1.

If the nonlinear effects of the reflection of the wave are truly negligible, it should be possible to bring the two waves into coincidence after allowance is made, in the case of curve 2, for ordinary reflection losses. In Fig. XIII-1, the large circles represent

*This research was supported in part by the U. S. Navy (Office of Naval Research) under Contract Nonr-1841(42). Reproduction in whole or in part is permitted for any purpose of the United States Government.

curve 2 after it has been expanded three times horizontally (since the actual acoustic path is three times that of curve 1), and has been adjusted vertically by a factor of 1.37.

The set of circles, within its larger range of scatter, may be said to agree with curve 1. Of course, the correctness of the scaling factor of 1.37 should be checked by measuring the third return of the pulse to the pickup transducer and comparing it with the first two curves. Then a vertical scaling factor of $(1.37)^2$ and a horizontal factor of 5 should be applied.

When the input voltage to the source transducer is increased to 80 volts rms, the wave envelope becomes so seriously distorted under the conditions of reflection that the wave amplitude is no longer well defined. It is possible that, when the experimental apparatus is altered to accommodate larger pulse trains, the structure of the distorted wave envelope will become more clear.

The present data (Fig. XIII-1) refutes some of the hypotheses derived from the data of Fig. XII-1 of Quarterly Progress Report No. 55, p. 139, which represents similar experimental conditions. To account for the disparity between the two figures, it is sufficient to assume that the gain of the signal amplifier drifted during the taking of the earlier data. The present curves have been repeated many times, and may be assumed to be free of such errors. The earlier indications of anomalous reflection at relatively low source strengths are thus invalid; however, certain anomalies are noted when the strength is increased by one order of magnitude.

H. L. Willke, Jr.

XIV. SPEECH COMMUNICATION*

Prof. M. Halle
Prof. K. N. Stevens
Prof. J. B. Dennis
Dr. A. S. House
Dr. G. Rosen
Dr. T. T. Sandel
Dr. W. S-Y. Wang
Jane B. Arnold
P. T. Brady
J. R. Carbonell
M. F. Dichter
O. Fujimura†
H. Fujisaki
M. H. L. Hecker
J. M. Heinz

A. BINAURAL HEARING: A TENTATIVE MODEL AND SOME RELATED EXPERIMENTS

In this study we have proposed a model that attempts to explain certain aspects of binaural hearing, such as sound localization and the binaural threshold shift (BTS). The BTS is defined as the change in the masked threshold of signals through binaural listening relative to monaural listening. The theoretical performance of the model is in qualitative agreement with the results of the classical, as well as the most recent psychoacoustic, experiments; furthermore, the model attempts to take into account the present status of knowledge about the ear and the nervous system at its different levels.

The model postulates an active process. It is assumed not only that the signals arriving at the two ears are processed and combined, but also that there is an adjusting mechanism that tends to optimize the result. This mechanism consists of adjustable transfer functions and switching devices controlled by means of feedback loops. In the model, sound localization is at a higher stage than the BTS, and localization judgments are made through a measure of the "effort" required to optimize the output to higher levels. It is recognized that the auditory signals do not arrive at the brain as replicas of complex audio waveforms; on the contrary, they are transformed, analyzed in the frequency domain, and finally pulse-coded when transmitted through neural paths. Furthermore, the idea that our brain behaves like a biological computer and the necessity for considering that any combination and processing of the signals arriving at the brain from both ears must deal with pulse-coded signals both lead to the conclusion that a switching logical process provides a much more satisfactory explanation than mathematical models based on crosscorrelation provide.

Some complementary and exploratory experiments were also performed. They were concerned with the influence of different factors, especially the space configuration, on the intelligibility of speech masked by a babble of four voices and with the masked threshold of lowpass-filtered bursts of noise in the presence of white noise.

---

*This research was supported in part by the U.S. Air Force (Air Force Cambridge Research Center, Air Research and Development Command) under Contract AF19(604)-6102; and in part by National Science Foundation.

†On leave from the Research Institute of Communication Science, University of Electro-Communications, Tokyo, Japan.

This report is an abstract of a thesis with the same title accepted by the Department of Electrical Engineering, M. I. T., September 1960, in partial fulfillment of the requirements for the degree of Master of Science.

J. R. Carbonell

B. PERCEPTION OF SOUNDS GENERATED BY TIME-VARIANT CIRCUITS

In the previous report (1) we described an experiment in which subjects were required to compare certain types of sounds that are generated by periodic pulsed excitation of a time-variant resonant circuit. The test stimulus was the output of the resonator when pulsed a fixed number of times; as the pulses were applied, the center frequency of the resonator moved linearly between two limits. Whenever the subject wished, he could hear a stimulus identical to the test stimulus, except that its resonant frequency remained stationary during the time of presentation. He could set this stationary frequency over a range of values by means of a continuously variable potentiometer, and his task was to make the comparison stimulus and test stimulus sound as nearly alike as possible. The results showed that for stimuli of 20-50 msec duration

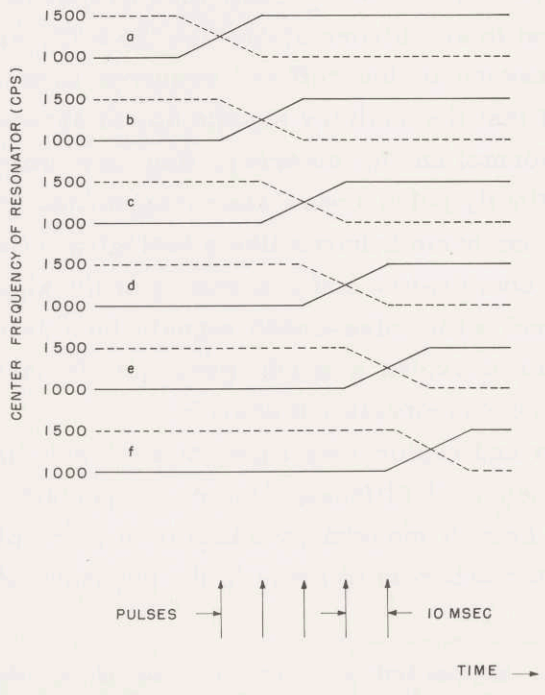

Fig. XIV-1. Stimuli used in the first test. The solid lines are paths of the resonator center frequency for rising resonances, the broken lines, for falling resonances. The five pulses used for each stimulus are shown at the base.

the matching was always made at a frequency that is very close to the final value of the frequency of the test stimulus (the last instantaneous frequency that the subject heard).

The initial experiment has been extended to include test stimuli similar to those described above, but with the difference that the time-variant portion was preceded or followed by a short interval in which the resonant frequency was stationary. The objective was to determine whether or not an initial stationary segment that preceded the time-variant segment would cause the subject to make judgments that were not in the region of the final frequency. In the first test, the resonator frequency was set to move from 1000 cps (f_1) to 1500 cps (f_2), or the reverse, from 1500 to 1000 cps. The transition was accomplished in 20 msec, and the resonant frequency was stationary before and after the transition. The resonator was pulsed five times at a rate of 100 pps, and consequently some of the pulses excited the resonator while it was stationary. The six stimuli used for rising resonances, represented by the solid lines of Fig. XIV-1, were characterized by six different starting times for the transition. The pulses are shown at the base of the figure. The first pulse of stimulus a occurs at f = 1250 cps; the rest occur at f = 1500 cps. In d, the third and fourth pulses excite the resonator while it is moving. Six other stimuli, shown by the broken lines in Fig. XIV-1, were used for the "falling-resonance" case. In a single test, each of the 12 stimuli was presented to a subject, and he was instructed to match each one with the comparison (steady-resonance) sound. The frequencies of the comparison stimuli were recorded. Each of the three subjects heard the test 12 times – a total of 36 presentations of a given stimulus to all subjects. The order of stimulus presentation was changed from test to test, with the result that any given stimulus was placed before and also after every other stimulus. The results are displayed in Fig. XIV-2. The solid lines indicate the mean values for the 36 decisions for the comparison frequency. The vertical bars indicate standard deviations in cycles per second.

Stimuli with time-variant portions of several durations were studied in a second test. The 10 stimuli used for this test are shown in Fig. XIV-3. As before, the times at which the pulses occur are indicated at the base of the figure. The significant difference between this test and the first one is that now the frequency ramps are of varying duration, with the result that they all terminate at f_2 at time 10 msec after the last pulse. (See reference 1 for details of stimulus generation, especially resonator decay rate.) Each of the three subjects made 10 matchings for each of the stimuli – a total of 30 presentations of each stimulus to all subjects. The results are displayed in Fig. XIV-4 and are interpreted in precisely the same way as those of Fig. XIV-2.

On the basis of these tests, the following observations can be made.

(i) When a subject is asked to match a sound that is characterized by a time-variant resonance with a sound that has a steady resonance, he has a strong tendency to set the steady resonance at a point corresponding to the final resonant frequency of

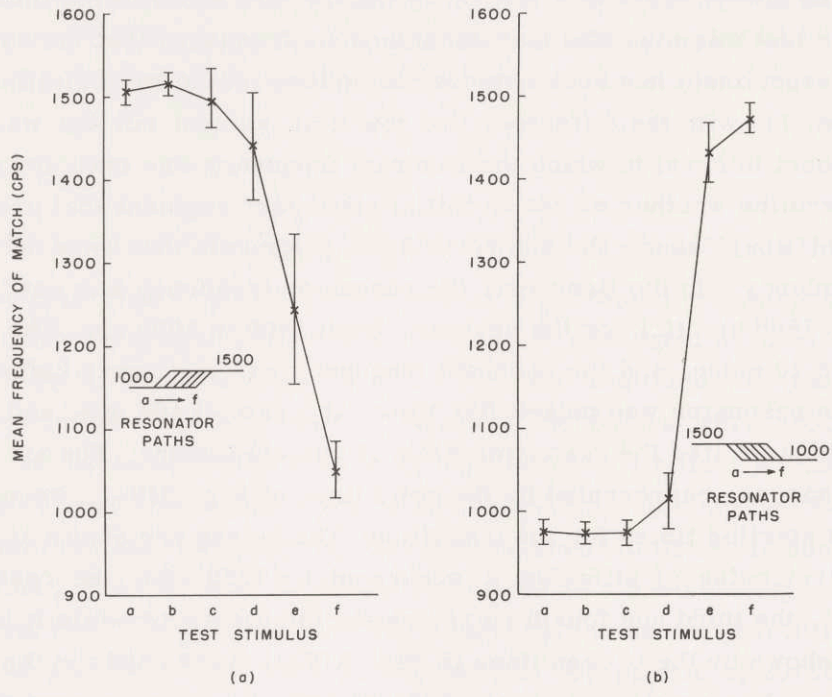

Fig. XIV-2. Results from the first test. (a) Rising resonances. (b) Falling resonances. Mean values of all the subjects' decisions, as well as the standard deviations, are plotted. Also shown is a compact display of resonator paths.

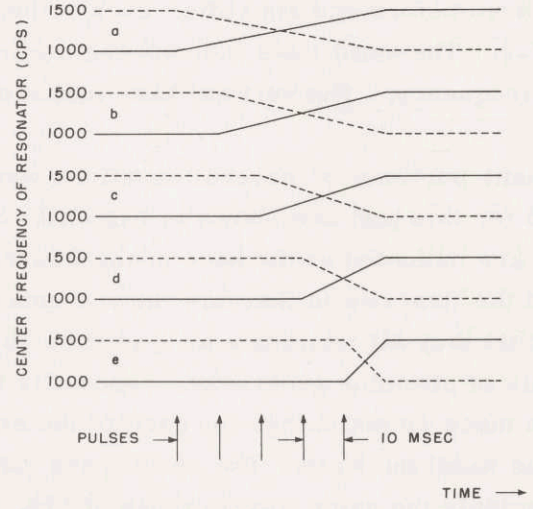

Fig. XIV-3. Stimuli used in second test. (Graphical details are the same as in Fig. XIV-1.)

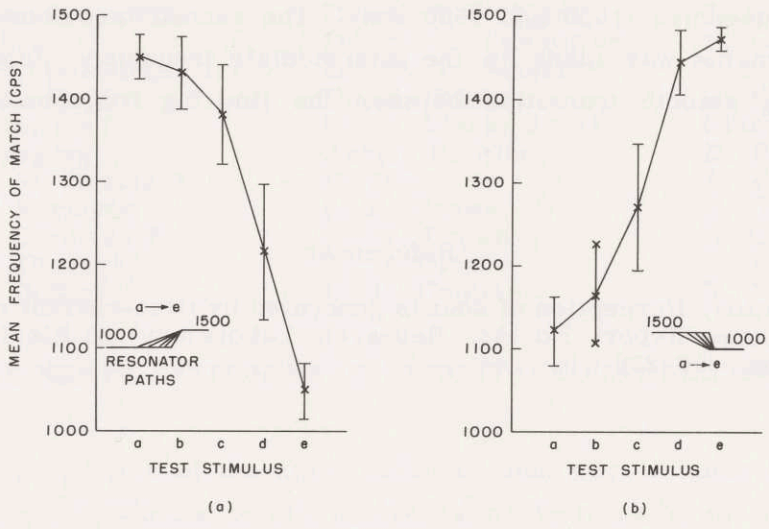

Fig. XIV-4. Results from the second test. (a) Rising resonances. (b) Falling resonances. (Graphical details are the same as in Fig. XIV-2.)

the variant-resonance sound. This effect is quite pronounced if the transition occurs near the beginning of the sound (stimuli a and b of Fig. XIV-2a and 2b), or if the transition occupies the greater part of the sound (stimuli a and b of Fig. XIV-4a and 4b). It is possible, however, with proper adjustment of the stimulus, to cause the subject to make his judgment at a frequency other than the end frequency.

(ii) The tendency to match to the end frequency is stronger for stimuli for which the resonant frequency ascends. Consider Fig. XIV-2a, stimulus f, in which the transition occurs at the very end of the sound. The subject makes a judgment at 1050 cps. With the transition occurring only 10 msec earlier, as in e, the subject has already made his judgment at a higher frequency, that is, at 1245 cps. At e in Fig. XIV-2b, the subject still has not changed his judgment to frequencies lower than the upper frequency and is still matching as if he considered the beginning portion of the sound as "most important."

(iii) The standard deviations are greater for stimuli for which matches were made at points in the intermediate frequency range between 1200 and 1300 cps. The subjects reported, on occasion, that these judgments were "harder." Therefore, we could conclude that in these cases the subjects were less sure of their answers.

(iv) The sensitivity to small (10-msec) changes in the timing of the beginnings of the ramps is quite high, especially in the test illustrated by Fig. XIV-2b. The matching frequency changes from 1015 to 4030 cps when we examine cases d and e, which differ by only a 10-msec change in the time of the onset of the ramp.

(v) A comparison of the two tests (Figs. XIV-2 and XIV-4) indicates that in the first test the subjects showed little tendency to set the matching frequency at points between

the two end frequencies (1000 and 1500 cps). The second test shows that a greater number of judgments was made in the intermediate frequency range; in fact, there is a reasonably smooth transition between the limiting frequencies as the stimulus is changed.

P. T. Brady

References

1. P. T. Brady, Perception of sounds generated by time-variant resonant circuits, Quarterly Progress Report No. 58, Research Laboratory of Electronics, M. I. T., July 15, 1960, pp. 218-220.

XV. COMMUNICATIONS BIOPHYSICS*

Prof. W. A. Rosenblith
Prof. M. Eden
Prof. M. H. Goldstein, Jr.
Prof. W. T. Peake
Dr. J. S. Barlow†
Dr. Eda Berger‡
Dr. M. A. B. Brazier†
Dr. B. G. Farley**
Dr. G. L. Gerstein††
Dr. E. M. Glaser‡‡
Dr. F. B. Goffin††
Dr. N. Y-S. Kiang
Dr. N. M. Onesto***
Dr. T. T. Sandel**
Dr. A. Yildiz
W. A. Clark, Jr.**
Aurice V. Albert
H. Blatt
J. E. Brown
R. M. Brown
A. H. Crist
C. D. Geisler
J. L. Hall II
P. Latour†††
S. L. Levine
C. E. Molnar
Clare Monck
D. F. O'Brien
A. P. Paul
C. C. Robinson
G. C. Vineyard
R. F. Webber
T. F. Weiss

A. PERIPHERAL NERVE RESPONSES TO PERCUTANEOUS ELECTRIC STIMULATION IN MAN

Some of the properties of the ulnar nerve in man were studied in experiments involving percutaneous stimulation of a peripheral nerve trunk by square pulses of current and percutaneous recording of the summated action potential by means of a gross electrode. Certain characteristics of these neural responses to single shocks and pairs of shock stimuli were determined (1).

Placing stainless-steel electrodes at the wrist and elbow (where the nerve is superficial) permits percutaneous stimulation and recording from the ulnar nerve in man (2). The skin under the electrodes was prepared to yield a minimal skin resistance. The subject was asked to relax his arm by minimizing his own electromyographic activity which was displayed to him at intervals throughout the recording session. The stimuli were square pulses of current, isolated from ground, of fixed duration (0.5 msec) and variable amplitude. The responses were recorded by a Grass Kymograph camera, and data reduction was achieved by an analog-to-digital device that produced punched cards which, in turn, were processed by an IBM 704 computer.

If a series of stimuli of increasing magnitude is presented, responses such as those shown in Fig. XV-1 are elicited. The responses are triphasic compound action potentials. Their amplitude increases and the latency of the "peak" of the response decreases slightly (from 7.7 msec to 7.3 msec in one subject) with increasing stimulus intensity.

---

*This work was supported in part by the U.S. Air Force under Contract AF19(604)-4112.

†Research Associate in Communication Sciences from the Neurophysiological Laboratory of the Neurology Service of the Massachusetts General Hospital.

‡Postdoctoral Fellow of the National Institute of Mental Health.

**Staff Member, Lincoln Laboratory, M.I.T.

††Postdoctoral Fellow of the National Institute of Neurological Diseases and Blindness.

‡‡Guest of the Research Laboratory of Electronics, from Johns Hopkins University.

***Research Associate in Communication Sciences and Fellow in the School for Advanced Study, M.I.T.

†††On leave from the Instituut voor Zintuigfysiologie RVO-TNO, Soesterberg, Netherlands.

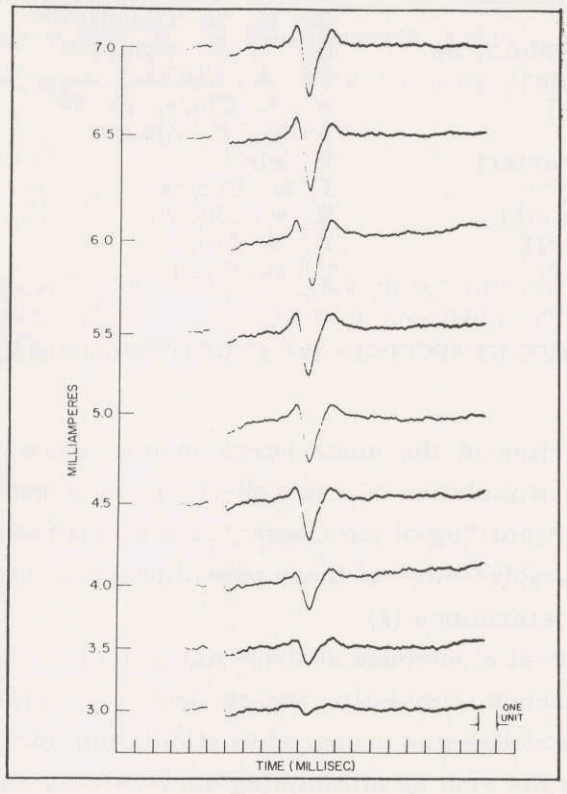

Fig. XV-1. Responses to square-pulse stimuli. The abscissa indicates time; numbers along the ordinate indicate the magnitude of the stimulus. (Session 11-23; Subject J. W.)

Since these responses show little "desynchronization" with increasing stimulus intensity, we can conclude that the response arises from the summation of action potentials of neural units, all of which exhibit nearly the same conduction velocity.

The functional dependence of the amplitude of the response on stimulus intensity is displayed by the so-called intensity function (Fig. XV-2). The intensity functions for all subjects were multilimbed, sometimes showing two limbs, sometimes as in Fig. XV-2, three. The amplitude of the response depends not only on the intensity of the stimulus delivered to the skin but also upon the placement of the stimulating electrode relative to the nerve at the wrist, and upon the impedance of the skin. Since the last two factors differ from session to session, data from different sessions cannot be compared in absolute values.

Moreover, the characteristics of an electrode may change within a single experimental session, and this change may produce rather large changes in the magnitude of the response for a given value of stimulus intensity (1). In Fig. XV-3, four sets of 100 responses each were taken for different electrode "positions." The electrode was

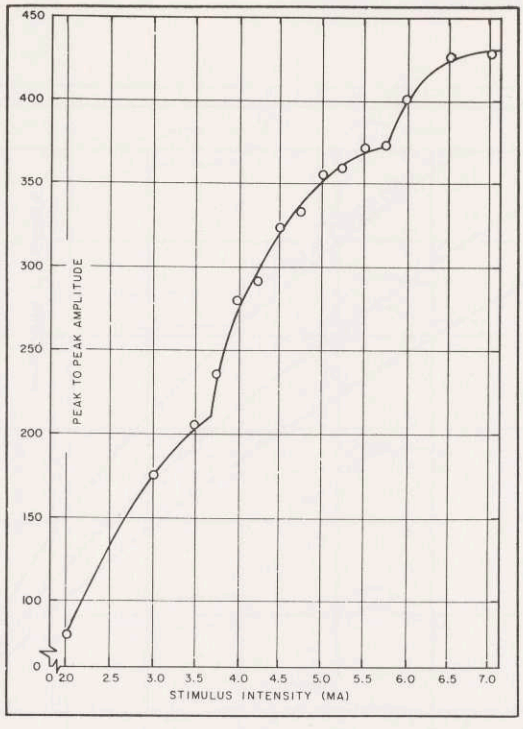

Fig. XV-2. Intensity function; the functional relationship between peak-to-peak amplitude of the response and stimulus intensity. Each point is the mean peak-to-peak amplitude of 40 responses. Stimulus intensity is plotted along the abscissa; the peak-to-peak amplitude (arbitrary units) is plotted along the ordinate. (Session 10-1; Subject N. L.)

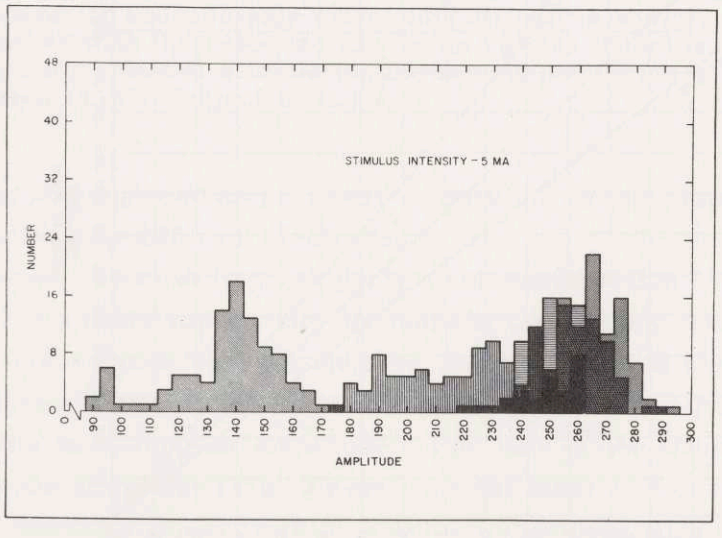

Fig. XV-3. Distribution of response amplitude for four electrode positions. Each shaded region represents 100 responses for different electrode positions. The electrode position strongly affects the mean value for each group of 100 responses. (Session 11-24; Subject G. M.)

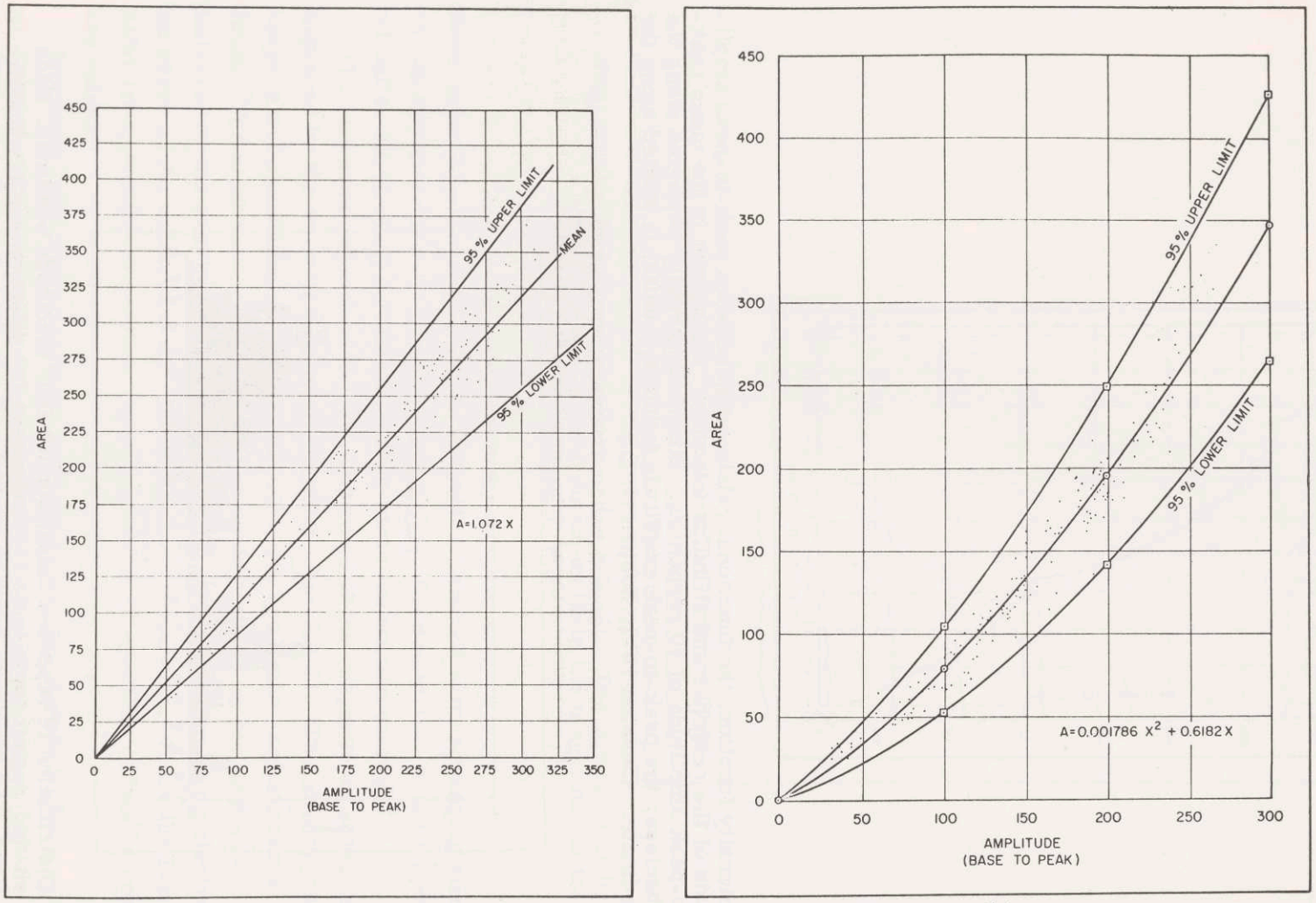

Fig. XV-4. Area under a response versus base-to-peak amplitude. The linear regression of the data yielded: (a) line of best fit, A = 1.072 X. (Session 10-20; Subject J. W.); (b) curve of best fit that was quadratic, A = 0.001786 X^2 + 0.6182 X. Note that these data demonstrate a desynchronizing of the gross response as the intensity is increased. (Session 9-4; Subject G. M.)

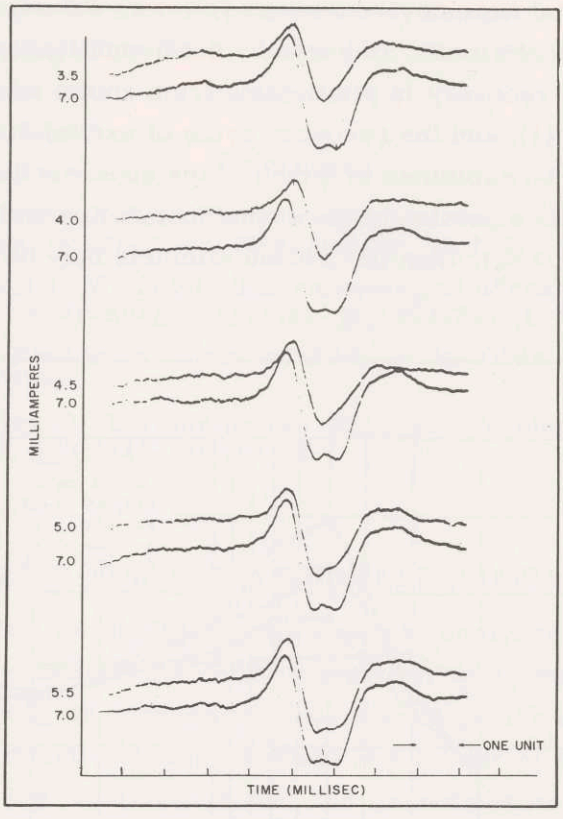

Fig. XV-5. Responses to square-pulse stimuli. The abscissa indicates time; numbers along the ordinate indicate the magnitude of the stimulus. The series of responses to successively increasing stimuli is shown, with each response compared with the response to a large (7-ma) stimulus. Notice the desynchronizing effect of stimulating the second population of neural structures. (Session 11-23; Subject K. K.)

removed each time and replaced as precisely as possible on the same spot; this procedure produced functionally different electrodes.

Since the observed response is presumably a summated action potential, the "area under a response" is a more appropriate measure of the activity than is the peak-to-peak amplitude. The relation between the area under a response and its base-to-peak amplitude was determined and is shown in Fig. XV-4; the base-to-peak amplitude is linearly related to the peak-to-peak amplitude. For half of the subjects, this area is linearly related to the amplitude (Fig. XV-4a); but the other half of the subjects showed a significant deviation from linearity (Fig. XV-4b). This departure from linearity may be attributable to the desynchronization of the response waveform which occurs in these subjects at higher stimulus intensities, as shown in Fig. XV-5.

If two square pulses of current separated by a short time interval are presented as stimuli, the response to the second stimulus shows a "recovery of responsiveness"

(Fig. XV-6) whose typical time course runs as follows: Subnormality from 0 to 3 msec; supernormality from 4 to 15 msec, followed by subnormality from 15 msec to 100 msec. This time course of the recovery is predictable from known properties of axons, such as threshold variability (3), and the recovery cycle of excitability (4). The supernormality that is observed can be explained in terms of the superexcitability of single axons. If the first stimulus excites a portion of the axonal population and the second stimulus is weaker than the first ($S_1 > S_2$), then the second stimulus may be presented to a population

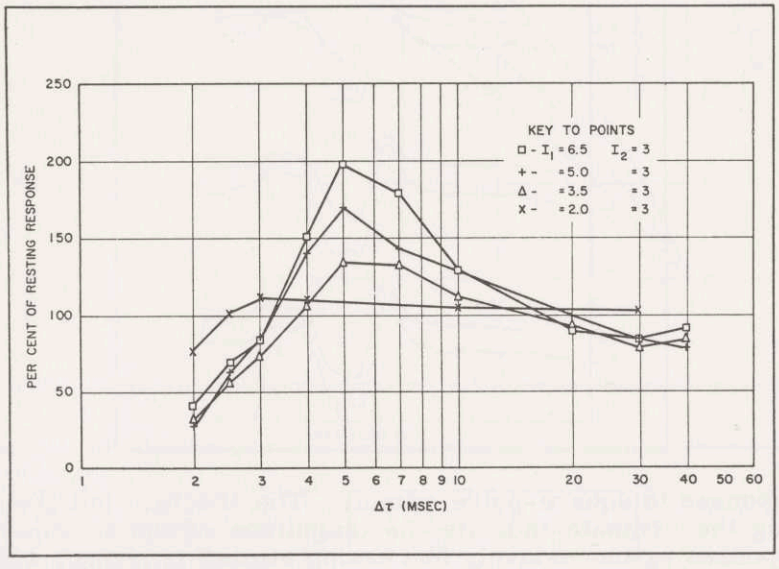

Fig. XV-6. Recovery of responsiveness. The relative amplitude (as a percentage of the resting response) is plotted along the ordinate; the numbers along the abscissa represent time separation, $\Delta\tau$, between conditioning and testing stimulus. Each point is the mean of 20, or more, responses. The recovery curves are parametric in I_1, with I_2 held constant. The larger I_1 was made, the larger the supernormality became. (Session 10-27; Subject N. L.)

of superexcitable axons, provided that the time interval between the stimuli is correctly chosen. Hence, S_2 will fire more axons in the superexcitable population than if it had been presented in isolation. This situation may explain the supernormality seen in Fig. XV-6. If both stimuli of the pair are equal, that is, $S_1 = S_2$, the response to S_2 may be expected to be slightly supernormal; units that have been rendered superexcitable by S_1 will be refired by S_2, and some of the units that had a threshold that was too high at the instant of S_1 presentation will have undergone spontaneous threshold changes that will allow them to be fired by S_2. Similar reasoning may be applied for the interval for which there is subnormality.

The experimental work for the writer's thesis (1) was performed in the IBM Research Center, Yorktown Heights, New York, under the direction of Dr. W. R. Uttal.

J. E. Brown

References

1. J. E. Brown, A Parametric Study of Neuroelectric Responses to Skin Stimuli, S. M. Thesis, Department of Electrical Engineering, M. I. T., 1960.

2. G. D. Dawson and J. W. Scott, The recording of nerve action potentials through skin in man, J. Neurol. Neurosurg. Psychiat. 12, 259-267 (1949).

3. C. Pecher, La fluctuation d'excitabilité de la fibre nerveuse, Arch. Int. Physiol. 49, 129-152 (1939).

4. H. T. Graham and R. Lorente de Nó, Recovery of blood perfused mammalian nerves, Am. J. Physiol. 123, 326-340 (1938).

B. SPECTRAL ANALYZER FOR ELECTROENCEPHALOGRAPHY*

This report describes an analog-digital spectral analyzer constructed entirely of commercially available instruments. The component instruments are all of general laboratory usefulness; plug-in connections hook them together to form the spectral analyzer which can be assembled and disassembled in a matter of minutes.

A requirement for the analyzer is that the potentials to be processed must be recorded on magnetic tape so that they can be replayed repeatedly. The elements and the instruments used in our analyzer are: magnetic tape recorder and reproducer system (Ampex Recorder/Reproducer FR-1107); variable electronic filter (Spencer-Kennedy Laboratories Variable Electronic Filter Model 302); squaring circuit (Ballantine True Root Mean Square Electronic Voltmeter Model 320); frequency modulator (FM units of the Ampex recorder); and electronic counter (Beckman/Berkeley Universal EPUT and Timer). A calibrated potentiometer was placed at the output of the electronic filter and was used in conjunction with the voltage range switch on the voltmeter to keep the input to the squaring circuit of the Ballantine voltmeter in the proper range. In each case there are instruments of other manufacturers that would serve as well as the ones we used. The component parts are assembled as shown in Fig. XV-7.

Spectral analysis is accomplished by measuring the energy in the filtered waveform for different settings of the filter. The procedure for measuring energy is as follows:

(i) The section of tape to be processed is replayed by the recorder.

(ii) The counter is set to zero at the start of the record and read at the end. (The

*This work was sponsored jointly by the U. S. Air Force Office of Scientific Research, Air Research and Development Command, through its European Office, under Contract AF 61 (052)-107 and by the Rockefeller Foundation.

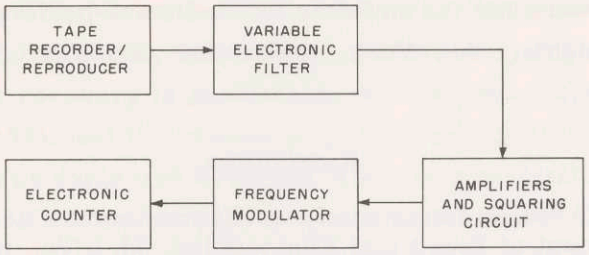

Fig. XV-7. Block diagram of the spectral analyzer.

Berkeley counter has a mode of operation "scan" in which it counts the number of events (cycles) in a length of time that is an integral number of seconds or tens of seconds. This mode is useful for "push-button" operation of the analyzer. The counter may also be arranged to count events in the time interval between stop and start pulses obtained from markers on the tape, or on a tape loop.)

(iii) A short circuit is placed on the input to the electronic filter and the counter is run for the same time interval as in the previous step.

(iv) The difference between the readings in steps (ii) and (iii) is proportional to the energy in the filtered signal.

Calibration in terms of mean-square voltage or rms voltage is obtained by recording a calibration signal on the tape and processing it.

The type and resolution of the spectral analysis depend on the way in which the electronic filters are used. EEG signals with a large part of their spectral content below 10 cps and very little above 100 cps are not adapted to direct analysis by commercial filters which have a higher frequency range. It is necessary, and convenient, to play back the EEG signals at a speed higher than that used in recording and thus to shift the frequency range proportionally higher. This also speeds up the analysis. We have obtained estimates of the power spectrum of EEG signals by analyzing them with low-pass filtering. The record is replayed for a number of settings of the filters. The resolution of the method is indicated in Fig. XV-8 in which the analysis was performed on a sinusoid. Of course, higher resolution (a more sudden step in the curve) is obtainable by cascading a number of filter sections.

If a measure of power spectral density rather than spectrum is desired it can be obtained by taking differences of points in the spectral plot, or directly, by using the filters in a bandpass configuration.

The analysis is now being applied to recordings from the cortex of chronic and acute preparations under differing physiological conditions. Figure XV-9 gives spectral plots from a chronic cat, asleep and awake. The record from the sleeping cat showed much "synchronized spindle activity," while the record during arousal would be characterized as "fast desynchronized activity." Note the greater proportion of power below 10 cps

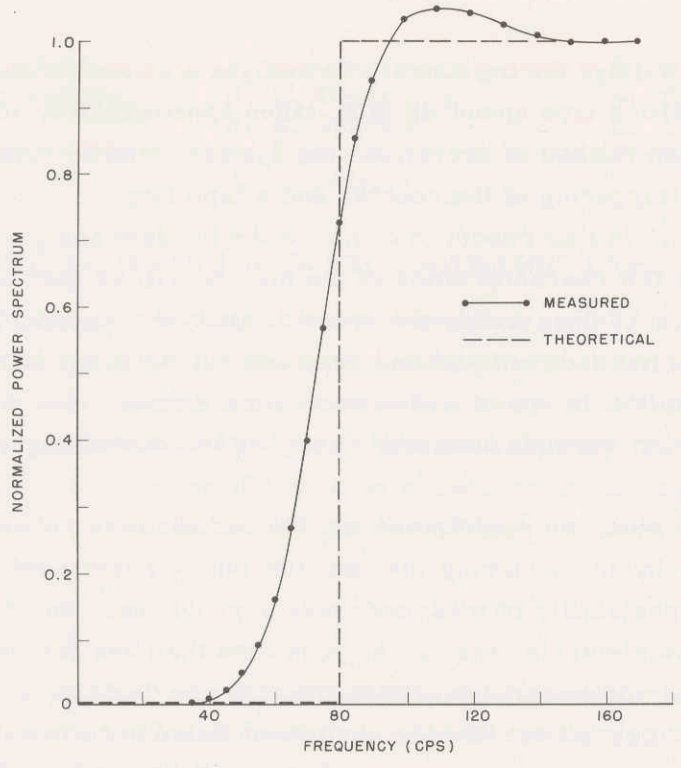

Fig. XV-8. Measured and theoretical power spectra of an 80-cps sinusoid. One section of the Spencer-Kennedy Laboratories filter, which gives an attenuation of 18 db per octave above cutoff frequency, was used.

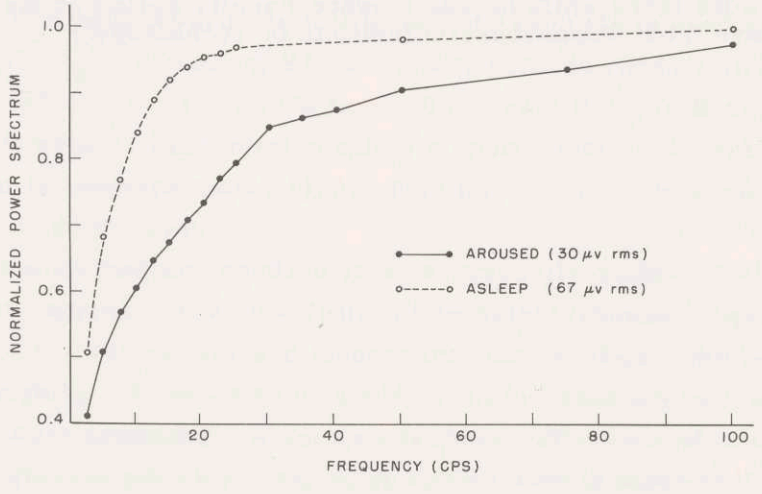

Fig. XV-9. Examples of spectral analysis. The analyzer was used to measure power spectrum and rms voltage of EEG from a chronic preparation. These potentials were recorded with electrodes on the dura of the frontal and temporal regions of the same side. The lengths of the records analyzed were: 160 sec, arousal; 240 sec, asleep.

and the higher rms voltage during sleep. To analyze a record of approximately four minutes duration, with a tape speed-up of 8, takes approximately 30 minutes. This time is for the push-button method of operation; the system could be considerably speeded up by using automatic triggering of the counter and a tape loop.

We cannot attempt in this report to compare the present analyzer with other EEG analyzers; however, a few characteristics of the method will be mentioned. By integrating over the entire length of the record, the spectral analyzer measures long-term characteristics of the EEG but does not pick out separate events in the course of the recording. Thus, the implicit model is one of a stationary time series. How well this model fits the experimental situation depends upon one's success in maintaining the preparation in a "steady state."

On the practical side, we might point out that the absolute accuracy of the analyzer is largely determined by the squaring circuit; for our arrangement it is approximately 5 per cent. The repeatability of measurements depends upon the drift in the frequency modulator and active elements; the variation is less than one per cent. The digital output is convenient for work when quantitative results are desired.

It should also be pointed out that the equipment listed here is quite costly and not standard in most EEG laboratories. An analyzer of the type described could be constructed at a cost far below the total cost of the instruments that we have employed.

M. H. Goldstein, Jr., L. Nicotra

(Dr. Leopoldo Nicotra is at the Istituto di Fisiologia, Università di Pisa. Dr. Goldstein carried out this work there while he was Science Faculty Fellow of the National Science Foundation on leave from Massachusetts Institute of Technology.)

XVI. NEUROPHYSIOLOGY*

W. S. McCulloch
H. J. C. Berendsen
M. Blum
J. D. Cowan
J. R. Cronly-Dillon
R. C. Gesteland
A. R. Johnson
P. Lele
J. Y. Lettvin
W. H. Pitts
A. Taub
L. A. M. Verbeek
P. D. Wall

A. ELECTROCHEMICAL METHODS IN HYDRODYNAMIC EXPERIMENTS

In the course of trying to develop an electrochemical model for olfactory stimulation, we have happened upon a number of electrochemical effects associated with fluid motion past electrodes. Certain of these were remarkable enough that, instead of taking measures to eliminate them, as is usually done in electrochemistry, we thought it worth while to try using these effects to make the motion visible or to measure fields of flow in experimental hydrodynamics. We have a number of such methods, of which the following seem to hold promise.

1. Electrochemiluminescence

In Quarterly Progress Reports Nos. 57 and 58 we showed that the bright glow produced at a platinum anode hydrofoil immersed in an aqueous alkaline solution of luminol (5-amino-2, 3-dihydro-1, 4-phthalazinedione, which is more likely to exist as 5-amino-3, 10-dihydroxy phthalazine) and H_2O_2 afforded a clear, detailed picture of the turbulent boundary layer about the hydrofoil. During the past few months we extended the scope and usefulness of the methods considerably.

In the first place, the phenomenon occurs in methanol as well as in water, provided that tetramethylammonium hydroxide in appropriate amounts is used as a base in place of NaOH, that $N(CH_3)_4Cl$ instead of KCl is used to provide conductivity, and that a solution of H_2O_2 in methanol is used (made from 30 per cent H_2O_2 in H_2O, thus introducing a small amount of water). This solution exhibits approximately the same pH as the purely aqueous one, that is, approximately 11.5. This measurement is made by diluting the methanolic solution with water.

However, if the methanolic solution is now gradually acidified with glacial acetic acid, novel effects appear. The glow from the turbulent boundary layer immediately next to the electrode dims rapidly and disappears, but the fluid wake behind the electrode begins to glow brightly. As more acid is added, an increasingly long section of the trailing fluid becomes luminous. When approximately 20-40 cm of it are visible, it has the maximum brightness per unit area; when the solution is made still more acid, the visible part of the trail continues to lengthen, up to a total distance of 3-4 meters

*This work was supported in part by Bell Telephone Laboratories, Incorporated; National Institutes of Health; and Teagle Foundation, Incorporated.

(a) (b)

Fig. XVI-1. Von Kármán vortex street resulting from circular flow past a cylindrical platinum anode. (a) Reynolds number, 90; (b) Reynolds number, 100.

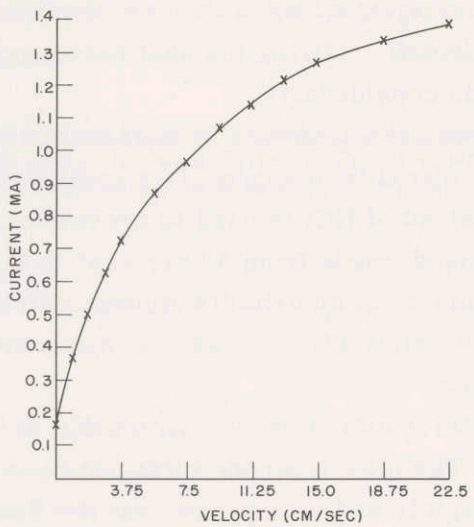

Fig. XVI-2. Values of electrode current at a constant potential for several rates of steady flow. The electrode is a platinum wire, 1-cm long and 0.5 mm in diameter, which is immersed in 1 N aqueous solution of KCl with 0.015 per cent H_2O_2 added.

at least, but the brightness decreases. Even at the acid extreme, the trail is still visible, and the solution (which is of course well buffered) shows, after dilution with water, a pH of approximately 5.3. This luminous wake can be seen to consist of fluid that has passed through the boundary layer immediately next to the anodal electrode itself. Figures XVI-1a and XVI-1b, which were obtained with a moderately acid solution, show a classical von Kármán vortex street, with the lines of flow from the boundary layer of a smooth platinum cylinder passing between the alternate members of the double row of vortices. The separation of the two rows is probably caused by the centrifugal currents set up in our system. The hydrofoil is placed in a rotating bath in order to avoid the complexities of constructing a linear flow chamber. This is arranged in such a way that both the hydrofoil and the bath can be rotated at different speeds around a common center; with this arrangement the trail can be held fixed with respect to the camera.

The series of changes that occur with increasing acidity is quite reversible. If $N(CH_3)_4OH$ is added gradually to the acidified solution, the luminous trails become shorter until, finally, the turbulent boundary layer at the electrode is again the only thing that glows. The shortening and lengthening process can be repeated any number of times.

It may be useful to include a recipe for making a solution that shows all of these effects, although the quantities given do not necessarily produce maximum brightness or the fastest pulse response: To a methanolic solution of 1/2 N tetramethylammonium chloride, add 100 mg/liter of luminol and 10 ml/liter of 3 per cent hydrogen peroxide in methanol (the 3 per cent solution is prepared from 30 per cent H_2O_2 in H_2O, diluted with methanol).

If 250 ml of this solution are used and $N(CH_3)_4OH$, which is 1 N in methanol, is added slowly, we find the effects shown in Table XVI-1. (The length of the visible trail is estimated crudely by eye, for it fades out gradually.)

The solution now has a pH of approximately 11.5. When we added 1 N acetic acid in methanol, the results were those shown in Table XVI-2.

It should be evident that this method of visualizing flows past solid objects has particular advantages. The subsequent history of the fluid originating in the whole boundary layer or any part of it can be traced as far as desired by painting part of the electrode without disturbing the flow in the boundary layer in any way. The electrode can be made in any shape and inclined at any angle to the stream. The current can be supplied to the electrode in pulses instead of continuously. The electrochemical reaction is sufficiently rapid that pulse rates as high as several hundred per second (or even several thousand per second under some conditions) will produce discrete bursts of luminous trail. In this way, the motion and the velocities in the wake can be measured for rapidly changing unsteady flow as easily as for steady flow.

Various changes in the technique are possible, and we are engaged in testing some

Table XVI-1.

Amount of base added (ml)	Length of trails (cm)
0.33	15
1	10
2	6
4	4 (with slight glow at surface)
5.25	No trail; bright turbulent boundary layer crawling over electrode.

Table XVI-2.

Amount of acid added (ml)	Length of trails (cm)	
1.3	1.5	(surface glow gone)
4	3.5	
6.6	10	
8	15	
10	21	trail very bright
12.5	28	trail very bright
14	30	trail very bright
15.5	56	intensity diminishing
17	91	intensity diminishing
18.5	140	intensity diminishing
22.4	245	intensity diminishing
26.3	300-400	intensity diminishing

of them. The system can be used with other organic solvents, particularly those that have kinematic viscosities widely different from water or methanol. Such solvents have Reynolds numbers (and therefore equivalent free-stream velocities) that are very different from that for water for the same actual system velocity. A decrease in the effective Reynolds number can be obtained easily. The luminol-in-water system described in Quarterly Progress Report No. 57 can be prepared by using almost any ratio of water to glycerol. But some solvents should cause a substantial change in the reverse direction. Thus, liquid sulfur dioxide would yield a Reynolds number 3.34 times larger than an aqueous solution moving at the same speed, and liquid ammonia would multiply the Reynolds number by 3.03. It seems likely that the reaction should function in such solvents (possibly with minor chemical changes). The system operates quite well at -50°C in methanol. Sulfur dioxide and ammonia would not be difficult to handle in a linear flow system, since they are both standard refrigerants. Liquid hydrogen cyanide also has a most favorable viscosity factor. Of the ordinary solvents, the most promising seem to be diethyl ether, which increases the Reynolds number by a factor of 2.7 over that for H_2O, and acetone, which increases the Reynolds number by a factor of 2.4. Others can be found, but the solvents mentioned also satisfy the indispensable condition of being fairly good ionizing solvents for some salts and therefore provide the necessary conductivity. For a given Reynolds number, these solvents allow a longer photographic exposure because of lower hydrofoil velocities.

We have not yet tested the usefulness of the second famous chemiluminescent substance, lucigenin (10, 10'-dimethyl-5, 5'-bisacridinium dinitrate). When its luminescence is produced in the bulk of a solution by a chemical catalyst, the light intensity is said to be 100 times that of luminol, or more. In the literature on this subject, it has been stated (1) that the luminescence of lucigenin also can be produced electrically, but at the cathode. It is conceivable that lucigenin may provide enough additional light to reduce the sensitivity required by our photographic apparatus. This apparatus has been improved since the photographs of Fig. XVI-1 were taken; we can now photograph the structure of the flow in much greater detail. We shall try lucigenin as soon as we synthesize a reasonable supply of it. (Luminol is available commercially, but lucigenin is not; directions for making it can be found in Albert's treatise on the acridines (2).)

We have not yet made a systematic analysis of the mechanism underlying the chemiluminescence of luminol, but we have made a few incidental observations which do not seem to have been noted previously. In most of the studies of aqueous solutions containing luminol and H_2O_2, the solutions were found to be strongly fluorescent below a certain critical pH (approximately 8 or 8.5). It was found impossible to evoke the luminescence by any catalyst whatever below this pH. Above this pH, the fluorescence vanishes, and a chemical catalyst (such as NaClO, $K_4Fe(CN)_6$, and iron and copper compounds) evokes luminescence which becomes gradually brighter and attains a

maximum at pH 11.5. This fact has caused much difficulty in comparing the fluorescence and luminescence spectra – a comparison that is desirable for theoretical purposes. In our slightly alkaline and acid solutions, a chemical catalyst must evidently be generated at the electrode and pass into the luminous trail. This catalyst must differ from those used previously with luminol, since it is effective in neutral or even acid solutions of a pH as low as 5.3. This catalyst is not dissolved in Cl_2. It might be methyl hypochlorite, since hypochlorite esters are supposed to be the first product of the chlorination of alcohols. It seems volatile, because if the pH is adjusted to produce the brightest trail, we sometimes find on top of the solution a heavy vapor that causes a bright glow when it is blown back on the solution surface.

2. Measurement of the Velocity of Flow

The rate of flow of a fluid can be measured by determining the polarographic current resulting from the reduction of dissolved oxygen at a platinum cathode that is maintained at the correct potential; the faster the flow, the quicker the renewal of the depleted oxygen in the diffusion layer around the electrode, and the greater the current. The method has not been very popular, largely owing to its limited sensitivity.

It is well known that the presence of H_2O_2 produces a great increase in the rate of reduction of oxygen at such an electrode (the catalytic current). We hoped that the addition of H_2O_2 to a moving electrolyte containing dissolved O_2 would substantially augment the change in electrode current with velocity. S. J. Wiesner found at once that it did. Figure XVI-2 shows the current as a function of the velocity of the fluid. We believe that this increase in sensitivity is sufficient to render the method very practical for measuring speeds in fields of flow. We have also found that the electrode current will follow rapid periodic fluctuations in fluid velocity of 100 cps or more. This method, therefore, seems suitable for measuring large accelerations. The aqueous solution was 1 N in KCl and contained 0.015 per cent H_2O_2. Wiesner also found that the less sensitive method mentioned above (that is, the solution without H_2O_2) could be modified somewhat to determine the direction of the streamlines as well as the speed at a single point along them. His preliminary trials were encouraging. He put one electrode upstream and forced enough current through it to deplete locally the surrounding electrolyte of dissolved oxygen and then used a second electrode downstream as a probe to measure the concentration of dissolved oxygen in the ordinary polarographic way. When this electrode was placed in the wake of the first there was a sharp drop in current; in this way the wake could be traced a considerable distance downstream. If the second electrode were placed immediately behind the first electrode, it would, of course, give the local direction of the streamline. The current through the first electrode would determine the speed. Presumably the sensitivity of this method would be much greater if H_2O_2 were added.

Because Wiesner's measurements were successful when the pH of the solution was approximately 8.3, it seems likely that this method could be adapted to the measurement of ocean currents as well as fluid flow in other natural circulatory systems. Although the experimental conditions will have to be changed, a useful method should not be difficult to realize, since the polarographic reduction of oxygen is a reaction that is known to be dependable in all kinds of fluids – even biological tissue.

We are indebted to A. J. Richardson of the Aeroelastic Laboratory, M. I. T., for his continuing advice and encouragement on the hydrodynamic aspects of these experiments.

R. C. Gesteland, B. Howland, J. Y. Lettvin, W. H. Pitts, S. J. Wiesner

References

1. V. Vojiir, Chemiluminescence surrounding the dropping Hg electrode, Collection Czechoslov. Chem. Commun. 19, 862-872 (1954); in Russian.

2. A. Albert, The acridines; their preparation, physical, chemical, and biological properties and uses (E. Arnold and Co., London, 1951).

B. SERVOANALYSIS OF POSTURAL REFLEXES

This project was undertaken to determine the characteristics and approximate linear model of the peripheral self-regulating servomechanism through which voluntary movement and the maintenance of limb posture are achieved. Since the "input" to the system can be neither adequately localized nor driven, the only valid sets of measurements that can be made are the system output impedance when the internal sources are "fixed" and the noise output under the same conditions. Apparatus was devised to perform the measurements on the wrist joint in a state of flection. The subject was asked to keep his hand lined up with a pointer while his hand was being perturbed mechanically with filtered gaussian noise from a low-impedance (force source) driving mechanism. The torque and angle signals were recorded on two-track tape for subsequent data processing. In performing the required task the subject was exerting an "intention clamp" upon the environment, with the result that his internal energy sources could be assumed to be as fixed as possible. Output noise measurements were made under the same conditions, but with the hand splint swinging free; the small angular deflections were recorded.

It is theoretically possible to derive a system function from input and output data by finding, for example, the autocorrelation function of the input and the crosscorrelation function of input and output and then finding the power density spectra by Fourier transformation. The ratio of the two power density spectra becomes the frequency-domain representation of the system function. The usual problems encountered are those of sampling errors and data truncation, but an even worse difficulty presented itself here. The autocorrelation of the applied torque and the crosscorrelation of that torque with the

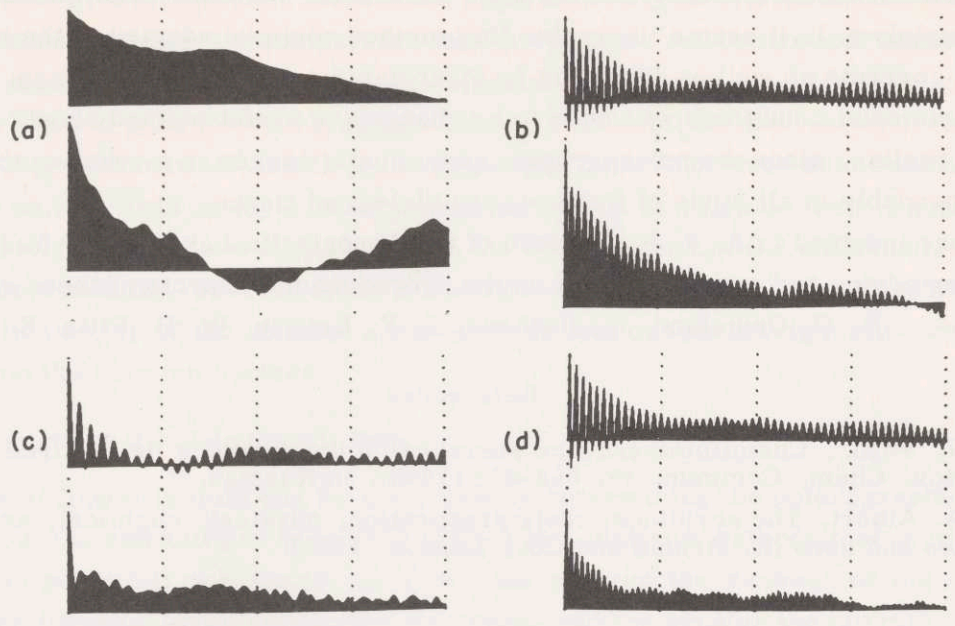

Fig. XVI-3. Autocorrelation functions of angular deflections of splint when driving torque is zero; total time shift = 8.5 sec.

(a) Top: normal subject, right hand strapped; θ_{rms} = 0.061 cm.
Bottom: normal subject, left hand free; θ_{rms} = 0.05 cm, f_{av} = 1.7 cps.

(b) Top: advanced Parkinsonism, right hand strapped; θ_{rms} = 0.172 cm, f_{av} = 6.2 cps.
Bottom: advanced Parkinsonism, right hand free; θ_{rms} = 0.236 cm, f_{av} = 6.6 cps.

(c) Top: cerebellar tremor, right hand strapped; θ_{rms} = 0.172 cm, f_{av} = 3.9 cps.
Bottom: cerebellar tremor, right hand free; θ_{rms} = 0.12 cm.

(d) Top: advanced Parkinsonism, right hand strapped (same as top of (b)).
Bottom: normal subject, voluntarily rigid, right hand strapped; θ_{rms} = 0.092 cm, f_{av} = 7.9 cps.

resulting angular deflection were practically identical; hence the transforms would differ by little more than a constant of proportionality, with the result that the impedance function amplitude spectrum would be so flat that the origin of the variations would, at best, be obscure. Consequently, computations in the time domain were performed by solving the convolution equation directly:

$$\phi_{TT}(\tau) = \int_{-\infty}^{\infty} h(t)\, \phi_{T\theta}(\tau - t)\, dt$$

where $\phi_{TT}(t)$ and $\phi_{T\theta}(t)$ are known, and we are to solve for h(t). Programs for the TX-0 computer were written for this computation; a discussion of their properties can be found in the thesis resulting from this work (1).

The result for all subjects, normal and abnormal, was an output impedance that

resembled in every respect the character of a simple spring constant. It is not intuitively obvious that under the conditions of lowpass, random, low-impedance perturbations the deflection at the joint should be proportional to the driving force for frequencies from 0.2 cps to 30 cps. Tracking studies have shown that a sinusoidal signal of sufficiently low frequency can be followed with a very high degree of accuracy. However, with the proper choice of conditions and constraints, it can be shown that the mean-square angular deflection of the limb is a minimum for the output admittance characteristics actually found; that is, $sH(s)$ is a realizable admittance, and the integral squared impulse response is fixed and nonoscillatory (specifically, $|H(\omega)|$ decreases monotonically with ω or is, at most, a constant).

Figure XVI-3 shows autocorrelation functions of the output noise of various subjects and indicates markedly different qualities that result from different nervous disorders. The θ_{rms} figure quoted is the root-mean-square deflection of the tip of the 9-inch splint; a hand "free" means that the subject was holding the splint approximately 6 inches from the pivot, between two finger tips, and with the entire arm supporting itself naturally from the shoulder. The f_{av} is an estimate of the most obvious frequency component present. The origin of time is at the left, and 8.5 seconds of autocorrelation function are shown. The lowest frequency component visible, which also appears to be the frequency of "spindling" of the higher frequencies, is the respiration artifact.

The major effect of the results upon the derivation of a linear model that describes the self-regulating postural mechanism is that the loop gains of the various feedbacks from muscle, joint, and tendon are so large that they mask entirely the mechanical effects of the masses and geometry of the system.

A. R. Johnson

References

1. A. R. Johnson, The Servo-Analysis of Postural Reflexes, Ph. D. Thesis, Department of Electrical Engineering, M. I. T., May 1960.

XVII. CIRCUIT THEORY*

Prof. S. J. Mason
Prof. H. J. Zimmermann
Prof. C. L. Searle
Prof. R. D. Thornton
J. T. Andreika
B. L. Diamond
R. Huibonhoa
W. C. Schwab

A. PHASE INVARIANTS

The circuit significance of the conjunctive, or inert, transformation was discussed in Quarterly Progress Report No. 56 (page 198). It was shown that imbedding an arbitrary network, with admittance [Y], in an inert network (that is, a network that conserves complex power) transforms the admittance by the conjunctive transformation.

$$[Y_1] = [T]^x[Y][T] \qquad (1)$$

$[T]^x$ = conjugate transpose of $[T]$

The purpose of this report is to show some interesting invariant properties of this transformation.

If Y is the admittance of a one-port network, then Eq. 1 may be written $Y_1 = |T|^2 Y$. It is thus apparent that the magnitude of Y_1 can be varied at will by varying the magnitude of T, but the phase angle of Y_1 must equal the phase angle of Y. Since the phase angle is the only invariant for a one-port network, we are encouraged to look for a generalized phase invariant for an n-port network.

Since the eigenvalues of [Y] have many interesting properties, we are led to wonder whether the phase angles of these eigenvalues are ever invariant under a conjunctive transformation. The answer is that they are invariant if $[Y][Y]^x = [Y]^x[Y]$. A matrix that commutes with its conjugate transpose is called "normal"; this class includes as important special cases matrices that are Hermitian, skew-Hermitian, symmetric, skew-symmetric, and/or unitary. The proof that the phase angles of the eigenvalues of a normal matrix are conjunctively invariant is straightforward.

PROOF 1. If [U] is unitary, then $[U]^x = [U]^{-1}$. By a classical theorem, a [U] can always be found to satisfy the relation $[U]^x[Y][U] = [D]$, where [D] contains the eigenvalues of [Y] on the diagonal and zeros elsewhere (1). By dividing the i^{th} row and column by the square root of the magnitude of the i^{th} eigenvalue, we can conjunctively transform Y into a diagonal matrix with the i^{th} diagonal element having unit magnitude and the same phase angle as the i^{th} eigenvalue.

As a practical example of this transformation, we can consider a 2×2 symmetric matrix.

---

*This work was supported in part by Purchase Order DDL B-00306 with Lincoln Laboratory, a center for research operated by Massachusetts Institute of Technology with the joint support of the U.S. Army, Navy, and Air Force under Air Force Contract AF 19(604)-5200.

Let $[Y] = \begin{bmatrix} a & b \\ b & c \end{bmatrix}$; $[Y_1] = [T]^x[Y][T]$

If $[T] = \begin{bmatrix} |w|^2 x^x & wz \\ w^x z^x & |z|^2 y \end{bmatrix}$; with x, y chosen to satisfy relations

$$ax + b(1+xy) + cy = 0$$

$$a^x x + b^x(1+xy) + c^x y = 0$$

and

$$|w|^{-2} = |a|x|^2 + b(x+x^x) + c|$$

$$|z|^{-2} = |a+b(y+y^x)+c|y|^2|$$

then $[Y_1] = \begin{bmatrix} \frac{A}{|A|} & 0 \\ 0 & \frac{B}{|B|} \end{bmatrix}$; A, B = eigenvalues of $[Y] = \frac{a+c}{2} \pm \left[\left(\frac{a-c}{2}\right)^2 + b^2\right]^{1/2}$

Since most nonsymmetric admittance matrices are not normal, we need to find a more general phase invariant. One approach is by analogy with the procedure for finding the phase angle of a scalar. If y is a scalar, we can write

$$y = \exp(\alpha+j\beta); \quad y^x = \exp(\alpha-j\beta); \quad y^{x,-1} = \exp(-\alpha+j\beta)$$

$$yy^{x,-1} = \exp(2j\beta)$$

Thus $\frac{1}{2j} \ln (yy^{x,-1}) = \beta \pm n\pi$, with n an integer. Except for the ambiguity of $\pm n\pi$, we can determine β from $yy^{x,-1}$. We might expect that the eigenvalues of $[Y][Y]^{x,-1}$ are invariant and could be interpreted as $\exp(2j\beta_i)$, where the β_i are the generalized phase invariants. The proof that the eigenvalues of $[Y][Y]^{x,-1}$ are invariant is relatively simple.

PROOF 2. If $[Y_1] = [T]^x[Y_o][T]$

$$\text{then } [Y_1][Y_1]^{x,-1} = [T]^x[Y_o][Y_o]^{x,-1}[T]^{x,-1}$$

$$\text{Hence } \mathrm{ev}\left([Y_1][Y_1]^{x,-1}\right) = \mathrm{ev}\left([Y_o][Y_o]^{x,-1}\right)$$

For the scalar phase relation, $yy^{x,-1}$ always has unit magnitude so that β is a real number. In the matrix relation, however, β may also occur in conjugate pairs. A proof that β must be real or occur in conjugate pairs follows.

PROOF 3. $(\mathrm{ev}[Y][Y]^{x,-1})^{x,-1} = \mathrm{ev}([Y][Y]^{x,-1})^{x,-1} = \mathrm{ev}[Y]^{x,-1}[Y] = \mathrm{ev}[Y][Y]^{x,-1}$

Hence, if $e^{j\beta_i} = \mathrm{ev}_i[Y][Y]^{x,-1}$, then there must be a β_k that satisfies the relation

$$\left(e^{j\beta_i}\right)^{x,-1} = \left(e^{j\beta_i}\right)^{x} = e^{j\beta_k} = \mathrm{ev}_k[Y][Y]^{x,-1}$$

and thus β must be real or occur in conjugate pairs.

One possible interpretation for a complex phase invariant can be deduced from an example. Let

$$[Y] = \begin{bmatrix} 0 & e^{a} \\ -e^{-a} & 0 \end{bmatrix} je^{j\beta}; \quad [Y]^{x,-1} = \begin{bmatrix} 0 & e^{-a} \\ -e^{a} & 0 \end{bmatrix} je^{j\beta} \tag{2}$$

$$[Y][Y]^{x,-1} = \begin{bmatrix} e^{2a} & 0 \\ 0 & e^{-2a} \end{bmatrix} e^{j2\beta}; \quad \frac{1}{2j}\ln\left(\mathrm{ev}[Y][Y]\right)^{x,-1} = \beta \pm ja \pm n\pi$$

The network described by $[Y]$ in Eq. 2 has the property that if it is terminated by equal source and load impedances with phase angles β, then the voltage gain will be e^{a} in one direction and e^{-a} in the other. Thus the imaginary part of the phase invariants is related to the gain of nonreciprocal networks.

The conjugate-pair phase invariants, $\beta \pm ja$, for a two-port network can be calculated as follows:

$$\text{If } [Y] = \begin{bmatrix} a & b \\ c & d \end{bmatrix}; \quad \mathrm{ev}[Y][Y]^{x,-1} = (\cosh 2a \pm \sinh 2a)\, e^{j2\beta}$$

where

$$\cosh 2a = \frac{|b|^2 + |c|^2 - (ad^{x}+a^{x}d)}{2|ad-bc|}; \quad \cos 2\beta = \frac{\mathrm{Re}\,(ad-bc)}{|ad-bc|} \tag{3}$$

If $\cosh 2a$ in Eq. 3 is less than unity, then the phase invariants are both real. Defining these real invariants as β_1 and β_2, we find that

$$\cos(\beta_1-\beta_2) = \frac{(ad^{x}+a^{x}d) - |b|^2 - |c|^2}{2|ad-bc|}; \quad \cos(\beta_1+\beta_2) = \frac{\mathrm{Re}\,(ad-bc)}{|ad-bc|}$$

The eigenvalues of $[Y][Y]^{x,-1}$ alone do not represent a complete set of invariants, and other methods must be used to determine completely a canonic form for Y. The problem of developing a complete and simple canonic form has not been fully solved.

R. D. Thornton

XVIII. NOISE IN ELECTRON DEVICES*

Prof. R. B. Adler
Prof. H. A. Haus
Prof. J. B. Wiesner
R. P. Rafuse

A. PARAMETRIC APPLICATIONS OF SEMICONDUCTOR CAPACITOR DIODES

This research has been completed. The results will be found in a thesis (of the same title) that was presented by R. P. Rafuse to the Department of Electrical Engineering, M. I. T., September 1960, and accepted in partial fulfillment of the requirements for the degree of Doctor of Science.

R. B. Adler

*This research was supported in part by Purchase Order DDL B-00306 with Lincoln Laboratory, a center for research operated by Massachusetts Institute of Technology with the joint support of the U. S. Army, Navy, and Air Force under Air Force Contract AF 19(604)-5200.

XIX. LINGUISTICS

Prof. R. Jakobson
Prof. A. N. Chomsky
Prof. M. Halle
Dr. R. H. Abernathy
Dr. G. H. Matthews
R. J. Parikh

A. MORPHOPHONEMIC CHANGE IN CROW AND HIDATSA

For the protolanguage of Crow and Hidatsa (1), the following three phonetic rules, from among others, are reconstructed. The phonetic rules of a language are ordered rules that indicate how sequences of phonemic, morphophonemic, and junctural symbols are phonetically interpreted (2).

P1. $\left\{\begin{matrix} e \\ o \\ a \end{matrix}\right\} a \longrightarrow a$

This rule states that if a nondiffuse vowel – that is, e, o or a – is immediately followed by the vowel, short a, the nondiffuse vowel becomes a and the original a is lost. By this rule forms like hátthaaci, kunvéaci, and phéaci become hátthaci, kunváci, and phá́ci.

P2. $\overset{+}{v}V_1 \longrightarrow \overset{\acute{}}{V}_1 ? V_1$

This rule states that the morphophoneme $\overset{+}{v}$ is replaced by a vowel that is accented, short, and in all other respects just like the vowel that follows it; and a glottal stop is placed between these two vowels. By this rule forms like kvuaci, kunvaci, and uvā become kú?uaci, kuná?aci, and uá?ā.

P3. ua ⟶ u

If a short a immediately follows the vowel u, the a becomes u and the original u is lost. By this rule forms like kú?uaci, and uá?āci become kú?uci and ú?āci.

Observe the following protolanguage forms that are made up of the verb stems hátha (break), kvu (give), kunve (carry), phé (eat), pvo (blow), and uvā (climb), the noun stem pvoki (feather), and the suffixes aci, which indicates that the action is like that denoted by the preceding verb stem, and ī, which indicates that the action denoted by the preceding verb stem is done repeatedly. These forms are arranged in three pairs of columns; the form of the first of each pair is in the phonemic representation – that is, the form that it has before the application of the phonetic rules – and the form of the second of each pair is its form after the application of the three phonetic rules P1, P2, and P3.

hátha	hátha	háthaaci	háthaci	háthaī	háthaī
kv̌u	kú?u	kv̌uaci	kú?uci	kv̌uī	kú?uī
kunv̌e	kuné?e	kunv̌eaci	kuná?aci	kunv̌eī	kuné?eī
phē	phē	phēaci	phāci	phēī	phēī
pv̌o	pó?o	pv̌oaci	pá?aci	pv̌oī	pó?oī
uv̌ā	ú?ā	uv̌āaci	ú?āci	uv̌āī	ú?āī
pv̌oki	pó?oki				

The forms that occur in Hidatsa can best be explained by postulating two innovations that are applied to the grammar of the protolanguage. The first of these innovations consists of the addition of a morphophonemic rule to the grammar. Morphophonemic rules precede phonetic rules in the grammar of a language and thus have the effect of changing the phonemic representation of the forms of the language; that is, the representation to which the phonetic rules apply. This added morphophonemic rule is

PH1. o| ⟶ u|

That is, morpheme-final o is replaced by u. With the addition of PH1 to the grammar of the protolanguage, a restructuring takes place; that is, the grammar of the protolanguage plus the morphophonemic rule PH1 is replaced by an equivalent, but formally simpler, grammar: Equivalent in that the same sentences are generated, and simpler in that there are fewer rules. This new grammar is the same as the grammar of the protolanguage in all respects except that each morpheme in the grammar that ends with an o is replaced by another that is just like it except that it ends in u. For example, the verb stem pv̌o is replaced by a verb stem pv̌u. Thus, the sentences of the language do not have the forms of the stem pv̌o, instead they have the forms

pv̌u pv̌uaci pv̌uī

The phonetic rules P1, P2, and P3 have come into Hidatsa without any changes; but through the action of the added morphophonemic rule PH1 and the resultant restructuring there are no longer any forms of pv̌o for them to apply to, whereas there are the forms of pv̌u. Thus, the new sequences produced by P1, P2, and P3 are

pú?u pú?uci pú?uī

Note that although the protolanguage form pá?aci becomes, in some sense, Hidatsa pú?uci, it is not true that the phonetic entities of the protolanguage form become individually those of the Hidatsa form; rather, the verb stem pv̌o is replaced by the verb stem pv̌u, and the rules of the grammar apply to pv̌u just as they do to any other verb stem of the language.

The second innovation that is applied to the grammar – that is, to the grammar that exists after the addition of PH1 and the resultant restructuring – is the addition of the

phonetic rule PH2, which follows all of the other phonetic rules of the language.

PH2. $V_1V_2 \longrightarrow V_1 ? V_2$

That is, a glottal stop is inserted between all sequences of two vowels. Since PH2 is a phonetic rule, it applies to the sequences of phonetic entities that result from the application of the other phonetic rules of the language. Thus, the phonetic rules of Hidatsa are those of the protolanguage plus PH2; and the results of the application of these phonetic rules are like those of the protolanguage in the first and second pairs of columns, and the third pair is now

hā́thaī	hā́tha?ī
kv̲uī	kú?u?ī
kunv̲eī	kné?e?ī
phḗī	phḗ?ī
pv̲uī	pú?u?ī
uv̲aī	ú?ā?ī

No restructuring takes place after the addition of PH2, for there is no equivalent but simpler grammar than that of the preceding grammar plus PH2.

The corresponding forms that occur in Crow are also explainable in terms of the grammar of the protolanguage plus several innovations. I shall discuss just one of these innovations – the addition of the morphophonemic rule PC1 after the other morphophonemic rules of the language and before the phonetic rules.

PC1. $\underline{\overset{+}{v}}V_1 \longrightarrow \bar{\acute{V}}_1$

That is, the morphophoneme $\underline{\overset{+}{v}}$ is removed, and the vowel following it is accented and lengthened. With the addition of PC1 to the grammar, a restructuring takes place which consists of replacing each morpheme in the language that contains the sequence $\underline{\overset{+}{v}}V_1$ with one that contains the vowel $\bar{\acute{V}}_1$ instead; and, since now the language no longer contains the morphophoneme $\underline{\overset{+}{v}}$, the phonetic rule P2 can be removed. Instead of forms of the stems kv̲u, kunv̲e, pv̲o, uv̲a, and pv̲oki, the language now contains forms of the stems kú, kné, pó, uá, and póki; and the phonetic rules P1 and P3, which have come into Crow without any changes, apply to these forms:

kū́	kū́	kū́aci	kū́ci	kūī́	kūī́
kné	kné	knéaci	knáci	knéī	knéī
pó	pó	póaci	páci	póī	póī
uá	uá	uáaci	uáci	uáī	uáī
póki	póki				

We have seen that by postulating innovations that are additions of morphophonemic rules to the grammar of the protolanguage – that is, changes that take place on the phonemic rather than on the phonetic level of the sentences of the language – we have been able to explain some of the sound correspondences of Crow and Hidatsa. In particular, we have explained why only three vowels need be reconstructed to account for the six correspondences in the following pairs, in which the first member of each pair is the Hidatsa form and the second member is the Crow form: kú?u/kū, kú?uci/kūci, kuné?e/kunē, kuná?aci/kunāci, pú?u/pō, pú?uci/pāci, and pó?oki/pōki. Note also that the description of the historical development of the forms of Hidatsa pv̆u is given in terms of regular sound change rather than sound change plus analogic change.

G. H. Matthews

References

1. G. H. Matthews, Syntactic change in Crow and Hidatsa, Quarterly Progress Report No. 58, Research Laboratory of Electronics, M.I.T., July 15, 1960, pp. 281-283.

2. M. Halle, Sound Pattern of Russian (Mouton and Company, 's-Gravenhage, 1959).

XX. SENSORY AIDS RESEARCH

Prof. S. J. Mason
J. C. Bliss
D. A. Cahlander
R. J. Dirkman
W. G. Kellner
D. G. Kocher
W. M. Macurdy
R. J. Massa
D. E. Troxel

A. AN ENCODER FOR A GRADE II BRAILLE TYPEWRITER

[This report is a summary of a thesis that was presented by R. J. Dirkman to the Department of Electrical Engineering, May 1960, in partial fulfillment of the requirements for the degree of Master of Science.]

The need for a device with which an operator without a highly specialized knowledge of Braille can transcribe one or more copies of printed material into Braille has long been present.

Standard English Braille is based on a pattern, or cell, containing 6 embossed dots arranged in two columns as shown below. (The vertical and horizontal spacing is 0.1 inch.)

. .
. .
. .

There are 63 possible combinations of these 6 dots which are used to represent letters of the alphabet, numerals, punctuation marks, signs, common groups of letters, and whole words.

Several levels, or "grades," of Standard English Braille are used. Grade I Braille is uncontracted; a one-to-one correspondence exists between the letters of a standard printed text and its Braille counterpart. Grade II Braille is moderately contracted; a total of 185 contractions includes words an common groups of letters that may be used as parts of words. Grade III Braille is a highly contracted form and has limited usage in applications where a short (coded) notation is convenient. Although strictly not a form of Standard English Braille, Grade One-and-a-Half Braille is used to a large extent for general publications.

The contracted forms of Braille result in space economy. For example, Grade II Braille requires an average of 3.5 cells per word, as compared with 5 cells for Grade I Braille.

An encoding system has been developed to facilitate the translation of text material into Grade II Braille. This system, intended for use with a standard typewriter keyboard, requires that the operator recognize the 185 contractions and remember a few simple rules regarding the formation of words.

The output from the encoder may be either an embossing mechanism which forms the dots of the Braille cell directly, or some form of recording equipment. Although it may seem convenient to produce the Braille in a form directly usable by the blind, several advantages result from the use of punched tape. The tape can be used to operate a

variety of secondary devices to produce the embossed Braille. These include plate-embossing machines similar to the stereotyper for automatically producing zinc plates suitable for printing Braille copies of the recording, or Braille reading machines that reproduce temporarily the Braille code recorded on punched tape. Each of these devices has been developed, and efforts are being made elsewhere to improve them.

Provision for correction of errors by the untrained (in Braille) operator would be a desirable feature. Since a typed copy of the material is available for proofreading, a punched tape would be advantageous because corrections can easily be made before the tape is used as an input to the auxiliary devices described above.

The encoding system operates as follows. The typist uses the standard keyboard to type uncontracted text material. The simultaneous use of a letter key and the shift key (indicating a capital letter) results in a two-symbol output (the letter cell preceded by the capital cell). When the typist recognizes a contraction, a foot pedal or similar device is depressed. The typist proceeds to type the letters of the contraction exactly as they appear in the English text. Depressing the contraction key or pedal stores all of the English letters of the contraction. These letters are then compared with all of the contractions in the encoder's memory. When the correct one is found, the encoder will punch out the correct Braille cell, or cells, for the contraction. The speed of the

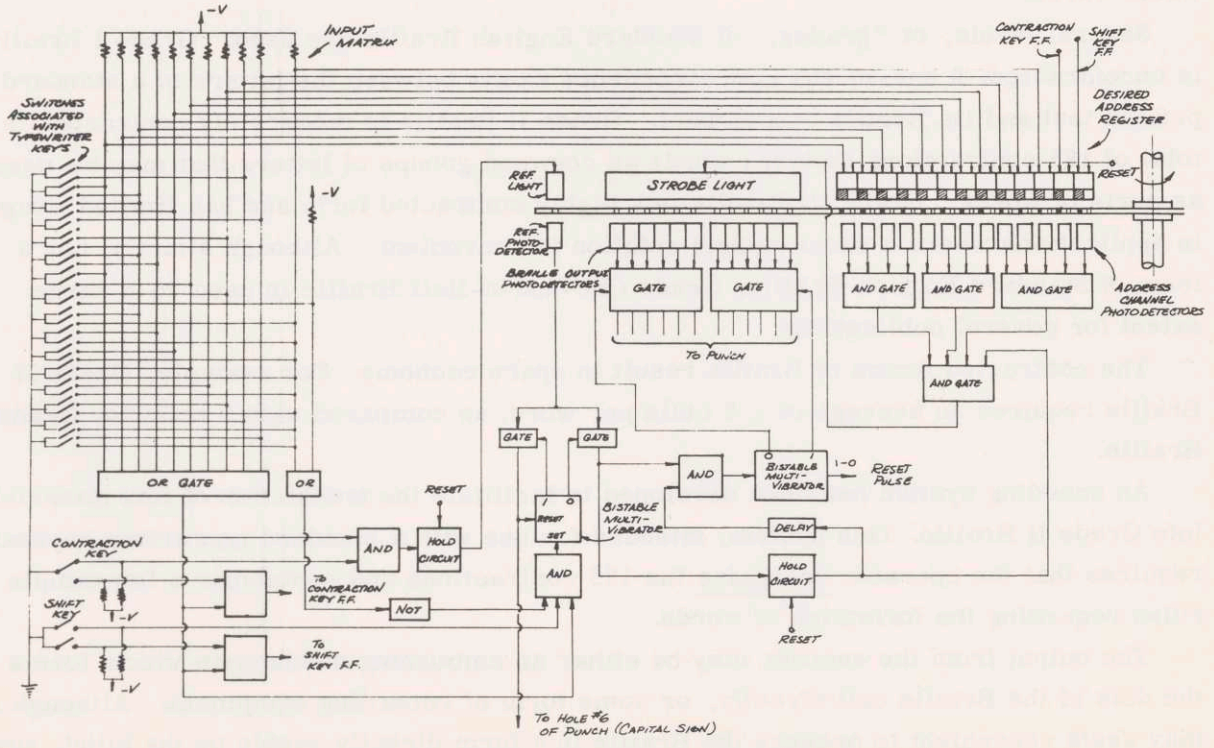

Fig. XX-1. Complete encoder system.

Braille output is sufficient to require no special pause on the part of the typist. It is anticipated that a typist with reasonable training will be able to use such a device at nearly normal typing speed.

The block diagram of the encoder is shown in Fig. XX-1. The keys of the typewriter activate switches that set up the typed symbols in an eleven-bit input code matrix. The machine memory consists of a photographic disk that is rotated at constant speed. The input code lights the right- or left-hand member of a binary light coding address. When a coincidence between the input code and the disk's light and dark coded areas occurs a strobe light is activated. At this time, the disk is in such a position that the proper Braille embosser output code is under the strobe lamp. Thus the correct symbol is printed out. If more than one symbol is required, as in the case of a contraction, the coincidence between input code and rotating disk will remain for several disk positions and the correct sequence of symbols will be printed in order. After a letter or contraction has been printed, the address register is reset and a new input code accepted. Many of the blocks in the diagram of Fig. XX-1 are required only for correct timing.

R. J. Massa

B. TACTILE STIMULATION OF THE FINGERS AS AN INFORMATION INPUT TO THE BLIND

A device has been constructed that permits the presentation of various patterns of poke probes to the eight fingers (thumbs are excluded). Compressed air is valved by an arrangement of flexo tape and brass plates. The air then actuates pneumatic plungers which force the poke probes against the fingers. An arrangement of six probes per finger permits the use of the Braille code for alphanumeric characters.

Preliminary tests were conducted with the following presentation pattern. A single

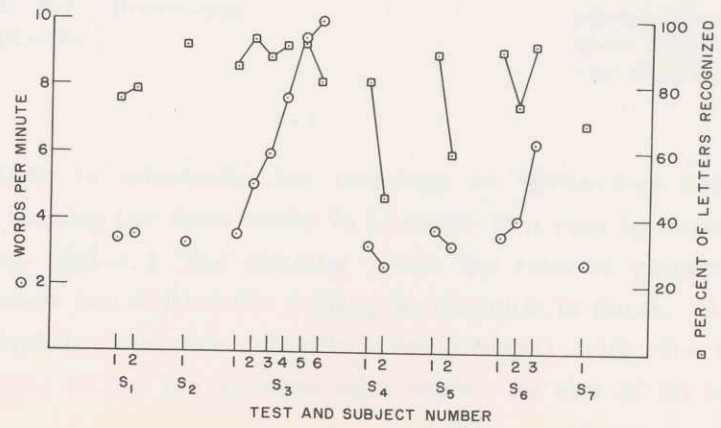

Fig. XX-2. Test results.

letter is presented to one finger at a time; the little finger of the left hand receives the first stimulus, and the other fingers are stimulated sequentially from left to right. This presentation scheme is realized with the aid of essentially two separate air valves. One valve uses only the seventh hole of the flexo tape and selects the finger to be stimulated, while the other employs the other six holes to determine the letter to be presented to a particular finger.

Seven blind subjects were given from one to six tests, each of which consisted of the presentation of 14 three-letter words and nonsense syllables drawn from the first 10 letters of the alphabet. Successive tests were conducted at speeds of 18, 26, 33, 42, 51, and 60 letters per minute, with the exception of the tests for subject No. 1, in which the speed of the first two tests was 18 letters per minute. Reading rates in words per minute are arrived at by multiplying the percentage of letters recognized by the speed in letters per minute and dividing by five. The results of these tests are shown graphically in Fig. XX-2. The percentage of letters recognized that was achieved demonstrated that the blind subjects were able to transfer a considerable amount of their knowledge of the Braille code to the stimulation patterns presented by this device. Two of the subjects exhibited a marked increase in reading rate with a substantially constant recognition percentage. This indicates that further tests should be conducted to determine the reading rates at which their learning curves saturate.

D. E. Troxel

XXI. SHOP NOTES

A. STOPCOCK BRACKET

A bracket for securing a glass stopcock on the flat and sometimes narrow surface of an angle-iron frame was designed several years ago and has been in practical use in the Physical Electronics Laboratory. The bracket is fabricated of sheet aluminum in a way to provide supports and a means of securing the stopcock at the tubulations on both sides of the stopcock barrel; thus a compact self-contained mounting is achieved. (See Fig. XXI-1.)

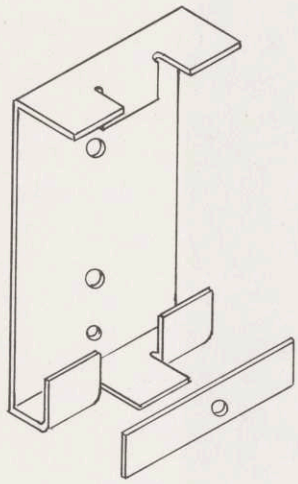

Fig. XXI-1. Bracket showing tabs bent for three-way stopcock.

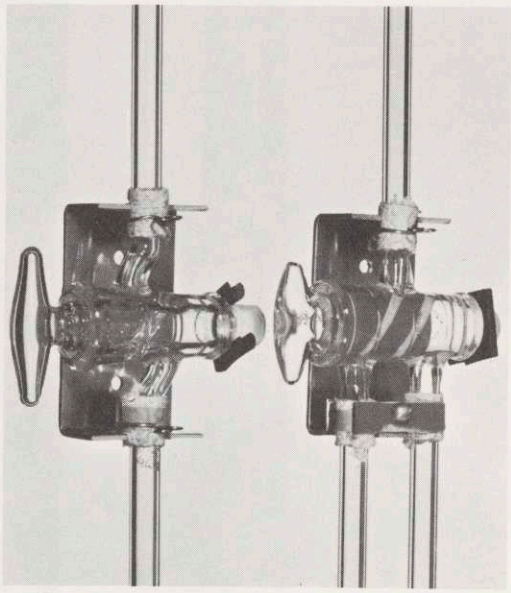

Fig. XXI-2. Two-way and three-way stopcocks attached to brackets to show relative sizes of bracket and stopcock.

The same blank is adaptable for two-way or three-way stopcocks by suitably bending the tabs, leaving the final bends to be made in a vise by hammering the tabs into position. (See Fig. XXI-2.) The spacing under the tabs is maintained with a spacing block. Mounting holes are drilled for bolting the bracket in place. A variety of mounting positions are possible such as mounting the bracket with the barrel perpendicular to the surface, as on the surface of a table, by use of an additional L-shaped bracket.

The bracket is particularly useful when it becomes necessary to add another

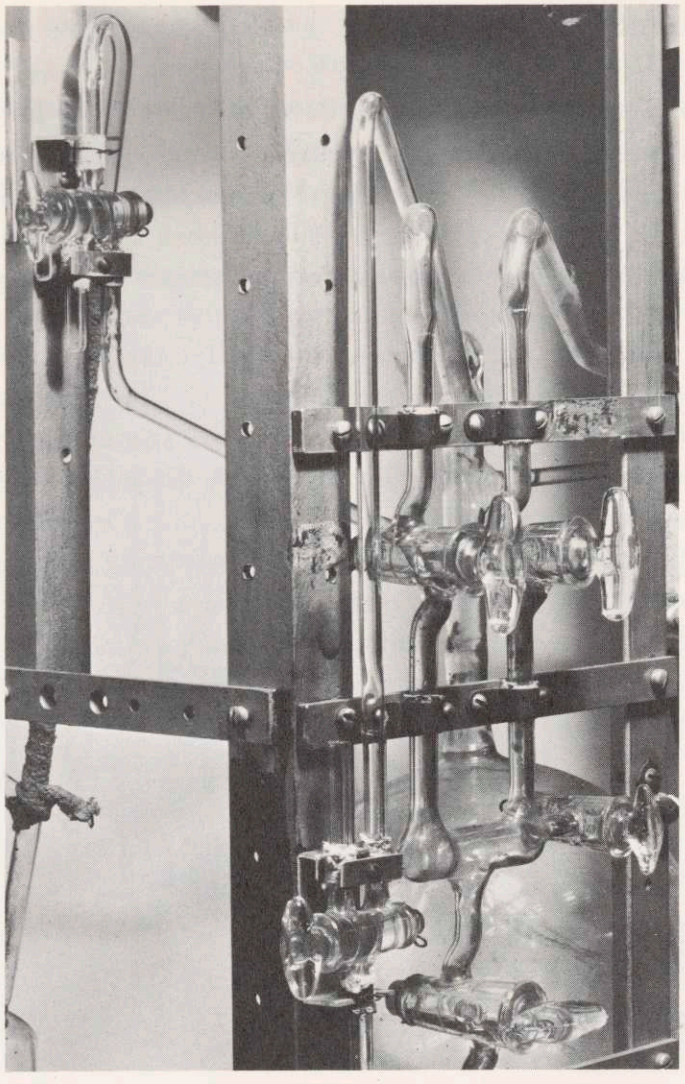

Fig. XXI-3. Brackets in position on a vacuum system.

stopcock to an existing system or when the space available may be hardly greater than the size of the stopcock itself. (See Fig. XXI-3.)

Rescaling the dimensions makes the design usable for a stopcock of any size.

L. E. Sprague